

Dynamic crack propagation in brittle materials : analyses based on fracture and damage mechanics

Citation for published version (APA):

Vroonhoven, van, J. C. W. (1996). *Dynamic crack propagation in brittle materials : analyses based on fracture and damage mechanics*. [Phd Thesis 1 (Research TU/e / Graduation TU/e), Mechanical Engineering]. Technische Universiteit Eindhoven. <https://doi.org/10.6100/IR456465>

DOI:

[10.6100/IR456465](https://doi.org/10.6100/IR456465)

Document status and date:

Published: 01/01/1996

Document Version:

Publisher's PDF, also known as Version of Record (includes final page, issue and volume numbers)

Please check the document version of this publication:

- A submitted manuscript is the version of the article upon submission and before peer-review. There can be important differences between the submitted version and the official published version of record. People interested in the research are advised to contact the author for the final version of the publication, or visit the DOI to the publisher's website.
- The final author version and the galley proof are versions of the publication after peer review.
- The final published version features the final layout of the paper including the volume, issue and page numbers.

[Link to publication](#)

General rights

Copyright and moral rights for the publications made accessible in the public portal are retained by the authors and/or other copyright owners and it is a condition of accessing publications that users recognise and abide by the legal requirements associated with these rights.

- Users may download and print one copy of any publication from the public portal for the purpose of private study or research.
- You may not further distribute the material or use it for any profit-making activity or commercial gain
- You may freely distribute the URL identifying the publication in the public portal.

If the publication is distributed under the terms of Article 25fa of the Dutch Copyright Act, indicated by the "Taverne" license above, please follow below link for the End User Agreement:

www.tue.nl/taverne

Take down policy

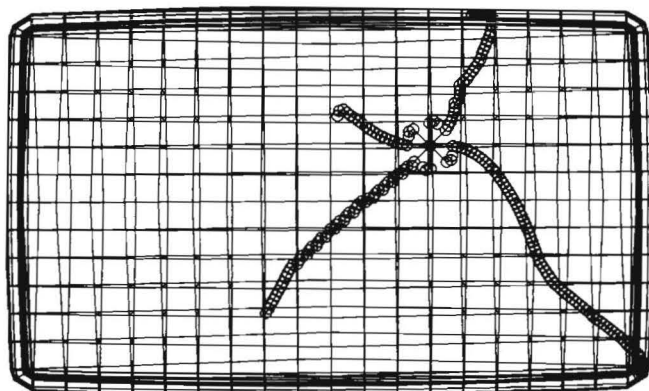
If you believe that this document breaches copyright please contact us at:

openaccess@tue.nl

providing details and we will investigate your claim.

Dynamic Crack Propagation in Brittle Materials: Analyses Based on Fracture and Damage Mechanics

Jos van Vroonhoven



**Dynamic Crack Propagation
in Brittle Materials:
Analyses Based on Fracture
and Damage Mechanics**

CIP-GEGEVENS KONINKLIJKE BIBLIOTHEEK, DEN HAAG

van Vroonhoven, Jozef Cornelis Walterus

Dynamic Crack Propagation in Brittle Materials: Analyses Based on Fracture and Damage Mechanics / J.C.W. van Vroonhoven.

Eindhoven: Philips Natuurkundig Laboratorium.

Thesis: Eindhoven University of Technology.

With references and summaries in English and Dutch.

Subject headings: fracture mechanics, damage mechanics, finite-element analysis, cathode-ray tubes.

ISBN 90-74445-23-3

On the cover: calculated crack pattern in screen of unsafe television picture tube without the metal rimband, caused by a ball-drop impact at the D-point.

© Philips Electronics N.V. 1996

The work presented in this thesis has been carried out at the Philips Research Laboratories in Eindhoven, the Netherlands, as part of the Philips Research programme.

**Dynamic Crack Propagation
in Brittle Materials:
Analyses Based on Fracture
and Damage Mechanics**

PROEFSCHRIFT

ter verkrijging van de graad van doctor aan de Technische Universiteit Eindhoven, op gezag van de Rector Magnificus, prof.dr. J.H. van Lint, voor een commissie aangewezen door het College van Dekanen in het openbaar te verdedigen op donderdag 29 februari 1996 om 16.00 uur

door

Jozef Cornelis Walterus van Vroonhoven

geboren te Eindhoven

Dit proefschrift is goedgekeurd door de promotoren:

prof.dr.ir. R. de Borst

prof.dr. J. Boersma

en de copromotor:

dr.ir. A.A.F. van de Ven

Kreeft: ... Het gevoel voor Schoonheid is het exclusieve gebied van Bewuste Geesten, geesten die door hun levenservaring een diepte hebben bereikt die zich aan verklaring door een pover stel regels onttrekt.

Achilles: Deze heldere verklaring van Schoonheid zal me altijd bijblijven. Ik neem aan dat iets dergelijks ook voor Waarheid geldt?

Kreeft: Zonder twijfel. Waarheid en Schoonheid hangen met elkaar samen als – als –

Achilles: Als, laat ik zeggen, wiskunde en muziek?

Uit: Douglas R. Hofstadter,
Gödel, Escher, Bach: een eeuwige gouden band.

Samenvatting

Nieuwe typen televisiebeeldbuizen moeten voldoen aan strenge eisen betreffende de veiligheid van de glasballon, voordat de nieuwe buizen op de markt geïntroduceerd mogen worden. Voor het testen van de veiligheid zijn internationale standaards zoals de „ball-drop test” ontwikkeld. Eén van de eisen bij deze test is dat er geen implosie van de beeldbuis optreedt, wanneer het glazen scherm wordt onderworpen aan een inslag van een stalen bal met voorgeschreven afmeting, gewicht en valhoogte. Beperkte scheurgroei is toegestaan. Het doel van het in dit proefschrift beschreven onderzoek is het ontwikkelen van analytische en numerieke methoden voor het berekenen van scheurgroei tijdens de ball-drop test en voor het bepalen van de glasveiligheid van nieuwe beeldbuisontwerpen. Het onderzoek heeft geleid tot twee nieuwe methoden voor de analyse van dynamische scheurgroei in brosse materialen: (i) de ontkoppelde dynamische breukaanpak en (ii) de hybride breuk/schade-aanpak.

De ontkoppelde dynamische breukaanpak is gebaseerd op de breukmechanica en op een (gedeeltelijke) ont koppeling van spanningsgolven en scheurgroei. Enerzijds wordt de scheurgroei bepaald door de spanningen in het materiaal. Anderzijds leidt scheurgroei tot een verandering van de geometrie en aldus tot een verstoring van de spanningsverdeling. Dit laatste effect wordt in de ontkoppelde aanpak buiten beschouwing gelaten. De methode bestaat uit twee delen. Eerst worden de dynamische spanningen als gevolg van de bal-inslag berekend met behulp van de eindige-elementenmethode, waarbij wordt aangenomen dat er geen scheurvorming optreedt. Vervolgens worden mogelijke scheurpatronen berekend op basis van deze spanningsgegevens. Door toepassing van de ontkoppelde aanpak op eenvoudige voorbeelden en op televisiebeeldbuizen zijn betrouwbare resultaten voor de scheurpatronen verkregen. Vanwege de relatief korte rekentijden is de ontkoppelde dynamische breukaanpak een efficiënte methode voor het analyseren van dynamische scheurgroei.

De hybride breuk/schade-aanpak is gebaseerd op een combinatie van breukmechanica en schademechanica in de context van de eindige-elementenmethode. Bij de punt van de scheur wordt breukmechanica toegepast. Het singuliere spanningsgedrag wordt beschreven met speciale elementen en de scheurgroei wordt berekend met behulp van bekende breukcriteria. De „staart” van de scheur wordt uitgesmeerd over een gebied met eindige breedte, waar schademechanica toegepast wordt en elementen met een verminderde elasticiteitsmodulus gebruikt worden. De interactie tussen spanningsgolven en scheurgroei wordt in deze aanpak volledig in rekening gebracht. Aangezien de resultaten van analyses met schademechanica vaak afhangen van de elementbreedte en van de elementenoriëntatie, zijn er diverse berekeningen uitgevoerd om de betrouwbaarheid van de hybride aanpak te onderzoeken. De resultaten laten zien, dat de berekende scheurpatronen niet afhangen van de elementenverdeling en steeds maximaal één element verwijderd zijn van de exacte scheurpatronen die volgen uit experimenten of theoretische beschouwingen. Deze resultaten worden beoordeeld als voldoende nauwkeurig. Ondanks de grote rekentijden blijkt de hybride breuk/schade-aanpak een bruikbare methode te zijn voor het berekenen van dynamische scheurgroei in twee-dimensionale en in eenvoudige drie-dimensionale structuren.

Summary

New designs of television picture tubes or cathode-ray tubes must satisfy strict requirements regarding the safety of the glass bulb, before the new tubes are allowed to be introduced into the market. To test the safety, international standards like the “ball-drop test” have been developed. This test demands that no implosion of the tube should occur, when the glass screen is subjected to an impact by a steel ball of prescribed size, weight, and energy. Limited crack propagation is permitted. The aim of the research presented in this thesis is to develop analytical and numerical methods for the calculation of crack propagation during the ball-drop test and for the determination of the glass safety of new tube designs. Two new methods for the analysis of dynamic crack propagation in brittle materials are proposed: (i) the uncoupled dynamic fracture approach and (ii) the hybrid fracture/damage approach.

The uncoupled dynamic fracture approach is based on fracture mechanics and on a (partial) uncoupling of stress waves and crack propagation. On the one hand, the crack propagation is determined by the stresses in the material. On the other hand, crack propagation leads to a change in the geometry and, thus, to a disturbance of the stress distribution. The latter effect is disregarded in the uncoupled approach. The method consists of two parts. First, the dynamic stresses due to the ball impact are calculated with the use of the finite-element method, where it is assumed that no crack initiation occurs. Next, possible crack patterns are calculated from these stress data. Reliable results for the crack patterns have been obtained from applications of the uncoupled approach to simple examples and to television picture tubes. Because of the relatively short computing times, the uncoupled dynamic fracture approach proves to be an efficient method for the analysis of dynamic crack propagation.

The hybrid fracture/damage approach is based on a combination of fracture mechanics and continuum damage mechanics within the context of the finite-element method. At the crack tip, fracture mechanics is employed. The singular stress behaviour is described by special elements and the crack propagation is calculated with the use of well-established fracture criteria. The “tail” of the crack is smeared out over a region of finite width, where damage mechanics is employed and elements with a reduced modulus of elasticity are used. The interaction between stress waves and crack propagation is fully incorporated in this approach. Since the results of analyses with continuum damage mechanics often depend on the element width and the element orientation, several calculations have been performed to investigate the reliability of the hybrid approach. The results reveal that the calculated crack paths do not depend on the element division and are always at most one element away from the exact crack paths that follow from experiments or theoretical considerations. These results are regarded as sufficiently accurate. Despite the large computing times, the hybrid fracture/damage approach appears to be a useful method for the calculation of dynamic crack propagation in two-dimensional and in simple three-dimensional structures.

Contents

Samenvatting	i
Summary	ii

I General 1

1 Introduction 3

1.1 Safety tests for television picture tubes	4
1.2 Fracture and damage mechanics	6
1.3 Analysis and approach	8
1.4 Outline of the thesis	11

2 Basic equations of mechanics 13

2.1 Deformation of linearly elastic bodies	13
2.2 Planar deformation	15
2.3 Anti-plane deformation	16
2.4 Plate bending	17

II Fracture Mechanics 25

3 Fracture mechanics concepts 27

3.1 Fracture in planar deformation	28
3.2 Fracture in anti-plane shear	34
3.3 Energy release rate	36
3.4 Fracture criteria	38
3.5 Effects of dynamic crack propagation	42

4 Fracture in plate bending 47

4.1 Bending fracture in Reissner's plate theory	48
4.2 Bending fracture in classical plate theory	55
4.3 Comparison of plate bending theories	63
4.4 Comparison with anti-plane shear	66
4.5 Combined tension and bending	68
4.6 Effects of crack closure	70
4.7 Effects of dynamic crack propagation	73
4.8 Conclusions	75

5	Curvilinear cracks	77
5.1	Planar deformation	77
5.2	Anti-plane deformation	80
5.3	Plate bending	91
5.4	Comparison of stress-intensity factors	103
5.5	Conclusions	105
6	Uncoupled fracture approach	107
6.1	Description of the method	107
6.2	Superposition principle	110
6.3	Application to standard tests	112
6.4	Application to television picture tubes	116
6.5	Conclusions	120
III	Damage Mechanics	121
7	The finite-element method	123
7.1	Concepts of the finite-element method	123
7.2	Standard finite elements	125
7.3	Singular elements for fracture	127
7.4	Softening elements for damage	129
7.5	Improved elements for bending and torsion	131
8	Hybrid fracture/damage approach	139
8.1	Discussion of continuum damage mechanics	139
8.2	Description of the hybrid approach	142
8.3	Extension to three dimensions	146
8.4	Time-step algorithm	147
8.5	Application to standard tests	149
8.6	Application to television picture tubes	155
8.7	Conclusions	157
IV	Conclusion and Perspective	159
9	Conclusion	161
9.1	The uncoupled dynamic fracture approach	161
9.2	The hybrid fracture/damage approach	162
9.3	Analysis of television picture tubes	163
10	Perspective	165
10.1	On fracture and damage mechanics	165
10.2	On finite-element technology	166

Appendices	168
A On path-independent integrals	171
A.1 Various integration contours	171
A.2 Calculation for planar deformation	173
A.3 Calculation for classical plate theory	174
B On double integrals	175
B.1 Formula of Poincaré-Bertrand	175
B.2 Solution for plate bending	176
C On damage and thermodynamics	179
C.1 Clausius-Duhem inequality	179
C.2 Isotropic damage	182
C.3 Orthotropic damage	183
C.4 Positive definite functions	185
Bibliography	187
Curriculum vitae	194
Dankwoord	195

Part I
General

Chapter 1

Introduction

Since the beginning of the twentieth century the theories of fracture and damage have evolved from ad-hoc simple models for specific mechanical problems to mature sciences in their own right. The pioneering work of Griffith [31] provided a first step towards the understanding of material failure. It was not until the destructive period of World War II, however, that the importance of examining fracture phenomena was fully perceived. From that time on, the interest in fracture mechanics has steadily increased. Investigations of Irwin [41, 42] and Orowan [70] have led to the evolution of energy concepts of fracture and the inclusion of plasticity effects. Contributions of various authors on the fundamentals of fracture are gathered in the series edited by Liebowitz [52].

A new approach to failure was proposed by Kachanov [44] and developed further in recent years among others by Chaboche [14, 15, 16] and Lemaitre [50]. Failure of a construction was not regarded as rupture of the material but as deterioration (softening) due to internal damage. Contrary to fracture mechanics where crack growth is synonymous to geometrical changes, these models assume a continuous, deformable body where failure is interpreted as a change in material structure. This new field of science is therefore named continuum damage mechanics.

Both theories, fracture and damage, are considered in this thesis and are applied to dynamic crack propagation in brittle materials. The dynamic effects are incorporated in the analyses; these effects include the crack-growth speed, accelerations, and wave propagation. We restrict ourselves to brittle materials without microstructure, like glass.

The specific area of application is the safety tests for television picture tubes or cathode-ray tubes. The background of this research is explained below. Because of the particular problems encountered in the study of dynamic brittle fracture, two new approaches are presented: (i) an uncoupled dynamic fracture approach in which the interaction between stress waves and crack propagation is only partially incorporated, and (ii) a hybrid fracture/damage approach in which the two theories are combined.

1.1 Safety tests for television picture tubes

New designs of television picture tubes must satisfy special requirements regarding the safety of the glass bulb. During operation, unintended mechanical hazards may occur. For example, the glass front screen may be hit by a sharp or hard object. When such a mechanical hazard occurs, the glass will fracture and crack patterns are formed in the screen. One cannot expect that the television set remains undamaged in such situations, because the strength of glass is limited. The TV will evidently have reached the end of its life, but it is undesirable that the impact leads to an implosion of the television tube. Since accidents cannot be avoided, special safety tests have been developed. All new designs of television tubes must satisfy very strict test requirements, before they are allowed to be introduced into the market.

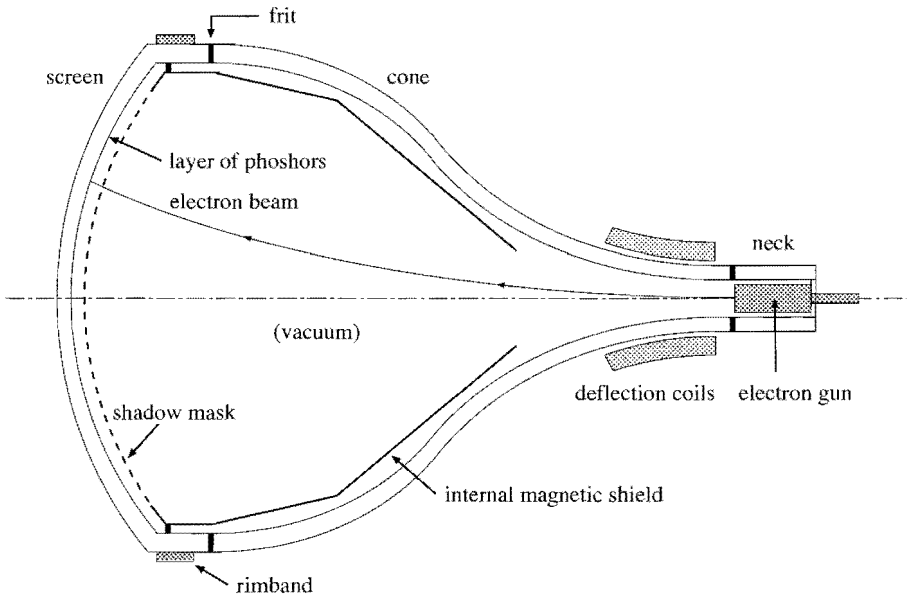


Figure 1.1: Cross section of television picture tube.

We start with a description of the TV-tube geometry and an explanation of frequently used terms. A cross section of a television picture tube is schematically shown in Fig. 1.1. The screen, the cone, and the neck are glass components which are sealed together by melting or with the use of frit. The combination of screen, cone and neck is called the glass bulb. The electron gun is located in the neck and contains the cathode which emits an electron beam. The electrons are deflected by a magnetic field generated by a set of deflection coils. The electrons pass the shadow mask, a perforated thin metal sheet which also serves as anode, and arrive at a (red, green or blue) phosphor dot. To protect from external magnetic fields which may distort the

deflection of the electron beam, an internal shield is added. The glass bulb with the shadow mask, the internal magnetic shield, the deflection coils, and the electron gun is called a cathode-ray tube or a television (picture) tube. When the tube is built into its housing and is completed with loudspeakers and additional electronics, it is called a television set.

Inside the television picture tube there is vacuum, which is required for a proper functioning of the electron gun. The internal vacuum introduces high compressive and tensile stresses in the glass. In order to alleviate these high tensile stresses, a metal rimband is added to the construction around the outer edge of the glass screen. The rimband is applied by heating and subsequent cooling. As a result, it shrinks around the screen boundary and induces extra compressive stresses, which partially compensate the tensile stress introduced by the internal vacuum of the tube. Practical experience reveals that the rimband pressure has a strong negative effect on possible crack propagation and thus a positive effect on the safety of the design.

We now turn to the impact safety tests. We distinguish between the “ball-drop test” and the “missile test” which are described in the documents of the Netherlands Norm and European Standard NEN-EN 60065 [26, 64] and of the Canadian Standard Association CAN/CSA and Underwriters Laboratory UL 1418 [12]. The first test, the ball-drop test, demands that no implosion of the tube should occur when a steel ball of pre-specified weight hits the screen. The impact position and impact energy are also prescribed according to the international test standards. The second test is the so-called missile test in which a heavy steel projectile is used in order to enforce an implosion of the television tube. In addition, scratches have been applied to the screen at critical positions. Cracks may initiate at these scratches and also at the point of impact. Both tests impose severe restrictions to the glass deposition. The maximum allowed weight of all glass particles that are blown away further than a critical distance from the TV set is limited to only a few grams.

The response of the television tube to the ball-drop and missile tests is essentially a dynamic process. In this process four different stages are distinguished, dependent on the time elapsed since the moment of impact:

1. Impact of the steel ball. Because of the contact between ball and screen, a Hertzian cone crack is created. This is a cone-shaped crack which starts near the boundary of the contact area between ball and screen and propagates through the thickness of the glass. As a consequence, a hole is punched out of the glass screen. This stage also involves the initiation of cracks originating from the hole and the initiation of stress waves in the glass. (For a discussion of Hertzian cone cracks we refer to Li and Hills [51] and for an extensive treatise of contact mechanics to Johnson [43].)
2. Dynamic fracture (crack and wave propagation). The stress waves which are initiated by the impact propagate through the screen. This gives rise to a dynamic stress state which will induce crack growth. Since the impact zone is embrittled by the punching of the hole, there are many small cracks. Only a

few of these cracks will extend and propagate over larger distances. Of course, this is influenced by the stress state. On the other hand, the propagating cracks will disturb the dynamic stresses. So, there exists an interaction between the fracture process and the stress waves.

3. Crack arrest or collapse. The requirement of the ball-drop test is that the tube does not implode. This means that all propagating cracks must stop. Crack growth requires energy. Therefore, crack arrest will occur when the amount of available energy is not sufficient to create new crack surfaces. If this is not the case or if the impact energy is too large (e.g. in the missile test), the tube will implode.
4. Glass deposition. When the tube collapses, the glass screen is fractured into smaller and larger pieces. The devacuation of the tube (ending the internal vacuum) involves an in-flow of air, resulting in the glass particles being blown away from the TV set.

The analysis of the dynamic and fracture phenomena in all these stages becomes increasingly complicated in course of time. The impact stage is well defined and the initiation of cracks and waves can be described with reasonably simple methods. The next stage of dynamic fracture becomes more difficult, but despite its complexity it is a challenging problem to tackle. This second stage of the fracture process is decisive for the next two stages: depending on the direction of crack propagation and the final length of the cracks, either crack arrest will occur or the tube will collapse. This also depends on the glass thickness which increases from the central region to the screen boundary and on the local stresses in the glass. Regarding the fourth and last stage of the impact tests involving the deposition of the glass, it is almost impossible to determine the final position of each glass particle after collapse.

The research presented in this thesis is focused on the ball-drop test. The main objective is the development of analytical and numerical methods for the calculation of the dynamic response of a television tube to a mechanical impact and for the determination of the glass safety of a given tube design. These methods can be used as design tools for the optimisation of the product itself and of the manufacturing processes. The formation of crack patterns plays a central role in the safety tests. Namely, the direction of crack propagation is of major importance in determining whether an implosion may occur and thus whether a tube design is safe or not. Since the crack propagation is influenced by the dynamic stresses in the glass, the analysis is based on the research disciplines dynamics, fracture mechanics, and continuum damage mechanics.

1.2 Fracture and damage mechanics

The analysis of fracture phenomena in brittle materials focuses on stress concentrations in the vicinity of crack tips. A crack introduces a discontinuity in the elastic

body and, within the scope of linear elasticity theory, the crack tip becomes a singular point where the stresses attain infinite values. The singular behaviour of the stress components is proportional to the inverse square root of the distance to the crack tip and the singularity is normalised by stress-intensity factors. This relationship is illustrated in Fig. 1.2 and can be represented in the simplified form

$$\sigma = \frac{K}{\sqrt{2\pi r}}, \quad (1.1)$$

where σ denotes the stress and r is the distance to the crack tip. The parameter K is a stress-intensity factor related to the external forces and the boundary conditions. A common fracture criterion for brittle materials is that crack extension will occur when the stress-intensity factor reaches a critical value, the fracture toughness, which is a material constant; see Broek [11] and Cherepanov [18]. As long as K is below this upper bound, the crack remains stationary.

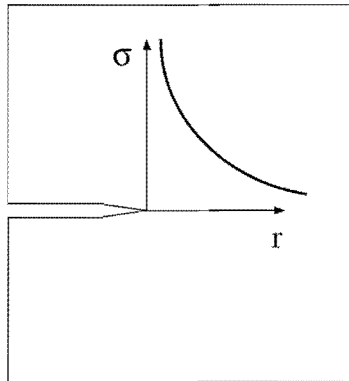


Figure 1.2: Stress singularity at crack tip.

From (1.1) it is clear that the yield stress will be exceeded at positions sufficiently close to the tip of the crack, introducing local plasticity and causing the material to flow. For ductile materials this plastic behaviour is essential in the fracture analysis. For brittle materials, however, there exists only limited plasticity or small-scale yielding which is confined to a very small neighbourhood around the crack tip; see England [22] and Rice [76, 77]. The principle of stress-intensity factors can thus be used for a wide class of brittle fracture problems.

The theory of continuum damage mechanics follows a different approach. Instead of a material discontinuity, the crack is modelled in a continuous, smeared way and internal parameters are introduced to represent material damage. The physical crack is replaced by a small zone where the material stiffness (the modulus of elasticity) is reduced. The interpretation is straightforward: the material strength decreases due to the presence of microscopic flaws or due to failure of molecular bonds; see Fig. 1.3.

This method works quite well for constructions where the damage stretches out over larger areas, such as materials with ductile or viscoplastic behaviour. It is believed that we can also obtain reliable results for brittle materials. The introduction of internal damage parameters affects the constitutive stress-strain relations. Basically, this is characterised by

$$\sigma = (1 - \mathcal{D}) E \varepsilon, \quad (1.2)$$

where σ and ε denote the stress and the strain, E is the Young's modulus of the original undamaged material, and \mathcal{D} a damage parameter. With the definition of the effective elasticity modulus $E_d = (1 - \mathcal{D})E$, the usual relationship $\sigma = E_d \varepsilon$ recurs. Adopting distinct relations (1.2) in different directions, we may obtain anisotropic behaviour of the damaged material.

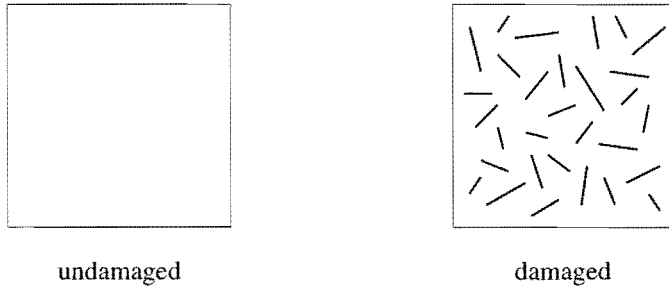


Figure 1.3: Material damage caused by microcracks.

The introduction of damage parameters implies that extra relations are needed to describe the rate of damage increase $\dot{\mathcal{D}}$ as a function of the stresses or strains and of the actual damage itself. This damage-evolution equation is usually chosen as an exponential relation. Chaboche [16] and Kachanov [44] suggest for example for creep damage

$$\dot{\mathcal{D}} = A \sigma^\alpha (1 - \mathcal{D})^{-\beta}, \quad (1.3)$$

where the scaling constant and the exponents are material-dependent constants to be determined experimentally. Although this extra equation prevents the mathematical formulation of the problem from being incomplete, other peculiarities of continuum damage mechanics will occur in practical applications.

1.3 Analysis and approach

The finite-element method has proved to be an efficient means for the solution of complicated mechanical problems involving non-linear constitutive behaviour and/or large geometries; see Hughes [37], MacNeal [56] and Zienkiewicz [100]. Standard elements have linear or quadratic interpolation of the displacements and, consequently,

the internal stresses are constant or linear. In fracture-mechanics applications it is necessary to describe the singular stresses (1.1) correctly. It is evident that standard finite elements cannot be used. To overcome this difficulty, special crack-tip elements have been developed, which include the stress singularity either by interpolation of the displacements with the use of square-root functions (Stern and Becker [86, 87]) or by application of quarter-point nodes on the element sides adjacent to the crack tip (Barsoum [3]).

The major advantage of fracture-mechanics methods is that they have been studied extensively such that a broad range of applicability has been found, and that these methods possess a high degree of accuracy. A strong disadvantage, however, occurs when the finite-element method is applied to problems of dynamic crack propagation. Because of the material rupture and the creation of new crack surfaces, the geometry of the elastic body changes continuously. This necessitates a continuous adaptation of the element mesh, a shift of the singular crack-tip elements to the new position of the crack tip, and an interpolation of the mechanical quantities from the old to the new element division. An overview of computational studies on dynamic crack propagation, including moving-finite-element techniques, is presented by Nishioka, Murakami and Takemoto [68]. In such procedures, the crack path is often assumed to be straight or otherwise to be known beforehand. When the crack propagates along an arbitrary curved path, many elements must be adapted. Since the assembly of all element contributions into one global stiffness matrix requires much computing time, a full-scale dynamic fracture analysis will be very time-consuming and is therefore considered inappropriate for the present impact problem. Two alternative methods for failure analysis are proposed.

1.3.1 Uncoupled dynamic fracture approach

An uncoupled fracture approach is proposed, based on dynamic stress calculations for the undamaged configuration. The dynamic response of the television tube to the impact is determined first with the use of the finite-element method and standard finite elements. It is assumed that the glass screen remains linearly elastic and that fracture does not occur. Afterwards, as a form of post-processing, predictions of crack patterns are derived from the dynamic stress data. The interaction between the crack propagation and the stress waves (as described at point 2 in Section 1.1) has only partially been accounted for in this uncoupled analysis, because the disturbing effect of the crack growth on the stress situation is neglected. Also, the mutual influence of multiple cracks is not incorporated. Of course, it cannot be expected that this uncoupled approach will produce highly accurate results for the entire fracture process, especially near the moment of collapse or implosion. Nevertheless, it is possible to analyse the first and second stages of crack growth with reasonable accuracy.

The great benefit of the uncoupled approach is that a fixed finite-element division is sufficient and that mesh adaptation is not necessary. In addition, several independent crack patterns can be determined from one dynamic stress calculation, which implies a

considerable reduction of computing time in comparison with a fully-coupled fracture analysis. Since the initial stages of fracture are of crucial importance for the overall safety of the television tube, it is sufficient to study the first and second stages of the impact tests. This corresponds precisely to the range of validity of the uncoupled fracture approach. Therefore, it is expected that the uncoupled approach will produce useful results with rather limited effort.

1.3.2 Hybrid fracture/damage approach

In order to include the interaction between dynamic stresses and crack growth in a coupled failure approach, the possible applications of continuum damage mechanics are investigated. Regarding finite-element implementations, there is a great advantage of damage-mechanics methods over fracture-mechanics methods. Namely, continuous mesh adaptation has become superfluous, because changes in the geometry do not occur. Instead, the elasticity parameters are adapted. There also exist some complications, however. The local damage-evolution law (1.3) for instance can be chosen rather arbitrarily, as long as it agrees with the global material response. Moreover, severe material degradation may lead to softening behaviour: the internal stresses decrease with increasing strain. As a result, the mathematical formulation of the problem becomes ill-posed. In such cases, it is often seen that the damage increase is highly susceptible to small variations in the local stress values and in the finite-element division, leading to pathological mesh dependences. On the one hand, these dependences concern the width of the damaged zone: refinement of the element mesh generally leads to higher values of the damage parameters in a region of smaller width. This effect is referred to as “localisation” and has been studied by various authors [4, 5, 49, 71, 85]. These papers are discussed in Section 8.1. On the other hand, the orientation of the finite elements plays an important role: it is often seen that damage accumulation appears along element boundaries and not in the required direction as derived from a fracture-mechanics analysis. This problem even occurs for simple geometries. These drawbacks restrict the applicability of continuum damage mechanics in its original form.

Because of the particular disadvantages of both fracture and damage mechanics, application of either method to problems of dynamic crack propagation was considered as not appropriate. Focusing on the positive aspects of the two theories, Horsten and van Vroonhoven [36] developed the idea of a hybrid fracture/damage approach. This approach consists of the following details. Subsequent positions of the crack tip are calculated, such that the crack path is known at every moment of the fracture process. Since the local stresses in the vicinity of the crack must be known with highest possible accuracy, fracture mechanics is employed and the special elements with singular stress behaviour are used at the crack tip. In order to avoid large-scale mesh adaptations, continuum damage mechanics is utilised to describe the “tail” of the crack. At these positions the modulus of elasticity is reduced in the direction perpendicular to the surfaces of the crack. In fact, we should not speak of a crack in the strict sense but of a damaged zone, since there is no geometrical discontinuity in the material.

This hybrid approach combines the accuracy of the singular crack-tip elements in fracture mechanics and the flexibility of crack representation in damage mechanics, such that the necessary mesh alterations during crack growth are avoided. Thus, we have developed an effective means for the analysis of crack propagation in combination with the finite-element method. We shall investigate the possible mesh dependences which often occur in damage-mechanics applications. These dependences must be excluded to ensure the correctness of the hybrid fracture/damage approach.

1.4 Outline of the thesis

Part I: General

The thesis is divided into four parts which successively focus on a general introduction, the uncoupled dynamic fracture approach, the hybrid fracture/damage approach, and a discussion of the results. The first part is concluded by Chapter 2 in which the basic equations of mechanics are summarised for later reference. The problems of plane stress and anti-plane shear and two theories for plate bending are presented for general dynamic loading conditions. In addition, formulations in terms of complex holomorphic functions are given for situations of static deformation.

Part II: Fracture Mechanics

This part focuses on the uncoupled dynamic fracture approach and starts with an overview of well-known fracture concepts in Chapter 3. This includes a discussion of: the principle of brittle fracture, stress-intensity factors, the three distinct modes of fracture, the energy release rate, and fracture criteria. The near-tip distributions of the stresses and displacements are given for both stationary and dynamically propagating cracks. Furthermore, the effect of rapid crack propagation on the elastodynamic stress-intensity factors is considered.

Chapter 4 is devoted to the fracture of thin plates by bending moments. This study is required in view of the perpendicular impact loading which involves considerable bending deformation. Two plate bending theories based on different assumptions are employed: the classical theory of Kirchhoff and the refined theory of Reissner. The near-tip bending moments, shear forces, rotations, and deflections are examined and expressed in terms of new bending stress-intensity factors. The correspondences and differences between both theories are investigated and a comparison with anti-plane deformation is made. In addition, the effects of crack closure and the combination of tension and bending are analysed.

Since crack propagation does not necessarily occur along straight lines, a study of stress-intensity factors for curvilinear cracks is performed in Chapter 5. This concerns planar deformation, anti-plane deformation, as well as out-of-plane bending. The

analysis is based on the theory of complex functions. The resulting expressions are utilised in the uncoupled dynamic fracture approach in Chapter 6. Applications to several test problems and to television picture tubes are presented.

Part III: Damage Mechanics

In the third part we explain the hybrid fracture/damage approach. The theoretical and numerical aspects necessary for a successful combination of fracture and damage mechanics are worked out in more detail. In Chapter 7 we discuss the essentials of the finite-element method, including the singular crack-tip elements for fracture applications and the softening elements for damage applications. Since bending deformation is important to the television impact problem, extra attention is given to the bending behaviour of the finite elements.

Chapter 8 starts with a critical review of continuum damage mechanics and continues with the implementation of the hybrid fracture/damage approach in a finite-element method. The elements of Chapter 7 are utilised in a specific combination, such that the dynamic fracture behaviour of brittle materials is described in a numerically effective manner. The hybrid approach is applied to fracture simulations of test specimens and television picture tubes.

Part IV: Conclusion and Perspective

Finally, in Chapter 9, we review the results of the theoretical studies on fracture in plate bending and on curvilinear cracks. We compare the results of the various numerical calculations performed with the use of the uncoupled dynamic fracture approach and the hybrid fracture/damage approach. The results of applications on television picture tubes are summarised. Open ends of the present research and some options for future research are put into perspective in Chapter 10.

Chapter 2

Basic equations of mechanics

In this chapter we present an overview of the equations that form the basis of the mathematical analysis of mechanics problems. Since these basic equations will be used frequently throughout this thesis, a summary is presented here for later reference. Derivations are not given but can be found in the literature as indicated. We restrict ourselves to the theory of small deformations or linear elasticity theory.

The first section deals with the loading of general three-dimensional configurations. The next sections focus on specific geometries and deformation situations, such as plane strain, (generalised) plane stress, and anti-plane shear. The equations for the bending of thin flat plates are also presented. We shall adopt classical plate theory and Reissner's theory. The analysis is restricted to isothermal situations; temperature effects are thus not included.

2.1 Deformation of linearly elastic bodies

Consider a deformable body consisting of a homogeneous, isotropic, linearly elastic material. The body comprises a domain $V \subset \mathbf{R}^3$ and is subjected to prescribed displacements and (time-dependent) forces on its outer boundary ∂V . In addition, volume forces may exist. The material behaviour is characterised by the Young's modulus of elasticity E , the Poisson contraction ratio ν , and the shear modulus $G = E/2(1 + \nu)$, while the density of the material equals ρ .

The deformation of the body is expressed in terms of displacements u_i , strains ε_{ij} , and stresses σ_{ij} , with respect to a Cartesian coordinate system $\{\mathbf{e}_x, \mathbf{e}_y, \mathbf{e}_z\}$, and with indices $i, j = x, y, z$. The notation $_{,i}$ is adopted for differentiation with respect to the coordinate i , while a superposed dot is used for the derivative with respect to time t . In addition, the Kronecker delta δ_{ij} is introduced, which equals 1 for $i = j$ and 0 for $i \neq j$, and the Einstein convention of summation over repeated indices is employed.

The deformation problem is described by kinematic relations, constitutive relations,

the equations of motion, and suitable boundary conditions; see Eringen [25, Sec. 6.5]. The prescribed displacements and the externally applied forces on the boundary ∂V are given by \bar{u}_i and \bar{p}_i , respectively, while the components of the outward normal to ∂V are denoted by n_i . The volume forces are equal to \bar{f}_i . The dynamic problem for deformation of a three-dimensional linearly elastic body is then formulated as follows. The static problem is obtained by putting $\rho \ddot{u}_i = 0$.

Problem of elastic deformation: determine displacements u_i , strains ε_{ij} , and stresses σ_{ij} as sufficiently smooth functions of x, y, z and t , satisfying the equations (with indices $i, j, k = x, y, z$)

$$\varepsilon_{ij} = \frac{1}{2}(u_{i,j} + u_{j,i}), \quad (2.1)$$

$$\sigma_{ij} = 2G \left(\varepsilon_{ij} + \frac{\nu}{1-2\nu} \varepsilon_{kk} \delta_{ij} \right), \quad (2.2)$$

$$\sigma_{ij,j} + \bar{f}_i = \rho \ddot{u}_i, \quad (2.3)$$

in the domain V occupied by the elastic body and subject to the conditions

$$u_i = \bar{u}_i \quad \text{on } S_u, \quad (2.4)$$

$$\sigma_{ij} n_j = \bar{p}_i \quad \text{on } S_p, \quad (2.5)$$

on the boundary $\partial V = S_u \cup S_p$ with S_u and S_p being disjoint.

For the dynamic problem additional initial conditions for the displacements u_i and their time derivatives \dot{u}_i are required. In most applications the volume forces \bar{f}_i will be disregarded. Because of the linearity of the equations, the superposition principle applies. This means that problems for general loading situations can be separated into several simpler problems which are analysed independently. After the separate analyses, the total deformation of the linearly elastic body is obtained by summation of all individual responses.

Elimination of the strains and the stresses from the relations (2.1)–(2.3) produces

$$u_{i,jj} + \frac{1}{1-2\nu} u_{j,ji} = \frac{\rho}{G} \ddot{u}_i, \quad (2.6)$$

which are known as the Navier differential equations for the displacements. It has been shown by Sternberg [88] that the solution to these equations can be written as the sum of the gradient of a scalar potential $\phi = \phi(x, y, z, t)$ and the curl of a divergence-free vector potential $\boldsymbol{\psi} = \psi_i(x, y, z, t) \mathbf{e}_i$, which is the Helmholtz additive decomposition. In vector notation this reads as

$$\mathbf{u} = \nabla \phi + \nabla \times \boldsymbol{\psi}, \quad \nabla \cdot \boldsymbol{\psi} = 0, \quad (2.7)$$

where bold-faced letters are used to indicate vectors. The potential functions satisfy appropriate wave equations

$$\phi_{,ii} - \frac{1}{c_d^2} \ddot{\phi} = 0, \quad (2.8)$$

$$\psi_{i,jj} - \frac{1}{c_s^2} \ddot{\psi}_i = 0, \quad (2.9)$$

where the dilatational and shear wave speeds for general three-dimensional problems are defined by

$$c_d = \sqrt{\frac{2G(1-\nu)}{\rho(1-2\nu)}}, \quad (2.10)$$

$$c_s = \sqrt{\frac{G}{\rho}}. \quad (2.11)$$

It is noted that $c_s < c_d$. The completeness of the representation (2.7)–(2.9) for the solutions to (2.6) has been proven in [88] and it is emphasised that the potential functions can be time-dependent, even in the case of static elasticity problems. This is explained as follows. When the potential functions are independent of time, the displacements satisfy the Laplace equation because of (2.8)–(2.9). Since this class of displacements is too much restricted in comparison with the general solution to the equation (2.6) with $\ddot{u}_i = 0$, the completeness of the representation (2.7) would be violated.

2.2 Planar deformation

The three-dimensional deformation problem in its general form is difficult to solve. However, several simplifications can be made when the elastic body has a certain degree of symmetry. For example, suppose the body has large thickness and let the z -axis coincide with the thickness direction. Assume that the deformation only occurs in the x - and y -directions and is independent of z . This is the situation of plane strain, because the displacement u_z and the strain components ε_{iz} ($i = x, y, z$) vanish. As a result, the shear stress components σ_{xz} and σ_{yz} are equal to zero, while the normal stress in the z -direction is derived from

$$\sigma_{zz} = \nu(\sigma_{xx} + \sigma_{yy}). \quad (2.12)$$

The problem of plane strain is similar to (2.1)–(2.5) but is reducible to two dimensions. All quantities are independent of the variable z and the indices are restricted to x, y . The elastic body may be taken as two-dimensional, occupying the domain V in the xy -plane with the boundary ∂V being a curve.

Another example of planar deformation concerns thin plate-like structures. Let the z -axis be perpendicular to the plate, while the x - and y -axes are in the plane of the plate. Now, it is assumed that the normal and shear stresses in the z -direction are zero, i.e., $\sigma_{iz} = 0$ for $i = x, y, z$. Thus, a situation of plane stress is obtained. Consequently, the shear strain components ε_{xz} and ε_{yz} are zero, while the strain in the z -direction is determined by

$$\varepsilon_{zz} = -\frac{\nu}{1-\nu}(\varepsilon_{xx} + \varepsilon_{yy}). \quad (2.13)$$

In many practical cases the stresses σ_{iz} only vanish after integration over the thickness of the plate. Obviously, the averaged quantities do not depend on the perpendicular

z -coordinate. This procedure results in the following problem which is usually referred to as generalised plane stress.

Problem of plane stress: determine displacements u_i , strains ε_{ij} , and stresses σ_{ij} as sufficiently smooth functions of x , y and t , satisfying the equations (with indices $i, j, k = x, y$)

$$\varepsilon_{ij} = \frac{1}{2}(u_{i,j} + u_{j,i}), \quad (2.14)$$

$$\sigma_{ij} = \frac{E}{1-\nu^2} \left((1-\nu)\varepsilon_{ij} + \nu\varepsilon_{kk}\delta_{ij} \right), \quad (2.15)$$

$$\sigma_{ij,j} = \rho\ddot{u}_i, \quad (2.16)$$

in the plane domain V occupied by the plate and subject to the conditions

$$u_i = \bar{u}_i \quad \text{on } S_u, \quad (2.17)$$

$$\sigma_{ij}n_j = \bar{p}_i \quad \text{on } S_p, \quad (2.18)$$

on the boundary $\partial V = S_u \cup S_p$ with S_u and S_p being disjoint.

Since $E/(1-\nu^2)$ equals $2G/(1-\nu)$, the problems of plane strain and of (generalised) plane stress are identical when the Poisson's ratio ν of plane strain is replaced by the quotient $\nu/(1+\nu)$. The shear modulus G is equal for both problems, while the Young's modulus E for plane stress corresponds to $E/(1-\nu^2)$ for plane strain.

The displacement solutions to the problems of plane strain and of (generalised) plane stress admit the representation (2.7) in terms of potential functions. Because of the geometrical simplifications, the scalar potential $\phi = \phi(x, y, t)$ is independent of z , whereas the vector potential has the form $\boldsymbol{\psi} = \psi(x, y, t)\mathbf{e}_z$. These functions satisfy the respective wave equations (2.8)–(2.9), where the summation over the repeated indices is now restricted to two dimensions ($i, j = x, y$). In the case of plane stress, the Poisson ratio must be adapted as described above, so that the velocities of the dilatational and shear waves become

$$c_d = \sqrt{\frac{2G}{\rho(1-\nu)}} = \sqrt{\frac{E}{\rho(1-\nu^2)}}, \quad (2.19)$$

$$c_s = \sqrt{\frac{G}{\rho}}. \quad (2.20)$$

2.3 Anti-plane deformation

Suppose that the thickness of the elastic body is large and let the z -axis again be in the thickness direction. Assume that the deformation occurs only in this direction and is independent of z . Thus, the displacements u_x and u_y vanish and the only non-zero strains and stresses are the xz - and yz -components. It is customary to denote

the shear stresses by τ_{iz} with $i = x, y$. Since the displacement is perpendicular to the xy -plane, this type of deformation is called anti-plane shear. The elastic body may be taken as two-dimensional, occupying the domain V in the xy -plane with the boundary ∂V being a curve. From (2.1)–(2.5) the following problem is deduced.

Problem of anti-plane shear: determine displacement u_z , strains ε_{iz} , and shear stresses τ_{iz} as sufficiently smooth functions of x, y and t , satisfying the equations (with index $i = x, y$)

$$\tau_{iz} = 2G \varepsilon_{iz} = G u_{z,i}, \quad (2.21)$$

$$\tau_{iz,i} = \rho \ddot{u}_z, \quad (2.22)$$

in the two-dimensional domain V occupied by the elastic body and subject to the conditions

$$u_z = \bar{u}_z \quad \text{on } S_u, \quad (2.23)$$

$$\tau_{iz} n_i = \bar{p} \quad \text{on } S_p, \quad (2.24)$$

on the boundary $\partial V = S_u \cup S_p$ with S_u and S_p being disjoint.

For the static problem with $\rho \ddot{u}_z = 0$, the displacement satisfies the Laplace equation $\Delta u_z = u_{z,ii} = 0$. Consequently, the normal displacement can be written as the real part of a complex holomorphic function $\phi(z)$ of the complex variable $z = x + iy$; see Cherepanov [18]. The function $\phi(z)$ and its derivative $\Phi(z) = \phi'(z)$ are holomorphic (or analytic) in the plane region occupied by the elastic body with possible cuts from internal holes to the outer boundary. Because of the two-dimensional geometry, no confusion with the perpendicular coordinate z can arise. If necessary, the latter coordinate will be denoted by x_3 . The displacement and the two stress components are now written in the form

$$u_z = \operatorname{Re} \phi(z), \quad (2.25)$$

$$\tau_{xz} - i \tau_{yz} = G \Phi(z). \quad (2.26)$$

The holomorphic function $\phi(z)$ is fully determined by the boundary conditions and by additional conditions at singular points such as crack tips.

2.4 Plate bending

Another simplification of the general three-dimensional deformation problem arises for elastic bodies with relatively small thickness, such as thin flat plates. Whereas the plane stress problem was concerned with planar loading of these geometries, this section deals with loading by out-of-plane bending moments.

Two different theories have been developed for the analysis of plate bending: the classical theory of Kirchhoff (see Timoshenko and Woinowsky-Krieger [90]) and the

more refined theory of Reissner [74, 75]. In both theories it is assumed that there is no deformation in the middle plane of the plate and that the normal stress in the direction perpendicular to the plate can be neglected. The differences concern among others the in-plane displacements and the rotations in the middle plane. Historically, the classical theory was developed prior to Reissner's theory, but for a better understanding of plate bending problems the latter will be discussed first.

2.4.1 Reissner's plate theory

Let the z -axis be in the direction perpendicular to the plate, with $z = 0$ along the middle plane and $z = \pm h/2$ along the upper and lower planes of the plate, where h is the plate thickness. The in-plane coordinates are denoted by x and y . Bending problems are usually formulated in terms of moment and stress resultants. These cross-sectional quantities are obtained by integration of the stresses over the thickness of the plate (see Mindlin [59] and Reissner [75]):

$$M_{ij} = \int_{-h/2}^{+h/2} \sigma_{ij} z \, dz, \quad (2.27)$$

$$Q_i = \int_{-h/2}^{+h/2} \sigma_{iz} \, dz, \quad (2.28)$$

where $i, j = x, y$. On the basis of these representations the in-plane and transverse stresses are approximated by linear and quadratic functions in z , respectively. Taking $\sigma_{ij} = 0$ for $z = 0$ and $\sigma_{iz} = 0$ for $z = \pm h/2$, with $i, j = x, y$, we may write

$$\sigma_{ij} = \frac{6 M_{ij}}{h^2} \cdot \frac{2z}{h}, \quad (2.29)$$

$$\sigma_{iz} = \frac{3 Q_i}{2h} \left(1 - \left(\frac{2z}{h} \right)^2 \right), \quad (2.30)$$

while the stress component σ_{zz} is assumed to vanish [74, 75].

The moment and stress resultants are coupled with the displacements by constitutive relations and elasticity constants. Instead of the Young's modulus E and the shear modulus G , new parameters are introduced for the analysis of plate bending. The bending rigidity D_b and the shear stiffness D_s are defined by

$$D_b = \frac{E h^3}{12(1 - \nu^2)}, \quad (2.31)$$

$$D_s = k G h, \quad (2.32)$$

where the constant k is the shear-correction factor. Strictly speaking, one must take $k = 1$ which corresponds with the exact three-dimensional theory. Reissner [74, 75] has shown by a variational method based on the elastic strain energy that $k = 5/6$ yields better results, although an inconsistency occurs. Mindlin [59] has adopted the value $k = \pi^2/12$ in his study of rotatory inertia and shear corrections in the wave

equations for plate bending. We shall adhere to Reissner's choice. With these bending constants the wave speeds (2.19)–(2.20) can be written as

$$c_d^2 = \frac{12 D_b}{\rho h^3}, \quad (2.33)$$

$$c_s^2 = \frac{6 D_b (1 - \nu)}{\rho h^3} = \frac{6 D_s}{5 \rho h}. \quad (2.34)$$

In Reissner's plate theory, it is assumed that infinitesimal fibers which are initially straight and perpendicular to the middle plane of the plate remain straight during deformation but may rotate over small angles Θ_x and Θ_y in the xz - and yz -planes. These angles are independent of the out-of-plane displacement (deflection) of the plate. The in-plane displacements are then given by [59, 74]

$$u_i = -z \Theta_i, \quad (2.35)$$

with $i = x, y$, while the out-of-plane displacement is assumed independent of z and written as $u_z = w(x, y)$. The function w is called the deflection of the plate. In his later work [75], Reissner showed that this function can be regarded as a weighted average of the out-of-plane displacement u_z over the plate thickness. A similar statement was made about the rotations. The expressions (2.35) and the relation $u_z = w$ are only approximations, which is due to the inconsistency appearing any plate theory. The rotation angles and the deflection are defined in [75] as

$$\Theta_i = -\frac{6}{h^2} \int_{-h/2}^{+h/2} \frac{2z}{h} u_i dz, \quad (2.36)$$

$$w = \frac{3}{2h} \int_{-h/2}^{+h/2} \left(1 - \left(\frac{2z}{h}\right)^2\right) u_z dz. \quad (2.37)$$

Analogous to the strains ε_{ij} in planar deformation, curvatures κ_{ij} are introduced as derivatives of the rotation angles. The equilibrium equations (2.3) are integrated over the plate thickness in a manner similar to (2.27)–(2.28). The boundary of the plate can be subjected to prescribed rotations and deflections and to prescribed bending moments and shear forces. The equations for plate bending due to dynamic loading are now given below; see also [59, 74, 75]. The corresponding static problem is obtained by putting $\frac{1}{12} \rho h^3 \ddot{\Theta}_i = 0$ and $\rho h \ddot{w} = 0$.

Problem of plate bending in Reissner's theory: determine deflection w , rotations Θ_i , curvatures κ_{ij} , bending moments M_{ij} , and shear forces Q_i as sufficiently smooth functions of x , y and t , satisfying the equations (with indices $i, j, k = x, y$)

$$\kappa_{ij} = \frac{1}{2} (\Theta_{i,j} + \Theta_{j,i}), \quad (2.38)$$

$$M_{ij} = -D_b \left((1 - \nu) \kappa_{ij} + \nu \kappa_{kk} \delta_{ij} \right), \quad (2.39)$$

$$Q_i = D_s (w_{,i} - \Theta_i), \quad (2.40)$$

$$M_{ij,j} - Q_i = -\frac{1}{12} \rho h^3 \ddot{\Theta}_i, \quad (2.41)$$

$$Q_{i,i} = \rho h \ddot{w}, \quad (2.42)$$

in the plane domain V occupied by the plate and subject to the conditions

$$\Theta_i = \bar{\Theta}_i \quad \text{on } S_\theta, \quad (2.43)$$

$$M_{ij} n_j = \bar{M}_i \quad \text{on } S_m, \quad (2.44)$$

on the boundary $\partial V = S_\theta \cup S_m$ with S_θ and S_m being disjoint, and

$$w = \bar{w} \quad \text{on } S_w, \quad (2.45)$$

$$Q_i n_i = \bar{Q} \quad \text{on } S_q, \quad (2.46)$$

on the boundary $\partial V = S_w \cup S_q$ with S_w and S_q being disjoint.

2.4.2 Classical plate theory

The classical theory of plate bending is based on the idea that infinitesimal fibers which are initially straight and perpendicular to the middle plane of the plate remain straight *and* perpendicular to the middle plane during deformation; see Timoshenko and Woinowsky-Krieger [90]. In other words, the shear strains ε_{xz} and ε_{yz} vanish. This is a stronger assumption than in Reissner's theory. One might also say that the shear stiffness D_s of the plate has an infinite value. Consequently, the relation (2.40) no longer applies and the rotations are equal to the gradient of the deflection:

$$\Theta_i = w_{,i}. \quad (2.47)$$

The in-plane displacements are then determined by the relations

$$u_i = -z w_{,i}, \quad (2.48)$$

for index $i = x, y$, while the curvatures are the second derivatives of the deflection, $\kappa_{ij} = w_{,ij}$. It is customary to substitute this relation into (2.39)–(2.41) and omit the kinematic relations (2.38).

Because of the connection (2.47), the boundary conditions (2.43) and (2.45) are no longer independent. The rotation $\Theta_s = w_{,s}$ in the tangential direction is completely determined by the boundary's deflection, but the rotation $\Theta_n = w_{,n}$ in the normal direction can still be prescribed as an independent condition. Similarly, the normal bending moment M_{nn} of (2.44) can be prescribed independently, while the torsional moment M_{ns} and the perpendicular shear force Q_n of (2.46) are related. The conditions for M_{ns} and Q_n are combined into one boundary condition for the generalised shear force $Q_n + M_{ns,s}$. Thus, it is sufficient to prescribe two independent boundary conditions on the boundary ∂V instead of three. This fact was first recognised by Kirchhoff. For further details we refer to [90]. The classical problem of plate bending is now given below.

Problem of plate bending in the classical theory: determine deflection w , bending moments M_{ij} , and shear forces Q_i as sufficiently smooth functions of x , y and t , satisfying the equations (with indices $i, j, k = x, y$)

$$M_{ij} = -D_b \left((1 - \nu) w_{,ij} + \nu w_{,kk} \delta_{ij} \right), \quad (2.49)$$

$$M_{ij,j} - Q_i = -\frac{1}{12} \rho h^3 \dot{w}_{,i}, \quad (2.50)$$

$$Q_{i,i} = \rho h \ddot{w}, \quad (2.51)$$

in the plane domain V occupied by the plate and subject to the conditions

$$w_{,n} = \bar{\Theta}_n \quad \text{on } S_\theta, \quad (2.52)$$

$$M_{nn} = \bar{M}_n \quad \text{on } S_m, \quad (2.53)$$

on the boundary $\partial V = S_\theta \cup S_m$ with S_θ and S_m being disjoint, and

$$w = \bar{w} \quad \text{on } S_w, \quad (2.54)$$

$$Q_n + M_{ns,s} = \bar{Q} \quad \text{on } S_q, \quad (2.55)$$

on the boundary $\partial V = S_w \cup S_q$ with S_w and S_q being disjoint.

In the case of a static analysis, one must put $\frac{1}{12} \rho h^3 \dot{w}_{,i} = 0$ and $\rho h \ddot{w} = 0$ in (2.50) and (2.51). Doing so, we observe that the deflection satisfies the biharmonic equation $\Delta \Delta w = w_{,iijj} = 0$. As a result, the solution to the static plate-bending problem can be represented in terms of complex holomorphic functions; see Savin [80, Ch. VI]. These representations are similar to those of Muskhelishvili [63] for problems of planar deformation. We introduce the complex coordinate $z = x + iy$ and denote the perpendicular coordinate by x_3 to avoid confusion. Now, there exist complex functions $\phi(z)$, $\psi(z)$, with derivatives $\Phi(z) = \phi'(z)$, $\Psi(z) = \psi'(z)$, and primitive function $\chi(z)$ with $\chi'(z) = \psi(z)$, which are holomorphic (or analytic) in the plane domain occupied by the plate with possible cuts from internal holes to the outer boundary, such that the displacements, the bending moments and the shear forces can be expressed as

$$w = \operatorname{Re} \{ \bar{z} \phi(z) + \chi(z) \}, \quad (2.56)$$

$$u_x + i u_y = -x_3 \left[\phi(z) + z \overline{\phi'(z)} + \overline{\psi(z)} \right], \quad (2.57)$$

$$M_{xx} + M_{yy} = -2(1 + \nu) D \left[\Phi(z) + \overline{\Phi(z)} \right], \quad (2.58)$$

$$M_{xx} - M_{yy} + 2i M_{xy} = -2(1 - \nu) D \left[z \overline{\Phi'(z)} + \overline{\Psi(z)} \right], \quad (2.59)$$

$$Q_x - i Q_y = -4D \Phi'(z), \quad (2.60)$$

where the notation $D = D_b$ is used for simplicity.

It proves convenient to eliminate the functions $\psi(z)$ and $\Psi(z)$ by the introduction of two new complex functions

$$\omega(z) = z \overline{\phi'(\bar{z})} + \overline{\psi(\bar{z})}, \quad (2.61)$$

$$\Omega(z) = \omega'(z) = z \overline{\Phi'(\bar{z})} + \overline{\Psi(\bar{z})}, \quad (2.62)$$

which have the property that the conjugates $\overline{\omega(\bar{z})}$ and $\overline{\Omega(\bar{z})}$ are holomorphic in the region occupied by the plate. In terms of these functions, the relations (2.56), (2.58) and (2.60) remain unaltered, while the relations (2.57) and (2.59) change into

$$u_x + i u_y = -x_3 \left[\omega(\bar{z}) + (z - \bar{z}) \overline{\phi'(z)} + \phi(z) \right], \quad (2.63)$$

$$M_{xx} - M_{yy} + 2i M_{xy} = -2(1 - \nu)D \left[\Omega(\bar{z}) + (z - \bar{z}) \overline{\Phi'(z)} - \overline{\Phi(z)} \right]. \quad (2.64)$$

The holomorphic functions are completely determined by the boundary conditions, by additional conditions at singular points such as crack tips, and by extra conditions for the single-valuedness of the displacements in the case of multiply connected domains.

As mentioned above, the torsional moment and the perpendicular shear force on the boundary cannot be described independently and are combined into the generalised shear force (2.55). One may also express the boundary condition (2.55) in terms of the generalised torque. With \mathbf{x}_0 being an arbitrary but fixed point in the domain V , this quantity is defined for any \mathbf{x} in V by

$$M_{ns}^* = M_{ns} + \int_{\mathbf{x}_0}^{\mathbf{x}} Q_n ds. \quad (2.65)$$

The parameter s is the arc length and the normal and tangential vectors, \mathbf{n} and \mathbf{s} , are chosen such that $\mathbf{n} \times \mathbf{s} = \mathbf{e}_3$. In the case of multiply connected domains, we must apply cuts from internal holes to the outer boundary. The generalised torque is determined up to an additional constant due to the arbitrariness of \mathbf{x}_0 . The definition (2.65) is also unique because of local equilibrium. Namely, for any closed contour L with interior $A \subset V$ such that $\partial A = L$, we have

$$\int_L Q_n ds = \int_{\partial A} Q_i n_i ds = \int_A Q_{i,i} ds = 0. \quad (2.66)$$

Thus, the definition of the generalised torque is independent of the choice of the arc from \mathbf{x}_0 to \mathbf{x} . The representation of the generalised torque with respect to a Cartesian coordinate system is not symmetric. The quantities M_{xy}^* and M_{yx}^* are different and are given by

$$M_{xy}^* = M_{xy} + \int_{y_0}^y Q_x dy, \quad (2.67)$$

$$M_{yx}^* = M_{yx} + \int_{x_0}^x Q_y dx. \quad (2.68)$$

According to Savin [80, Ch. VI], the perpendicular shear force acting on an arbitrary arc AB with normal and tangential vectors satisfying $dz/ds = i(n_x + i n_y)$, equals

$$\begin{aligned} \int_A^B Q_n ds &= \operatorname{Re} \left\{ \int_A^B (Q_x - i Q_y) (n_x + i n_y) ds \right\} \\ &= 2i D \left[\Phi(z) - \overline{\Phi(z)} \right]_A^B. \end{aligned} \quad (2.69)$$

The normal bending moment M_{nn} and the generalised torque M_{ns}^* are given by

$$\begin{aligned} M_{nn} + i M_{ns}^* + i C &= M_{nn} + i M_{ns} + i \int_{s_0}^s Q_n ds + i C \\ &= (1 - \nu) D \left[\kappa \Phi(z) + \overline{\Phi(z)} - \left(\Omega(\bar{z}) + (z - \bar{z}) \overline{\Phi'(z)} - \overline{\Phi(z)} \right) (n_x - i n_y)^2 \right], \end{aligned} \quad (2.70)$$

where C is an arbitrary real integration constant. The parameter κ differs from the usual values for planar deformation; for bending problems it is given by

$$\kappa = -\frac{3 + \nu}{1 - \nu}. \quad (2.71)$$

Part II

Fracture Mechanics

Chapter 3

Fracture mechanics concepts

The basic principles of fracture mechanics have been summarised briefly in Section 1.2 of the introductory chapter and will be discussed here in more detail. The description of stress concentrations in the vicinity of cracks in brittle materials is based on stress-intensity factors K which are normalising constants for the singular stresses near the crack tip as demonstrated by the relation (1.1). Brittle fracture is characterised by the occurrence of small-scale yielding (see England [22] and Rice [76, 77]) as opposed to ductile fracture where larger areas of plasticity are present. The yielding is confined to a small area, the fracture-process zone. This zone is immediately surrounded by a region, where the material remains linearly elastic and the singular stress field applies, which is therefore called the region of K -dominance.

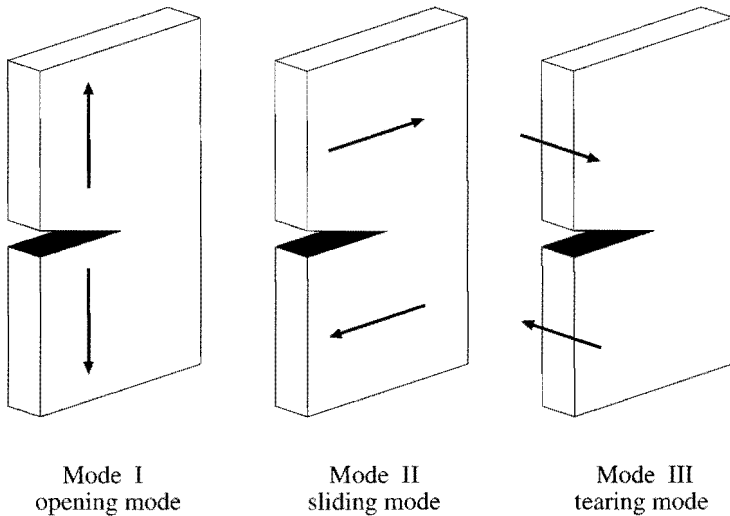


Figure 3.1: Three modes of fracture.

The concepts of linear elastic fracture mechanics are illustrated on the basis of the problems of planar deformation and of anti-plane shear. Three distinct modes of fracture may occur, depending on the orientation of the applied loads with respect to the crack; see Fig. 3.1. A crack is an internal boundary of the elastic body where the material is discontinuous. This boundary consists of two parts: the crack surfaces, also called crack flanks. The line joining the crack surfaces is the crack front (in two dimensions: the crack tip). Each mode is associated with a different stress-intensity factor. The crack-opening mode (mode I) occurs when the elastic body is loaded by tensile forces acting perpendicular to the crack surfaces. Shear forces parallel to the crack flanks and perpendicular to the crack front result in fracture by the sliding mode (mode II), while shear forces parallel to the crack front give rise to fracture by the tearing mode (mode III). In general situations a combination of these modes will be present and crack extension will take place in a direction different from the initial orientation of the crack.

In this chapter we summarize the results for the near-tip stresses of the various fracture modes and we distinguish between geometries with stationary cracks and those with dynamic crack propagation. In addition, several fracture criteria are discussed, based on the critical values of the stress-intensity factors, the local near-tip stresses, and on the amount of energy which is available for crack growth. Conditions for the onset of fracture and expressions for the determination of the crack-growth direction are presented. Prior to a study of the fracture criteria, it is necessary to investigate the stresses in the vicinity of the crack tip.

3.1 Fracture in planar deformation

3.1.1 Static solution

Consider a linearly elastic body containing a crack of arbitrary shape and being loaded under planar conditions as described in Section 2.2. We shall focus on situations of plane stress. Firstly, we consider the static problem, such that we may put $\rho \ddot{u}_i = 0$ in the equations (2.14)–(2.16). Since our attention is focused on the crack tip, it is allowed to employ a standard interior asymptotic expansion and to replace the crack by a semi-infinite slit; see Achenbach and Bažant [1] and Freund [28, Secs. 2.1, 4.2]. In order to obtain the near-tip stress solutions, the origin of the Cartesian coordinate system $\{\mathbf{e}_x, \mathbf{e}_y\}$ is located at the crack tip and the crack is positioned along the negative x -axis; see Fig. 3.2.

It is assumed that the crack surfaces are stress-free, such that $\bar{p}_i = 0$ may be put in the boundary conditions (2.18) with S_p equal to the crack surfaces. The conditions at large distance from the crack are disregarded, because we focus on the crack-tip region. The solution to the static plane-stress problem is given in several textbooks, e.g., Broek [11, Sec. 3.3], Cherepanov [18, Sec. 3-5], Freund [28, Sec. 2.1], Irwin [42]. Stress-intensity factors K_I and K_{II} are introduced as normalising constants for the

symmetric and anti-symmetric parts of the local crack-tip stress fields. These factors are the fracture parameters of the corresponding modes I and II and are expressed in units MPa $\sqrt{\text{m}}$ or $\text{N m}^{-3/2}$. With the use of local polar coordinates r and θ specified by $x = r \cos \theta$, $y = r \sin \theta$ with $r > 0$, $-\pi \leq \theta \leq \pi$, the stress-intensity factors are defined by

$$K_I = \lim_{r \rightarrow 0} \sqrt{2\pi r} \sigma_{yy}(r, 0), \quad (3.1)$$

$$K_{II} = \lim_{r \rightarrow 0} \sqrt{2\pi r} \sigma_{xy}(r, 0). \quad (3.2)$$

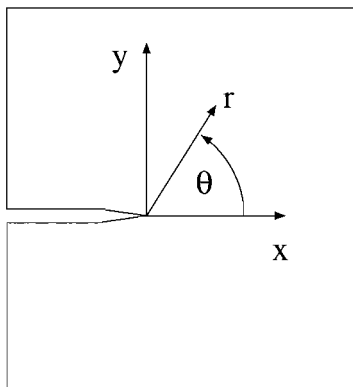


Figure 3.2: Local crack-tip coordinates.

The solution for the stress components can be expressed as [11, 18, 28, 42]

$$\sigma_{ij}(r, \theta) = \frac{K_I}{\sqrt{2\pi r}} f_{ij}^I(\theta) + \frac{K_{II}}{\sqrt{2\pi r}} f_{ij}^{II}(\theta) + \sigma_{ij}^0 + O(\sqrt{r}), \quad (3.3)$$

for distance $r \rightarrow 0$ and indices $i, j = x, y$. The term σ_{ij}^0 indicates the finite stresses at the crack tip. The angular variations for modes I and II are well-known functions and are illustrated in Fig. 3.3. For the crack-opening mode we have

$$f_{xx}^I(\theta) = \cos \frac{1}{2}\theta \left(1 - \sin \frac{1}{2}\theta \sin \frac{3}{2}\theta \right), \quad (3.4)$$

$$f_{yy}^I(\theta) = \cos \frac{1}{2}\theta \left(1 + \sin \frac{1}{2}\theta \sin \frac{3}{2}\theta \right), \quad (3.5)$$

$$f_{xy}^I(\theta) = \sin \frac{1}{2}\theta \cos \frac{1}{2}\theta \cos \frac{3}{2}\theta, \quad (3.6)$$

while the functions for the sliding mode are given by

$$f_{xx}^{II}(\theta) = -\sin \frac{1}{2}\theta \left(2 + \cos \frac{1}{2}\theta \cos \frac{3}{2}\theta \right), \quad (3.7)$$

$$f_{yy}^{II}(\theta) = \sin \frac{1}{2}\theta \cos \frac{1}{2}\theta \cos \frac{3}{2}\theta, \quad (3.8)$$

$$f_{xy}^{II}(\theta) = \cos \frac{1}{2}\theta \left(1 - \sin \frac{1}{2}\theta \sin \frac{3}{2}\theta \right). \quad (3.9)$$

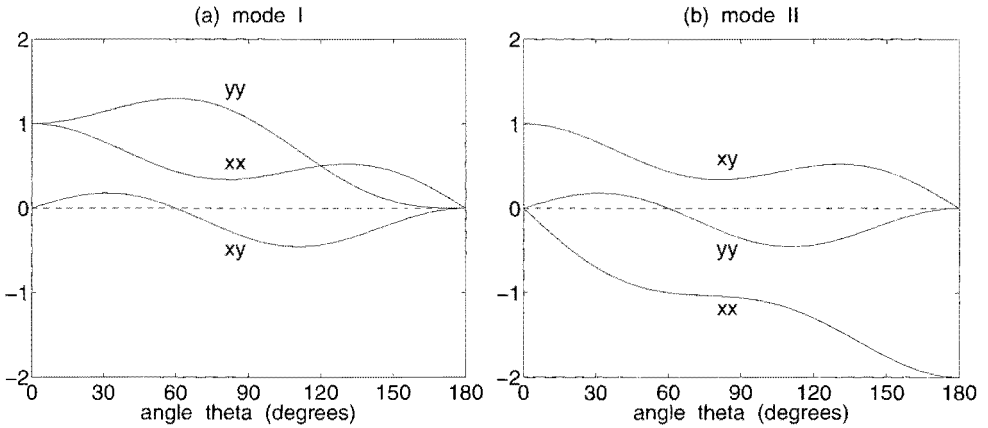


Figure 3.3: Angular variations of the singular stresses $f_{ij}^I(\theta)$ and $f_{ij}^{II}(\theta)$ of modes I and II for indices $i, j = x, y$.

We note that the singular stress behaviour is also valid for stationary (non-propagating) cracks under dynamic loading conditions such as transient forces. In those situations, the same angular variations and the same inverse square-root singularity are found, but the stress-intensity factors become time-dependent [28, Sec. 2.1].

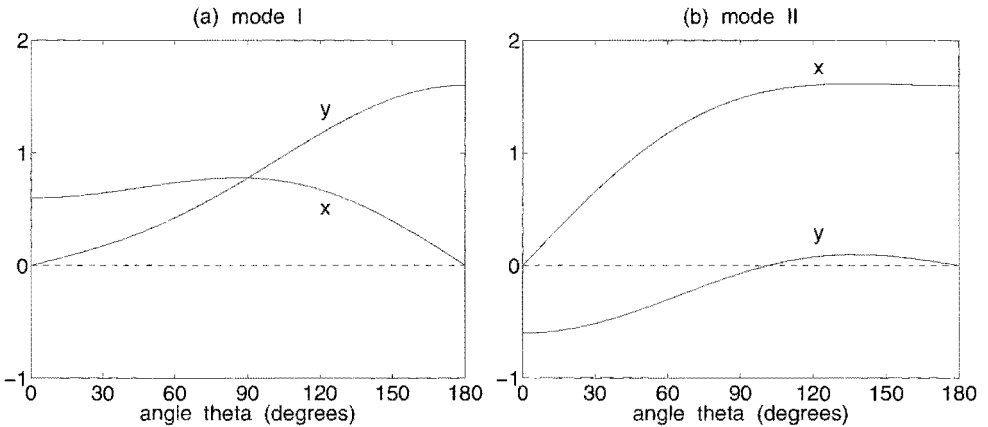


Figure 3.4: Angular variations of the displacements $u_i^I(\theta)$ and $u_i^{II}(\theta)$ of modes I and II for index $i = x, y$ and Poisson's ratio $\nu = 0.25$.

The corresponding displacements near the crack tip are given by [18, 42]

$$u_i(r, \theta) = u_i^0 + \frac{K_I}{G} \sqrt{\frac{r}{2\pi}} u_i^I(\theta) + \frac{K_{II}}{G} \sqrt{\frac{r}{2\pi}} u_i^{II}(\theta) + O(r), \quad (3.10)$$

for distance $r \rightarrow 0$ and index $i = x, y$, where u_i^0 are the crack-tip displacements. The angular functions are shown in Fig. 3.4 and are given by

$$u_x^I(\theta) = \cos \frac{1}{2}\theta \left(\frac{1-\nu}{1+\nu} + \sin^2\left(\frac{1}{2}\theta\right) \right), \quad (3.11)$$

$$u_y^I(\theta) = \sin \frac{1}{2}\theta \left(\frac{2}{1+\nu} - \cos^2\left(\frac{1}{2}\theta\right) \right), \quad (3.12)$$

$$u_x^{II}(\theta) = \sin \frac{1}{2}\theta \left(\frac{2}{1+\nu} + \cos^2\left(\frac{1}{2}\theta\right) \right), \quad (3.13)$$

$$u_y^{II}(\theta) = \cos \frac{1}{2}\theta \left(-\frac{1-\nu}{1+\nu} + \sin^2\left(\frac{1}{2}\theta\right) \right). \quad (3.14)$$

3.1.2 Dynamic solution

Next, the problem for a propagating crack is considered. It was shown by Achenbach and Bažant [1] and Freund [28, Ch. 4] that effects of crack rotation and acceleration do not play a role in the near-tip singular stress field. Therefore, these effects are not taken into account in the present investigation. The crack is taken as a semi-infinite slit with its tip positioned at $x = l(t)$, $y = 0$ at time t . The velocity of crack growth equals $c = \dot{l}(t)$ in the x -direction and is restricted to the range $0 \leq c < c_s$. A moving Cartesian coordinate system is introduced with its origin attached to the crack tip, similar as in Fig. 3.2, with coordinates

$$\hat{x} = x - l(t), \quad \hat{y} = y. \quad (3.15)$$

Also, local polar coordinates (r, θ) are introduced such that $\hat{x} = r \cos \theta$, $\hat{y} = r \sin \theta$ with $r > 0$ and $-\pi \leq \theta \leq \pi$. Because of the moving frame of reference, it is convenient to express the singular stresses in terms of distorted polar coordinates (r_d, θ_d) and (r_s, θ_s) associated with the dilatational and shear wave speeds c_d and c_s as given in (2.19)–(2.20). The radii r_d and r_s are defined by

$$r_d = r \gamma_d, \quad \gamma_d(c, \theta) = \sqrt{1 - (c \sin \theta / c_d)^2}, \quad (3.16)$$

$$r_s = r \gamma_s, \quad \gamma_s(c, \theta) = \sqrt{1 - (c \sin \theta / c_s)^2}, \quad (3.17)$$

while the polar angles θ_d and θ_s are in the same quadrant as θ and are defined by

$$\tan \theta_d = \alpha_d \tan \theta, \quad \alpha_d(c) = \sqrt{1 - (c/c_d)^2}, \quad (3.18)$$

$$\tan \theta_s = \alpha_s \tan \theta, \quad \alpha_s(c) = \sqrt{1 - (c/c_s)^2}. \quad (3.19)$$

In addition, we introduce the Rayleigh function

$$R(c) = 4\alpha_d\alpha_s - (1 + \alpha_s^2)^2. \quad (3.20)$$

The equation $R(c) = 0$ has a double root $c = 0$ and two single roots $c = \pm c_R$ with $0 < c_R < c_s$. The root c_R defines the Rayleigh speed of surface waves, which depends on Poisson's ratio. For $0 \leq \nu \leq 0.50$, we find that the ratio c_R/c_s varies from 0.8740

to 0.9325 in the case of plane stress, and from 0.8740 to 0.9553 in the case of plane strain. The Rayleigh wave speed is the physical upper bound of the crack-growth speed for cracks in planar deformation. This relates to the energy dissipation during crack growth. When the crack-growth speed exceeds the Rayleigh wave speed, the function $R(c)$ becomes negative and energy is radiated from the advancing crack tip; see Cherepanov [18, Sec. 5-4] and Freund [28, Sec. 4.3]. Since this is physically impossible, it is required that $0 \leq c < c_R$.

The solution to the elastodynamic equations (2.14)–(2.16) satisfying homogeneous (stress-free) boundary conditions (2.18) along the crack surfaces was derived in [1] and [28, Sec. 4.3]. The stress components in the vicinity of a crack tip moving at instantaneous speed c are given by

$$\sigma_{ij}(r, \theta; c) = \frac{K_I}{\sqrt{2\pi r}} F_{ij}^I(\theta, c) + \frac{K_{II}}{\sqrt{2\pi r}} F_{ij}^{II}(\theta, c) + \sigma_{ij}^0 + O(\sqrt{r}), \quad (3.21)$$

for distance $r \rightarrow 0$ and indices $i, j = x, y$. The dynamic stress-intensity factors are defined in the same manner as in (3.1)–(3.2) and may depend on the crack-growth speed. The angular variations for modes I and II are well known [1, 28] and are displayed in Fig. 3.5 for several crack-growth speeds. The functions $F_{ij}^I(\theta, c)$ for the crack-opening mode can be expressed as

$$F_{xx}^I(\theta, c) = \frac{(1 + \alpha_s^2)(1 + 2\alpha_d^2 - \alpha_s^2) \cos \frac{1}{2}\theta_d}{R\sqrt{\gamma_d}} - \frac{4\alpha_d\alpha_s \cos \frac{1}{2}\theta_s}{R\sqrt{\gamma_s}}, \quad (3.22)$$

$$F_{yy}^I(\theta, c) = \frac{-(1 + \alpha_s^2)^2 \cos \frac{1}{2}\theta_d}{R\sqrt{\gamma_d}} + \frac{4\alpha_d\alpha_s \cos \frac{1}{2}\theta_s}{R\sqrt{\gamma_s}}, \quad (3.23)$$

$$F_{xy}^I(\theta, c) = \frac{2\alpha_d(1 + \alpha_s^2)}{R} \left(\frac{\sin \frac{1}{2}\theta_d}{\sqrt{\gamma_d}} - \frac{\sin \frac{1}{2}\theta_s}{\sqrt{\gamma_s}} \right), \quad (3.24)$$

while the functions $F_{ij}^{II}(\theta, c)$ for the sliding mode are given by

$$F_{xx}^{II}(\theta, c) = \frac{-2\alpha_s(1 + 2\alpha_d^2 - \alpha_s^2) \sin \frac{1}{2}\theta_d}{R\sqrt{\gamma_d}} + \frac{2\alpha_s(1 + \alpha_s^2) \sin \frac{1}{2}\theta_s}{R\sqrt{\gamma_s}}, \quad (3.25)$$

$$F_{yy}^{II}(\theta, c) = \frac{2\alpha_s(1 + \alpha_s^2)}{R} \left(\frac{\sin \frac{1}{2}\theta_d}{\sqrt{\gamma_d}} - \frac{\sin \frac{1}{2}\theta_s}{\sqrt{\gamma_s}} \right), \quad (3.26)$$

$$F_{xy}^{II}(\theta, c) = \frac{4\alpha_d\alpha_s \cos \frac{1}{2}\theta_d}{R\sqrt{\gamma_d}} - \frac{(1 + \alpha_s^2)^2 \cos \frac{1}{2}\theta_s}{R\sqrt{\gamma_s}}. \quad (3.27)$$

It is noted that the functions $F_{ij}^I(\theta, c)$ and $F_{ij}^{II}(\theta, c)$ are singular for $c = c_R$ and change their sign for $c > c_R$, because of the factor $R(c)$ in the denominator. This demonstrates that the Rayleigh wave speed is the upper bound for the crack-growth speed.

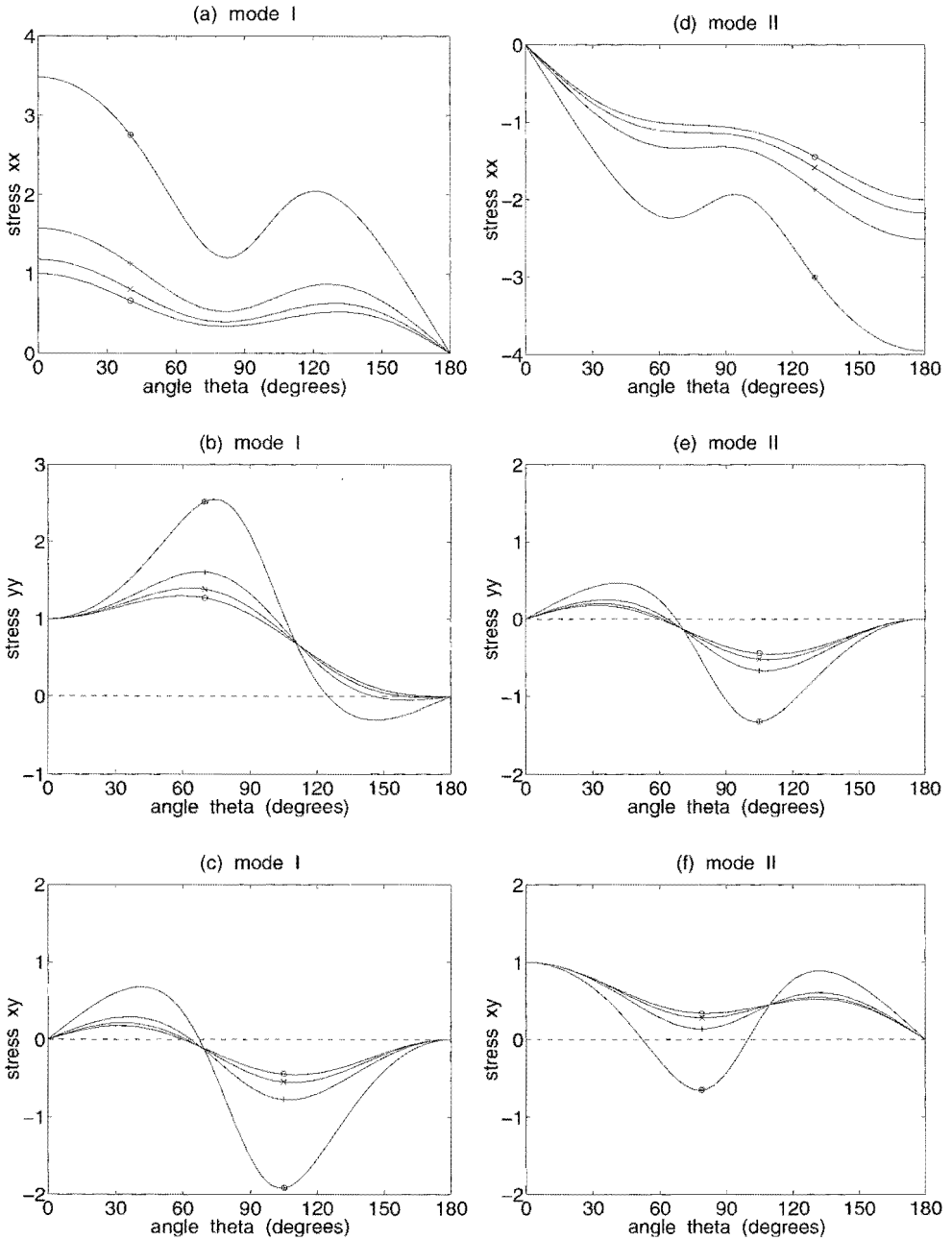


Figure 3.5: Angular variations of the dynamic singular stresses $F_{ij}^I(\theta, c)$ and $F_{ij}^{II}(\theta, c)$ of modes I and II for indices $i, j = x, y$ and Poisson's ratio $\nu = 0.25$ in plane stress and for crack-growth speeds $c/c_s = 0$ (marked by o), 0.4 (\times), 0.6 ($+$), and 0.8 (\oplus).

The corresponding displacements for dynamic fracture are [28, Sec. 4.3]

$$u_i(r, \theta; c) = u_i^0 + \frac{K_I}{G} \sqrt{\frac{r}{2\pi}} U_i^I(\theta, c) + \frac{K_{II}}{G} \sqrt{\frac{r}{2\pi}} U_i^{II}(\theta, c) + O(r), \quad (3.28)$$

for distance $r \rightarrow 0$ and index $i = x, y$, where u_i^0 are the crack-tip displacements. The angular functions are given by

$$U_x^I(\theta, c) = \frac{2}{R} \left((1 + \alpha_s^2) \gamma_d^{\frac{1}{2}} \cos \frac{1}{2} \theta_d - 2\alpha_d \alpha_s \gamma_s^{\frac{1}{2}} \cos \frac{1}{2} \theta_s \right), \quad (3.29)$$

$$U_y^I(\theta, c) = \frac{2}{R} \left(-(1 + \alpha_s^2) \alpha_d \gamma_d^{\frac{1}{2}} \sin \frac{1}{2} \theta_d + 2\alpha_d \gamma_s^{\frac{1}{2}} \sin \frac{1}{2} \theta_s \right), \quad (3.30)$$

$$U_x^{II}(\theta, c) = \frac{2}{R} \left(2\alpha_s \gamma_d^{\frac{1}{2}} \sin \frac{1}{2} \theta_d - (1 + \alpha_s^2) \alpha_s \gamma_s^{\frac{1}{2}} \sin \frac{1}{2} \theta_s \right), \quad (3.31)$$

$$U_y^{II}(\theta, c) = \frac{2}{R} \left(2\alpha_d \alpha_s \gamma_d^{\frac{1}{2}} \cos \frac{1}{2} \theta_d - (1 + \alpha_s^2) \gamma_s^{\frac{1}{2}} \cos \frac{1}{2} \theta_s \right). \quad (3.32)$$

These results for the near-tip fields during dynamic crack propagation depend only on the instantaneous crack-growth speed. Consequently, the near-tip stresses and displacements for nonuniform motion ($\dot{c} \neq 0$) and for steady-state crack propagation ($\dot{c} = 0$) are identical [1, 28]. In the limit of no crack propagation, i.e., for $c \rightarrow 0$, the angular variations tend to the corresponding values (3.4)–(3.9) and (3.11)–(3.14) for stationary cracks,

$$\lim_{c \rightarrow 0} F_{ij}^I(\theta, c) = f_{ij}^I(\theta), \quad (3.33)$$

$$\lim_{c \rightarrow 0} F_{ij}^{II}(\theta, c) = f_{ij}^{II}(\theta), \quad (3.34)$$

$$\lim_{c \rightarrow 0} U_i^I(\theta, c) = u_i^I(\theta), \quad (3.35)$$

$$\lim_{c \rightarrow 0} U_i^{II}(\theta, c) = u_i^{II}(\theta). \quad (3.36)$$

3.2 Fracture in anti-plane shear

Consider a linearly elastic body containing a crack of arbitrary shape and subjected to anti-plane deformation as described in Section 2.3, such that the crack is loaded under mode III conditions. Local crack-tip coordinates as in Fig. 3.2 are introduced with the z -axis perpendicular to the xy -plane, along the crack front. Again, the crack flanks are assumed stress-free and conditions at large distance from the crack are disregarded. The solution to the static problem of anti-plane shear is presented by Broek [11, Sec. 3.3], Cherepanov [18, Sec. 3-5], Freund [28, Sec. 2.1], and Irwin [42]. The singular shear stress components are normalised by the stress-intensity factor K_{III} which is defined by

$$K_{III} = \lim_{r \rightarrow 0} \sqrt{2\pi r} \tau_{yz}(r, 0). \quad (3.37)$$

The shear-stress components in the vicinity of the crack tip, i.e. for distance $r \rightarrow 0$, are given by [11, 18, 28, 42]

$$\tau_{iz}(r, \theta) = \frac{K_{III}}{\sqrt{2\pi r}} f_{iz}^{III}(\theta) + \tau_{iz}^0 + O(\sqrt{r}), \quad (3.38)$$

with index $i = x, y$ and τ_{iz}^0 being a finite shear stress at the crack tip. The angular variations are well-known functions, viz.

$$f_{xz}^{III}(\theta) = -\sin \frac{1}{2}\theta, \quad (3.39)$$

$$f_{yz}^{III}(\theta) = \cos \frac{1}{2}\theta. \quad (3.40)$$

The displacement near the crack tip can be expressed as [18, Sec. 3-5]

$$u_z(r, \theta) = u_z^0 + \frac{K_{III}}{G} \sqrt{\frac{2r}{\pi}} \sin \frac{1}{2}\theta + O(r), \quad (3.41)$$

for $r \rightarrow 0$ and with u_z^0 being the crack-tip displacement. Similar to Subsection 3.1.1, the near-tip solution (3.38)–(3.41) is also valid for dynamic loading of stationary cracks. Only the stress-intensity factor (3.37) will vary with time.

The solution for a propagating crack with instantaneous velocity $c = c(t)$ and loaded in anti-plane shear is expressed in the same moving frame of reference as defined in (3.15). The singular shear stresses are obtained as [28, Sec. 4.2]

$$\tau_{iz}(r, \theta; c) = \frac{K_{III}}{\sqrt{2\pi r}} F_{iz}^{III}(\theta, c) + \tau_{iz}^0 + O(\sqrt{r}), \quad (3.42)$$

for distance $r \rightarrow 0$ and index $i = x, y$. The elastodynamic stress-intensity factor K_{III} is defined by (3.37) and may depend on the crack-growth speed. Expressed in terms of γ_s , α_s and θ_s (see (3.17) and (3.19)), the angular variations are given by

$$F_{xz}^{III}(\theta, c) = -\frac{\sin \frac{1}{2}\theta_s}{\alpha_s \sqrt{\gamma_s}}, \quad (3.43)$$

$$F_{yz}^{III}(\theta, c) = \frac{\cos \frac{1}{2}\theta_s}{\sqrt{\gamma_s}}. \quad (3.44)$$

The displacement for dynamic fracture is equal to [28, Sec. 4.2]

$$u_z(r, \theta; c) = u_z^0 + \frac{K_{III}}{\alpha_s G} \sqrt{\frac{2r}{\pi}} \gamma_s^{\frac{1}{2}} \sin \frac{1}{2}\theta_s + O(r), \quad (3.45)$$

with u_z^0 being the crack-tip displacement.

These results apply to both steady-state and nonuniform crack propagation [1, 28]. In the limit for $c \rightarrow 0$, the angular variations tend to the corresponding values (3.39)–(3.41) for stationary cracks. Thus, we have (with index $i = x, y$)

$$\lim_{c \rightarrow 0} F_{iz}^{III}(\theta, c) = f_{iz}^{III}(\theta). \quad (3.46)$$

3.3 Energy release rate

Because of the stress singularity, a concentration of energy occurs in the neighbourhood of the crack tip. Fracture will take place when the available energy exceeds a critical level. This is expressed in terms of the energy release rate which is defined as the amount of energy required to separate the material and dissipated per unit area of crack extension. For thin plate-like structures it is common to multiply this amount by the plate thickness (or to integrate over the thickness of the plate) and to express this rate as energy dissipated per unit length of crack extension. The dissipated energy equals the work performed when the newly created crack is closed over an infinitesimal distance Δa . This work is calculated from the stresses $\sigma_{iy}(r, 0)$ in the direction ahead of the crack and from the crack-flank displacements $u_i(\Delta a - r, \pi) - u_i(\Delta a - r, -\pi)$ with $0 < r < \Delta a$. The dependences on c and possibly on z have been suppressed for clarity. The energy release rate is then determined by

$$\mathcal{G} = \lim_{\Delta a \rightarrow 0} \frac{1}{2\Delta a} \int_{-h/2}^{+h/2} \int_0^{\Delta a} \sigma_{iy}(r, 0) [u_i(\Delta a - r, \pi) - u_i(\Delta a - r, -\pi)] dr dz, \quad (3.47)$$

with summation over the index $i = x, y, z$. This method of the crack-closure integral was developed by Irwin [41, 42]; see also [11, 18] or Young and Sun [98, 99].

The connection with the stress-intensity factors is derived by substitution of the near-tip solutions. Thus, the energy release rate for dynamic fracture at crack speed c in a plate of thickness h loaded under plane-stress or anti-plane conditions is calculated as

$$\mathcal{G} = \frac{h}{E} \left(A_I(c) K_I^2 + A_{II}(c) K_{II}^2 \right) + \frac{h}{2G} A_{III}(c) K_{III}^2, \quad (3.48)$$

where the velocity-dependent coefficients are given by Freund [28, Ch. 5] and also by Nishioka and Atluri [67]. With the use of the definitions (3.18)–(3.19) of α_d and α_s and the definitions (2.19)–(2.20) of c_d and c_s , we find

$$A_I(c) = \frac{(1 + \nu)(1 - \alpha_s^2)\alpha_d}{R} = \frac{2(\alpha_d^2 - \alpha_s^2)\alpha_d}{R}, \quad (3.49)$$

$$A_{II}(c) = \frac{(1 + \nu)(1 - \alpha_s^2)\alpha_s}{R} = \frac{2(\alpha_d^2 - \alpha_s^2)\alpha_s}{R}, \quad (3.50)$$

$$A_{III}(c) = \frac{1}{\alpha_s}. \quad (3.51)$$

In the limit of a stationary crack, i.e., for $c \rightarrow 0$, these coefficients tend to unity and the energy release rate (3.48) reduces to the well-known results of [11, 18, 67]. On the other hand, the coefficients $A_I(c)$ and $A_{II}(c)$ become infinite of the order $O[(c - c_R)^{-1}]$ when the Rayleigh wave speed is approached, while the coefficient $A_{III}(c)$ is of the order $O[(c - c_s)^{-1}]$ when the crack speed tends to the shear-wave speed.

An alternative method for the calculation of the energy release rate has been developed by Rice [76] and is based on path-independent contour integrals or so-called J -integrals. This technique has been elaborated further by Atluri [2] for a wide class

of materials having properties as finite strains, inelasticity, rate sensitivity and elastoviscoplastic behaviour. Freund [28, Ch. 5] and Nishioka and Atluri [67] applied these integrals to dynamic fracture of linearly elastic bodies undergoing infinitesimal elastic deformation, which is also assumed in this thesis.

Consider a circular contour C in the xy -plane with center at the crack tip and lying entirely inside the region of K -dominance. The end points of the contour are on the lower and upper crack surfaces and the components of the outward normal are denoted by n_i ; see Fig. 3.6. For indices $i, j = x, y, z$ and $k = x, y$ (or 1, 2), we define the integrals [2, 28, 67, 76]

$$J_k = \lim_{C \rightarrow 0} \int_{-h/2}^{+h/2} \int_C \left((W + T) n_k - \sigma_{ij} n_j u_{i,k} \right) ds dz, \quad (3.52)$$

with $W = \frac{1}{2} \sigma_{ij} \varepsilon_{ij}$ and $T = \frac{1}{2} \rho \dot{u}_i \dot{u}_i$ being the elastic and kinetic energy densities, respectively. The limit $C \rightarrow 0$ is to be understood as the limit for a contour C shrinking onto the crack tip. The integrals J_k form a vector $\mathbf{J} = J_k \mathbf{e}_k$ in the xy -plane. An interpretation of this vector is given in the next section where fracture criteria are discussed.

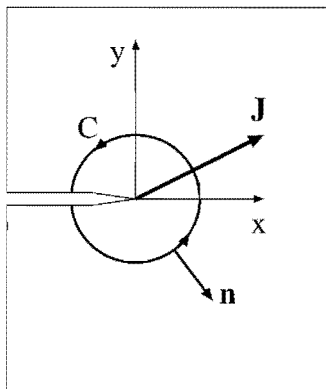


Figure 3.6: Integration path for the J -integrals.

The J -integrals can also be calculated for other than circular contours, shrinking onto the crack tip. In Appendix A it is shown that J_1 is independent of the shape of the contour C (the integration path) when the crack surfaces are stress-free. Therefore, the integral J_1 is often called path-independent. This property also holds true for J_2 but only for stationary cracks and not for dynamic fracture. In practical calculations, e.g. based on the finite-element method, it is more convenient to use an integration path which is not located in the proximity of the crack tip but at some remote position. Expressions for J_k which involve an integral along a contour outside the region of K -dominance, are presented in Appendix A and [67]. These expressions contain extra contributions due to integration paths along the crack flanks and, in the case of

dynamic loading, an extra surface or volume integral to incorporate the elastodynamic effects.

Ahuri [2] has proved that the integral J_1 coincides with the energy release rate \mathcal{G} . This can also be shown by evaluation of J_1 for a shrinking circular [67] or rectangular [28, Ch. 5] contour via substitution of the elastodynamic near-tip solutions. So, we have

$$J_1 = \mathcal{G}. \quad (3.53)$$

Evaluation of the integral J_2 for a shrinking circular contour yields

$$J_2 = -\frac{2h}{E} A_{IV}(c) K_I K_{II}, \quad (3.54)$$

where the coefficient $A_{IV}(c)$ is given in [67] and by (A.3) of Appendix A. When the crack-growth speed approaches zero, this coefficient tends to unity and the expression (3.54) reduces to the results of [18, Ch. 5]. The coefficient is of the order $O[(c - c_R)^{-2}]$ for crack-growth speeds approaching the Rayleigh wave speed. It is emphasised that J_2 depends on the shape of the shrinking contour (for dynamic fracture only). For non-circular contours symmetric with respect to the x -axis, expressions for J_2 similar to (3.54) are obtained with different coefficients $A_{IV}(c)$. For example, the result for a shrinking rectangular contour is given in (A.4) of Appendix A. When the contour is not symmetric with respect to the x -axis, the expression for J_2 may contain additional terms with K_I^2 , K_{II}^2 and K_{III}^2 (Boersma [8]). The velocity-dependent coefficients of these terms depend on the shape of the shrinking contour and vanish for zero crack propagation ($c = 0$).

3.4 Fracture criteria

In fracture mechanics we distinguish between (i) crack initiation, which is the sudden rupture of initially undamaged material, and (ii) crack extension, which is the growth of pre-existing cracks. The mechanism of crack initiation can be explained by a micro-mechanical approach. When the local stresses at a certain position exceed a critical value, molecular bonds will fail. For granular materials such as concrete or rock, but also for fiber-reinforced composites, the matrix material between the grains or fibers will fracture. As soon as a sufficient number of minuscule flaws has originated on the microscopic level, interlinkage of the microcracks may occur. Finally, the strength of the material has decreased so far that the remaining bonds cannot withstand the increased tension and fail too. This becomes apparent on the macroscopic level in the form of crack initiation.

In this thesis we restrict ourselves to the growth of pre-existing cracks. Regarding the area of application, it is reasonable to assume that crack initiation has occurred and that at least one crack is present in the material. The deformation of an elastic body is governed by the equations and boundary conditions (2.1)–(2.5). These equations are not sufficient for the analysis of cracks. An additional postulate on the fracture

behaviour must be supplied: a so-called fracture criterion; see Broek [11, Ch. 2], Cherepanov [18, Ch. 1] and Freund [28, Sec. 7.4], who elaborated further the ideas of Griffith [31], Irwin [42] and Orowan [70]. We shall discuss two fracture criteria that can be employed to decide whether an existing crack will extend, and if so, in which direction. Although the ideas underlying these criteria are different, their predictions are in good agreement with each other and with experimental data.

We start with a stationary crack ($c = 0$) located along a semi-infinite slit and loaded under mode I conditions. Because of the symmetric loading, the crack extends in the direction $\theta = 0$ ahead of the crack. The first fracture criterion is based on the stress-intensity factor; see [11, Ch. 1] and [18, Sec. 4-1]. It is postulated that crack growth will occur when the stress-intensity factor exceeds the critical limit K_{Ic} , the fracture toughness of the material, that is

$$K_I \geq K_{Ic}. \quad (3.55)$$

The second fracture criterion is based on the energy release rate; see Broek [11, Sec. 1.7], Cherepanov [18, Secs. 4-2, 5-1] and also Irwin [42]. It is postulated that crack extension will take place when the energy stored in the immediate surroundings of the crack tip is sufficient to break the material and to induce fracture. This energy is released during crack extension. The critical level for the energy release rate is denoted by \mathcal{G}_c and the fracture criterion is

$$\mathcal{G} \geq \mathcal{G}_c. \quad (3.56)$$

The two fracture criteria are equivalent, since the stress-intensity factor K_I and the energy release rate \mathcal{G} are connected by (3.48). By putting $c = 0$ in (3.48), a relationship between the fracture toughness and the critical energy release rate is derived, namely

$$\mathcal{G}_c = \frac{h K_{Ic}^2}{E}. \quad (3.57)$$

Next, we consider a stationary crack located along a semi-infinite slit and loaded by a combination of modes I and II. We assume $K_I > 0$, which corresponds to crack opening instead of crack closure, while K_{II} can be positive or negative. The critical stress and the direction of crack extension are to be determined. As a generalisation of (3.55), we discuss a criterion based on the circumferential tensile stress in the vicinity of the crack tip. This stress component is calculated from the singular stress field (3.3)–(3.9) and is given by

$$\begin{aligned} \sigma_{\theta\theta}(r, \theta) &= \sigma_{xx} \sin^2 \theta - 2 \sigma_{xy} \sin \theta \cos \theta + \sigma_{yy} \cos^2 \theta \\ &= \frac{K_{\theta\theta}(\theta)}{\sqrt{2\pi r}} = \frac{1}{\sqrt{2\pi r}} \left(K_I \cos^3\left(\frac{1}{2}\theta\right) - 3 K_{II} \sin\left(\frac{1}{2}\theta\right) \cos^2\left(\frac{1}{2}\theta\right) \right). \end{aligned} \quad (3.58)$$

Experimental research has led to the following hypotheses; see e.g. [11, Sec. 14.5] and [18, Sec. 4-3] and also Erdogan and Sih [23]. Fracture occurs when the maximum

of the effective stress-intensity factor $K_{\theta\theta}$ reaches the critical value K_{IC} . The crack extends in the direction $\theta = \theta_p$ for which $K_{\theta\theta}$ is maximum. The critical stress-intensity factor and the angle θ_p of crack growth are thus determined by

$$K_{\theta\theta}(\theta_p) = K_{IC}, \quad \left. \frac{dK_{\theta\theta}}{d\theta} \right|_{\theta_p} = 0, \quad \left. \frac{d^2K_{\theta\theta}}{d\theta^2} \right|_{\theta_p} < 0. \quad (3.59)$$

The solution for θ_p is given by

$$\theta_p^{(S)} = 2 \arctan \left(\frac{K_I - \sqrt{K_I^2 + 8K_{II}^2}}{4K_{II}} \right), \quad (3.60)$$

where the superscript S refers to the circumferential stress criterion. Substitution of this result into the equation (3.59)¹ yields the condition for crack extension

$$K_{\theta\theta}(\theta_p) = \frac{4\sqrt{2}K_{II}^3 \left(K_I + 3\sqrt{K_I^2 + 8K_{II}^2} \right)}{\left(K_I^2 + 12K_{II}^2 - K_I \sqrt{K_I^2 + 8K_{II}^2} \right)^{\frac{3}{2}}} = K_{IC}. \quad (3.61)$$

The crack-growth angle $\theta_p^{(S)}$ is plotted as a function of the ratio K_{II}/K_I in Fig. 3.7 and approaches $2 \arctan(-\frac{1}{2}\sqrt{2}) \approx -70.5^\circ$, when K_I vanishes while K_{II} remains non-zero. In the case that the fracture process is dominated by mode I, which occurs very often for brittle materials, the expressions (3.60)–(3.61) can be approximated by the first two terms of their Taylor expansions for $K_{II}/K_I \rightarrow 0$, viz.

$$\left(1 + \frac{3}{2} \left(\frac{K_{II}}{K_I} \right)^2 + O \left(\left(\frac{K_{II}}{K_I} \right)^4 \right) \right) K_I = K_{IC}, \quad (3.62)$$

$$\theta_p^{(S)} = -2 \frac{K_{II}}{K_I} + \frac{14}{3} \left(\frac{K_{II}}{K_I} \right)^3 + O \left(\left(\frac{K_{II}}{K_I} \right)^5 \right). \quad (3.63)$$

The second fracture criterion (3.56) is generalised with the use of the J -integrals of Section 3.3, which are considered as components of the vector $\mathbf{J} = J_k \mathbf{e}_k$. Since the integrals J_k have the dimension of energy per unit length or also the dimension of force, the vector \mathbf{J} can be regarded as the energy flux into the crack tip [18] or as the crack-extension force [11, 41, 42]. The fracture criterion states that crack extension will occur when the length of the vector \mathbf{J} reaches the critical energy release rate \mathcal{G}_c , while the crack extends in the direction $\theta = \theta_p$ of \mathbf{J} ; see [18, Ch. 5]. With the use of (3.48) and (3.53)–(3.54) with $c = 0$, the fracture criterion can be expressed as

$$\left(J_1^2 + J_2^2 \right)^{\frac{1}{2}} = \frac{h}{E} \left(K_I^4 + 6K_I^2 K_{II}^2 + K_{II}^4 \right)^{\frac{1}{2}} = \mathcal{G}_c, \quad (3.64)$$

while the crack-growth angle is determined by

$$\theta_p^{(J)} = \arctan \left(\frac{J_2}{J_1} \right) = \arctan \left(\frac{-2K_I K_{II}}{K_I^2 + K_{II}^2} \right), \quad (3.65)$$

where the superscript J refers to the J -integral criterion. The angle $\theta_p^{(J)}$ is also plotted in Fig. 3.7. When the fracture process is dominated by mode I, a Taylor expansion of (3.64)–(3.65) for small values of the ratio K_{II}/K_I can be employed. The leading terms of the expansions are exactly the same as in the approximations (3.62)–(3.63) pertaining to the circumferential stress criterion. Differences only occur in the terms of higher order in K_{II}/K_I .

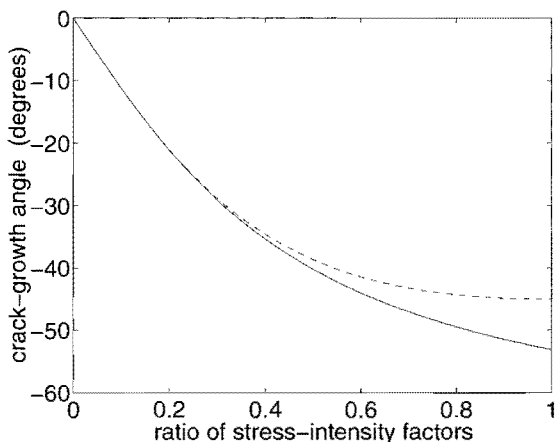


Figure 3.7: Crack-growth angles $\theta_p^{(S)}$ (—) of circumferential stress criterion and $\theta_p^{(J)}$ (- -) of J -integral criterion, as functions of the ratio K_{II}/K_I .

Interchanging the stress-intensity factors K_I and K_{II} in (3.64) and in (3.65) does not alter the results. In addition, it is noted that the absolute value of $\theta_p^{(J)}$ is at most $\pi/4$ radians or 45° . This reveals that the expressions (3.64) and (3.65) are not suitable in the case when the fracture process is dominated by mode II, i.e., when $|K_{II}| > K_I$. In these cases it is more appropriate to use the expressions (3.60) and (3.61) of the circumferential stress criterion. This is particularly relevant to the beginning of fracture of pre-existing cracks, since these cracks are often subjected to non-symmetric loads where fracture by mode II is dominant. During continued fracture and without sudden changes in the externally applied forces, however, smooth crack surfaces are observed. The crack extends in such a way that a certain degree of symmetry in loading is preserved with respect to the tangent plane to the crack surfaces at the crack tip. As a result, fracture occurs mainly in mode I and the stress-intensity factor K_{II} becomes negligible [18, Sec. 4-3], so that the two fracture criteria are equivalent.

Another difference between the fracture criteria pertains to material characteristics. Stress-intensity factors are defined as normalising constants of the singular stresses under the assumption of small-scale yielding. As a result, they only apply to materials with a relatively small zone of plasticity around the crack tip. This class of materials is

called brittle or quasi-brittle and comprises materials as glass, ceramics and concrete. Materials for which the plastic zone surrounding the crack tip is significant to the fracture process are called ductile. Metals for example belong to this category, because the yield stress is at a low level and is reached rather quickly, while the ultimate failure stress is larger by several orders of magnitude. Even glass may behave in a ductile manner when it is loaded under compression, for instance during indenter tests. Obviously, the concept of stress-intensity factors does not apply to ductile material behaviour because of the large amount of plasticity involved. For this type of materials the fracture criterion based on the energy release rate is more suitable.

3.5 Effects of dynamic crack propagation

In the preceding section we have discussed fracture criteria for stationary cracks. In this section we shall deal with propagating cracks. The behaviour of the singular stresses and the corresponding displacements near the crack tip is fixed to a large extent. The singularity by the inverse square root of the distance to the crack tip is a characteristic feature of the near-tip stresses, while the variations with the polar angle are pre-determined. The only remaining “degrees of freedom” are the stress-intensity factors which are related to the externally applied forces, the boundary conditions, and the geometry of the elastic body including crack size and crack speed. Generally, these dependences of the elastodynamic stress-intensity factor can be denoted by $K_I = K_I(\sigma, a, c)$, where σ represents the applied forces, a the crack length, and $c = \dot{a}$ the crack speed. The dependence on other geometrical parameters has been omitted for clarity. When σ and a are known, the fracture criterion (3.55) or (3.56) provides an equation for the crack-growth speed c . The dependences of K_I and \mathcal{G} on c are discussed below.

The monograph of Freund [28] provides an extensive treatment of various aspects of dynamic fracture mechanics. It is shown in [28, Ch. 6] that the dynamic stress-intensity factor $K_I(\sigma, a, c)$ for a propagating crack is equal to the stress-intensity factor $K_I(\sigma, a, 0)$ for the static equilibrium state of a stationary crack of the same size a and subjected to the same external forces σ , multiplied by a universal function of the crack speed c . This important result can be expressed as

$$K_I(\sigma, a, c) = k_I(c) K_I(\sigma, a, 0), \quad (3.66)$$

where $k_I(c)$ is the (dimensionless) universal function of crack speed for mode I with $0 \leq c \leq c_R$ and is plotted in Fig. 3.8. This representation holds true for cracks propagating at constant speed as well as for arbitrary crack-tip motion due to transient loading conditions [28, Ch. 7].

Similar representations are derived for the stress-intensity factors of modes II and III, but the universal function of crack speed attains a different form for each of these modes. Useful approximations to the universal functions for modes I and II are given

by [28, Sec. 6.4]

$$k_I(c) = \frac{1 - c/c_R}{\sqrt{1 - c/c_d}}, \quad (3.67)$$

$$k_{II}(c) = \frac{1 - c/c_R}{\sqrt{1 - c/c_s}}, \quad (3.68)$$

where $0 \leq c \leq c_R$. The universal function of crack speed for mode III is defined for $0 \leq c \leq c_s$ and is represented by the exact formula [28, Sec. 6.4]

$$k_{III}(c) = \sqrt{1 - c/c_s}. \quad (3.69)$$

The universal functions have the common property that they decrease monotonically from unity to zero for crack speeds increasing from zero to the Rayleigh wave speed (for mode III: the shear-wave speed). This behaviour is illustrated in Fig. 3.8. The monotonicity is explained by the physical argument that higher stress levels lead to higher crack-growth speeds. Because of the linearity of the deformation problem, an increase in σ produces a higher equilibrium stress-intensity factor. Since the dynamic stress-intensity factor equals K_{Ic} , the universal function of crack speed must decrease for higher stresses and thus for higher crack speeds.

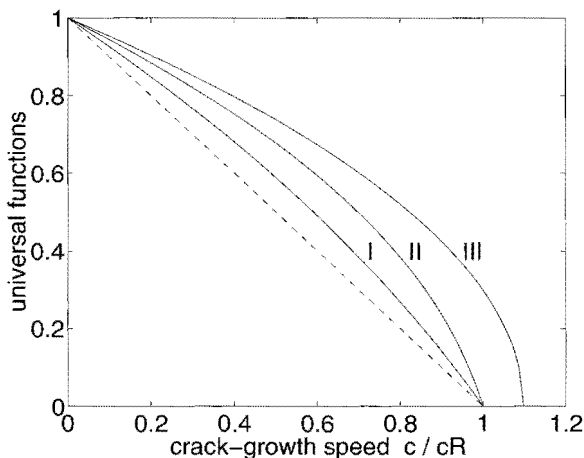


Figure 3.8: Universal functions $k_I(c)$, $k_{II}(c)$ and $k_{III}(c)$ as functions of the dimensionless crack-growth speed c/c_R for Poisson's ratio $\nu = 0.25$. A straight dashed line is added for comparison.

Because of the relation (3.48) between the energy release rate and the stress-intensity factors, we can derive a representation similar to (3.66) for the energy release rate

$\mathcal{G}(\sigma, a, c)$ for a crack of length a , subject to external forces σ , and propagating at speed c . Substituting (3.66) into (3.48), we obtain for mode I fracture that

$$\mathcal{G}(\sigma, a, c) = \frac{h}{E} A_I(c) k_I^2(c) K_I^2(\sigma, a, 0) = g_I(c) \mathcal{G}(\sigma, a, 0). \quad (3.70)$$

Thus, the energy release rate for a propagating crack is equal to its value for the corresponding equilibrium situation with a stationary crack, multiplied by a universal function of crack speed. Similar expressions are obtained for the other fracture modes. The universal functions of crack speed are $g_i(c) = A_i(c) k_i^2(c)$ with index $i=I, II, III$ and are plotted in Fig. 3.9. The coefficients $A_i(c)$ are given by (3.49)–(3.51) and the functions $k_i(c)$ by (3.67)–(3.69). The functions $g_i(c)$ are also monotonically decreasing with increasing crack speed; see Fig. 3.9. Acceptable approximations to the universal functions for modes I and II are

$$g_I(c) = (1 - c/c_R) \sqrt{1 - c/c_d}, \quad (3.71)$$

$$g_{II}(c) = 1 - c/c_R, \quad (3.72)$$

where $0 \leq c \leq c_R$. The universal function for mode III is given for $0 \leq c \leq c_s$ by the exact formula

$$g_{III}(c) = \sqrt{\frac{1 - c/c_s}{1 + c/c_s}}. \quad (3.73)$$

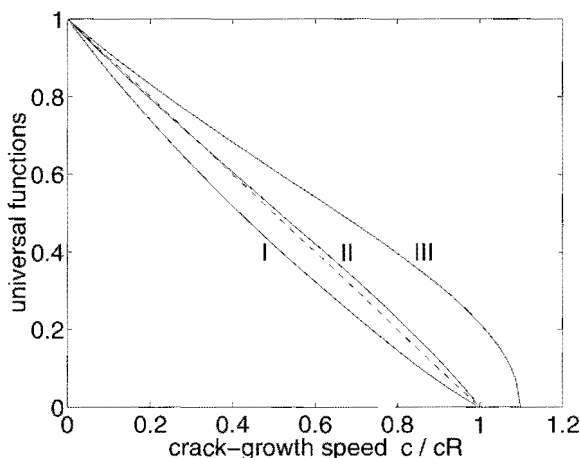


Figure 3.9: Universal functions $g_I(c)$, $g_{II}(c)$ and $g_{III}(c)$ as functions of the dimensionless crack-growth speed c/c_R for Poisson's ratio $\nu = 0.25$. A straight dashed line is added for comparison.

We can now formulate a fracture criterion for dynamic problems with propagating cracks, which enables us to determine the crack-growth speed. Consider an elastic

body with a crack propagating at (yet unknown) speed c under mode I conditions. The equilibrium energy release rate $\mathcal{G}(\sigma, a, 0)$ is determined by the externally applied forces and the boundary conditions, and can be calculated for example by means of the finite-element method. Next, the crack-growth speed can be obtained from the fracture criterion (3.56) with equality sign and where \mathcal{G} is interpreted as the dynamic energy release rate. With the use of relation (3.70) we find

$$g_I(c) \mathcal{G}(\sigma, a, 0) = \mathcal{G}_c, \quad (3.74)$$

which is to be considered as an equation for the crack-growth speed c .

Chapter 4

Fracture in plate bending

In addition to the three traditional modes of fracture considered in Chapter 3, one can also define three fracture modes for the bending of thin plates; see Fig. 4.1. The bending modes are indicated by arabic instead of roman numerals to distinguish them from the previous modes. The normal-bending mode (mode 1) corresponds to the crack-opening mode of planar deformation and is induced by bending moments symmetric with respect to the crack flanks. The twisting mode (mode 2) is similar to mode II of in-plane loading and is induced by torsional or twisting moments which are anti-symmetric with respect to the crack flanks. When the plate is loaded by shear forces in the direction perpendicular to the plate, bending fracture may occur in the shearing mode (mode 3). There exists great similarity between the latter bending mode and the tearing mode (mode III).

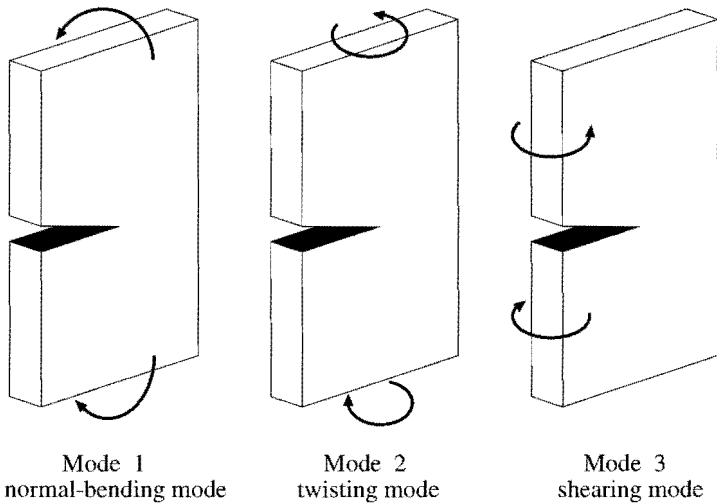


Figure 4.1: Three modes of fracture in plate bending.

In this chapter we present expressions for the singular bending moments in the vicinity of the crack tip, the corresponding shear forces, the deflection of the plate, and for the rotations of the middle plane. The analyses have been carried out in both Reissner's plate theory and the classical plate bending theory of Kirchhoff. The results for dynamically propagating cracks are new, whereas the results for stationary cracks have been derived previously by Hui and Zehnder [38]. The near-tip stress distributions for the two plate theories are compared with each other and also with the near-tip stress fields of planar deformation and anti-plane shear.

It is assumed that the bending loads are applied in combination with in-plane tensile forces, such that crack closure does not occur. If the crack surfaces do come into contact, the compressive stresses can be incorporated by adding extra terms to the stress-intensity factors; see Young and Sun [97]. Because of the principle of superposition, the problem of plate bending is analysed independently from the problem of plane stress. Stress-intensity factors for situations of combined tension and bending are introduced and some results on the energy release rate are derived.

4.1 Bending fracture in Reissner's plate theory

Consider a flat plate of thickness h consisting of a linearly elastic material, containing a crack of arbitrary shape, and being subjected to bending moments as described in Subsection 2.4.1. The analyses of static and dynamic fracture can be carried out simultaneously. So, the coordinates \hat{x} and \hat{y} of (3.15) and also the local polar coordinates r and θ with the origin attached to the moving crack tip are used. The instantaneous crack-growth speed at time t is denoted by $c = c(t)$.

For the analysis of the singular behaviour of the bending moments and shear forces, the mechanical quantities are expanded into series in powers of the distance r to the crack tip. In this procedure it turns out that a separation into two independent problems is allowed. Firstly, we obtain a problem of the singular bending moments, the curvatures and the rotations, which is similar to the problem of planar deformation (modes I and II). Secondly, we obtain a problem of the singular shear forces and the deflection, which is similar to the problem of anti-plane shear (mode III).

The series expansions must satisfy the following conditions. Firstly, it follows from the analysis of the boundary conditions [1, 28, 67] that the series can only contain terms with powers $r^{\frac{1}{2}p}$ for integer values of p . Secondly, the displacements (deflection and rotations) attain finite values at the crack tip. Thirdly, the elastic energy density is an integrable function of the spatial coordinates. These conditions impose restrictions on the exponents in the series expansion, such that the bending moments and the shear forces are of the order $O(r^{-\frac{1}{2}})$ for $r \rightarrow 0$. Consequently, the series expansions of the mechanical quantities in local polar coordinates r and θ are of the form [67]

$$w = \sum_{p=1}^{\infty} w^{(p)}(r, \theta, t) = \sum_{p=1}^{\infty} r^{\frac{1}{2}p} \tilde{w}^{(p)}(\theta, t),$$

$$\begin{aligned}
\Theta_i &= \sum_{p=1}^{\infty} \Theta_i^{(p)}(r, \theta, t) = \sum_{p=1}^{\infty} r^{\frac{1}{2}p} \tilde{\Theta}_i^{(p)}(\theta, t), \\
\kappa_{ij} &= \sum_{p=1}^{\infty} \kappa_{ij}^{(p)}(r, \theta, t) = \sum_{p=1}^{\infty} r^{\frac{1}{2}p-1} \tilde{\kappa}_{ij}^{(p)}(\theta, t), \\
M_{ij} &= \sum_{p=1}^{\infty} M_{ij}^{(p)}(r, \theta, t) = \sum_{p=1}^{\infty} r^{\frac{1}{2}p-1} \tilde{M}_{ij}^{(p)}(\theta, t), \\
Q_i &= \sum_{p=1}^{\infty} Q_i^{(p)}(r, \theta, t) = \sum_{p=1}^{\infty} r^{\frac{1}{2}p-1} \tilde{Q}_i^{(p)}(\theta, t).
\end{aligned} \tag{4.1}$$

It is noted that the deflection $w^{(0)}$ and the rotations $\Theta_i^{(0)}$ of the crack tip ($r = 0$) have been omitted, since they are constant and therefore not relevant to the near-tip solutions. The bending moments $M_{ij}^{(1)}$ and the shear forces $Q_i^{(1)}$, which are of the order $O(r^{-\frac{1}{2}})$ for $r \rightarrow 0$, are called the singular terms.

These expansions are substituted into the equations (2.38)–(2.42) and the boundary conditions (2.43)–(2.46). Because of the moving frame of reference, we must transform the total time derivatives to spatial derivatives according to the following rules. For any function $g = g(\hat{x}, \hat{y}, t)$ we have

$$\dot{g} = \frac{dg}{dt} = \frac{\partial g}{\partial t} - c \frac{\partial g}{\partial \hat{x}}, \tag{4.2}$$

$$\ddot{g} = \frac{d^2g}{dt^2} = \frac{\partial^2 g}{\partial t^2} - 2c \frac{\partial^2 g}{\partial t \partial \hat{x}} - \dot{c} \frac{\partial g}{\partial \hat{x}} + c^2 \frac{\partial^2 g}{\partial \hat{x}^2}. \tag{4.3}$$

Substituting the series expansions (4.1) into (4.2)–(4.3), we observe that differentiation with respect to \hat{x} or \hat{y} lowers the exponents of r by one, while (partial) differentiation with respect to time lets the exponents unchanged. Equating the terms with equal exponents of r results in separate systems of equations for the singular bending moments and the singular shear forces; see below. Because of (4.2)–(4.3), the dependence on time t in the two problems of the singular terms can be interpreted as a dependence on the coordinate \hat{x} . Therefore, we shall omit the argument t from the leading terms in the series expansions (4.1).

4.1.1 Problems of singular bending moments and shear forces

For index $p = 1$, the following problem of the singular bending moments is obtained. According to (4.3) the total time derivative $\ddot{\Theta}_i^{(1)}$ is equal to $c^2 \Theta_{i, \hat{x}\hat{x}}^{(1)}$ plus other terms, which are neglected since they are of higher order in r . For stationary cracks ($c = 0$) these derivatives vanish.

Problem of singular bending moments: determine rotations $\Theta_i^{(1)}$, curvatures $\kappa_{ij}^{(1)}$, and bending moments $M_{ij}^{(1)}$ as sufficiently smooth functions of \hat{x} , \hat{y} and t , satisfying the equations (with indices $i, j = \hat{x}, \hat{y}$)

$$\kappa_{ij}^{(1)} = \frac{1}{2} \left(\Theta_{i,j}^{(1)} + \Theta_{j,i}^{(1)} \right), \tag{4.4}$$

$$M_{ij}^{(1)} = -D_b \left((1 - \nu) \kappa_{ij}^{(1)} + \nu \kappa_{kk}^{(1)} \delta_{ij} \right), \quad (4.5)$$

$$M_{ij,j}^{(1)} = -\frac{1}{12} \rho h^3 \ddot{\Theta}_i^{(1)}, \quad (4.6)$$

in the plane domain V occupied by the plate and subject to the conditions

$$\Theta_i^{(1)} = \overline{\Theta}_i^{(1)} \quad \text{on } S_\theta, \quad (4.7)$$

$$M_{ij}^{(1)} n_j = \overline{M}_i^{(1)} \quad \text{on } S_m, \quad (4.8)$$

on the boundary $\partial V = S_\theta \cup S_m$ with S_θ and S_m being disjoint.

In addition, the problem of the singular shear forces is deduced, where the time derivative $\dot{w}^{(1)}$ of the deflection is equated to $c^2 w_{,\hat{x}\hat{x}}^{(1)}$. In static fracture situations, these terms are identically zero.

Problem of singular shear forces: determine deflection $w^{(1)}$ and shear forces $Q_i^{(1)}$ as sufficiently smooth functions of \hat{x} , \hat{y} and t , satisfying the equations (with index $i = \hat{x}, \hat{y}$)

$$Q_i^{(1)} = D_s w_{,\hat{x}}^{(1)}, \quad (4.9)$$

$$Q_{i,i}^{(1)} = \rho h \ddot{w}^{(1)}, \quad (4.10)$$

in the plane domain V occupied by the plate and subject to the conditions

$$w^{(1)} = \overline{w}^{(1)} \quad \text{on } S_w, \quad (4.11)$$

$$Q_i^{(1)} n_i = \overline{Q}^{(1)} \quad \text{on } S_q, \quad (4.12)$$

on the boundary $\partial V = S_w \cup S_q$ with S_w and S_q being disjoint.

It is clear from the problems defined in this subsection that the *singular* bending moments and the *singular* shear forces are independent. The connection between the bending moments, curvatures and rotations on one hand and the shear forces and deflection on the other hand, as reflected in the relations (2.40) and (2.41), appears only in the terms of higher order in r , i.e., the terms with indices $p > 1$.

4.1.2 Singular bending moments

The equations (4.4)–(4.8) for the problem of the singular bending moments show great similarity with the equations (2.14)–(2.18) for the problem of plane stress. It is possible to compare the rotations $\Theta_i^{(1)}$ with the in-plane displacements u_i and the singular bending moments $M_{ij}^{(1)}$ with the stress components σ_{ij} of modes I and II ($i, j = x, y$). The plate thickness h is incorporated such that corresponding quantities have the same dimensions. In Table 4.1 we present the correspondence between the bending and plane-stress quantities. The density ρ and Poisson's ratio ν for bending

bending	plane stress	units
$\Theta_i^{(1)}$	$\frac{-2 u_i}{h}$	—
$\kappa_{ij}^{(1)}$	$\frac{-2 \varepsilon_{ij}}{h}$	m^{-1}
$M_{ij}^{(1)}$	$\frac{h^2 \sigma_{ij}}{6}$	Nm/m
D_b	$\frac{E h^3}{12(1 - \nu^2)}$	Nm

Table 4.1: Correspondence between bending and plane-stress quantities.

are equal to their values for plane stress, while the bending rigidity D_b is defined by (2.31).

As a result of this correspondence, the expressions for the near-tip bending moments and rotations in mode 1 and 2 bending fracture are derived immediately from the singular stress and displacement fields for modes I and II as given in the preceding chapter. For dynamic crack growth at instantaneous speed c , the singular bending moments are obtained from the solution (3.21) for the stress components and the rotations are obtained from the expression (3.28) for the displacements. In terms of the local polar coordinates the result is expressed as

$$M_{ij}^{(1)}(r, \theta; c) = \frac{h^2 K_1}{6 \sqrt{2\pi r}} F_{ij}^I(\theta, c) + \frac{h^2 K_2}{6 \sqrt{2\pi r}} F_{ij}^{II}(\theta, c), \quad (4.13)$$

$$\Theta_i^{(1)}(r, \theta; c) = -\frac{h^2 K_1}{3D_b(1 - \nu)} \sqrt{\frac{r}{2\pi}} U_i^I(\theta, c) - \frac{h^2 K_2}{3D_b(1 - \nu)} \sqrt{\frac{r}{2\pi}} U_i^{II}(\theta, c), \quad (4.14)$$

with the angular functions given by (3.22)–(3.27) and (3.29)–(3.32), respectively. The constants K_1 and K_2 are the stress-intensity factors for plate bending in modes 1 and 2; see Fig. 4.1. They have the same dimension as K_I and K_{II} and may depend on the crack-growth speed. The bending stress-intensity factors are defined by

$$K_1 = \lim_{r \rightarrow 0} \frac{6 \sqrt{2\pi r}}{h^2} M_{yy}(r, 0; c), \quad (4.15)$$

$$K_2 = \lim_{r \rightarrow 0} \frac{6 \sqrt{2\pi r}}{h^2} M_{xy}(r, 0; c). \quad (4.16)$$

Because of the factor $6/h^2$, the stress-intensity factors K_1 and K_2 are also normalising constants for the in-plane stresses (2.29) in the upper plane ($z = h/2$) of the plate. In the case of stationary cracks ($c = 0$), the near-tip solutions for the bending moments and the rotations reduce to their static limits, which coincide with the formulae given

by Hui and Zehnder [38]. It is remarkable that the angular variations of the singular bending moments in Reissner's theory coincide with those of the singular stresses for planar deformation. This was shown in [38] for static fracture, but it has been proved here that this statement also holds true for elastodynamic crack propagation.

4.1.3 Singular shear forces

Analogously, there exists a similarity between the equations (4.9)–(4.12) for the problem of the singular shear forces and the equations (2.21)–(2.24) for the problem of anti-plane shear. This means that we can compare the deflection $w^{(1)}$ of the plate with the displacement u_z in anti-plane shear and the singular shear forces $Q_i^{(1)}$ with the shear stresses τ_{iz} of mode III fracture ($i = x, y$). This comparison is not trivial for two reasons.

Firstly, Reissner's theory of plate bending involves the shear-correction factor $k = 5/6$, which appears in the definition (2.32) of the shear stiffness D_s . Therefore, we compare $k w^{(1)}$ with the displacement u_z . Secondly, the shear stresses τ_{iz} of anti-plane shear are independent of z , while the shear stresses in the cross section of the plate are quadratic functions of z according to (2.30). Integration of the latter shear stresses over the plate thickness produces the shear forces $Q_i^{(1)}$. As a result, we may compare the singular shear forces $Q_i^{(1)}$ of mode 3 bending fracture with $h \tau_{iz}$ of fracture in anti-plane shear. The correspondences between all quantities are summarised in Table 4.2. The shear stiffness D_s is defined by (2.32), while the density ρ and Poisson's ratio ν for mode 3 bending fracture are equal to their values for mode III fracture.

bending	anti-plane shear	units
$k w^{(1)}$	u_z	m
$Q_i^{(1)}$	$h \tau_{iz}$	N/m
D_s	$k G h$	N/m

Table 4.2: Correspondence between bending and anti-plane shear quantities.

Despite the correspondences, there exists a dissimilarity between the two problems due to the shear-correction factor $k = 5/6$. This becomes apparent for situations of dynamic fracture. Elimination of the shear stresses τ_{iz} from (2.21)–(2.22) produces a wave equation for the displacement u_z and elimination of the shear forces $Q_i^{(1)}$ from (4.9)–(4.10) produces a wave equation for the deflection $w^{(1)}$ of the plate. We find respectively

$$u_{z,ii} - \frac{\rho}{G} \ddot{u}_z = 0, \quad (4.17)$$

$$w_{,ii}^{(1)} - \frac{\rho}{kG} \ddot{w}^{(1)} = 0. \quad (4.18)$$

Clearly, two different characteristic wave speeds occur: the usual shear-wave speed c_s as in (2.20) or (2.34), and a modified velocity $c_k = c_s \sqrt{k}$. Consequently, the solutions are the same only for $k = 1$ and different otherwise. Since the angular functions $F_{iz}^{III}(\theta, c)$ in (3.43)–(3.44) depend on the crack-growth speed through the ratio c/c_s , we must replace c_s with c_k for mode 3 bending and use the ratio c/c_k instead. Alternatively, the same result is obtained when the crack-growth speed c is replaced with the modified crack-growth speed $\tilde{c} = c/\sqrt{k}$, which is defined such that $c/c_k = \tilde{c}/c_s$. The solution for the singular shear forces in the case of dynamic fracture is now derived from (3.42) as

$$Q_i^{(1)}(r, \theta; c) = \frac{2h K_3}{3\sqrt{2\pi r}} F_{iz}^{III}(\theta, \tilde{c}), \quad (4.19)$$

with the angular functions as in (3.43)–(3.44), where we must use the parameters $\tilde{\gamma}_s$, $\tilde{\alpha}_s$ and $\tilde{\theta}_s$ as defined by (3.17) and (3.19) with the crack-growth speed c replaced by the modified crack-growth speed \tilde{c} .

The parameter K_3 is the stress-intensity factor, which is chosen such that it is the normalising constant for the maximum shear stress σ_{yz} in the middle plane ($z = 0$) of the plate; see (2.30) and also Hui and Zehnder [38] and Young and Sun [98]. The stress-intensity factor K_3 has the same dimension as K_{III} , may still depend on the crack-growth speed c , and is defined by

$$K_3 = \lim_{r \rightarrow 0} \sqrt{2\pi r} \sigma_{yz}(r, 0; c) \Big|_{z=0} = \lim_{r \rightarrow 0} \frac{3\sqrt{2\pi r}}{2h} Q_y(r, 0; c). \quad (4.20)$$

The deflection of the plate is derived from Table 4.2 and the solution (3.45) for mode III fracture as

$$w^{(1)}(r, \theta; c) = \frac{4 K_3}{5 \tilde{\alpha}_s G} \sqrt{\frac{2r}{\pi}} \tilde{\gamma}_s^{\frac{1}{2}} \sin \frac{1}{2} \tilde{\theta}_s, \quad (4.21)$$

where the factor $4/5$ stems from the quotient of the factor $2/3$ in (4.19) and the shear-correction factor $5/6$. Thus, we see that corresponding angular variations are obtained for fracture in modes 3 and III. In the limit of zero crack growth, i.e. for $c \rightarrow 0$, the dynamic results above reduce to their static equivalents

$$Q_i^{(1)}(r, \theta) = \frac{2h K_3}{3\sqrt{2\pi r}} f_{iz}^{III}(\theta), \quad (4.22)$$

$$w^{(1)}(r, \theta) = \frac{4 K_3}{5 G} \sqrt{\frac{2r}{\pi}} \sin \frac{1}{2} \theta, \quad (4.23)$$

with the angular functions $f_{iz}^{III}(\theta)$ given by (3.39)–(3.40). For later use we also give the higher-order term $w^{(3)}$ of the expansion (4.1) of the deflection, which term depends on Poisson's ratio and the stress-intensity factors K_1 and K_2 . The linear term $w^{(2)}$ relates to rigid-body motions and is of less importance. For a stationary crack we obtain from [38] that

$$w^{(3)}(r, \theta) = \frac{h^2 r^{3/2}}{6D_b(1-\nu^2)\sqrt{2\pi}} \left\{ K_1 \left(\frac{1}{3}(7+\nu) \cos \frac{3}{2}\theta - (1-\nu) \cos \frac{1}{2}\theta \right) - K_2 \left(\frac{1}{3}(5+3\nu) \sin \frac{3}{2}\theta - (1-\nu) \sin \frac{1}{2}\theta \right) \right\}. \quad (4.24)$$

4.1.4 Energy release rate

The energy release rate due to bending moments and shear forces is calculated from the expression (3.47). The expressions (2.29)–(2.30) for the stress components in the cross section of the plate are substituted, while the in-plane displacements are given by (2.35) and the deflection is assumed to be independent of z . Carrying out the integration with respect to z in (3.47) and suppressing the dependence on the crack-growth speed c , we obtain the following expression for the energy release rate:

$$\mathcal{G} = \lim_{\Delta a \rightarrow 0} \left\{ \frac{1}{2\Delta a} \int_0^{\Delta a} Q_y(r, 0) [w(\Delta a - r, \pi) - w(\Delta a - r, -\pi)] dr - \frac{1}{2\Delta a} \int_0^{\Delta a} M_{iy}(r, 0) [\Theta_i(\Delta a - r, \pi) - \Theta_i(\Delta a - r, -\pi)] dr \right\}. \quad (4.25)$$

With the use of the near-tip solutions of the preceding subsections the energy release rate for dynamic bending fracture in Reissner's theory is determined. It is found that

$$\mathcal{G} = \frac{h}{3E} \left(A_I(c) K_1^2 + A_{II}(c) K_2^2 \right) + \frac{4h}{15G} A_{III}(\tilde{c}) K_3^2, \quad (4.26)$$

where the velocity-dependent coefficients are given by (3.49)–(3.51). For stationary cracks these coefficients are equal to unity and the corresponding energy release rate coincides with results of Hui and Zehnder [38] and Young and Sun [98, 99].

The integrals J_k ($k = 1, 2$) can also be expressed in terms of the bending moments and shear forces. The contour C in (3.52) is again taken as a circle inside the region of K -dominance with the outward normal having components n_i with $n_z = 0$. In view of the behaviour (2.29)–(2.30) and (2.35) of the stresses and displacements in the cross section of the plate, the elastic and kinetic energy densities transform into

$$W = \frac{1}{2} \sigma_{ij} \varepsilon_{ij} + \tau_{iz} \varepsilon_{iz} = -\frac{6z^2}{h^3} M_{ij} \kappa_{ij} + \frac{3Q_i Q_i}{4h D_s} \left(1 - \left(\frac{2z}{h} \right)^2 \right), \quad (4.27)$$

$$T = \frac{1}{2} \rho \left(z^2 \dot{\Theta}_i \dot{\Theta}_i + \dot{w}^2 \right) = \frac{1}{2} \rho c^2 \left(z^2 \Theta_{i,\hat{x}} \Theta_{i,\hat{x}} + w_{,\hat{x}}^2 \right), \quad (4.28)$$

with $i, j = x, y$, while the stress-work term becomes

$$\sigma_{ij} n_j u_{i,k} = -\frac{12z^2}{h^3} M_{ij} n_j \Theta_{i,k} + \frac{3Q_i n_i w_{,k}}{2h} \left(1 - \left(\frac{2z}{h} \right)^2 \right). \quad (4.29)$$

Substitution into (3.52) and subsequent integration over the thickness of the plate yields the expression for the J -integrals in plate bending. As a generalisation of the static formulae [38] we find (with indices $i, j, k = x, y$ or $1, 2$)

$$J_k = \lim_{C \rightarrow 0} \left\{ \int_C \left[\left(-\frac{1}{2} M_{ij} \kappa_{ij} + \frac{\rho h^3}{24} \dot{\Theta}_i \dot{\Theta}_i \right) n_k + M_{ij} n_j \Theta_{i,k} \right] ds + \int_C \left[\left(\frac{Q_i Q_i}{2D_s} + \frac{1}{2} \rho h \dot{w}^2 \right) n_k - Q_i n_i w_{,k} \right] ds \right\}. \quad (4.30)$$

Since we apply the limit for the contour C shrinking onto the crack tip, we may replace all quantities in the integrand of (4.30) with the corresponding leading terms of the series expansions (4.1). The first integral in (4.30) corresponds to the bending modes 1 and 2 and is similar to the expression (3.52) for modes I and II; see also Table 4.1. This first integral differs by only a multiplicative factor $1/3$ from the results (3.48) and (3.54). The second integral in (4.30) corresponds to the shear mode 3 and is similar to the expression (3.52) for mode III; see Table 4.2. This second integral differs by a multiplicative factor $8/15$ from the results (3.48) and (3.54), which is due to the different scaling of the shear stresses and to the shear-correction factor. In addition, we must replace the crack-growth speed c with the modified crack-growth speed $\tilde{c} = c\sqrt{6/5}$ in the case of mode 3 fracture. Combining the two integrals in (4.30), we obtain the relations between the J -integrals and the bending stress-intensity factors.

We find that the integral J_1 is equal to the energy release rate (4.26), viz. $J_1 = \mathcal{G}$. This integral is independent of the shape of the contour C and is therefore called path-independent. For the integral J_2 we find that

$$J_2 = -\frac{2h}{3E} A_{IV}(c) K_1 K_2, \quad (4.31)$$

where the coefficient $A_{IV}(c)$ is a function of the crack-growth speed, which depends on the shape of the contour C ; see Section 3.3 and Appendix A. Evaluation of J_2 for shrinking circular and rectangular contours produces different expressions for the coefficient $A_{IV}(c)$, which are given in formulae (A.3) and (A.4). When the contour C is not symmetric with respect to the x -axis, the expression (4.31) may contain additional terms with K_1^2 , K_2^2 and K_3^2 .

4.2 Bending fracture in classical plate theory

Consider a linearly elastic, thin flat plate of thickness h containing an arbitrary crack and being loaded by bending moments as described in Subsection 2.4.2. This configuration resembles the one of the preceding section with the difference that the rotations must now satisfy the relations (2.47). This implies that the shear stiffness D_s as defined in (2.32) and the shear-wave velocity c_s of (2.34) attain infinite values. In addition, the boundary conditions for the torsional moment and the perpendicular shear force must be combined.

4.2.1 Static solution

Firstly, the solution for stationary cracks ($c = 0$) is investigated. Cartesian coordinates x and y and polar coordinates r and θ with the origin at the crack tip are introduced; see Fig. 3.2. The plate is subjected to remote loading by bending and torsional moments in combination with perpendicular shear forces, while the crack surfaces are

not loaded and remain stress-free. The deformation of the plate is governed given by the equations (2.49)–(2.51) with zero accelerations, i.e., with $\frac{1}{12}\rho h^3 \ddot{w}_{,i} = 0$ and $\rho h \ddot{w} = 0$. Elimination of the bending moments M_{ij} and the shear forces Q_i from these equations produces the biharmonic equation

$$\Delta \Delta w = 0, \quad (4.32)$$

where $\Delta w = w_{,ii}$ is the Laplace operator. Since the crack flanks are stress-free, we impose homogeneous boundary conditions (2.53) and (2.55). Expressing these conditions in terms of the deflection w leads to the relations

$$w_{,yy} + \nu w_{,xx} = 0, \quad (4.33)$$

$$w_{,yyy} + (2 - \nu) w_{,xxy} = 0, \quad (4.34)$$

valid on the crack flanks where $x < 0$, $y = \pm 0$ or $r > 0$, $\theta = \pm \pi$.

Since our interest lies in the near-tip stress and displacement fields, we employ series expansions in powers of the distance r to the crack tip similar to the expansions (4.1). The series expansions for classical plate theory must satisfy the same conditions as those for Reissner's theory; see the beginning of Section 4.1. These conditions imply that the bending moments are of the order $O(r^{-1/2})$ for $r \rightarrow 0$, and that the term $w^{(1)}$ of the series representation of the deflection vanishes. The singular bending moments $M_{ij}^{(1)}$ are normalised by stress-intensity factors, which are denoted by small letters to distinguish them from those for Reissner's theory. The stress-intensity factor k_1 is the normalising constant for the symmetric bending moment M_{yy} and the factor k_2 for the generalised torque M_{yx}^* , which is defined in (2.65) and (2.68), in the direction $\theta = 0$ ahead of the crack. In agreement with Erdogan, Tuncel and Paris [24], Hui and Zehnder [38], and Sih, Paris and Erdogan [84], we define

$$k_1 = \lim_{r \rightarrow 0} \frac{6\sqrt{2\pi r}}{h^2} M_{yy}(r, 0), \quad (4.35)$$

$$k_2 = \lim_{r \rightarrow 0} \frac{6\sqrt{2\pi r}}{h^2} M_{yx}^*(r, 0). \quad (4.36)$$

It is noted that in [98] the stress-intensity factor k_2 was defined in relation to M_{xy} and consequently differs by a factor $(1 + \nu)/(3 + \nu)$; see below.

Now, we calculate the solution to the biharmonic equation (4.32) subject to the boundary conditions (4.33)–(4.34). Since the term $w^{(1)}$ of the series expansion of the deflection vanishes and the term $w^{(2)}$ relates to rigid-body motions, we focus on the term $w^{(3)}$ which is of interest to the near-tip fields. The result is taken from [38]:

$$w^{(3)}(r, \theta) = \frac{h^2 r^{3/2}}{6D_b(3 + \nu)\sqrt{2\pi}} \left\{ k_1 \left(\frac{7 + \nu}{3(1 - \nu)} \cos \frac{3}{2}\theta - \cos \frac{1}{2}\theta \right) - k_2 \left(\frac{5 + 3\nu}{3(1 - \nu)} \sin \frac{3}{2}\theta - \sin \frac{1}{2}\theta \right) \right\}. \quad (4.37)$$

The corresponding terms $\Theta_i^{(1)} = w_i^{(3)}$ in the series expansions of the rotations are obtained by differentiation (see (2.47))

$$\Theta_x^{(1)}(r, \theta) = \frac{h^2}{3D_b(3+\nu)} \sqrt{\frac{r}{2\pi}} \left\{ k_1 \cos \frac{1}{2}\theta \left(\frac{1+\nu}{1-\nu} + \sin^2\left(\frac{1}{2}\theta\right) \right) + k_2 \sin \frac{1}{2}\theta \left(\frac{-2}{1-\nu} + \cos^2\left(\frac{1}{2}\theta\right) \right) \right\}, \quad (4.38)$$

$$\Theta_y^{(1)}(r, \theta) = \frac{h^2}{3D_b(3+\nu)} \sqrt{\frac{r}{2\pi}} \left\{ k_1 \sin \frac{1}{2}\theta \left(\frac{-2}{1-\nu} - \cos^2\left(\frac{1}{2}\theta\right) \right) + k_2 \cos \frac{1}{2}\theta \left(-\frac{1+\nu}{1-\nu} + \sin^2\left(\frac{1}{2}\theta\right) \right) \right\}. \quad (4.39)$$

The corresponding singular bending moments $M_{ij}^{(1)}$ are obtained by differentiation of the rotations or from second-order derivatives of the deflection; see (2.49). Contrary to the results (4.13) by Reissner's theory, the bending moments for classical plate theory depend on Poisson's ratio ν (see also [24, 38, 84]).

$$M_{ij}^{(1)}(r, \theta) = \frac{h^2 k_1}{6\sqrt{2\pi r}} g_{ij}^I(\theta, \nu) + \frac{h^2 k_2}{6\sqrt{2\pi r}} g_{ij}^{II}(\theta, \nu), \quad (4.40)$$

where the angular variations $g_{ij}^I(\theta, \nu)$ for the normal-bending mode are equal to

$$g_{xx}^I(\theta, \nu) = \frac{\nu-1}{\nu+3} \cos \frac{1}{2}\theta \left(1 - \sin \frac{1}{2}\theta \sin \frac{3}{2}\theta \right), \quad (4.41)$$

$$g_{yy}^I(\theta, \nu) = \frac{\nu-1}{\nu+3} \cos \frac{1}{2}\theta \left(\frac{\nu+3}{\nu-1} + \sin \frac{1}{2}\theta \sin \frac{3}{2}\theta \right), \quad (4.42)$$

$$g_{xy}^I(\theta, \nu) = \frac{\nu-1}{\nu+3} \sin \frac{1}{2}\theta \left(\frac{2}{1-\nu} + \cos \frac{1}{2}\theta \cos \frac{3}{2}\theta \right), \quad (4.43)$$

while the angular variations $g_{ij}^{II}(\theta, \nu)$ for the twisting mode are

$$g_{xx}^{II}(\theta, \nu) = \frac{\nu-1}{\nu+3} \sin \frac{1}{2}\theta \left(\frac{2(1+\nu)}{1-\nu} - \cos \frac{1}{2}\theta \cos \frac{3}{2}\theta \right), \quad (4.44)$$

$$g_{yy}^{II}(\theta, \nu) = \frac{\nu-1}{\nu+3} \sin \frac{1}{2}\theta \cos \frac{1}{2}\theta \cos \frac{3}{2}\theta, \quad (4.45)$$

$$g_{xy}^{II}(\theta, \nu) = \frac{\nu-1}{\nu+3} \cos \frac{1}{2}\theta \left(\frac{\nu+1}{\nu-1} - \sin \frac{1}{2}\theta \sin \frac{3}{2}\theta \right). \quad (4.46)$$

The shear forces Q_i are derived by differentiation of the bending moments M_{ij} according to the equation (2.50) with $\frac{1}{12}\rho h^3 \ddot{w}_i = 0$. These shear forces have an essential singularity of order $O(r^{-3/2})$ for $r \rightarrow 0$, which is a typical effect of the classical plate theory [38]. As a result, we must adapt the series representation (4.1) for the shear forces and let the summation index start at $p = -1$. The leading terms $Q_i^{(-1)}$ are found to be

$$Q_x^{(-1)}(r, \theta) = \frac{-\pi h^2}{3(3+\nu)(2\pi r)^{3/2}} \left(k_1 \cos \frac{3}{2}\theta - k_2 \sin \frac{3}{2}\theta \right), \quad (4.47)$$

$$Q_y^{(-1)}(r, \theta) = \frac{-\pi h^2}{3(3+\nu)(2\pi r)^{3/2}} \left(k_1 \sin \frac{3}{2}\theta + k_2 \cos \frac{3}{2}\theta \right). \quad (4.48)$$

It is now possible to calculate the leading terms of the generalised torques which are given by the equations (2.67) and (2.68). We integrate the shear forces $Q_i^{(-1)}$ and disregard the integration constant. Combining the results with the expression for $M_{xy}^{(1)}$, we find

$$M_{xy}^{*(1)}(r, \theta) = \frac{h^2}{6\sqrt{2\pi r}} \cdot \frac{\nu-1}{\nu+3} \left\{ k_1 \sin \frac{1}{2}\theta \left(\frac{4}{1-\nu} + \cos \frac{1}{2}\theta \cos \frac{3}{2}\theta \right) + k_2 \cos \frac{1}{2}\theta \left(1 - \sin \frac{1}{2}\theta \sin \frac{3}{2}\theta \right) \right\}, \quad (4.49)$$

$$M_{yx}^{*(1)}(r, \theta) = \frac{h^2}{6\sqrt{2\pi r}} \cdot \frac{\nu-1}{\nu+3} \left\{ k_1 \sin \frac{1}{2}\theta \cos \frac{1}{2}\theta \cos \frac{3}{2}\theta + k_2 \cos \frac{1}{2}\theta \left(\frac{\nu+3}{\nu-1} - \sin \frac{1}{2}\theta \sin \frac{3}{2}\theta \right) \right\}. \quad (4.50)$$

From the latter representation, the scaling property of the bending stress-intensity factor k_2 becomes clear; see (4.36). Namely, we have $M_{yx}^{*(1)}(r, 0) = h^2 k_2 / 6\sqrt{2\pi r}$ in the direction ahead of the crack.

4.2.2 Dynamic solution

The dynamic problem (2.49)–(2.51) of plate bending in the classical theory can be reduced to one equation for the deflection only. Elimination of the bending moments and the shear forces results in a partial differential equation of fourth order

$$\Delta\Delta w - \frac{\rho h^3}{12 D_b} \Delta\ddot{w} + \frac{\rho h}{D_b} \ddot{w} = 0, \quad (4.51)$$

where $\Delta w = w_{,ii}$ is the Laplace operator and \ddot{w} is the second derivative with respect to time. Furthermore, we have the property that $12 D_b / \rho h^3 = c_d^2$ by (2.33).

We use the Cartesian coordinates (\hat{x}, \hat{y}) and the polar coordinates (r, θ) with the origin attached to the crack tip, which moves at speed c ; see (3.15). The solution procedure is identical to that for the static problem. The deflection is represented by a series expansion as in (4.1) with the term $w^{(1)}$ being equal to zero and the term $w^{(2)}$ corresponding to rigid-body motions. The series expansion for the shear forces starts with the leading term $Q_i^{(-1)}$. The bending moments and the rotations have representations similar to those in (4.1) with leading terms $M_{ij}^{(1)}$ and $\Theta_i^{(1)}$, respectively. Transformation of (4.51) to the moving frame of reference with the use of (4.3) yields the following differential equation for the term $w^{(3)}$, viz.

$$\Delta\Delta w^{(3)} - \frac{c^2}{c_d^2} \Delta w_{,\hat{x}\hat{x}}^{(3)} = 0, \quad (4.52)$$

or equivalently, expressed in the distorted polar coordinates (r_d, θ_d) defined in (3.16) and (3.18),

$$\left(\frac{\partial^2}{\partial r^2} + \frac{1}{r} \frac{\partial}{\partial r} + \frac{1}{r^2} \frac{\partial^2}{\partial \theta^2} \right) \left(\frac{\partial^2}{\partial r_d^2} + \frac{1}{r_d} \frac{\partial}{\partial r_d} + \frac{1}{r_d^2} \frac{\partial^2}{\partial \theta_d^2} \right) w^{(3)} = 0. \quad (4.53)$$

It is customary [59, 90] to omit the middle term in (4.51), because it is of order $O(h^2/L^2)$ in comparison with the third term, with h being the plate thickness and L some (large) in-plane length measure. In the present situation, however, the in-plane length measure is small, because we focus on the crack-tip region and on the dynamic crack-growth effects. Omission of the middle term in (4.51) would imply that the term $w^{(3)}$ of the series expansion of the deflection satisfies the biharmonic equation, because the second term in (4.52) would be absent. Consequently, the near-tip dynamic solution would be equal to the near-tip static solution and a study of the dynamic effects is not possible. Moreover, Mindlin [59] has shown that the equation (4.51) can be inferred from higher-order plate theory by neglecting the transverse shear deformation and retaining the rotatory inertia terms. For these reasons, we shall retain the middle term in (4.51). Pursuing this dynamic fracture problem in classical plate theory is especially useful, because it enables us to investigate the validity of this theory in the neighbourhood of cracks. The limited validity near boundaries is a well-known feature of the classical plate theory [90] and is due to the combined boundary conditions for the torsional moment and the perpendicular shear force.

The term $w^{(3)}$ of the series expansion of the deflection is of order $O(r^{3/2})$ and gives rise to singular bending moments $M_{ij}^{(1)}$ of order $O(r^{-1/2})$ and to shear forces $Q_i^{(-1)}$ having an essential singularity of order $O(r^{-3/2})$ at the crack tip. These cross-sectional quantities are related to the deflection by the equations (2.49)–(2.51). For situations of dynamic fracture, the relations between the leading terms of the respective series expansions can be written as (with $i, j, k = x, y$)

$$M_{ij}^{(1)} = -D_b \left((1 - \nu) w_{,ij}^{(3)} + \nu w_{,kk}^{(3)} \delta_{ij} \right), \quad (4.54)$$

$$Q_i^{(-1)} = M_{ij,j}^{(1)} + \frac{D_b c^2}{c_d^2} w_{,\hat{x}\hat{x}i}^{(3)} = -D_b \left(\alpha_d^2 w_{,\hat{x}\hat{x}}^{(3)} + w_{,\hat{y}\hat{y}}^{(3)} \right)_{,i}, \quad (4.55)$$

where α_d is defined by (3.18). The equation (2.51) reduces to $Q_{i,i}^{(-1)} = 0$. This is in perfect agreement with the differential equation (4.52).

The boundary conditions for the dynamic fracture problem differ from (4.33)–(4.34) for the static fracture problem. From the relations (2.53), (2.55) and (4.54)–(4.55) the boundary values of the normal bending moment and the generalised shear force are derived. On the crack flanks where $r > 0$ and $\theta = \pm\pi$, we have

$$M_{yy}^{(1)} = -D_b \left(w_{,\hat{y}\hat{y}}^{(3)} + \nu w_{,\hat{x}\hat{x}}^{(3)} \right) = 0, \quad (4.56)$$

$$Q_y^{(-1)} + M_{xy,x}^{(1)} = -D_b \left(w_{,\hat{y}\hat{y}\hat{y}}^{(3)} + (1 - \nu + \alpha_d^2) w_{,\hat{x}\hat{x}\hat{y}}^{(3)} \right) = 0. \quad (4.57)$$

The solution to the differential equation (4.53) subject to the dynamic boundary conditions (4.56)–(4.57) is derived in a straightforward manner. The term $w^{(3)}$ of the series expansion of the deflection depends on the local polar coordinates, the crack-growth speed c , and Poisson's ratio ν . We define the elastodynamic bending stress-intensity factors k_1 and k_2 for classical plate theory in the same manner as in (4.35)–(4.36). These parameters may depend on the crack-growth speed. The term

$w^{(3)}$ is now given by

$$w^{(3)}(r, \theta; c) = \frac{h^2 (2r)^{3/2}}{18D_b S \sqrt{\pi}} \left\{ k_1 \left(-(\alpha_d^2 - \nu) \gamma_d^{3/2} \cos \frac{3}{2} \theta_d + (1 - \nu) \alpha_d \cos \frac{3}{2} \theta \right) + k_2 \left(-(1 - \nu) \gamma_d^{3/2} \sin \frac{3}{2} \theta_d + (\alpha_d^2 - \nu) \sin \frac{3}{2} \theta \right) \right\}, \quad (4.58)$$

where γ_d is defined by (3.16) and the function $S = S(c, \nu)$ in the denominator by

$$S(c, \nu) = (1 - \nu)^2 \alpha_d - (\alpha_d^2 - \nu)^2 = (1 - \alpha_d) \left(\alpha_d (1 + \alpha_d)^2 - (\alpha_d + \nu)^2 \right). \quad (4.59)$$

The corresponding terms $\Theta_i^{(1)} = w_i^{(3)}$ in the series expansions of the rotations are obtained by differentiation (see (2.47))

$$\Theta_x^{(1)} = \frac{h^2}{3D_b S} \sqrt{\frac{r}{2\pi}} \left\{ k_1 \left(-(\alpha_d^2 - \nu) \gamma_d^{\frac{1}{2}} \cos \frac{1}{2} \theta_d + (1 - \nu) \alpha_d \cos \frac{1}{2} \theta \right) + k_2 \left(-(1 - \nu) \gamma_d^{\frac{1}{2}} \sin \frac{1}{2} \theta_d + (\alpha_d^2 - \nu) \sin \frac{1}{2} \theta \right) \right\}, \quad (4.60)$$

$$\Theta_y^{(1)} = \frac{h^2}{3D_b S} \sqrt{\frac{r}{2\pi}} \left\{ k_1 \left((\alpha_d^2 - \nu) \alpha_d \gamma_d^{\frac{1}{2}} \sin \frac{1}{2} \theta_d - (1 - \nu) \alpha_d \sin \frac{1}{2} \theta \right) + k_2 \left(-(1 - \nu) \alpha_d \gamma_d^{\frac{1}{2}} \cos \frac{1}{2} \theta_d + (\alpha_d^2 - \nu) \cos \frac{1}{2} \theta \right) \right\}. \quad (4.61)$$

The corresponding singular bending moments $M_{ij}^{(1)}$ are obtained by differentiation according to (4.54). The dependence on the crack-growth speed c and Poisson's ratio ν is explicitly incorporated in the arguments of the angular variations. We find

$$M_{ij}^{(1)}(r, \theta; c) = \frac{h^2 k_1}{6 \sqrt{2\pi r}} G_{ij}^I(\theta; c, \nu) + \frac{h^2 k_2}{6 \sqrt{2\pi r}} G_{ij}^{II}(\theta; c, \nu) \quad (4.62)$$

with the angular variations $G_{ij}^I(\theta; c, \nu)$ for the normal-bending mode given by

$$G_{xx}^I = \frac{1}{S} \left((1 - \nu \alpha_d^2) (\alpha_d^2 - \nu) \gamma_d^{-\frac{1}{2}} \cos \frac{1}{2} \theta_d - (1 - \nu)^2 \alpha_d \cos \frac{1}{2} \theta \right), \quad (4.63)$$

$$G_{yy}^I = \frac{1}{S} \left(-(\alpha_d^2 - \nu)^2 \gamma_d^{-\frac{1}{2}} \cos \frac{1}{2} \theta_d + (1 - \nu)^2 \alpha_d \cos \frac{1}{2} \theta \right), \quad (4.64)$$

$$G_{xy}^I = \frac{1}{S} \left((1 - \nu) (\alpha_d^2 - \nu) \alpha_d \gamma_d^{-\frac{1}{2}} \sin \frac{1}{2} \theta_d - (1 - \nu)^2 \alpha_d \sin \frac{1}{2} \theta \right), \quad (4.65)$$

while the angular variations $G_{ij}^{II}(\theta; c, \nu)$ for the twisting mode are

$$G_{xx}^{II} = \frac{1}{S} \left((1 - \nu) (\nu \alpha_d^2 - 1) \gamma_d^{-\frac{1}{2}} \sin \frac{1}{2} \theta_d + (1 - \nu) (\alpha_d^2 - \nu) \sin \frac{1}{2} \theta \right), \quad (4.66)$$

$$G_{yy}^{II} = \frac{(1 - \nu) (\alpha_d^2 - \nu)}{S} \left(\gamma_d^{-\frac{1}{2}} \sin \frac{1}{2} \theta_d - \sin \frac{1}{2} \theta \right), \quad (4.67)$$

$$G_{xy}^{II} = \frac{1}{S} \left((1 - \nu)^2 \alpha_d \gamma_d^{-\frac{1}{2}} \cos \frac{1}{2} \theta_d - (1 - \nu) (\alpha_d^2 - \nu) \cos \frac{1}{2} \theta \right). \quad (4.68)$$

As in the case of a stationary crack, the shear forces Q_i for a propagating crack have an essential singularity of order $O(r^{-3/2})$ for $r \rightarrow 0$. The leading terms $Q_i^{(-1)}$ of the series expansion are derived from (4.55). We obtain

$$Q_x^{(-1)} = \frac{(\alpha_d^2 - 1) \pi h^2}{6 S (2\pi r)^{3/2}} \left((1 - \nu) \alpha_d k_1 \cos \frac{3}{2} \theta - (\alpha_d^2 - \nu) k_2 \sin \frac{3}{2} \theta \right), \quad (4.69)$$

$$Q_y^{(-1)} = \frac{(\alpha_d^2 - 1) \pi h^2}{6 S (2\pi r)^{3/2}} \left((1 - \nu) \alpha_d k_1 \sin \frac{3}{2} \theta + (\alpha_d^2 - \nu) k_2 \cos \frac{3}{2} \theta \right). \quad (4.70)$$

Next, the generalised torques (2.67) and (2.68) are determined for dynamic crack growth. The shear forces $Q_i^{(-1)}$ are integrated and combined with the expression for $M_{xy}^{(1)}$. It is found that the leading terms of the series expansions are given by

$$M_{xy}^{*(1)} = \frac{h^2}{6S \sqrt{2\pi r}} \left\{ k_1 (1 - \nu) \alpha_d \left((\alpha_d^2 - \nu) \gamma_d^{-\frac{1}{2}} \sin \frac{1}{2} \theta_d + (\alpha_d^2 + \nu - 2) \sin \frac{1}{2} \theta \right) + k_2 \left((1 - \nu)^2 \alpha_d \gamma_d^{-\frac{1}{2}} \cos \frac{1}{2} \theta_d + (\alpha_d^2 - \nu) (\alpha_d^2 + \nu - 2) \cos \frac{1}{2} \theta \right) \right\}, \quad (4.71)$$

$$M_{yx}^{*(1)} = \frac{h^2}{6S \sqrt{2\pi r}} \left\{ k_1 (1 - \nu) (\alpha_d^2 - \nu) \alpha_d \left(\gamma_d^{-\frac{1}{2}} \sin \frac{1}{2} \theta_d - \sin \frac{1}{2} \theta \right) + k_2 \left((1 - \nu)^2 \alpha_d \gamma_d^{-\frac{1}{2}} \cos \frac{1}{2} \theta_d - (\alpha_d^2 - \nu)^2 \cos \frac{1}{2} \theta \right) \right\}. \quad (4.72)$$

In analogy with the static problem, we observe the scaling properties of the elastodynamic bending stress-intensity factors. Namely, we have $M_{yy}^{(1)} = h^2 k_1 / 6\sqrt{2\pi r}$ and $M_{yx}^{*(1)} = h^2 k_2 / 6\sqrt{2\pi r}$ in the direction $\theta = 0$ ahead of the crack, in agreement with the definitions (4.35)-(4.36). Finally, we remark that the dynamic solutions reduce to the static solutions of Subsection 4.2.1 in the limit for zero crack growth ($c \rightarrow 0$).

4.2.3 Energy release rate

The energy release rate \mathcal{G} in the classical plate theory is calculated from an adapted version of (4.25), because the first integral in that formula diverges due to the essential singularity of the perpendicular shear forces. The term with the product $Q_y w$ is integrated by parts and the integration constant is neglected. In the resulting expression we recognise the generalised torque M_{yx}^* defined in (2.68), such that we finally obtain

$$\mathcal{G} = \lim_{\Delta a \rightarrow 0} \left\{ -\frac{1}{2 \Delta a} \int_0^{\Delta a} M_{yy}(r, 0; c) [w_{,y}(\Delta a - r, \pi; c) - w_{,y}(\Delta a - r, -\pi; c)] dr - \frac{1}{2 \Delta a} \int_0^{\Delta a} M_{yx}^*(r, 0; c) [w_{,x}(\Delta a - r, \pi; c) - w_{,x}(\Delta a - r, -\pi; c)] dr \right\} \quad (4.73)$$

in analogy with Young and Sun [98, 99]. With the use of the near-tip solutions of the preceding subsections we derive that the energy release rate for dynamic bending

fracture in the classical theory is equal to

$$\mathcal{G} = \frac{h}{3E} \cdot \frac{1+\nu}{3+\nu} \left(a_1(c) k_1^2 + a_2(c) k_2^2 \right), \quad (4.74)$$

where the coefficients $a_1(c)$ and $a_2(c)$ depend on the crack-growth speed c by

$$a_1(c) = \frac{(1-\nu)(3+\nu)(1-\alpha_d^2)\alpha_d}{2S}, \quad (4.75)$$

$$a_2(c) = \frac{(1-\nu)(3+\nu)(1-\alpha_d^2)}{2S}. \quad (4.76)$$

The parameters α_d and $S = S(c, \nu)$ are defined in (3.18) and (4.59), respectively. A third coefficient $a_3(c)$ does not exist due to the coupling between the torsion and perpendicular shear effects. For stationary cracks ($c = 0$) the coefficients are equal to unity and the expression (4.74) becomes equal to the results of [38, 98, 99].

The J -integrals in the classical theory are derived from the expression (4.30) in Reissner's theory. The shear stiffness D_s must be taken equal to infinity and the relations (2.47) must be substituted for the rotations. In the next step, the term $Q_i n_i w_{,k}$ is integrated by parts and the expression (2.68) for the generalised torque M_{yx}^* is used. This procedure leads to (with $i, j, k = x, y$ or $1, 2$)

$$\begin{aligned} J_k &= \lim_{C \rightarrow 0} \int_C \left[\left(-\frac{1}{2} M_{ij} w_{,ij} + \frac{\rho h^3}{24} \dot{w}_{,i} \dot{w}_{,i} + \frac{1}{2} \rho h \dot{w}^2 \right) n_k + M_{ij} n_j w_{,ik} - Q_i n_i w_{,k} \right] ds \\ &= \lim_{C \rightarrow 0} \int_C \left[\left(-\frac{1}{2} M_{ij} w_{,ij} + \frac{\rho h^3}{24} \dot{w}_{,i} \dot{w}_{,i} + \frac{1}{2} \rho h \dot{w}^2 \right) n_k + M_{nn} w_{,nk} + M_{ns}^* w_{,sk} \right] ds. \end{aligned} \quad (4.77)$$

Since the limit for the contour C shrinking onto the crack tip is applied, all quantities in the integrand of (4.77) may be replaced with the corresponding leading terms of the series expansions. It is then observed that the contribution of the term $\frac{1}{2} \rho h \dot{w}^2$ vanishes.

Evaluation of (4.77) yields expressions for J_1 and J_2 in terms of the stress-intensity factors. Again, we find that the integral J_1 is equal to the energy release rate \mathcal{G} and is independent of the shape of the contour C . The integral J_2 is given by

$$J_2 = \frac{2h(1-\nu^2)}{3E(3+\nu)^2} a_4(c) k_1 k_2, \quad (4.78)$$

where the coefficient $a_4(c)$ depends on the crack-growth speed c and on the shape of the contour C . This coefficient has been calculated for circular and rectangular shrinking contours and the results are given in (A.5) and (A.6) of Appendix A.3, respectively. In the limit of zero crack propagation, i.e., for $c \rightarrow 0$, the coefficient $a_4(c)$ tends to unity. When the contour C is not symmetric with respect to the x -axis, additional terms with k_1^2 and k_2^2 may be present in the expression (4.78).

4.3 Comparison of plate bending theories

The differences between the plate theories of Kirchhoff and of Reissner concern the shear deformation in the transverse direction. In Kirchhoff's classical plate theory it is assumed that perpendicular line elements remain perpendicular to the middle plane during bending deformation, while in Reissner's theory such line elements may rotate and a finite shear stiffness D_s is introduced. An immediate consequence of these assumptions is that the deflection and the rotations are independent variables in Reissner's theory, whereas the connection (2.47) exists in the classical theory. Both plate theories have been applied to bending fracture of plates containing a crack. This section discusses the differences between the two plate theories, regarding the solutions in the vicinity of the crack tip for the bending modes 1 and 2 in both cases of dynamic fracture and of (quasi)-static fracture. (A deformation problem which is not static in the strict sense, for example due to time-dependent external forces, is called quasi-static when the dynamic effects such as accelerations can be neglected.) The solutions for the shear mode 3 and the related tearing mode III are discussed in the next section, together with the combined shear and torsion effects in classical plate theory.

4.3.1 Static near-tip solutions

Because of the relative simplicity of the near-tip fields, the solutions for stationary cracks ($c = 0$) are considered first. We start with a comparison of the singular bending moments $M_{ij}^{(1)}$ which are given by (4.13) with angular variations (3.4)–(3.9) for Reissner's theory and by (4.40) with angular variations (4.41)–(4.46) for the classical plate theory. It is remarkable that the angular variations $g_{ij}^I(\theta, \nu)$ and $g_{ij}^{II}(\theta, \nu)$ in the classical theory are dependent on Poisson's ratio ν , while the functions $f_{ij}^I(\theta)$ and $f_{ij}^{II}(\theta)$ for Reissner's theory are not. An important observation is that these functions become equal in the limit for $\nu \rightarrow \infty$. That is, for $i, j = x, y$,

$$f_{ij}^I(\theta) = \lim_{\nu \rightarrow \infty} g_{ij}^I(\theta, \nu), \quad (4.79)$$

$$f_{ij}^{II}(\theta) = \lim_{\nu \rightarrow \infty} g_{ij}^{II}(\theta, \nu). \quad (4.80)$$

In addition, the generalised torques $M_{xy}^{*(1)}$ and $M_{yx}^{*(1)}$ attain the same limit as the torsional moment $M_{xy}^{(1)}$ in classical plate theory; see (4.43), (4.46) and (4.49)–(4.50).

This is a strange phenomenon because usually $0 < \nu < 0.5$ in practical applications. Therefore, this limit has no clear physical interpretation and must be regarded as a formal mathematical substitution. A possible explanation can be as follows. In classical plate theory the shear stiffness D_s has an infinite value, while in Reissner's theory it is related to the bending rigidity D_b , Poisson's ratio ν , and the plate thickness h . Using (2.31)–(2.32) with $k = 5/6$ and the relation $E = 2G(1 + \nu)$, we have

$$D_b = \frac{D_s h^2}{5(1 - \nu)}. \quad (4.81)$$

The results of the classical theory can only resemble those of Reissner's theory, when the infinite shear stiffness D_s is "compensated" in some way. Since the bending rigidity D_b and the plate thickness h are finite, there is the alternative of putting $\nu = \infty$ in order that the equation (4.81) is "satisfied". Although this reasoning is somewhat vague, no other explanation seems suitable.

Next, the perpendicular shear forces Q_i are examined. It is noted that they are of different orders: $Q_i = O(r^{-1/2})$ in Reissner's theory by (4.22) and $Q_i = O(r^{-3/2})$ in the classical theory by (4.47)–(4.48) forming an essential singularity. This results from the fact that the number of boundary conditions in classical plate theory is restricted to two, while in Reissner's theory it is still possible to prescribe three independent boundary conditions, as usual in mechanics problems. Consequently, a true comparison of the shear forces is not possible. In analogy with the singular bending moments, we put $\nu = \infty$ in the solution for the shear forces in classical plate theory. Since a factor $3 + \nu$ appears in the denominator of the expressions (4.47)–(4.48), it is observed that the leading terms $Q_i^{(-1)}$ of the shear forces vanish in the limit as $\nu \rightarrow \infty$. Thus, the essential singularities are eliminated.

Great similarity is observed between the terms $w^{(3)}$ of the deflection of the plate for the two theories; see (4.24) and (4.37). The dependences on the polar angle θ coincide and the terms only differ by a multiplicative factor $(1 + \nu)/(3 + \nu)$. The rotations in Reissner's theory are given by (4.14) with angular variations (3.11)–(3.14), while those in the classical theory are given by (4.38)–(4.39). Although several similarities exist, the angular variations are not identical. Application of the limit $\nu \rightarrow \infty$, however, yields equal results for the functions $(1 - \nu)\Theta_i^{(1)}$ in both plate theories.

We also compare the energy release rates and the J -integrals for crack-growth speed $c = 0$. We confine ourselves to fracture modes 1 and 2. While the bending moments in the classical theory show great dependence on Poisson's ratio, the influence of ν on the energy release rate \mathcal{G} and the integrals J_k is rather limited. The results (4.26) and (4.74) for $\mathcal{G} = J_1$ in the two plate theories differ by a factor $(1 + \nu)/(3 + \nu)$ and the results (4.31) and (4.78) for J_2 by a factor $-(1 - \nu^2)/(3 + \nu)^2$. These factors tend to unity in the limit for $\nu \rightarrow \infty$.

Finally, we seek a comparison between the bending stress-intensity factors k_1 and k_2 of the classical plate theory on the one hand and the bending stress-intensity factors K_1 and K_2 of Reissner's theory on the other hand. Of course, the two plate theories are different and a true comparison is not possible. Nevertheless, it is useful to seek such a comparison, because that would enable us to derive the stress-intensity factors of the more complicated Reissner's theory when k_1 and k_2 are known from an analysis in the classical theory. The comparison between the stress-intensity factors can be derived on the basis of the similarities between the respective bending moments, deflections, or energy release rates. These three options are elaborated below.

1. The first possibility is to impose that (the singular terms of) the normal bending moments M_{yy} for both theories are equal and that the torsional moment M_{xy} of Reissner's theory and the generalised torque M_{yx}^* of the classical plate theory are

equal, in the direction $\theta = 0$ ahead of the crack. This is a reasonable assumption, since the singular bending moments were normalised in the same manner; see definitions (4.15)–(4.16) and (4.35)–(4.36). As a consequence of this imposition we find that

$$\frac{k_1}{K_1} = \frac{k_2}{K_2} = 1. \quad (4.82)$$

2. The second possibility is to impose that the terms $w^{(3)}$ of order $O(r^{3/2})$ of the deflection for the classical theory and for Reissner's theory coincide. This is also a reasonable assumption, because the terms $w^{(3)}$ have equal dependence on the polar angle θ , as discussed above. This imposition leads us to

$$\frac{k_1}{K_1} = \frac{k_2}{K_2} = \frac{3 + \nu}{1 + \nu}. \quad (4.83)$$

3. The third possibility is to impose that the energy release rates \mathcal{G} for the two plate theories are equal. This assumption is based on the physical consideration that the energy dissipation during crack growth must be the same in the two different approaches. From this imposition we draw the same conclusion as Young and Sun [99], namely

$$\frac{k_1}{K_1} = \frac{k_2}{K_2} = \left(\frac{3 + \nu}{1 + \nu} \right)^{\frac{1}{2}}. \quad (4.84)$$

Since the energy release rate is an important physical quantity for the analysis of fracture processes, the third relation (4.84) between the stress-intensity factors of the two plate bending theories seems most acceptable. In addition, this relation is sort of "average" between the relations (4.82) and (4.83).

4.3.2 Dynamic near-tip solutions

Let us again start with an examination of the singular bending moments. The results of Reissner's theory are given by (4.13) with angular variations (3.22)–(3.27). These angular functions consist of two separate parts: one corresponding to dilatational waves with speed c_d and expressed in terms of the distorted polar angle θ_d , and the other corresponding to shear waves with speed c_s and expressed in terms of the distorted polar angle θ_s . The results of classical plate theory are given by (4.62) with angular variations (4.63)–(4.68). It is seen that these angular functions only depend on the dilatational-wave parameters c_d and θ_d and on the undistorted polar angle θ , but not on the shear-wave parameters c_s and θ_s . This effect is caused by the differential equation (4.52), which is a combination of a (dilatational) wave equation and a Laplace equation. The fact that there is no contribution of shear waves is due to the infinite shear stiffness D_s in the classical plate theory. Other consequences of $D_s = \infty$ are that the shear-wave speed c_s also attains an infinite value according to (2.34), whereupon the parameters α_s and γ_s become equal to unity and the polar angles θ_s and θ coincide according to (3.17) and (3.19). Similar to the static solution,

the dynamic near-tip bending moments in the classical theory depend on Poisson's ratio ν .

As we have seen for stationary cracks, taking the limit for $\nu \rightarrow \infty$ in the solution by classical plate theory produces results that match the solution by Reissner's theory; see (4.79)–(4.80). On the other hand, Reissner's theory resembles the classical Kirchhoff theory when the shear stiffness D_s is assigned an infinite value. This implies that $c_s \rightarrow \infty$, $\alpha_s = 1$, $\gamma_s = 1$, and $\theta_s = \theta$. Applying these substitutions, we observe that the angular variations (3.22)–(3.27) and (4.63)–(4.68) have the properties

$$\lim_{c_s \rightarrow \infty} F_{ij}^I(\theta, c) = \lim_{\nu \rightarrow \infty} G_{ij}^I(\theta; c, \nu), \quad (4.85)$$

$$\lim_{c_s \rightarrow \infty} F_{ij}^{II}(\theta, c) = \lim_{\nu \rightarrow \infty} G_{ij}^{II}(\theta; c, \nu), \quad (4.86)$$

with indices $i, j = x, y$. Hence, the singular bending moments become equal when $K_1 = k_1$ and $K_2 = k_2$ is assumed.

The shear forces $Q_i^{(-1)}$ in the classical plate theory, as given by (4.69)–(4.70), have an essential singularity of order $O(r^{-3/2})$, while the shear forces $Q_i^{(1)}$ in Reissner's theory, as given by (4.19), are of order $O(r^{-1/2})$. When we let $\nu \rightarrow \infty$ in the former results, the essential singularity vanishes because the function $S(c, \nu)$ as defined in (4.59) in the denominator is approximated by $(\alpha_d - 1)\nu^2$, while the numerators are only linear in ν . As a consequence, the generalised torques $M_{xy}^{*(1)}$ and $M_{yx}^{*(1)}$ become equal to the torsional moment $M_{xy}^{(1)}$ in the classical theory after the same formal limit transitions; see (4.71)–(4.72).

A comparison of the leading terms (4.21) and (4.58) of the deflections is not possible, because these terms are of different orders $O(r^{1/2})$ and $O(r^{3/2})$. On the other hand, the rotations (4.14) of Reissner's theory can very well be compared with the rotations (4.60)–(4.61) of classical plate theory. When the same limits as for the bending moments are applied, i.e. $\nu \rightarrow \infty$ in the Kirchhoff results and $c_s \rightarrow \infty$ in the Reissner results, it is concluded that the products $(1 - \nu)\Theta_i$ show perfect correspondence. This conclusion can also be drawn for the energy release rates (4.26) and (4.74), when only the contributions of modes 1 and 2 are considered.

4.4 Comparison with anti-plane shear

In this section, we discuss bending fracture in the shear mode (mode 3) and restrict ourselves to stationary cracks ($c = 0$). The shear mode arises in the loading of plates by perpendicular shear forces and is characterised by the stress-intensity factor K_3 in Reissner's theory. Since the torsional moments and the perpendicular shear forces are combined in the classical plate theory, their effects are jointly represented by the stress-intensity factor k_2 . Therefore, it is likely that a connection between K_2 and K_3 on the one hand and k_2 on the other hand will exist. This connection is derived from the energy release rates (4.26) and (4.74) with $c = 0$. Regarding the normal-bending mode (mode 1), we obtain (4.84) for the stress-intensity factors k_1 of the classical

theory and K_1 of Reissner's theory. Regarding the combination of modes 2 and 3, we obtain, as a supplement to the relation (4.84) for the stress-intensity factors k_2 and K_2 , that

$$\frac{1+\nu}{3+\nu} k_2^2 = K_2^2 + \frac{8(1+\nu)}{5} K_3^2, \quad (4.87)$$

which agrees with the conclusions drawn by Hui and Zehnder [38] and Knops [45].

The stress-intensity factor K_3 has been introduced as the normalising constant for the singular shear forces $Q_i^{(1)}$ in Reissner's theory; see (4.20) and (4.22). Since the shear forces $Q_i^{(-1)}$ in the classical theory have an essential singularity, it is neither possible nor relevant to compare the results of single mode 3 fracture for the two plate theories. It is more appropriate to seek a comparison between the stress-intensity factors K_3 and K_{III} , because the problem (4.9)–(4.12) for the shear mode 3 of plate bending corresponds to the problem (2.21)–(2.24) for the tearing mode III of anti-plane shear.

The definitions (3.37) and (4.20) of the stress-intensity factors K_{III} and K_3 in terms of the shear stresses σ_{yz} and τ_{yz} are similar. According to Table 4.2, we must compare $h\tau_{iz}$ of mode III with $Q_i^{(1)}$ of mode 3. From (3.38) and (4.22) we deduce the following equivalence relation between the stress-intensity factors, namely [94]

$$K_3 = \frac{3}{2} K_{III}. \quad (4.88)$$

The same relation is obtained from a comparison of the displacement u_z (see (3.41)) with the deflection $w^{(1)}$ (see (4.23)), where the shear-correction factor $k = 5/6$ must be accounted for by Table 4.2. The latter is due to the fact that the deflection is an averaged value of the out-of-plane displacement for plate bending; see (2.37).

Next, we examine the contributions of fracture modes 3 and III to the energy release rates in (3.48) and (4.26). Equating these contributions for stationary cracks, i.e., with crack-growth speeds $c = 0$ and $\bar{c} = 0$, Knops [45] arrived at

$$K_3 = \sqrt{\frac{15}{8}} K_{III}. \quad (4.89)$$

We believe, however, that this inference is incorrect, since the shear-correction factor has not been taken into account. Multiplying the mode 3 contribution in (4.26) by $5/6$ and equating the result to the mode III contribution in (3.48) yields the correct expression (4.88).

Strictly speaking, a relation between K_{III} and K_3 cannot be derived, because these parameters refer to different geometries. The stress-intensity factor K_{III} relates to problems of anti-plane shear and corresponds to geometries with large thickness, where the shear stresses are assumed to be constant in the direction parallel to the crack front. The factor K_3 , on the contrary, relates to thin plate-like structures, for which the transverse shear stresses are quadratic functions of z over the cross section of the plate. So, depending on the type of geometry, it becomes apparent which stress-intensity factor, K_3 or K_{III} , should be used in a specific problem.

Hui and Zehnder [38] suggested on the basis of equation (4.87) that the stress-intensity factors K_2 and K_3 cannot be independent: when k_2 is determined from the external loading conditions, a relation between K_2 and K_3 and Poisson's ratio ν is obtained. In the light of the analysis above, it seems more likely that a relation between K_2 , K_3 and K_{III} exists [94]. Unfortunately, such a relation has not been obtained, neither in [38, 94] nor in the present investigation.

These considerations indicate that general situations of mixed-mode fracture of arbitrary geometries can adequately be described by five independent stress-intensity factors [94], namely K_I and K_{II} for the crack-opening and sliding modes, K_1 and K_2 for the normal-bending and twisting modes, and either K_{III} for the tearing mode or K_3 for the shear mode.

4.5 Combined tension and bending

When a thin flat plate containing a crack is loaded by a combination of in-plane tensile forces and out-of-plane bending moments, the fracture behaviour of the plate can be described by the stress-intensity factors K_I , K_{II} for modes I and II of planar deformation and by the factors K_1 , K_2 for modes 1 and 2 of bending deformation. These factors may depend on the crack-growth speed c in the case of dynamic fracture. Concerning the bending modes we apply Reissner's plate theory, which yields similar angular variations of the near-tip stress distributions as a plane-stress analysis does.

The problems of planar deformation and plate bending have been studied separately in Sections 3.1 and 4.1. The solutions for the in-plane stresses σ_{ij} are given by (3.21) for modes I and II and by (2.29) and (4.13) for modes 1 and 2. These solutions are added to obtain the solution to the problem of combined tension and bending. With the superscript T indicating the total response due to the tensile forces and the bending moments, the singular stress components are given by

$$\begin{aligned} \sigma_{ij}^T(r, \theta, z; c) &= \sigma_{ij}(r, \theta; c) + \frac{12z M_{ij}(r, \theta; c)}{h^3} \\ &= \frac{K_S(z)}{\sqrt{2\pi r}} F_{ij}^I(\theta, c) + \frac{K_A(z)}{\sqrt{2\pi r}} F_{ij}^{II}(\theta, c), \end{aligned} \quad (4.90)$$

where $i, j = x, y$ and z is the coordinate in the direction perpendicular to the plate with $-h/2 \leq z \leq +h/2$. The angular variations $F_{ij}^I(\theta, c)$ and $F_{ij}^{II}(\theta, c)$ are given by (3.22)–(3.27). The stress-intensity factors $K_S(z)$ and $K_A(z)$ correspond to the loads that are symmetrically and anti-symmetrically applied with respect to the crack surfaces; they are defined by [93]

$$K_S(z) = K_I + \frac{2z}{h} K_1, \quad (4.91)$$

$$K_A(z) = K_{II} + \frac{2z}{h} K_2. \quad (4.92)$$

The fracture behaviour can then be described with these new factors. Assuming $K_1 > 0$, it is observed that the stress-intensity factor $K_S(z)$ becomes largest in the upper plane of the plate. When the crack-opening and normal-bending modes are dominant over the sliding and twisting modes, the maximum stress-intensity factor $K_S(h/2) = K_I + K_1$ will be determinative in the fracture process.

The solutions for the displacements u_i are given by (3.28) for modes I and II and by (2.35) and (4.14) for modes 1 and 2. Adding these solutions, we obtain the total displacements for the combined tension-bending problem:

$$\begin{aligned} u_i^T(r, \theta, z; c) &= u_i(r, \theta; c) - z \Theta_i(r, \theta; c) \\ &= u_i^0 + \frac{K_S(z)}{G} \sqrt{\frac{r}{2\pi}} U_i^I(\theta, c) + \frac{K_A(z)}{G} \sqrt{\frac{r}{2\pi}} U_i^{II}(\theta, c), \end{aligned} \quad (4.93)$$

where $i = x, y$ and u_i^0 are the crack-tip displacements. The angular variations $U_i^I(\theta, c)$ and $U_i^{II}(\theta, c)$ are given by (3.29)–(3.32).

We now turn to the calculation of the energy release rate \mathcal{G} and of the J -integrals. The representations (4.90) and (4.93) of the near-tip stress and displacement fields are substituted into the expressions (3.47) and (3.52). Carrying out the integration over the thickness of the plate first reveals that the integrals split into three parts: two parts relating to the tension and to the bending effects, which are even in z , and one part relating to the mixed effects, which is odd in z and vanishes after integration. Carrying out the integration over the interval $[0, \Delta a]$ in (3.47) and over the contour C in (3.52) first yields integral expressions similar to the results (3.48) for \mathcal{G} and J_1 and (3.54) for J_2 . By either method, we obtain as generalisation of the results in [38, 93] that

$$\begin{aligned} \mathcal{G} = J_1 &= \frac{1}{E} \int_{-h/2}^{+h/2} \left(A_I(c) K_S^2(z) + A_{II}(c) K_A^2(z) \right) dz \\ &= \frac{h}{E} \left(A_I(c) K_I^2 + A_{II}(c) K_{II}^2 \right) + \frac{h}{3E} \left(A_I(c) K_1^2 + A_{II}(c) K_2^2 \right), \quad (4.94) \\ J_2 &= -\frac{2}{E} \int_{-h/2}^{+h/2} A_{IV}(c) K_S(z) K_A(z) dz \\ &= -\frac{2h}{E} A_{IV}(c) K_I K_{II} - \frac{2h}{3E} A_{IV}(c) K_1 K_2, \end{aligned} \quad (4.95)$$

where the coefficients $A_I(c)$ and $A_{II}(c)$ are given in (3.49) and (3.50) and $A_{IV}(c)$ in (A.3) or (A.4) of Appendix A. In the limit for stationary cracks, i.e. for crack-growth speed $c \rightarrow 0$, these coefficients all tend to unity.

Since the mixed terms with $K_I K_2$ or $K_{II} K_1$ vanish, the results (4.94)–(4.95) are equal to the summation of (3.48) and (4.26) for \mathcal{G} and J_1 and of (3.54) and (4.31) for J_2 . We also observe that identical results are obtained, when we substitute the stress-intensity factors $K_S(z)$ and $K_A(z)$ for K_I and K_{II} in the expressions (3.48) and (3.54) and integrate over the thickness of the plate. This means that the stress-intensity factors $K_S(z)$ and $K_A(z)$ for the symmetrically and anti-symmetrically applied loads are suitable parameters for the description of the fracture process under conditions combined tension and bending.

4.6 Effects of crack closure

Up till now it has been assumed that the plate is loaded by in-plane tensile forces and out-of-plane bending moments in such a fashion that the crack surfaces do not come into contact. This means that the crack-opening displacement of mode I must exceed the crack-closing displacement associated with the rotations of the normal-bending mode I. If this is not the case, crack closure occurs and the theories in their present form will predict penetration of opposite crack faces. Since this is evidently physically incorrect, it is necessary to incorporate an extra contact force such that penetration is excluded. This was performed by Young and Sun [97] for pure bending of plates using classical plate theory. The present analysis is aimed at combined tension and bending and utilises both Reissner's and the classical plate theories. We restrict ourselves to stationary cracks (crack-growth speed $c = 0$).

4.6.1 Analysis in Reissner's plate theory

Consider a thin flat plate of thickness h containing a central crack of length $2a$ and being symmetrically loaded on its outer boundary by a bending moment M and a tensile force N per unit length. Within the scope of Reissner's theory, the singular stress σ_{yy}^T in the direction ahead of the crack and the displacements u_y^T of the crack surfaces are given by (4.90) and (4.93), viz.

$$\sigma_{yy}^T(r, 0, z) = \frac{K_S(z)}{\sqrt{2\pi r}}, \quad (4.96)$$

$$u_y^T(r, \pm\pi, z) = u_y^0 \pm \frac{2K_S(z)}{Eh} \sqrt{\frac{2r}{\pi}}, \quad (4.97)$$

where r is the distance to the right crack tip and z is the coordinate perpendicular to the plate. The stress-intensity factor $K_S(z)$ is given by (4.91) with [24, 84, 99]

$$K_I = \frac{N\sqrt{\pi a}}{h}, \quad (4.98)$$

$$K_1 = \frac{6M\sqrt{\pi a}}{h^2}. \quad (4.99)$$

From these expressions it is clear that the distance between the crack surfaces (also called the crack-opening displacement and equal to $u_y^T(r, \pi, z) - u_y^T(r, -\pi, z)$) is negative in the lower plane ($z = -h/2$) of the plate when

$$M > \frac{Nh}{6}. \quad (4.100)$$

This would imply penetration of opposite crack surfaces; see Fig. 4.2(a). To avoid penetration, contact forces P are introduced in the lower plane ($z = -h/2$) of the plate, where the crack surfaces come into contact; see Fig. 4.2(b). The contact force not only introduces an extra force P in the same direction as N , but also an extra

bending moment of magnitude $Ph/2$ and opposite to the original moment M . As a result, the total stress-intensity factor after addition of the extra force and bending moment is equal to

$$\begin{aligned} K(z) &= K_S(z) + \frac{P\sqrt{\pi a}}{h} - \frac{6zP\sqrt{\pi a}}{h^2} \\ &= \left[(N+P) + \frac{12z}{h^2} \left(M - \frac{1}{2}Ph \right) \right] \frac{\sqrt{\pi a}}{h}. \end{aligned} \quad (4.101)$$

The expressions (4.96)–(4.97) for the stress σ_{yy}^T and the displacement u_y^T remain valid, but the stress-intensity factor $K_S(z)$ must be replaced by $K(z)$ of (4.101).

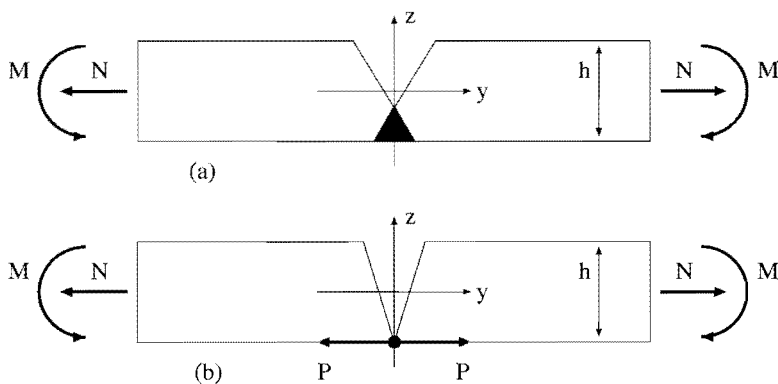


Figure 4.2: Cross-sectional view of crack closure (a) with penetration of the crack surfaces, (b) with extra contact forces.

The contact force P required to avoid penetration is related to the applied tensile force N and bending moment M . Its value is determined by the condition that the crack-opening displacement at $z = -h/2$ must be precisely zero. As argued above, this displacement should not be negative, but a positive value is also excluded because in that case the crack surfaces are not in contact with each other. Thus, we require $K(-h/2) = 0$, whereupon it follows from (4.101) that the contact force equals

$$P = \frac{3M}{2h} - \frac{N}{4}. \quad (4.102)$$

The physical condition that the force P must be positive to have contacting crack surfaces, is in agreement with relation (4.100). Substitution of (4.102) into (4.101) finally yields the total stress-intensity factor

$$K(z) = \frac{3\sqrt{\pi a}}{2h^2} \left(M + \frac{1}{2}Nh \right) \left(1 + \frac{2z}{h} \right). \quad (4.103)$$

Then, the total stress-intensity factor in the upper plane ($z = h/2$) of the plate equals

$$K\left(\frac{1}{2}h\right) = \frac{3}{2}K_I + \frac{1}{2}K_1, \quad (4.104)$$

with K_I and K_1 given by (4.98)–(4.99). This result differs from the sum $K_I + K_1$, as would follow from (4.91), where crack-closure effects are not taken into account.

4.6.2 Analysis in classical plate theory

The same analysis as in the preceding subsection can be performed with the use of classical plate theory. Consider a thin flat plate of thickness h containing a central crack of length $2a$ and being symmetrically loaded on its outer boundary by a bending moment M and a tensile force N per unit length, which is a generalisation of the work of Young and Sun [97]. We assume that crack closure occurs and we introduce the contact force P in the lower plane ($z = -h/2$) of the plate to avoid penetration of opposite crack surfaces; see Fig. 4.2. As a result of this extra force, the stress-intensity factor K_I of the crack-opening mode and the factor k_1 of the normal-bending mode are given by [24, 84, 99]

$$K_I = (N + P) \frac{\sqrt{\pi a}}{h}, \quad (4.105)$$

$$k_1 = \left(M - \frac{1}{2}Ph\right) \frac{\sqrt{\pi a}}{h^2}. \quad (4.106)$$

The total singular stress σ_{yy}^T in the direction ahead of the crack is now derived from a combination of (3.3), (2.29) and (4.40), which yields the same expression as (4.96) with the total stress-intensity factor given by (4.101). The total displacements u_y^T of the crack surfaces are derived from a combination of (3.10), (2.35) and (4.39), which yields

$$u_y^T(r, \pm\pi, z) = u_i^0 \pm \frac{2\sqrt{2a\bar{r}}}{Eh} \left[(N + P) + \frac{12z(1 + \nu)}{h^2(3 + \nu)} \left(M - \frac{1}{2}Ph\right) \right]. \quad (4.107)$$

The contact force P is determined by the condition that no penetration of the crack surfaces may occur, i.e., the crack-opening displacement $u_y^T(r, \pi, z) - u_y^T(r, -\pi, z)$ must be zero in the lower plane $z = -h/2$. This results in

$$P = \frac{3(1 + \nu)M}{(3 + 2\nu)h} - \frac{(3 + \nu)N}{2(3 + 2\nu)}. \quad (4.108)$$

It is noted that the expression (4.102) is recovered by letting $\nu \rightarrow \infty$. This agrees with prior observations that the results of the classical plate theory with an infinite value assigned to Poisson's ratio resemble those of Reissner's theory; see Section 4.3. The total stress-intensity factor is obtained from (4.101) after substitution of (4.108). We find

$$K(z) = \frac{3(3 + \nu)(M + \frac{1}{2}Nh)\sqrt{\pi a}}{(3 + 2\nu)h^2} \left(\frac{1 + \nu}{3 + \nu} + \frac{2z}{h} \right), \quad (4.109)$$

with $-h/2 \leq z \leq +h/2$. The total stress-intensity factor in the upper plane of the plate is then equal to

$$K\left(\frac{1}{2}h\right) = \frac{3(2+\nu)}{3+2\nu} K_I + \frac{2+\nu}{3+2\nu} k_1, \quad (4.110)$$

where K_I and k_1 are the stress-intensity factors for the situation without crack closure, which are given by (4.105)–(4.106) with $P = 0$. This result agrees with [97] but it deviates from (4.104) because of the dependence on Poisson's ratio. Putting $\nu = \infty$ makes the results coincide. Since Reissner's theory is more accurate, the expression (4.104) is preferred to (4.110).

4.7 Effects of dynamic crack propagation

The dynamic effects of crack propagation have been treated in Section 3.5 for the three traditional fracture modes I, II, and III. It was shown there that the elastodynamic stress-intensity factor equals the factor for the static equilibrium state multiplied by a universal function of crack speed; see (3.66)–(3.69). In the present section, the influence of crack propagation on the bending stress-intensity factors is discussed within the scope of Reissner's theory.

An exact analysis for bending fracture, similar to the work of Freund [28] for planar deformation, is extremely difficult to achieve. The problem is to determine a relationship between the dynamic stress-intensity factor for a propagating crack and the static stress-intensity factor for the equilibrium situation. This relationship is derived from the fundamental solution for a plate containing a semi-infinite straight crack along the x -axis, loaded by a pair of concentrated bending moments applied at fixed and opposite positions on the crack flanks, while the crack propagates at constant speed. The corresponding problem for a pair of concentrated forces in planar deformation has been solved in [28, Ch. 6] with the use of integral transforms (one-sided Laplace transformation on time t and two-sided Laplace transformation on the coordinate x) and the Wiener-Hopf technique. For details on these methods we refer to Carrier, Krook and Pearson [13], de Hoop [35], and Noble [69].

The bending problem in Reissner's theory is governed by the equations (2.38)–(2.42). Elimination of the bending moments and the perpendicular shear forces yields three differential equations for the deflection w and the rotations Θ_i ($i = x, y$). With the notation $f = \Theta_{x,y} - \Theta_{y,x}$ for the curl and $g = \Theta_{x,x} + \Theta_{y,y}$ for the divergence of the rotations, we find

$$\Delta f - \frac{1}{c_s^2} \ddot{f} = \frac{10}{h^2} f, \quad (4.111)$$

$$\Delta g - \frac{1}{c_d^2} \ddot{g} = -\frac{\rho h}{D_b} \ddot{w}, \quad (4.112)$$

$$\Delta w - \frac{1}{c_k^2} \ddot{w} = g, \quad (4.113)$$

where $\Delta f = f_{,ii}$ is the Laplace operator and c_d and c_s are the dilatational and shear wave speeds given by (2.33)–(2.34). The modified shear-wave speed $c_k = c_s \sqrt{5/6}$ has been introduced previously in Subsection 4.1.3. Substitution of (4.113) into (4.112) produces the fourth-order differential equation (see also Mindlin [59]):

$$\Delta\Delta w - \left(\frac{1}{c_d^2} + \frac{1}{c_k^2} \right) \Delta\ddot{w} + \frac{1}{c_d^2 c_k^2} w^{iv} + \frac{\rho h}{D_b} \ddot{w} = 0, \quad (4.114)$$

where w^{iv} denotes the fourth-order time derivative. Putting $c_k = \infty$ (i.e. $D_s = \infty$) in (4.114), we see that this equation reduces to (4.51) in the classical plate theory. The principal difficulty in obtaining the fundamental solution to the bending problem lies in the fact that the equations (4.111)–(4.113) are not proper wave equations because of the non-zero right-hand sides. Since these equations involve derivatives of different orders, the solution procedure by integral transforms and by the Wiener-Hopf technique does not apply and the inverse transforms cannot be obtained by the method of de Hoop [35].

Because we have not been able to establish the exact relation between the dynamic and the equilibrium stress-intensity factors for the plate bending problem, we shall postulate this relationship. From the results of Sections 3.3 and 4.1.4 it is observed that the dependence of the energy release rate \mathcal{G} on the crack-growth speed is similar for planar and bending deformations. The velocity-dependent coefficients in the expressions (3.48) and (4.26) for \mathcal{G} are the same. Moreover, the near-tip behaviour of the in-plane stresses (3.21) resembles that of the singular bending moments (4.13). This leads us to the assumption that the relation for the dynamic bending stress-intensity factor is similar to the relation (3.66) of Section 3.5. The elastodynamic stress-intensity factor for bending in mode 1 is denoted by $K_1 = K_1(m, a, c)$ where m represents the applied moments, a the crack length, and $c = \dot{a}$ the crack speed. It is postulated that, analogous to (3.66),

$$K_1(m, a, c) = k_I(c) K_1(m, a, 0), \quad (4.115)$$

where $k_I(c)$ is the universal function of crack speed (3.67) for the crack-opening mode (mode I). $K_1(m, a, 0)$ is the stress-intensity factor for the corresponding equilibrium state of a stationary crack of the same a and loaded by the same instantaneous moments m as for the dynamic situation. Similar postulates can be made for the other bending modes.

The energy release rate for bending fracture under mode 1 conditions is now derived in a straightforward manner analogous to (3.70). From a combination of (4.26) and (4.115) it is found that the energy release rate $\mathcal{G}(m, a, c)$ for a crack of length a , subject to external moments m , and propagating at speed $c = \dot{a}$, is given by the expression

$$\mathcal{G}(m, a, c) = \frac{h}{3E} A_I(c) k_I^2(c) K_1^2(m, a, 0) = g_I(c) \mathcal{G}(m, a, 0), \quad (4.116)$$

where $g_I(c)$ is the universal function of crack speed (3.71) and $\mathcal{G}(m, a, 0)$ is the energy release rate as calculated for the equilibrium situation. Similar relations can be obtained for the other bending modes.

It is emphasised that we have no rigorous proof for the expressions presented in this section. The postulates are based on the hypothesis that the description by Reissner's theory of dynamic fracture in plate bending does not differ from that in planar deformation. This is a reasonable assumption as has been argued above.

4.8 Conclusions

Thin flat plates undergoing bending deformation have been examined on the basis of the classical theory of Kirchhoff and the more refined theory of Reissner. The singular bending moments near the crack tip have been determined and normalised by stress-intensity factors. In addition, the deflection of the plate, the rotations of the middle plane, and the singular shear forces near the crack tip have been calculated for both stationary and dynamically propagating cracks. We have also investigated the influence of crack closure. The correspondences and differences between the near-tip solutions for the two plate bending theories have been discussed and are summarised as follows.

1. The singular bending moments in Reissner's theory and the singular stresses in planar deformation have the same angular variations. Consequently, the corresponding stress-intensity factors can be added to yield effective stress-intensity factors for general symmetric and anti-symmetric loading due to combined tension and bending; see (4.91)–(4.92).
2. The singular bending moments in the classical theory have different angular variations which depend on Poisson's ratio ν . The angular variations become equal to those in Reissner's theory when we put $\nu = \infty$. In the case of dynamic fracture we must also assign an infinite value to the shear-wave speed c_s in the results by Reissner's theory. These effects are due to the infinite shear stiffness in the classical plate theory.
3. Contrary to the Reissner solution, the shear forces in classical plate theory have an essential singularity of order $O(r^{-3/2})$ as the distance r to the crack tip tends to zero ($r \rightarrow 0$). The essential singularity vanishes in the limit for $\nu \rightarrow \infty$. This is another effect of the infinite shear stiffness.
4. The deflection of the plate in Reissner's theory has a term of order $O(r^{1/2})$ related to mode 3 fracture and a term of order $O(r^{3/2})$ related to modes 1 and 2. The former term resembles the displacement in mode III fracture and is not present in the solution by classical theory. The latter term has the same angular variation as the corresponding term of the deflection in classical theory (in the case of a stationary crack), but it differs by a multiplicative factor $(1+\nu)/(3+\nu)$. The rotations of the middle plane have different angular variations in the two theories.

5. The expressions for the energy release rate in Reissner's theory and in the classical plate theory deviate by a multiplicative factor $(1 + \nu)/(3 + \nu)$ in the case of stationary cracks. For dynamically propagating cracks, the results by the two plate theories become equal after putting both $\nu = \infty$ and $c_s = \infty$.
6. On the basis of identical energy release rates, we have established relations between the stress-intensity factors k_1 of the classical plate theory and K_1 of Reissner's theory (see (4.84)) and between the stress-intensity factors k_2 , K_2 and K_3 (see (4.87)). These relations can be useful, when the stress-intensity factors of the classical theory are known and we want to determine those in Reissner's theory.
7. A simple relation between the stress-intensity factors of modes 3 and III has been derived, namely $K_3 = \frac{3}{2}K_{III}$ (see (4.88)). These factors cannot be used simultaneously, because they assume a different behaviour for the shear stresses across the thickness of the structure at hand. The appropriate stress-intensity factor for fracture of thick solids is K_{III} , whereas the factor K_3 is more suitable for thin plate-like geometries. It is believed that a more complicated connection between K_2 , K_3 and K_{III} may exist, but such a relation has not been established.
8. The effects of crack closure in situations of combined tension and bending can be easily incorporated in the expression for the stress-intensity factor. An extra contact force is introduced to avoid penetration of opposite crack surfaces in the lower plane of the plate. This leads to a change in the effective stress-intensity factor in the upper plane of the plate.
9. The dependence of the elastodynamic bending stress-intensity factors on the crack-growth speed is not supported by an exact analysis. We have postulated that the relationship with the stress-intensity factors for static equilibrium in plate bending is governed by the same universal functions of crack speed as the relationship between the stress-intensity factors for the dynamic and equilibrium situations in planar deformation.
10. It is concluded that fracture of arbitrary structures under general loading conditions can be analysed with five independent stress-intensity factors: K_I and K_{II} for the crack-opening and sliding modes, K_1 and K_2 for the normal-bending and twisting modes, and either K_{III} for the tearing mode or K_3 for the shear mode. When the bending deformation is studied with the use of classical plate theory, we may also use K_I and K_{II} for modes I and II of planar deformation, k_1 and k_2 for modes 1 and 2 of bending deformation, and K_{III} for mode III of anti-plane shear.

Chapter 5

Curvilinear cracks

In general situations of mixed-mode fracture, cracks will not be rectilinear due to influences of asymmetric loading. Even initially straight cracks may extend in other directions. Consequently, the analysis of continued crack propagation necessitates the study of curvilinear cracks and it proves indispensable to obtain expressions for the stress-intensity factors in terms of the crack shape.

The stress-intensity factors K_I and K_{II} for fracture by modes I and II of an elastic body containing a slightly curved crack have been calculated by Cotterell and Rice [19] and the factor K_{III} for fracture by mode III in [94]. The bending stress-intensity factors k_1 and k_2 for thin flat plates containing a curvilinear through crack have been determined in [93] on the basis of the classical plate theory. The present chapter contains the papers [93, 94] with some textual modifications.

The analysis is based on the description of mechanics problems in terms of complex holomorphic functions; see Muskhelishvili [63] and Savin [80]. Special attention is given to the conditions for single-valuedness of the displacements, because the domain occupied by the elastic body is multiply connected due to the presence of the crack. The boundary conditions at the crack surfaces (the crack flanks) give rise to Hilbert problems for the complex functions. The actual crack is replaced by a straight cut in the complex plane and a linearisation with respect to the crack-shape function is performed. The stress-intensity factors depend on the crack shape, the stresses and bending moments exerted on the crack flanks, and the uniform stresses and bending moments applied at large distance from the crack.

5.1 Planar deformation

Consider a thin flat plate of thickness h , consisting of homogeneous, isotropic, linearly elastic material, containing a through crack of arbitrary curved shape, and being otherwise unbounded. The in-plane Cartesian coordinates are denoted by x and y , and the perpendicular coordinate by z where $-h/2 \leq z \leq +h/2$. The crack is described

by the shape function $y = \lambda(x)$ with $-a \leq x \leq +a$ and is assumed to be uniform over the plate thickness. The coordinate system is chosen such that the two crack tips are on the x -axis, i.e. $\lambda(\pm a) = 0$; see Fig. 5.1. The upper and lower crack flanks are denoted by L^+ and L^- and the internal contour (the crack) by $L = L^+ \cup L^-$.

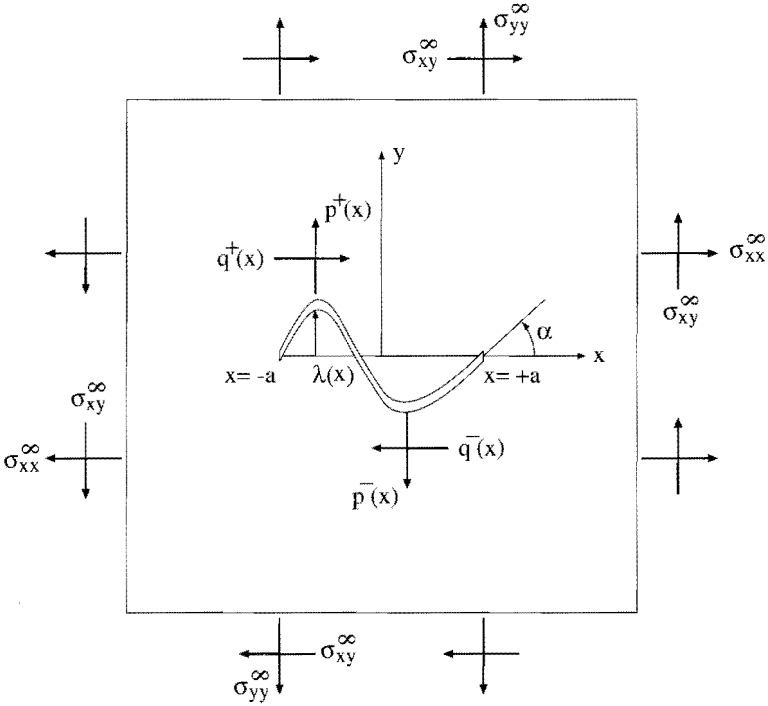


Figure 5.1: Plate with curvilinear crack in plane stress.

The normal and tangential vectors to the crack flanks (see Fig. 5.2) are given by $\mathbf{n} = \sin \theta \mathbf{e}_x - \cos \theta \mathbf{e}_y$ and $\mathbf{s} = \cos \theta \mathbf{e}_x + \sin \theta \mathbf{e}_y$, where $\theta = \theta^\pm$ is the angle between the tangent and the positive x -direction. We have $\theta^+ \in [-\pi/2, +\pi/2]$ for the upper crack flank L^+ and $\theta^- \in [\pi/2, 3\pi/2]$ for the lower crack flank L^- . This angle depends on the slope of the crack by $\tan \theta = \lambda'(x)$. The inclination angle at the right crack tip is denoted by $\alpha = \theta^+(a)$ and is shown in Fig. 5.1.

The present section focuses on plane-stress situations which are described by the equations (2.14)–(2.18). Following the analysis of Cotterell and Rice [19], we assume that there are no tractions on the upper and lower planes $z = \pm h/2$ of the plate, and that the crack surfaces are subjected to prescribed stresses in the normal and tangential directions; see Fig. 5.1. The stresses in the point $(x, y) = (t, \lambda(t))$ are

$$\sigma_{nn} = -p^\pm(t) = -p(t), \tag{5.1}$$

$$\sigma_{ns} = +q^\pm(t) = +q(t), \tag{5.2}$$

for $-a \leq t \leq +a$, which are equal for the upper and lower crack flanks. (For straight cracks with $\lambda(t) = 0$, the simplifications $\sigma_{nn} = \sigma_{yy}$ and $\sigma_{ns} = -\sigma_{xy}$ hold true.) Zero stresses are applied at infinity. The solution to this problem is derived in [19] with the use of complex functions and a linearisation with respect to the crack-shape function. The stress-intensity factors are thus correct up to first order in $\lambda(t)$. Integration by parts of the results in [19, Eqns. (18)–(19)] produces

$$K_I = \frac{1}{\sqrt{\pi a}} \int_{-a}^{+a} \left[p(t) + \left(\lambda'(t) - \frac{3}{2} \alpha \right) q(t) \right] \left(\frac{a+t}{a-t} \right)^{\frac{1}{2}} dt - \frac{1}{\sqrt{\pi a}} \int_{-a}^{+a} \frac{a \lambda(t) q(t)}{(a+t)^{\frac{1}{2}} (a-t)^{\frac{3}{2}}} dt, \quad (5.3)$$

$$K_{II} = \frac{1}{\sqrt{\pi a}} \int_{-a}^{+a} \left[q(t) - \left(\lambda'(t) - \frac{1}{2} \alpha \right) p(t) \right] \left(\frac{a+t}{a-t} \right)^{\frac{1}{2}} dt - \frac{1}{\sqrt{\pi a}} \int_{-a}^{+a} \frac{a \lambda(t) p(t)}{(a+t)^{\frac{1}{2}} (a-t)^{\frac{3}{2}}} dt. \quad (5.4)$$

In [19] the results have been compared with the exact solution for a circular-arc crack and good agreement has been observed over a wide range of arc angles. So, these expressions can be useful for curved cracks with large deviation from a straight line.

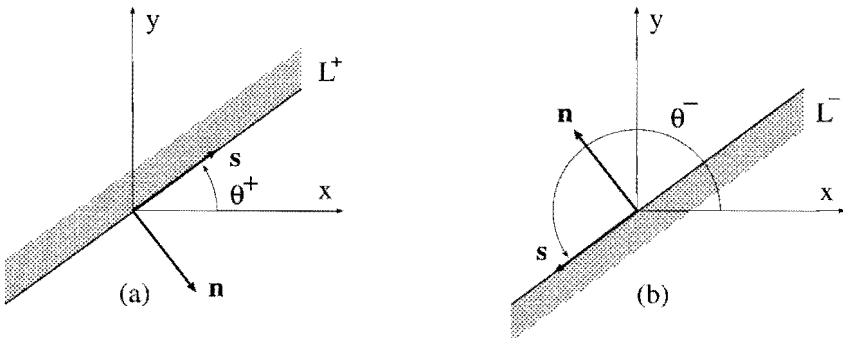


Figure 5.2: Normal and tangential vectors (a) on upper crack flank and (b) on lower crack flank.

The stress-intensity factors for uniform stresses σ_{ij}^∞ at infinity can be derived from (5.3)–(5.4); see [93]. The loading configuration is equivalent to that with stresses of opposite sign, $\sigma_{ij} = -\sigma_{ij}^\infty$, being applied to the crack surfaces. With the linearised normal and tangential vectors $\mathbf{n}^\pm = \pm(\lambda'(t) \mathbf{e}_x - \mathbf{e}_y)$ and $\mathbf{s}^\pm = \pm(\mathbf{e}_x + \lambda'(t) \mathbf{e}_y)$ on L^\pm up to first order in $\lambda'(t)$, the stresses on the crack surfaces are obtained as

$$\begin{aligned} \sigma_{nn} = -p(t) &= \sigma_{xx} n_x^2 + 2\sigma_{xy} n_x n_y + \sigma_{yy} n_y^2 \\ &= -\sigma_{yy}^\infty + 2\lambda'(t) \sigma_{xy}^\infty, \end{aligned} \quad (5.5)$$

$$\begin{aligned}\sigma_{ns} = +q(t) &= \sigma_{xx} n_x s_x + \sigma_{xy}(n_x s_y + n_y s_x) + \sigma_{yy} n_y s_y \\ &= \sigma_{xy}^\infty + \lambda'(t) (\sigma_{yy}^\infty - \sigma_{xx}^\infty).\end{aligned}\quad (5.6)$$

The stress-intensity factors are now readily derived by substitution of (5.5)–(5.6) into (5.3)–(5.4), which leads to

$$K_I = \left(\sigma_{yy}^\infty - \frac{3}{2} \alpha \sigma_{xy}^\infty \right) \sqrt{\pi a}, \quad (5.7)$$

$$K_{II} = \left(\sigma_{xy}^\infty + \frac{1}{2} \alpha \sigma_{yy}^\infty + \mathcal{A}(\sigma_{yy}^\infty - \sigma_{xx}^\infty) \right) \sqrt{\pi a}, \quad (5.8)$$

where the dimensionless crack-shape parameter \mathcal{A} is defined by

$$\mathcal{A} = \frac{1}{\pi a} \int_{-a}^{+a} \lambda'(t) \left(\frac{a+t}{a-t} \right)^{\frac{1}{2}} dt. \quad (5.9)$$

The results (5.7)–(5.8) for uniform stresses at infinity are to be added to (5.3)–(5.4) to produce new expressions for the stress-intensity factors in general loading configurations. In conjunction with the previous load case, it is interesting to study the situation where uniformly distributed stresses are applied to the crack surfaces. Substitution of $p(t) = p$ and $q(t) = q$ into (5.3)–(5.4) yields

$$K_I = \left(p + \left(2\mathcal{A} - \frac{3}{2} \alpha \right) q \right) \sqrt{\pi a}, \quad (5.10)$$

$$K_{II} = \left(q + \frac{1}{2} \alpha p \right) \sqrt{\pi a}. \quad (5.11)$$

Comparison of these results with (5.7)–(5.8) reveals some remarkable similarities. Identification of p and q with σ_{yy}^∞ and σ_{xy}^∞ shows that the terms of order zero coincide. This is obvious because the two loading configurations are equivalent for straight cracks. Concerning the terms of first order, the dependence on the inclination angle α is exactly the same, whereas the parameter \mathcal{A} appears differently in the respective expressions. The differences are equal to

$$\Delta K_I = -2\mathcal{A} \sigma_{xy}^\infty \sqrt{\pi a}, \quad (5.12)$$

$$\Delta K_{II} = \mathcal{A} (\sigma_{yy}^\infty - \sigma_{xx}^\infty) \sqrt{\pi a}, \quad (5.13)$$

which correspond to the occurrence of $\lambda'(t)$ in (5.5)–(5.6). Thus, we may say that the parameter \mathcal{A} is a measure for the amount by which the curved crack deviates from a straight line, and for the influence thereof on the stress-intensity factors.

5.2 Anti-plane deformation

5.2.1 Problem specification

Consider a thick, linearly elastic solid, containing an internal crack of finite size and arbitrary curved shape, and being otherwise unbounded. The geometry is uniform

with respect to the z -axis, which is in the thickness direction parallel to the crack fronts. The in-plane coordinates x and y and the crack-shape function $\lambda(x)$ are defined as in the previous section. This configuration is loaded under conditions of anti-plane shear, such that fracture occurs in the tearing mode (mode III). The analysis of this fracture problem is presented in [94].

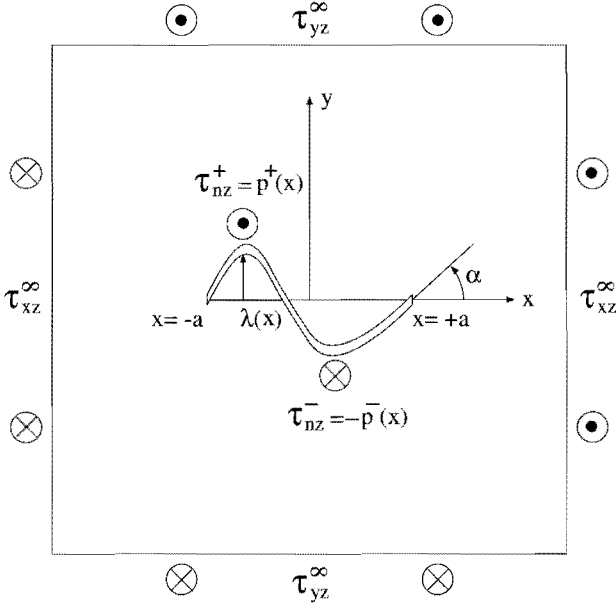


Figure 5.3: Plate with curvilinear crack in anti-plane shear.

The deformation problem is described by the real equations (2.21)–(2.22) or, equivalently, by the complex equations (2.25)–(2.26) for the holomorphic function $\phi(z)$ and its derivative $\Phi(z) = \phi'(z)$ with complex coordinate $z = x + iy$. The stresses are singular at the end points $z = \pm a$ of the crack and, as usual in fracture-mechanics problems, are proportional to the inverse square root of the distance to the crack tip. As a result, the complex functions have a similar singular behaviour. Since the order of the singularity is not known a priori, the following general condition is imposed to ensure the integrability of the elastic energy density in the vicinity of the crack tips. For $z \rightarrow \pm a$, we have

$$\Phi(z) = O\left((z \mp a)^{-\delta}\right), \quad (5.14)$$

where δ is some constant with $0 \leq \delta < 1$.

Boundary conditions on crack surfaces

We impose that the upper and lower crack surfaces are subjected to shear stresses $p^\pm(t)$ in the perpendicular direction with parameter $t \in [-a, +a]$; see Fig. 5.3. The normal to the crack surfaces is given by $n_x + i n_y = -i e^{i\theta}$ as in Fig. 5.2. Using (2.24)

and (2.26) and denoting by $\Phi^\pm(z)$ the limit of $\Phi(z)$ for $z \rightarrow t + i\lambda(t)$ on L^\pm , we can express the boundary conditions as

$$\begin{aligned}\tau_{nz}^\pm &= \operatorname{Re} [(\tau_{xz} - i\tau_{yz})(n_x + in_y)] \\ &= \frac{\mu}{2i} [\Phi^\pm(z) e^{i\theta^\pm} - \overline{\Phi^\pm(z)} e^{-i\theta^\pm}] = \begin{cases} p^+(t) & \text{on } L^+, \\ -p^-(t) & \text{on } L^-, \end{cases} \end{aligned} \quad (5.15)$$

where $\mu = G$ is the shear modulus of the material.

The resulting force P on the crack surfaces is calculated by integration of the shear stress over the contour L . With s being the arc length and $ds/dt = \pm\sqrt{1 + [\lambda'(t)]^2}$ on L^\pm , this force is given by

$$P = \int_L \tau_{nz} ds = \int_{-a}^{+a} [p^+(t) - p^-(t)] \sqrt{1 + [\lambda'(t)]^2} dt. \quad (5.16)$$

Conditions at infinity

Since the elastic body is taken as unbounded, extra conditions at infinity are required. It is assumed that the transverse shear stresses attain finite values at infinite distance from the crack. In the limit for $|z| = \sqrt{x^2 + y^2} \rightarrow \infty$, it is imposed that

$$\tau_{xz} \rightarrow \tau_{xz}^\infty, \quad \tau_{yz} \rightarrow \tau_{yz}^\infty. \quad (5.17)$$

This condition and the expression (5.16) are transformed into conditions for the complex functions at infinity. Firstly, it is noted that on the basis of (5.15) and with the property $dz/ds = e^{i\theta}$, the force P can be represented as

$$P = \operatorname{Im} \left[\int_L \mu \Phi(z) dz \right] = \frac{\mu}{2i} [\phi(z) - \overline{\phi(z)}]_L, \quad (5.18)$$

with $[\cdot]_L$ indicating the increment in the enclosed expression when the contour L is encircled in clockwise direction. Secondly, since the shear stresses and the displacement are single-valued in the domain occupied by the elastic body, the equations (2.25)–(2.26) imply that the function $\Phi(z)$ and the real part of $\phi(z)$ are single-valued in $\mathbf{C} \setminus L$. Consequently, we can write the function $\phi(z)$ as

$$\phi(z) = A \cdot \log(z - a) + \phi^*(z), \quad (5.19)$$

where $\phi^*(z)$ is single-valued in $\mathbf{C} \setminus L$ and the real constant A is related to the increment in the imaginary part of $\phi(z)$. For a proper definition of the logarithm, the complex plane is cut from $z = +a$ to $z = -a$ along the crack L and from $z = -a$ to infinity along the negative x -axis. The representation (5.19) ensures the single-valuedness of the displacement u_z and, consequently, no additional conditions are required. From a combination of (5.18) and (5.19) we deduce that $A = -P/2\pi\mu$.

The behaviour of the complex functions at infinity is now obtained by expanding the single-valued function $\phi^*(z)$ in a Laurent series. In accordance with (5.17), we find

$$\phi(z) = \Gamma z - \frac{P}{2\pi\mu} \log z + c + O\left(\frac{1}{z}\right), \quad (5.20)$$

$$\Phi(z) = \Gamma - \frac{P}{2\pi\mu} \cdot \frac{1}{z} + O\left(\frac{1}{z^2}\right), \quad (5.21)$$

for $z \rightarrow \infty$, where the constant c may be put equal to zero without loss of generality and where the complex constant Γ is given by

$$\Gamma = \frac{\tau_{xz}^\infty - i \tau_{yz}^\infty}{\mu}. \quad (5.22)$$

Stress-intensity factor

Due to the crack, stress singularities arise at the two crack tips. In the standard situation of a semi-infinite straight crack positioned along the negative x -axis (see Fig. 5.4(a)), the limiting behaviour of the displacement and the shear stresses in the vicinity of the crack tip is well-known; see (3.38)–(3.41). The stress-intensity factor K_{III} is the normalising constant for the singular shear stresses in the direction $\theta = 0$ ahead of the crack. This parameter can be calculated from the singular behaviour of the complex functions; see Cherepanov [18, Sec. 3-5] and Sih [83]. From (2.26) and (3.37) and with $z = \bar{z} = r \rightarrow 0$, it follows for the straight crack that

$$K_{III} = \lim_{r \rightarrow 0} \sqrt{2\pi r} \tau_{yz}(r, 0) = \frac{\mu i}{2} \lim_{z \rightarrow 0} \sqrt{2\pi z} \left(\Phi(z) - \overline{\Phi(z)} \right). \quad (5.23)$$

The stress-intensity factor for a curved crack is expressed in terms of the angle α at the tip and of the shear stress $\tau_{\alpha z}$ in the direction $\theta = \alpha$ ahead of the crack; see Fig. 5.4(b). In that direction the complex variable is equal to $z = a + r e^{i\alpha}$ with $r > 0$. In a manner analogous to (5.15) we obtain the stress-intensity factor:

$$K_{III} = \lim_{r \rightarrow 0} \sqrt{2\pi r} \tau_{\alpha z}(r, \alpha) = \frac{\mu i}{2} \lim_{r \rightarrow 0} \sqrt{2\pi r} \left(\Phi(z) e^{i\alpha} - \overline{\Phi(z)} e^{-i\alpha} \right). \quad (5.24)$$

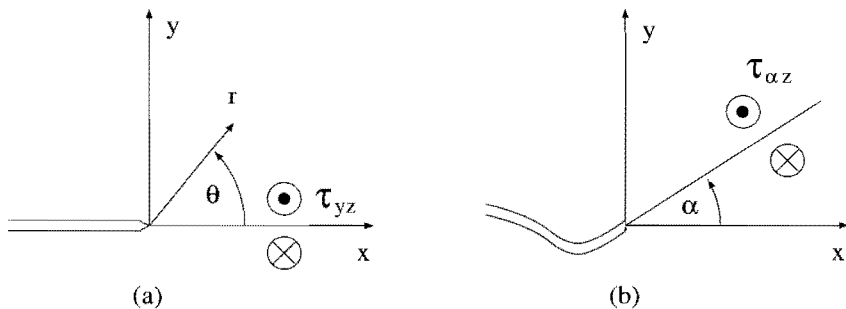


Figure 5.4: Crack-tip geometry (a) for straight crack and (b) for curved crack.

5.2.2 Linearisation for slightly curved cracks

The problem of anti-plane shear as formulated above can only be solved in exact form for rectilinear and circular-arc cracks; see Chao and Huang [17] and Sih [83]. The

solution procedure is based on the method of Muskhelishvili [62, 63] and starts with the introduction of the conjugate function

$$\Omega(z) = \overline{\Phi(\bar{z})} \quad (5.25)$$

for a straight crack and

$$\Omega(z) = \frac{R^2}{z^2} \overline{\Phi(R^2/\bar{z})} \quad (5.26)$$

for a crack along a circular arc of radius R .

In the case of arbitrary curvilinear cracks, however, it is not possible to define an appropriate conjugate function $\Omega(z)$. Therefore, we must rely on perturbation methods and perform a linearisation with respect to the crack-shape function. Although the linearised problem provides approximate solutions for curved cracks which deviate from a straight line only by a small amount, the results can be useful to investigate crack propagation due to non-symmetric loading, especially the initial stages of fracture.

The linearisation process is similar to that in [19]. The crack is assumed to have a smooth shape resembling a straight cut. Mathematically, this condition is expressed in the norm of the crack-shape function

$$\Lambda = \|\lambda\| = \left(\frac{1}{2a} \int_{-a}^{+a} |\lambda(t)|^2 dt \right)^{\frac{1}{2}}. \quad (5.27)$$

It is imposed that this norm is much smaller than the crack size ($\Lambda/a \ll 1$), and that the norm $\|\lambda'\|$ of the derivative is much smaller than unity and of the same order as Λ/a . In the linearisation process only the terms of order zero (corresponding to a straight crack) and the terms of first order in Λ/a and/or $\|\lambda'\|$ are retained. In addition, it is assumed that the function $\Phi(z)$ can be continued analytically over the crack up to the straight line connecting the two crack tips. The analytically continued function is denoted by $F(z)$ and is holomorphic in the complex plane with a straight cut $[-a, +a]$. The function $F(z)$ is expanded with respect to the crack-shape function $\lambda(t)$ and written as

$$\Phi(z) \sim F(z) = F_0(z) + F_1(z) + O(\Lambda^2), \quad (5.28)$$

where $F_0(z)$ and $F_1(z)$ are the functions of zeroth and first order. These functions are holomorphic in $\mathbb{C} \setminus [-a, +a]$ and satisfy condition (5.14) at the crack tips. At infinity, the function $F_0(z)$ has limiting behaviour as in (5.21) with Γ given by (5.22) and P by (5.16) with the square root replaced by unity. The behaviour of $F_1(z)$ at infinity is similar, but now $\Gamma = 0$ and $P = 0$ must be substituted.

Since the linearised crack resembles a straight line, it is advantageous to introduce the functions $G_0(z) = \overline{F_0(\bar{z})}$ and $G_1(z) = \overline{F_1(\bar{z})}$, analogous to the conjugate function in (5.25). The limiting values of $\Phi(z)$ on the crack flanks L^\pm , i.e. for $z \rightarrow t + i\lambda(t)$, can now be expressed in terms of the boundary values of $F_0(z)$ and $F_1(z)$ on either side of the cut $[-a, +a]$. With $-a \leq t \leq +a$ we have

$$\frac{\Phi^\pm(z)}{z} = F_0^\pm(t) + i\lambda(t) F_0^{\prime\pm}(t) + F_1^\pm(t) + O(\Lambda^2), \quad (5.29)$$

$$\frac{\Phi^\pm(z)}{z} = G_0^\mp(t) - i\lambda(t) G_0^{\prime\mp}(t) + G_1^\mp(t) + O(\Lambda^2). \quad (5.30)$$

The angle θ^\pm of crack inclination appears in linearised form as $e^{i\theta^\pm} = \pm(1 + i\lambda'(t))$ on L^\pm . The boundary conditions (5.15) are linearised with the use of these properties. Omitting terms of second and higher order, we obtain

$$p^\pm(t) = \frac{\mu}{2i} \left[F_0^\pm(t) - G_0^\mp(t) + F_1^\pm(t) - G_1^\mp(t) + \left(i\lambda(t) [F_0^\pm(t) + G_0^\mp(t)] \right)' \right]. \quad (5.31)$$

After the solution for the complex functions has been derived, the stress-intensity factor K_{III} is calculated. The linearised form of (5.24) for slightly curved cracks is

$$K_{III} = \frac{\mu i}{2} \lim_{r \rightarrow 0} \sqrt{2\pi r} \left[F_0(a+r) - G_0(a+r) + F_1(a+r) - G_1(a+r) + \left(i\alpha r [F_0(a+r) + G_0(a+r)] \right)' \right]. \quad (5.32)$$

From their limiting behaviour as $z \rightarrow a$, it can be deduced that the functions $F_0(z)$ and $G_0(z)$ have opposite contributions to the stress-intensity factor [18, 83]. As a result, the final term of (5.32) vanishes and a simplified expression for K_{III} is obtained. In the next subsection it is proved that the contributions of $F_0(z)$ and $G_0(z)$ are indeed opposite.

5.2.3 Solution for straight cracks

In the next step of the solution procedure, the linearised boundary conditions (5.31) are split into boundary conditions for the zero-order and for the first-order functions. Addition and subtraction of the boundary values lead to the Hilbert problems below for the functions of order zero. For $-a \leq t \leq +a$ we have

$$(F_0 - G_0)^+(t) + (F_0 - G_0)^-(t) = \frac{2i}{\mu} [p^+(t) + p^-(t)], \quad (5.33)$$

$$(F_0 + G_0)^+(t) - (F_0 + G_0)^-(t) = \frac{2i}{\mu} [p^+(t) - p^-(t)]. \quad (5.34)$$

The theory of singular integral equations and Hilbert problems and its application in mechanics have been treated extensively by Muskhelishvili [62, 63]. For details of the analysis we refer to these monographs.

The solution to the Hilbert problems utilises the Plemelj function $X(z) = \sqrt{z^2 - a^2}$. This function is holomorphic in the domain $\mathbf{C} \setminus [-a, +a]$ and attains limiting values $X^\pm(t) = \pm i\sqrt{a^2 - t^2}$ on either side of the cut, while $X(z) = z + O(1/z)$ at infinity. The solution to the Hilbert problems (5.33)–(5.34) is given by

$$F_0(z) - G_0(z) = \frac{1}{\pi\mu X(z)} \int_{-a}^{+a} \frac{X^+(t) [p^+(t) + p^-(t)]}{t - z} dt + \frac{P_0(z)}{X(z)}, \quad (5.35)$$

$$F_0(z) + G_0(z) = \frac{1}{\pi\mu} \int_{-a}^{+a} \frac{p^+(t) - p^-(t)}{t - z} dt + Q_0(z), \quad (5.36)$$

where $P_0(z)$ and $Q_0(z)$ are polynomials. From the condition (5.21) at infinity it is deduced that

$$P_0(z) = \frac{2z \tau_{yz}^\infty}{\mu i}, \quad (5.37)$$

$$Q_0(z) = \frac{2 \tau_{xz}^\infty}{\mu}. \quad (5.38)$$

The stress-intensity factor for the straight crack is now easily derived from the formula (5.32) and the solution (5.35). We obtain

$$K_{III} = \tau_{yz}^\infty \sqrt{\pi a} + \frac{1}{2\sqrt{\pi a}} \int_{-a}^{+a} [p^+(t) + p^-(t)] \left(\frac{a+t}{a-t} \right)^{\frac{1}{2}} dt, \quad (5.39)$$

which is in agreement with the result of Sih [83] for symmetric loading ($p^+(t) = p^-(t)$).

Under the assumption that the functions $p^\pm(t)$ are finite at the end point $t = a$, it immediately follows from the solution (5.36) and [62, 63] that

$$\lim_{z \rightarrow a} \sqrt{2\pi(z-a)} (F_0(z) + G_0(z)) = 0. \quad (5.40)$$

This proves the statements that the contributions of the functions $F_0(z)$ and $G_0(z)$ to the stress-intensity factor K_{III} are opposite, and that the last term in (5.32) vanishes.

5.2.4 Solution for slightly curved cracks

The stress-intensity factor for a curved crack consists of two parts. Firstly, there is the contribution of the terms of order zero, which coincides with the result (5.39) for a straight crack. Secondly, there is the contribution of the first-order terms in (5.32), which is denoted by $K_{III}^{(1)}$. This second part is determined in the present subsection and is calculated from

$$K_{III}^{(1)} = \frac{\mu i}{2} \lim_{r \rightarrow 0} \sqrt{2\pi r} (F_1(a+r) - G_1(a+r)), \quad (5.41)$$

where it has been used that the last term in (5.32) vanishes in view of (5.40).

The functions $F_1(z)$ and $G_1(z)$ of first order are derived from Hilbert problems on the straight cut $[-a, +a]$. Addition and subtraction of the first-order terms in the boundary conditions (5.31) yield

$$(F_1 - G_1)^+(t) + (F_1 - G_1)^-(t) = b_1(t) = [-i \lambda(t) b_3(t)]', \quad (5.42)$$

$$(F_1 + G_1)^+(t) - (F_1 + G_1)^-(t) = b_2(t) = [-i \lambda(t) b_4(t)]', \quad (5.43)$$

for $-a \leq t \leq +a$, where the functions $b_3(t)$ and $b_4(t)$ are given by

$$b_3(t) = (F_0 + G_0)^+(t) + (F_0 + G_0)^-(t), \quad (5.44)$$

$$b_4(t) = (F_0 - G_0)^+(t) - (F_0 - G_0)^-(t). \quad (5.45)$$

The solution to the Hilbert problems (5.42)–(5.43) is derived in a standard manner [62, 63]. For $z \in \mathbf{C} \setminus [-a, +a]$ the first-order functions are given by

$$F_1(z) - G_1(z) = \frac{1}{2\pi i X(z)} \int_{-a}^{+a} \frac{X^+(t) b_1(t)}{t - z} dt + \frac{P_1(z)}{X(z)}, \quad (5.46)$$

$$F_1(z) + G_1(z) = \frac{1}{2\pi i} \int_{-a}^{+a} \frac{b_2(t)}{t - z} dt + Q_1(z), \quad (5.47)$$

where $P_1(z)$ and $Q_1(z)$ are polynomials. It follows from their behaviour at infinity that these polynomials vanish.

Since only the difference $F_1(z) - G_1(z)$ is relevant to the stress-intensity factor, the solution procedure is restricted to the first Hilbert problem. To this end, the function $b_3(t)$ is elaborated further. With the use of (5.36) it is found that

$$b_3(t) = \frac{4\tau_{xz}^\infty}{\mu} + \frac{2}{\pi\mu} \int_{-a}^{+a} \frac{p^+(s) - p^-(s)}{s - t} ds, \quad (5.48)$$

where the symbol f denotes the Cauchy principal value of the integral. Substitution of (5.46) into (5.41) now produces the first-order part of the stress-intensity factor. The following result is obtained from (5.42) and (5.48) and integration by parts:

$$\begin{aligned} K_{III}^{(1)} &= \frac{-\mu i}{4\sqrt{\pi a}} \int_{-a}^{+a} b_1(t) \left(\frac{a+t}{a-t} \right)^{\frac{1}{2}} dt \\ &= \frac{\mu}{4\sqrt{\pi a}} \int_{-a}^{+a} \frac{a \lambda(t) b_3(t)}{(a+t)^{\frac{1}{2}} (a-t)^{\frac{3}{2}}} dt \\ &= -\mathcal{A} \tau_{xz}^\infty \sqrt{\pi a} \\ &\quad + \frac{1}{2\pi \sqrt{\pi a}} \int_{-a}^{+a} \frac{a \lambda(t)}{(a+t)^{\frac{1}{2}} (a-t)^{\frac{3}{2}}} \int_{-a}^{+a} \frac{p^+(s) - p^-(s)}{s - t} ds dt, \end{aligned} \quad (5.49)$$

where it was used that $\lambda(\pm a) = 0$. The dimensionless crack-shape parameter \mathcal{A} is defined by (5.9). The last part of (5.49) contains a double integral; it is proved in Appendix B.1 that the order of integration may be interchanged. Thus, a new expression is obtained in which the functions $p^\pm(t)$ are multiplied by a principal value integral involving the crack-shape function $\lambda(t)$; see (5.50).

Finally, the first-order contribution (5.49) is added to the result (5.39) for a straight crack. This yields the linearised expression for the stress-intensity factor of a curved crack loaded under mode III conditions:

$$\begin{aligned} K_{III} &= \left(\tau_{yz}^\infty - \mathcal{A} \tau_{xz}^\infty \right) \sqrt{\pi a} \\ &\quad + \frac{1}{2\sqrt{\pi a}} \int_{-a}^{+a} \left[p^+(t) + p^-(t) \right] \left(\frac{a+t}{a-t} \right)^{\frac{1}{2}} dt \\ &\quad + \frac{1}{2\pi \sqrt{\pi a}} \int_{-a}^{+a} \left[p^+(t) - p^-(t) \right] \int_{-a}^{+a} \frac{a \lambda(s)}{(a+s)^{\frac{1}{2}} (a-s)^{\frac{3}{2}} (t-s)} ds dt. \end{aligned} \quad (5.50)$$

Loading configurations with symmetry properties result in simplified expressions for the stress-intensity factor. In the case of opposite stresses on the crack flanks, we have

$\tau_{nz}^+ = -\tau_{nz}^-$ and thus $p^+(t) = p^-(t) = p(t)$. A symmetric anti-plane shear situation is obtained, for which the stress-intensity factor is given by

$$K_{III} = \left(\tau_{yz}^\infty - \mathcal{A} \tau_{xz}^\infty \right) \sqrt{\pi a} + \frac{1}{\sqrt{\pi a}} \int_{-a}^{+a} p(t) \left(\frac{a+t}{a-t} \right)^{\frac{1}{2}} dt. \quad (5.51)$$

Another simplification is obtained in the case of a concentrated load on the upper crack flank, i.e., for $p^+(t) = P \delta(t - t_0)$ and $p^-(t) = 0$, where $\delta(t)$ is the Dirac delta function. The expression (5.50) for the stress-intensity factor K_{III} reduces to

$$K_{III} = \frac{P}{2\sqrt{\pi a}} \left(\frac{a+t_0}{a-t_0} \right)^{\frac{1}{2}} + \frac{P}{2\pi\sqrt{\pi a}} \int_{-a}^{+a} \frac{a\lambda(t)}{(a+t)^{\frac{1}{2}}(a-t)^{\frac{3}{2}}(t_0-t)} dt. \quad (5.52)$$

5.2.5 Examples

We shall now present specific solutions for the mode III stress-intensity factor for some particular shear-stress distributions and particular crack geometries. The accuracy and the applicability of the linearised result (5.50) for K_{III} are also investigated.

Uniform stresses at infinity

The first example concerns a fractured elastic solid loaded by uniform shear stresses applied at large distance from the crack, while the crack surfaces remain stress-free. The result is directly derived from (5.50), viz.

$$K_{III} = \left(\tau_{yz}^\infty - \mathcal{A} \tau_{xz}^\infty \right) \sqrt{\pi a}. \quad (5.53)$$

This loading configuration is equivalent to the situation where no stresses are applied at infinity, but where the crack surfaces are loaded by shear stresses of opposite sign, i.e., $\tau_{nz} = \tau_{xz} n_x + \tau_{yz} n_y$ with $\tau_{xz} = -\tau_{xz}^\infty$ and $\tau_{yz} = -\tau_{yz}^\infty$. The linearised normal vector on L^\pm is given by $\mathbf{n}^\pm = \pm(\lambda'(t) \mathbf{e}_x - \mathbf{e}_y)$ with $-a \leq t \leq +a$. As a result, the stresses on the crack surfaces are equal to

$$p^+(t) = p^-(t) = \tau_{yz}^\infty - \lambda'(t) \tau_{xz}^\infty. \quad (5.54)$$

Substitution of these shear stresses into (5.50) indeed produces the same result for the stress-intensity factor as in (5.53).

Uniform stresses on crack surfaces

A slightly different solution is obtained, when the crack surfaces are loaded by uniform shear stresses, i.e., $p^+(t) = p^-(t) = p$ with p being constant, while no stresses are applied at infinity. It is found from (5.51) that

$$K_{III} = p \sqrt{\pi a}. \quad (5.55)$$

Identification of p with τ_{yz}^∞ reveals that the difference between (5.53) and (5.55) is limited to the first-order term containing the constant \mathcal{A} . The occurrence of this

crack-shape parameter corresponds exactly to the presence of $\lambda'(t)$ in (5.54). Similar to Section 5.1, we conclude that the parameter \mathcal{A} is a measure for the amount by which the curved crack deviates from a straight line, and for the influence thereof on the stress-intensity factor.

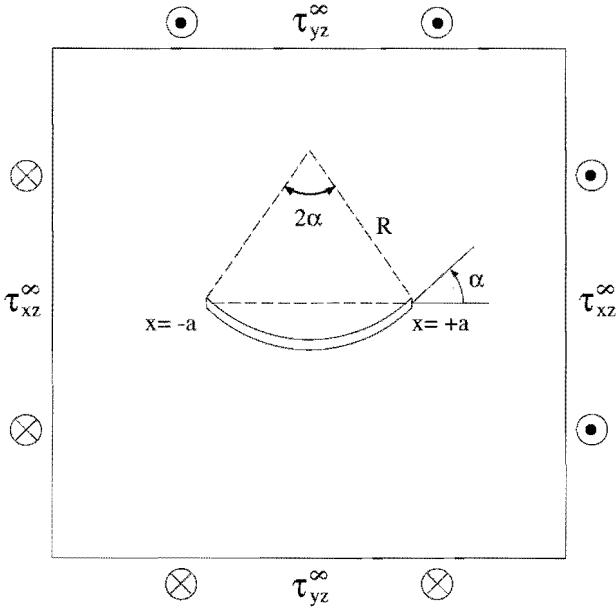


Figure 5.5: Elastic solid with crack along circular arc.

Crack along circular arc

As a third example, the circular-arc crack is considered. This geometry provides an appropriate exercise to examine the range of validity of the linearised solution. The crack is located along a circle of radius R and has an opening angle 2α ; see Fig. 5.5. The exact solution for this crack geometry is determined by Chao and Huang [17] and Sih [83]. The mode III stress-intensity factor equals

$$\begin{aligned}
 K_{III} &= \left(\tau_{yz}^\infty \cos\left(\frac{1}{2}\alpha\right) - \tau_{xz}^\infty \sin\left(\frac{1}{2}\alpha\right) \right) \sqrt{\pi R \sin \alpha} \\
 &+ \frac{1}{2\sqrt{\pi R \sin \alpha}} \int_{-\alpha}^{+\alpha} \left[p^+(R \sin \theta) + p^-(R \sin \theta) \right] \left(\frac{\sin\left(\frac{1}{2}(\alpha + \theta)\right)}{\sin\left(\frac{1}{2}(\alpha - \theta)\right)} \right)^{\frac{1}{2}} R d\theta \\
 &+ \frac{\sin\left(\frac{1}{2}\alpha\right)}{2\sqrt{\pi R \sin \alpha}} \int_{-\alpha}^{+\alpha} \left[p^+(R \sin \theta) - p^-(R \sin \theta) \right] R d\theta. \quad (5.56)
 \end{aligned}$$

This result is compared with the present perturbation solution. The exact crack-shape

function $\lambda(x)$ can be approximated by a quadratic function:

$$y = \lambda(x) = \sqrt{R^2 - a^2} - \sqrt{R^2 - x^2} \approx \frac{x^2 - a^2}{2R}, \quad (5.57)$$

for $-a \leq x \leq +a$ with $a = R \sin \alpha$. This function represents a curve of parabolic shape and is acceptable for small values of a/R . The linearised stress-intensity factor K_{III} is derived by substitution of the approximate crack-shape function (5.57) into (5.50). The inclination angle α at the right crack tip is approximated by $\tan \alpha = \lambda'(a) \approx a/R$ and the crack-shape parameter (5.9) is calculated as $\mathcal{A} \approx a/(2R)$. In addition, we have $a = R \sin \alpha \approx R \alpha$, while the integration variable can be written as $t = R \sin \theta \approx R \theta$. We find that

$$\begin{aligned} K_{III} &= \left(\tau_{yz}^\infty - \frac{a}{2R} \tau_{xz}^\infty \right) \sqrt{\pi a} \\ &+ \frac{1}{2\sqrt{\pi a}} \int_{-a}^{+a} [p^+(t) + p^-(t)] \left(\frac{a+t}{a-t} \right)^{\frac{1}{2}} dt \\ &+ \frac{1}{2\sqrt{\pi a}} \cdot \frac{a}{2R} \int_{-a}^{+a} [p^+(t) - p^-(t)] dt, \end{aligned} \quad (5.58)$$

which agrees with (5.56) up to the terms of first order in α or a/R .

The linearised result is also compared with the exact solution for uniform loading at infinity. The crack surfaces remain stress-free. To this end, the crack-shape parameter \mathcal{A} is calculated more precisely. Substitution of the exact crack-shape function (5.57) for the circular arc into (5.9) yields

$$\mathcal{A} = \frac{2R}{\pi a} \left(\mathbf{K}\left(\frac{a}{R}\right) - \mathbf{E}\left(\frac{a}{R}\right) \right) = \frac{2}{\pi \sin \alpha} \left(\mathbf{K}(\sin \alpha) - \mathbf{E}(\sin \alpha) \right), \quad (5.59)$$

where $a = R \sin \alpha$. The functions \mathbf{K} and \mathbf{E} are the complete elliptic integrals of the first and second kind; see Gradshteyn and Ryzhik [30, Sec. 8.11]. This result for \mathcal{A} is substituted into (5.53) to obtain the linearised stress-intensity factor. Following the notation of Sih [83], we express the shear stresses at infinity in terms of the applied load τ^∞ and the loading angle γ by

$$\tau_{xz}^\infty + i \tau_{yz}^\infty = \tau^\infty e^{i\gamma}, \quad (5.60)$$

while we normalise the numerical values of K_{III} from (5.53) and (5.56) with respect to the standard stress-intensity factor $K_0 = \tau^\infty \sqrt{\pi a}$.

The results are presented graphically in Fig. 5.6 as function of α . From these results we observe that the linearised solution is accurate with a relative error of at most 5% up to arc-opening angles $\alpha < 30^\circ$. Thus, we conclude that the linearised solution provides acceptable approximations over a rather wide range of arc-opening angles. It is expected that this conclusion equally applies to general curvilinear cracks for a broad class of crack-shape variations.

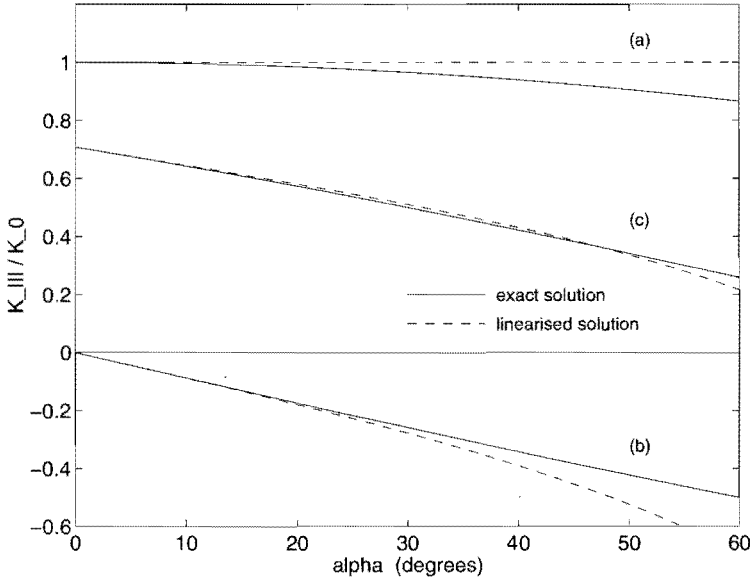


Figure 5.6: Exact and linearised stress-intensity factors of mode III for a crack along a circular arc, subject to uniform shear stress at infinity with loading angle (a) $\gamma = \pi/2$, or (b) $\gamma = 0$, or (c) $\gamma = \pi/4$.

5.3 Plate bending

5.3.1 Problem specification

Consider a thin flat plate of thickness h , consisting of homogeneous, isotropic, linearly elastic material, containing a through crack of arbitrary curved shape, and being otherwise unbounded. The crack is described by the shape function $y = \lambda(x)$, with $-a \leq x \leq +a$, in the same manner as in Section 5.1. The plate is loaded by uniform bending moments at large distance from the crack, while distributed bending moments and generalised torques are applied at the upper and lower crack surfaces; see Fig. 5.7. This problem has been investigated in [93].

The bending of the plate is described in the classical plate theory by the equations (2.49)–(2.51) or, equivalently, by the equations (2.56)–(2.64) in terms of the complex holomorphic functions $\phi(z)$, $\psi(z)$, $\omega(z)$ and their derivatives $\Phi(z) = \phi'(z)$, $\Psi(z) = \psi'(z)$, $\Omega(z) = \omega'(z)$ with complex coordinate $z = x + iy$. Because of the stress singularities at the crack tips, the complex functions are singular at these points. To ensure the integrability of the elastic energy density, we require that for $z \rightarrow \pm a$

$$\Phi(z), \Psi(z), \Omega(z) = O\left((z \mp a)^{-\delta}\right), \quad (5.61)$$

where δ is some constant with $0 \leq \delta < 1$.

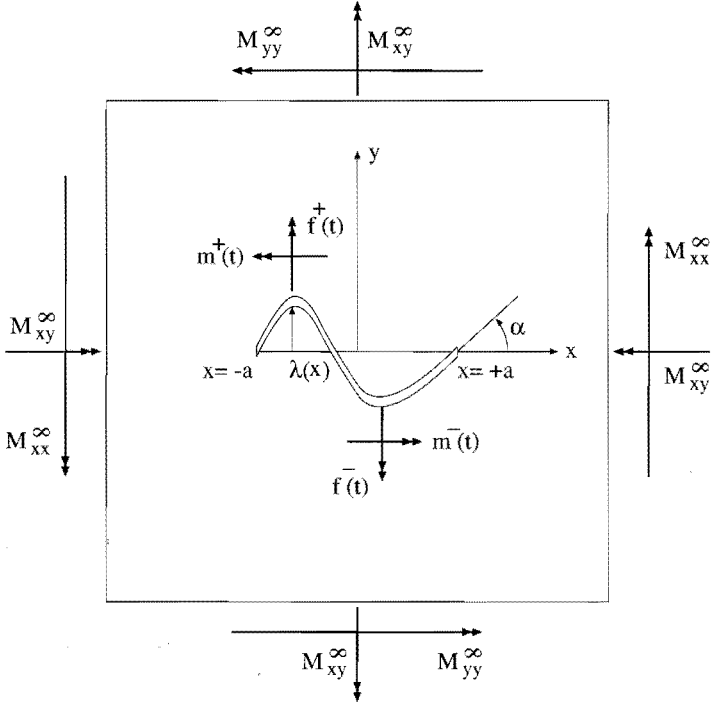


Figure 5.7: Plate with curvilinear crack subjected to bending moments.

Boundary conditions on crack surfaces

We impose that the upper and lower crack surfaces are subjected to normal bending moments and generalised torques; see (2.65) and Fig. 5.7. The normal and tangential vectors to the crack surfaces are defined in Fig. 5.2. The boundary conditions in $z = t + i\lambda(t)$ on L^\pm , with $-a \leq t \leq +a$, are given by

$$M_{nn}^\pm = -m^\pm(t), \tag{5.62}$$

$$M_{ns}^{*\pm} = M_{ns} + \int_{s_0}^{s(t)} Q_n ds = f^\pm(t), \tag{5.63}$$

where $s = s(t)$ is the arc length along L and $Q_n = Q_x n_x + Q_y n_y$. Using (2.70) and $dz/ds = i(n_x + i n_y) = e^{i\theta}$ and denoting by $\Phi^\pm(z)$ the limit of $\Phi(z)$ for $z \rightarrow t + i\lambda(t)$ on L^\pm , we can express the boundary conditions as

$$M_{nn}^\pm + i M_{ns}^{*\pm} + i C = -(m - i f)^\pm(t) + i C \\ = (1 - \nu)D \left[\kappa \Phi^\pm(z) + \overline{\Phi^\pm(z)} + e^{-2i\theta^\pm} \left(\Omega^\mp(\bar{z}) + (z - \bar{z})\overline{\Phi'^\pm(z)} - \overline{\Phi^\pm(z)} \right) \right], \tag{5.64}$$

where C is a real but yet unknown integration constant which is determined from conditions at infinity. The parameter κ depends on Poisson's ratio, but differs from the usual values for planar deformation. In the case of bending, κ is given by (2.71).

The resulting force P in the z -direction acting on the crack is determined with the use of (2.69). Because of overall equilibrium of the plate, it is necessary that this force be equal to zero. Integration of Q_n yields

$$P = \int_L Q_n ds = 2iD \left[\Phi(z) - \overline{\Phi(\bar{z})} \right]_L = 0. \quad (5.65)$$

The resulting moments M_x and M_y about the x - and y -axes acting on the crack are calculated by integration over the internal contour L . After integration of Q_n by parts and with the use of (2.62), (2.69), (2.70), (5.64), and (5.65), it is found that

$$\begin{aligned} M_x + iM_y &= \int_L [-M_{ny} + iM_{nx} + yQ_n - ixQ_n] ds \\ &= \int_L [i(n_x + in_y)(M_{nn} + iM_{ns}) - izQ_n] ds \\ &= \int_L \left[M_{nn} + iM_{ns} + i \int_{s_0}^s Q_n ds + iC \right] dz - \left[iz \int_{s_0}^s Q_n ds \right]_L \\ &= D \left[(1 - \nu) (\kappa \phi(z) + z \phi'(z) + \overline{\psi(z)}) + 2z (\Phi(z) - \overline{\Phi(\bar{z})}) \right]_L \\ &= - \int_{-a}^{+a} \left[(m - if)^+(t) - (m - if)^-(t) \right] \left(\frac{dz}{dt} \right) dt, \end{aligned} \quad (5.66)$$

where the constant C gives no contribution since L is a closed contour; see Savin [80]. The notation $[\cdot]_L$ indicates the increment in the enclosed expression when the contour L is encircled in clockwise direction, such that the material is at the left-hand side of the contour. In the case of symmetrically applied moments on the upper and lower crack surfaces, it is obvious that these resulting moments vanish.

Conditions at infinity

Since the elastic body is taken as unbounded, extra conditions at infinity are required. We assume that the moments tend to finite values at infinite distance from the crack. For $|z| = \sqrt{x^2 + y^2} \rightarrow \infty$ and with indices $i, j = x, y$, we impose that

$$M_{ij} \rightarrow M_{ij}^\infty. \quad (5.67)$$

In the next subsection, these conditions are combined with additional requirements for the single-valuedness of the bending moments and the displacements. These requirements are necessary, since the elastic body comprises a multiply connected domain because of the presence of the crack.

Stress-intensity factors

The bending moments are singular at both crack tips and their limiting behaviour near the tip of a semi-infinite straight crack along the negative x -axis is well-known; see (4.40)–(4.46). The bending stress-intensity factors k_1 and k_2 are the normalising constants for the singular normal bending moment and the singular generalised torque in the direction $\theta = 0$ ahead of the crack. With $z = \bar{z} = r \rightarrow 0$, we deduce from (2.70)

and (4.35)–(4.36) that for rectilinear cracks

$$\begin{aligned} k_1 - i k_2 &= \frac{6}{h^2} \lim_{r \rightarrow 0} \sqrt{2\pi r} \left(M_{yy}(r, 0) - i M_{yx}^*(r, 0) \right) \\ &= \frac{6(1-\nu)D}{h^2} \lim_{z \rightarrow 0} \sqrt{2\pi z} \left(\kappa \Phi(z) + \Omega(\bar{z}) \right). \end{aligned} \quad (5.68)$$

The bending stress-intensity factors for a curvilinear crack are expressed in terms of the inclination angle α at the tip and of the normal bending moment and generalised torque $M_{\alpha\alpha} - i M_{\alpha r}^*$ in the direction $\theta = \alpha$ ahead of the crack, where the complex coordinate equals $z = a + r e^{i\alpha}$ with $r > 0$. With the use of (2.70) we obtain

$$\begin{aligned} k_1 - i k_2 &= \frac{6}{h^2} \lim_{r \rightarrow 0} \sqrt{2\pi r} \left(M_{\alpha\alpha}(r, \alpha) - i M_{\alpha r}^*(r, \alpha) \right) \\ &= \frac{6(1-\nu)D}{h^2} \lim_{r \rightarrow 0} \sqrt{2\pi r} \left[\kappa \Phi(z) + \overline{\Phi(\bar{z})} \right. \\ &\quad \left. + e^{-2i\alpha} \left(\Omega(\bar{z}) + r (e^{i\alpha} - e^{-i\alpha}) \overline{\Phi'(z)} - \overline{\Phi(z)} \right) \right]. \end{aligned} \quad (5.69)$$

5.3.2 Conditions for single-valued displacements

The bending problem of the cracked plate has been expressed in terms of the complex functions $\Phi(z)$ and $\Psi(z)$ or, equivalently, in terms of $\Phi(z)$ and $\Omega(z)$. These functions must satisfy additional requirements in order that all physical quantities (such as bending moments, shear forces, and displacements) are single-valued in the domain occupied by the elastic body.

From the relations (2.58)–(2.60) it is deduced that the functions $\Phi'(z)$ and $\Psi(z)$ and the real part of $\Phi(z)$ must be single-valued. When the plate contains multiple holes, the imaginary part of $\Phi(z)$ may still have a jump when an internal hole is encircled. This jump can be identified with the resulting perpendicular force acting on that hole, as in (5.65). The forces acting on each of the holes must add up to zero to meet the equilibrium of the entire plate. In the present situation of a plate with one hole (the crack), the force P must vanish and, as a result, the complex functions $\Phi(z)$ and $\Psi(z)$ are both single-valued in the domain $\mathbf{C} \setminus L$. Subsequent integration of these functions produces:

$$\phi(z) = \gamma \log(z - a) + \phi^*(z), \quad (5.70)$$

$$\psi(z) = \gamma' \log(z - a) + \psi^*(z), \quad (5.71)$$

$$\chi(z) = \gamma'' \log(z - a) + \gamma' z \log(z - a) + \chi^*(z), \quad (5.72)$$

where the functions $\phi^*(z)$, $\psi^*(z)$ and $\chi^*(z)$ are holomorphic and single-valued in $\mathbf{C} \setminus L$. For a proper definition of the logarithm, the complex plane is cut from $z = +a$ to $z = -a$ along the contour L and from $z = -a$ to infinity along the negative x -axis.

The complex constants γ , γ' and γ'' are derived from the resulting moments acting on the crack contour and from additional requirements for the single-valuedness of the

displacements. Substitution of (5.70)–(5.72) into (5.66)⁴ yields

$$M_x + i M_y = 2\pi i (1 - \nu) D (\bar{\gamma}' - \kappa \gamma). \quad (5.73)$$

The single-valuedness of the in-plane displacements (see (2.57)) imposes the condition

$$\left[\phi(z) + z \overline{\phi'(z)} + \overline{\psi(z)} \right]_L = 2\pi i (\bar{\gamma}' - \gamma) = 0. \quad (5.74)$$

From a combination of (2.71) and (5.73)–(5.74), it is deduced that

$$\gamma = \frac{M_x + i M_y}{8\pi i D}, \quad (5.75)$$

$$\gamma' = -\frac{M_x - i M_y}{8\pi i D}. \quad (5.76)$$

The constant γ'' is partly determined by the requirement for single-valuedness of the deflection of the plate; see (2.56). With the use of (5.70), (5.72) and (5.74), we find

$$[w]_L = \text{Im} \{ 2\pi \gamma'' \} = 0. \quad (5.77)$$

This condition is elaborated further, such that we can determine the real constant C which has been introduced in (5.64) as an integration constant.

The behaviour of the complex functions at infinity is now obtained by expanding the single-valued functions $\phi^*(z)$ and $\psi^*(z)$ in Laurent series. In accordance with (5.67), we find

$$\Phi(z) = \Gamma + \frac{M_x + i M_y}{8\pi i D} \cdot \frac{1}{z} - \frac{\beta}{z^2} + O\left(\frac{1}{z^3}\right), \quad (5.78)$$

$$\Psi(z) = \Gamma' - \frac{M_x - i M_y}{8\pi i D} \cdot \frac{1}{z} - \frac{\gamma''}{z^2} + O\left(\frac{1}{z^3}\right), \quad (5.79)$$

$$\Omega(z) = \bar{\Gamma} + \bar{\Gamma}' + \frac{M_x + i M_y}{8\pi i D} \cdot \frac{1}{z} + \frac{\bar{\beta} - \bar{\gamma}''}{z^2} + O\left(\frac{1}{z^3}\right), \quad (5.80)$$

for $z \rightarrow \infty$, where β is an unknown complex constant. The complex constants Γ and Γ' are given by

$$\Gamma = -\frac{M_{xx}^\infty + M_{yy}^\infty}{4(1 + \nu)D} + i A, \quad (5.81)$$

$$\Gamma' = \frac{M_{yy}^\infty - M_{xx}^\infty + 2i M_{xy}^\infty}{2(1 - \nu)D}, \quad (5.82)$$

where A may be put equal to zero without loss of generality, so that Γ is real.

Finally, it is observed from (5.77)–(5.80) that the coefficient of the term of order $O(1/z^2)$ in the expansion of $\Omega(z) - \Phi(z)$ must have zero imaginary part. From this condition we shall determine the real constant C . The condition is expressed in $\Omega(z)$ and $\Phi(z)$ for convenience, since the mathematical problem is formulated in terms of these two functions.

5.3.3 Linearisation for slightly curved cracks

In analogy with Subsection 5.2.2, a linearisation with respect to $\lambda(t)$ is performed. The crack shape is assumed to be smooth and approximately a straight line. Furthermore, we assume that the functions $\Phi(z)$ and $\overline{\Omega(\bar{z})}$, which are analytic in the complex plane with a cut along the crack L , can be continued analytically over the upper and lower crack surfaces to the straight line connecting the two crack tips. The analytically continued functions are denoted by $F(z)$ and $\overline{W(\bar{z})}$, where the functions $F(z)$ and $W(z)$ are holomorphic in the complex plane with a straight cut $[-a, +a]$. The linearisation process continues by writing these two new functions in the form of (5.28) with functions $F_0(z)$ and $W_0(z)$ of zeroth order and functions $F_1(z)$ and $W_1(z)$ of first order in $\Lambda = \|\lambda\|$. The four latter functions are also holomorphic in $\mathbf{C} \setminus [-a, +a]$ and have singularities at the two crack tips $z = \pm a$ as in (5.61). The limiting values of $\Phi(z)$ and $\Omega(\bar{z})$ on the crack flanks L^\pm , i.e. for $z \rightarrow t + i\lambda(t)$, can now be expressed in terms of the boundary values of $F_0(z)$, $F_1(z)$ and $W_0(z)$, $W_1(z)$ on either side of the straight cut. With $-a \leq t \leq +a$ we have

$$\Phi^\pm(z) = F_0^\pm(t) + i\lambda(t)F_0'^\pm(t) + F_1^\pm(t) + O(\Lambda^2), \quad (5.83)$$

$$[\Omega(\bar{z})]^\pm = W_0^\mp(t) - i\lambda(t)W_0'^\mp(t) + W_1^\mp(t) + O(\Lambda^2). \quad (5.84)$$

The angle θ^\pm of crack inclination appears in linearised form as $e^{-2i\theta^\pm} = 1 - 2i\lambda'(t)$ on L^\pm . The boundary conditions (5.64) are linearised with the use of these properties. Omitting terms of second and higher order, we obtain

$$\begin{aligned} -(m - if)^\pm(t) + iC &= (1 - \nu)D \left\{ \kappa F_0^\pm(t) + W_0^\mp(t) + \kappa F_1^\pm(t) + W_1^\mp(t) \right. \\ &\quad \left. + i\lambda(t) \left[\kappa F_0'^\pm(t) + W_0'^\mp(t) \right]' + \left[2i\lambda(t) \left(\overline{F_0^\pm(t)} - W_0^\mp(t) \right) \right]' \right\}, \end{aligned} \quad (5.85)$$

where the constant C must be decomposed as $C = C_0 + C_1$. These constants are determined from requirements that the coefficients of the terms of order $O(1/z^2)$ in the expansions of $W_0(z) - F_0(z)$ and $W_1(z) - F_1(z)$ at infinity must have zero imaginary parts.

The resulting moments (5.66) acting on the crack contour are split into two parts of zeroth and first order:

$$M_x^0 + iM_y^0 = - \int_{-a}^{+a} \left[(m - if)^+(t) - (m - if)^-(t) \right] dt, \quad (5.86)$$

$$M_x^1 + iM_y^1 = -i \int_{-a}^{+a} \left[(m - if)^+(t) - (m - if)^-(t) \right] \lambda'(t) dt, \quad (5.87)$$

after substitution of $dz/dt = 1 + i\lambda'(t)$. Consequently, the limiting behaviour at infinity of the functions $F_0(z)$ and $W_0(z)$ is given by (5.78) and (5.80) with $M_x + iM_y$ replaced by $M_x^0 + iM_y^0$, while the behaviour of the functions $F_1(z)$ and $W_1(z)$ is obtained by putting $\Gamma = \Gamma' = 0$ and replacing $M_x + iM_y$ by $M_x^1 + iM_y^1$.

The stress-intensity factors are derived from (5.69). The functions $\Phi(z)$ and $\Omega(z)$ are replaced by expansions in terms of $F_0(z)$, $F_1(z)$ and of $W_0(z)$, $W_1(z)$. We use that

the functions $\sqrt{r} F_0(a+r)$ and $-2r^{3/2} F'_0(a+r)$ have equal limits for $r \rightarrow 0$. We use a similar property for $W_0(a+r)$. Thus, we obtain the linearised expression for the stress-intensity factors of a curvilinear crack:

$$k_1 - i k_2 = \frac{6(1-\nu)D}{h^2} \lim_{r \rightarrow 0} \sqrt{2\pi r} \left[\left(1 - \frac{i\alpha}{2}\right) \kappa F_0(a+r) + i\alpha \overline{F_0(a+r)} + \left(1 - \frac{3i\alpha}{2}\right) W_0(a+r) + \kappa F_1(a+r) + W_1(a+r) \right]. \quad (5.88)$$

In the next subsection, it will be proved that $\kappa F_0(z)$ and $W_0(z)$ provide equal contributions, so that a simplified expression for the stress-intensity factors results.

5.3.4 Solution for straight cracks

The linearised boundary conditions (5.85) are separated into contributions of zeroth and first order. Upon addition and subtraction of the boundary values on either side of the cut, two Hilbert problems are obtained. For $-a \leq t \leq +a$ we have

$$(\kappa F_0 + W_0)^+(t) + (\kappa F_0 + W_0)^-(t) = 2S(t) + 2i\tilde{C}_0, \quad (5.89)$$

$$(\kappa F_0 - W_0)^+(t) - (\kappa F_0 - W_0)^-(t) = 2U(t), \quad (5.90)$$

where $\tilde{C}_0 = C_0/(1-\nu)D$ and the functions $S(t)$ and $U(t)$ are defined by

$$S(t) = \frac{-1}{2(1-\nu)D} \left[(m - if)^+(t) + (m - if)^-(t) \right], \quad (5.91)$$

$$U(t) = \frac{-1}{2(1-\nu)D} \left[(m - if)^+(t) - (m - if)^-(t) \right]. \quad (5.92)$$

We again introduce the Plemelj function $X(z) = \sqrt{z^2 - a^2}$, which is holomorphic in $\mathbb{C} \setminus [-a, +a]$. This function equals $X^\pm(t) = \pm i\sqrt{a^2 - t^2}$ on either side of the cut, while we have $X(z) = z + O(1/z)$ at infinity. The solution to the Hilbert problems (5.89)–(5.90) is now given by

$$\kappa F_0(z) + W_0(z) = \frac{1}{\pi i X(z)} \int_{-a}^{+a} \frac{X^+(t) S(t)}{t - z} dt + \frac{P_0(z)}{X(z)} + i\tilde{C}_0 \left(1 - \frac{z}{X(z)}\right), \quad (5.93)$$

$$\kappa F_0(z) - W_0(z) = \frac{1}{\pi i} \int_{-a}^{+a} \frac{U(t)}{t - z} dt + Q_0(z), \quad (5.94)$$

where the functions $P_0(z)$ and $Q_0(z)$ are polynomials. The conditions (5.78)–(5.80) at infinity imply that

$$P_0(z) = \left((\kappa + 1)\Gamma + \overline{\Gamma^v} \right) z - \frac{(1 + \nu) \left(M_x^0 + i M_y^0 \right)}{4\pi i (1 - \nu) D}, \quad (5.95)$$

$$Q_0(z) = (\kappa - 1)\Gamma - \overline{\Gamma^v}. \quad (5.96)$$

The constant C_0 is determined from the requirement that the term of order $O(1/z^2)$ in the Laurent expansion of $W_0(z) - F_0(z)$ at infinity must have a coefficient with zero imaginary part. We find

$$\begin{aligned} C_0 &= -M_{xy}^\infty + \frac{1+\nu}{2\pi a^2} \int_{-a}^{+a} (m^+(t) - m^-(t)) t dt \\ &\quad - \frac{1}{\pi a^2} \int_{-a}^{+a} (f^+(t) + f^-(t)) \sqrt{a^2 - t^2} dt. \end{aligned} \quad (5.97)$$

Under the assumption that the applied bending moments $m^\pm(t)$ and generalised torques $f^\pm(t)$ (and thus the function $U(t)$ in (5.92)) are finite at the end point $t = a$, it immediately follows from the solution (5.94) and [62, 63] that

$$\lim_{z \rightarrow a} \sqrt{2\pi(z-a)} (\kappa F_0(z) - W_0(z)) = 0. \quad (5.98)$$

This proves the statement that $\kappa F_0(z)$ and $W_0(z)$ provide equal contributions to the stress-intensity factors k_1 and k_2 . Therefore, the last term in (5.32) vanishes.

The zero-order part of the bending stress-intensity factors (5.68) is calculated by multiplying (5.93) with $\sqrt{2\pi(z-a)}$ and taking the limit for $z \rightarrow a$. We find

$$\begin{aligned} k_1 &= \frac{6}{h^2} M_{yy}^\infty \sqrt{\pi a} + \frac{3}{h^2 \sqrt{\pi a}} \int_{-a}^{+a} [m^+(t) + m^-(t)] \left(\frac{a+t}{a-t}\right)^{\frac{1}{2}} dt \\ &\quad - \frac{3(1+\nu)}{2h^2 \sqrt{\pi a}} \int_{-a}^{+a} [f^+(t) - f^-(t)] dt, \end{aligned} \quad (5.99)$$

$$\begin{aligned} k_2 &= \frac{3}{h^2 \sqrt{\pi a}} \int_{-a}^{+a} [f^+(t) + f^-(t)] \left(\frac{2t-a}{a}\right) \left(\frac{a+t}{a-t}\right)^{\frac{1}{2}} dt \\ &\quad + \frac{3(1+\nu)}{2h^2 \sqrt{\pi a}} \int_{-a}^{+a} [m^+(t) - m^-(t)] \left(\frac{2t+a}{a}\right) dt. \end{aligned} \quad (5.100)$$

Note that the expression for the stress-intensity factor k_2 is not influenced by the uniform torsional moment M_{xy}^∞ at infinity. This agrees with the results of Merkulov [58], but is in contrast with (5.8) where the stress-intensity factor K_{II} does depend on the shear stress σ_{xy}^∞ applied at infinity.

When concentrated moments are applied on the crack, another result of Merkulov [58] is obtained. When $m^+(t) = M_0 \delta(t-t_0)$, $f^+(t) = H_0 \delta(t-t_0)$, and $m^-(t) = f^-(t) = 0$ is inserted, where $\delta(t)$ is the Dirac delta function, it is found that

$$k_1 = \frac{3M_0}{h^2 \sqrt{\pi a}} \left(\frac{a+t_0}{a-t_0}\right)^{\frac{1}{2}} - \frac{3H_0(1+\nu)}{2h^2 \sqrt{\pi a}}, \quad (5.101)$$

$$k_2 = \frac{3H_0(2t_0-a)}{h^2 a \sqrt{\pi a}} \left(\frac{a+t_0}{a-t_0}\right)^{\frac{1}{2}} + \frac{3M_0(1+\nu)(2t_0+a)}{2h^2 a \sqrt{\pi a}}. \quad (5.102)$$

In the case of symmetric loading, the distributions of the applied moments on the lower and upper crack flanks are equal: $m^\pm(t) = m(t)$ and $f^\pm(t) = f(t)$. The expressions

(5.99)–(5.100) attain the simpler form

$$k_1 = \frac{6}{h^2} M_{yy}^\infty \sqrt{\pi a} + \frac{6}{h^2 \sqrt{\pi a}} \int_{-a}^{+a} m(t) \left(\frac{a+t}{a-t} \right)^{\frac{1}{2}} dt, \quad (5.103)$$

$$k_2 = \frac{6}{h^2 \sqrt{\pi a}} \int_{-a}^{+a} f(t) \left(\frac{2t-a}{a} \right) \left(\frac{a+t}{a-t} \right)^{\frac{1}{2}} dt. \quad (5.104)$$

5.3.5 Solution for slightly curved cracks

In this section the first-order terms of the stress-intensity factors for curvilinear cracks are calculated. For the sake of simplicity, the applied bending and torsional moments are restricted to symmetric distributions, i.e. $m^\pm(t) = m(t)$ and $f^\pm(t) = f(t)$. As a result, the expressions (5.103)–(5.104) for the stress-intensity factors of order zero may be used. The Hilbert problem for the functions $F_1(z)$ and $W_1(z)$ of first order is derived from the boundary conditions (5.85). Restriction to first-order terms yields

$$\begin{aligned} \kappa F_1^\pm(t) + W_1^\mp(t) &= i\tilde{C}_1 - i\lambda(t) \left[\kappa F_0^\pm(t) + W_0^\mp(t) \right]' \\ &\quad - \left[2i\lambda(t) \left(\overline{F_0^\pm(t)} - W_0^\mp(t) \right) \right]', \end{aligned} \quad (5.105)$$

where the constant \tilde{C}_1 equals $C_1/(1-\nu)D$. Addition and subtraction of (5.105) leads to the Hilbert problems

$$(\kappa F_1 + W_1)^+(t) + (\kappa F_1 + W_1)^-(t) = b_1(t), \quad (5.106)$$

$$(\kappa F_1 - W_1)^+(t) - (\kappa F_1 - W_1)^-(t) = b_2(t), \quad (5.107)$$

where the functions $b_1(t)$ and $b_2(t)$ denote the sum and the difference of the right-hand sides of (5.105), respectively. The precise form of these functions is given in Appendix B.2. The solution to the Hilbert problems (5.106)–(5.107) is given by

$$\kappa F_1(z) + W_1(z) = \frac{1}{2\pi i X(z)} \int_{-a}^{+a} \frac{X^+(t) b_1(t)}{t-z} dt + \frac{P_1(z)}{X(z)}, \quad (5.108)$$

$$\kappa F_1(z) - W_1(z) = \frac{1}{2\pi i} \int_{-a}^{+a} \frac{b_2(t)}{t-z} dt + Q_1(z), \quad (5.109)$$

where the functions $P_1(z)$ and $Q_1(z)$ are polynomials. The conditions at infinity imply that these polynomials vanish.

The contribution of the functions $F_1(z)$ and $W_1(z)$ to the stress-intensity factors is obtained from (5.88) by taking the following limit in (5.108). We find

$$\begin{aligned} \frac{6(1-\nu)D}{h^2} \lim_{r \rightarrow 0} \left\{ \sqrt{2\pi r} \left[\kappa F_1(a+r) + W_1(a+r) \right] \right\} \\ = -\frac{3(1-\nu)D}{h^2 \sqrt{\pi a}} \int_{-a}^{+a} b_1(t) \left(\frac{a+t}{a-t} \right)^{\frac{1}{2}} dt. \end{aligned} \quad (5.110)$$

A detailed elaboration of this solution and the determination of C_1 are presented in the Appendix B.2. The expression (5.110) is worked out in (B.12).

The contribution of the functions $F_0(z)$ and $W_0(z)$ to the stress-intensity factors for a curved crack is obtained from (5.88) with (5.98). Let the factors (5.103)–(5.104) be denoted by k_1^o and k_2^o . Then, this contribution is given by

$$\begin{aligned} & \frac{6(1-\nu)D}{h^2} \lim_{r \rightarrow 0} \left\{ \sqrt{2\pi r} \left[2\kappa(1-i\alpha)F_0(a+r) + i\alpha\overline{F_0(a+r)} \right] \right\} \\ & = \left(k_1^o - \frac{2\kappa+1}{2\kappa} \alpha k_2^o \right) - i \left(k_2^o + \frac{2\kappa-1}{2\kappa} \alpha k_1^o \right). \end{aligned} \quad (5.111)$$

The stress-intensity factors for a thin flat plate containing a curved crack and loaded by bending and torsional moments are now obtained by summation of the results (5.110) and (5.111). With the use of (B.12) we derive the final result:

$$\begin{aligned} k_1 & = \frac{6\sqrt{\pi a}}{h^2} \left(M_{yy}^\infty - 2\mathcal{A} M_{xy}^\infty \right) + \frac{6}{h^2\sqrt{\pi a}} \int_{-a}^{+a} g_1(t) \left(\frac{a+t}{a-t} \right)^{\frac{1}{2}} dt \\ & - \frac{6}{\kappa h^2\sqrt{\pi a}} \int_{-a}^{+a} \frac{a\lambda(t)f(t)}{(a+t)^{\frac{1}{2}}(a-t)^{\frac{3}{2}}} dt, \end{aligned} \quad (5.112)$$

$$\begin{aligned} k_2 & = \frac{6\sqrt{\pi a}}{h^2} \left\{ \mathcal{B} \left(\frac{1}{\kappa} M_{yy}^\infty - M_{xx}^\infty \right) + \left(\frac{\kappa+1}{\kappa} (\mathcal{B} - \mathcal{A}) + \frac{2\kappa-1}{2\kappa} \alpha \right) M_{yy}^\infty \right\} \\ & + \frac{6}{h^2\sqrt{\pi a}} \int_{-a}^{+a} g_2(t) \left(\frac{a+t}{a-t} \right)^{\frac{1}{2}} dt \\ & - \frac{6}{\kappa h^2\sqrt{\pi a}} \int_{-a}^{+a} \frac{(2t-a)\lambda(t)m(t)}{(a+t)^{\frac{1}{2}}(a-t)^{\frac{3}{2}}} dt \\ & + \frac{12(\kappa+1)}{\kappa h^2(\pi a)^{\frac{3}{2}}} \int_{-a}^{+a} m(t) \sqrt{a^2-t^2} \int_{-a}^{+a} \frac{\lambda(s)}{\sqrt{a^2-s^2}(t-s)} ds dt, \end{aligned} \quad (5.113)$$

where the integrand functions $g_1(t)$ and $g_2(t)$ are defined by

$$g_1(t) = m(t) + \left(\lambda'(t) - \frac{\kappa+1}{\kappa} \mathcal{A} + \left(\frac{\kappa+1}{\kappa} \mathcal{A} - \frac{2\kappa+1}{2\kappa} \alpha \right) \left(\frac{2t-a}{a} \right) \right) f(t), \quad (5.114)$$

$$g_2(t) = \left(\frac{2\kappa-1}{2\kappa} \alpha - \frac{2\lambda(t)}{\kappa a} - \lambda'(t) \left(\frac{2t-a}{a} \right) \right) m(t) + \left(\frac{2t-a}{a} \right) f(t). \quad (5.115)$$

The last term in (5.113) contains a double integral in which the inner, singular integral \oint is calculated by taking the Cauchy principal value. It is proved in Appendix B.1 that interchanging the order of integration is allowed. The dimensionless crack-shape parameter \mathcal{B} is defined by

$$\mathcal{B} = \frac{1}{\pi a} \int_{-a}^{+a} \lambda'(t) \left(\frac{2t-a}{a} \right) \left(\frac{a+t}{a-t} \right)^{\frac{1}{2}} dt, \quad (5.116)$$

analogous to the definition (5.9) of the parameter \mathcal{A} . It follows that

$$\mathcal{A} - \mathcal{B} = \frac{2}{\pi a^2} \int_{-a}^{+a} \lambda'(t) \sqrt{a^2-t^2} dt = \frac{2}{\pi a^2} \int_{-a}^{+a} \frac{t\lambda(t)}{\sqrt{a^2-t^2}} dt. \quad (5.117)$$

We note that the parameters \mathcal{A} and \mathcal{B} are equal for symmetric cracks with even shape functions, i.e. with $\lambda(t) = \lambda(-t)$ for $-a \leq t \leq +a$.

5.3.6 Examples

The expressions derived for the bending stress-intensity factors are illustrated with a few examples. Simplified expressions for k_1 and k_2 are obtained by substitution of special distributions of the bending moments and specific crack-shape functions.

Uniform moments at infinity

As a first example, a thin flat plate loaded by bending moments (5.67) at infinity is considered. The surfaces of the curved crack are stress-free. The stress-intensity factors for this bending problem immediately follow from (5.112)–(5.113), viz.

$$k_1 = \frac{6\sqrt{\pi a}}{h^2} (M_{yy}^\infty - 2\mathcal{A}M_{xy}^\infty), \quad (5.118)$$

$$k_2 = \frac{6\sqrt{\pi a}}{h^2} \left\{ \mathcal{B} \left(\frac{1}{\kappa} M_{yy}^\infty - M_{xx}^\infty \right) + \left(\frac{\kappa+1}{\kappa} (\mathcal{B} - \mathcal{A}) + \frac{2\kappa-1}{2\kappa} \alpha \right) M_{yy}^\infty \right\}. \quad (5.119)$$

The same expressions are obtained for an equivalent loading configuration, where no bending moments are applied at infinity, but where the crack surfaces are loaded by moments of opposite sign, i.e., $M_{ij} = -M_{ij}^\infty$ and $Q_i = 0$. The bending moment and the generalised torque on the crack surfaces are determined with the use of the linearised tangential and normal vectors $\mathbf{s}^\pm = \pm(\mathbf{e}_x + \lambda'(t)\mathbf{e}_y)$ and $\mathbf{n}^\pm = \pm(\lambda'(t)\mathbf{e}_x - \mathbf{e}_y)$ on L^\pm . Omitting second and higher-order terms we find

$$\begin{aligned} M_{nn}^\pm = -m(t) &= M_{xx}n_x^2 + 2M_{xy}n_xn_y + M_{yy}n_y^2 \\ &= -M_{yy}^\infty + 2\lambda'(t)M_{xy}^\infty, \end{aligned} \quad (5.120)$$

$$\begin{aligned} M_{ns}^{\pm\pm} = +f(t) &= M_{xx}n_xs_x + M_{xy}(n_xs_y + n_ys_x) + M_{yy}n_ys_y \\ &= M_{xy}^\infty + \lambda'(t)(M_{yy}^\infty - M_{xx}^\infty). \end{aligned} \quad (5.121)$$

Substitution of these loading distributions into (5.112)–(5.113) indeed produces the same results for the stress-intensity factors as in (5.118)–(5.119).

Uniform moments on crack surfaces

As a second example, we examine the situation where the crack surfaces are loaded by uniform bending moments $m(t) = m$ and generalised torques $f(t) = f$. No bending moments are applied at infinity. The stress-intensity factors for this configuration are derived from (5.112)–(5.115) as

$$k_1 = \frac{6m\sqrt{\pi a}}{h^2}, \quad (5.122)$$

$$k_2 = \frac{6m\sqrt{\pi a}}{h^2} \left(\frac{\kappa+1}{\kappa} (\mathcal{B} - \mathcal{A}) + \frac{1-\kappa}{\kappa} \mathcal{B} + \frac{2\kappa-1}{2\kappa} \alpha \right). \quad (5.123)$$

We note that there is no contribution of the generalised torque f . These results resemble those of the first example. Identification of m and f with M_{yy}^∞ and M_{xy}^∞ in (5.118)–(5.119) shows that the terms of order zero are identical. This is obvious because the two examples are equivalent in the case of straight cracks. The first-order

terms, however, are different. The crack-tip angle α appears equally in formulae (5.118)–(5.119) and (5.122)–(5.123); the differences are confined to the terms with the crack-shape parameters \mathcal{A} and \mathcal{B} . Subtraction of the results yields

$$\Delta k_1 = \frac{6\sqrt{\pi a}}{h^2} \left(-2\mathcal{A} M_{xy}^\infty \right), \quad (5.124)$$

$$\Delta k_2 = \frac{6\sqrt{\pi a}}{h^2} \mathcal{B} \left(M_{yy}^\infty - M_{xx}^\infty \right). \quad (5.125)$$

These differences precisely correspond to the occurrence of $\lambda'(t)$ in the expressions (5.120)–(5.121) for the bending moments on the crack flanks. Multiplication of this derivative with appropriate factors and integration over the interval $[-a, +a]$ produces \mathcal{A} and \mathcal{B} ; see (5.9) and (5.116). Therefore, these parameters are measures for the amount by which the crack deviates from a straight line, and for the influence thereof on the stress-intensity factors k_1 and k_2 , respectively.

Crack along circular arc

For the third example, a crack along a circular arc of radius R is chosen, having an opening angle 2α ; see Fig. 5.5. The crack-shape function $\lambda(x)$ is given by (5.57). The parameters \mathcal{A} and \mathcal{B} for this crack geometry are equal (see (5.117)) and are given by (5.59). The plate is subjected to pure bending by $M_{xx}^\infty = M_{yy}^\infty = M$ and to uniform torsion by $M_{xy}^\infty = H$ at infinity. The crack surfaces remain stress-free. The linearised stress-intensity factors are derived from (5.118)–(5.119) and are equal to

$$k_1 = \frac{6\sqrt{\pi a}}{h^2} \left(M - 2\mathcal{A}H \right), \quad (5.126)$$

$$k_2 = \frac{6\sqrt{\pi a}}{h^2} \left(\left(\frac{1}{\kappa} - 1 \right) \mathcal{A} + \left(1 - \frac{1}{2\kappa} \right) \alpha \right) M. \quad (5.127)$$

The exact solution has been calculated by Merkulov [58] and is given by

$$k_1 = \frac{6\sqrt{\pi R \sin \alpha}}{h^2} \left(\frac{\kappa \cos(\frac{1}{2}\alpha)}{\kappa + \sin^2(\frac{1}{2}\alpha)} M - \frac{1}{2} \sin(\frac{1}{2}\alpha) (1 + 3 \cos \alpha) H \right), \quad (5.128)$$

$$k_2 = \frac{6\sqrt{\pi R \sin \alpha}}{h^2} \left(\frac{\kappa \sin(\frac{1}{2}\alpha)}{\kappa + \sin^2(\frac{1}{2}\alpha)} M - \frac{3}{2} \sin(\frac{1}{2}\alpha) \sin \alpha H \right). \quad (5.129)$$

The numerical values of k_1 and k_2 from (5.126)–(5.127) and from (5.128)–(5.129) are normalised with respect to the standard stress-intensity factors $k_0 = 6M\sqrt{\pi a}/h^2$ and $6H\sqrt{\pi a}/h^2$ with $a = R \sin \alpha$. The results are presented graphically in Fig. 5.8 as function of α , for Poisson's ratio $\nu = 0.25$ or $\kappa = -13/3$. The stress-intensity factor k_2 for uniform torsion has been omitted from the figure, because the linearised result (5.127) vanishes and the exact solution (5.129) is of second order in α .

We observe that the relative error in the results for pure bending is at most 5% for arc-opening angles $\alpha < 40^\circ$ concerning k_1 and for angles $\alpha < 25^\circ$ concerning k_2 . The linearised stress-intensity factor k_1 for uniform torsion is only accurate within 10% up

to angles $\alpha < 20^\circ$. Thus, we conclude that rather acceptable approximations for the bending stress-intensity factors for cracks along circular arcs are obtained. On the basis of these results, we expect that the formulae (5.112)–(5.113) can also be used to derive the stress-intensity factors k_1 and k_2 for arbitrary, slightly curved cracks.

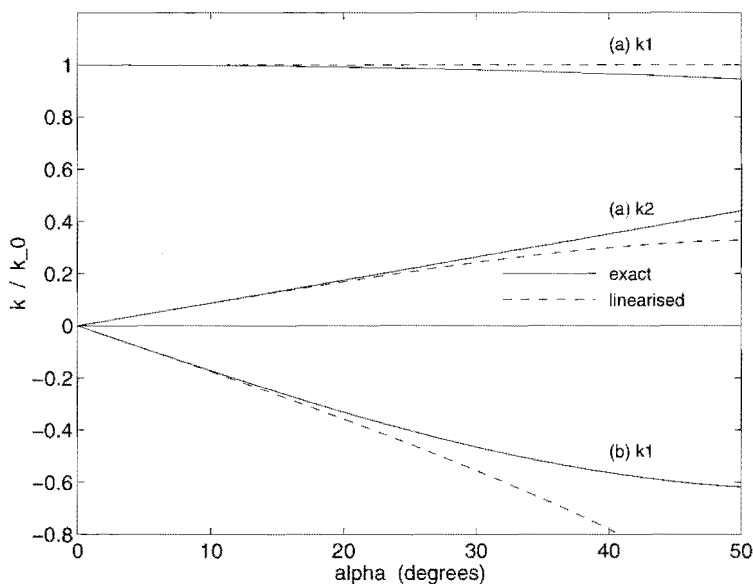


Figure 5.8: Exact and linearised bending stress-intensity factors of modes 1 and 2 for a crack along a circular arc, subject to (a) pure bending and (b) uniform torsion.

5.4 Comparison of stress-intensity factors

The stress-intensity factors k_1 and k_2 of plate bending show several similarities with the factors K_I and K_{II} of planar deformation, but there exist some differences. Firstly, the solutions (5.103)–(5.104) are compared with the expressions (5.3)–(5.4) and (5.7)–(5.8) for a straight crack. We observe that the stress-intensity factor k_2 does not depend on the torsional moment M_{xy}^∞ applied at infinity. This is in contrast with the shear stress σ_{xy}^∞ which does appear in the expression for K_{II} . Another dissimilarity between the respective stress-intensity factors concerns the factor $(2t - a)/a$ in the integrand functions. This factor is typical for the bending problem, since it does not occur in the expressions for K_I and K_{II} of the plane-stress problem.

Secondly, the expressions (5.3)–(5.4) and (5.7)–(5.8) are compared with the solutions (5.112)–(5.113) for a curvilinear crack. A common feature of these solutions is that

the stress-intensity factors of modes I and 1 have zero-order terms which depend on σ_{yy}^∞ and $p(t)$ and on M_{yy}^∞ and $m(t)$, respectively, and first-order terms which depend on σ_{xy}^∞ and $q(t)$ and on M_{xy}^∞ and $f(t)$, respectively, multiplied by suitable expressions involving the crack-shape function $\lambda(t)$. Regarding the factors of modes II and 2, the dependence of their zeroth and first-order terms on the loading components is precisely the other way around.

Furthermore, we notice that the expressions (5.112)–(5.113) for plate bending are much more complicated than the expressions (5.3)–(5.4) for planar deformation. This relates to the presence of the parameter κ in the boundary conditions (5.64) and (5.85) on the crack surfaces. As a consequence, this parameter also appears in the Hilbert problems for the complex functions and, thus, in the solution for the stress-intensity factors. On the other hand, in the case of planar deformation, the expressions for the stress components do not contain a constant κ , but only those for the displacements do [63, Sec. 32]. In addition, the integration constant C in (5.64) gives an essential contribution to the bending stress-intensity factors. This constant should not be set equal to zero, since it is related to the conditions for single-valued displacements.

It is instructive to compare the stress-intensity factors (5.112)–(5.113) of the plate bending problem with the factors (5.3)–(5.4) and (5.7)–(5.8) of the plane-stress problem, when we put $\kappa = 1$ and disregard the extra multiplicative factor $(2t - a)/a$ in the integrand functions (5.114)–(5.115). Putting $\kappa = 1$ means in fact that Poisson's ratio is taken equal to infinity because of (2.71). This corresponds to the observations in Chapter 4, where putting $\nu = \infty$ resulted in equal near-tip singular bending moments for Reissner's theory and the classical plate theory. Ignoring the typical factor $(2t - a)/a$ firstly implies that the crack-shape parameters \mathcal{A} and \mathcal{B} become the same. Secondly, the term $(2/a)\lambda(t)m(t)$ can be omitted from the integrand function $g_2(t)$, because it stems from differentiation of the multiplicative factor; see (B.14). When the factor $(2t - a)/a$ is disregarded in this way and with $\kappa = 1$, the expressions (5.112)–(5.113) reduce to

$$\begin{aligned} \tilde{k}_1 &= \frac{6\sqrt{\pi a}}{h^2} \left(M_{yy}^\infty - 2\mathcal{A} M_{xy}^\infty \right) \\ &+ \frac{6}{h^2\sqrt{\pi a}} \int_{-a}^{+a} \left[m(t) + \left(\lambda'(t) - \frac{3}{2}\alpha \right) f(t) \right] \left(\frac{a+t}{a-t} \right)^{\frac{1}{2}} dt \\ &- \frac{6}{h^2\sqrt{\pi a}} \int_{-a}^{+a} \frac{a\lambda(t)f(t)}{(a+t)^{\frac{1}{2}}(a-t)^{\frac{3}{2}}} dt, \end{aligned} \quad (5.130)$$

$$\begin{aligned} \tilde{k}_2 &= \frac{6\sqrt{\pi a}}{h^2} \left\{ \frac{1}{2}\alpha M_{yy}^\infty + \mathcal{A} \left(M_{yy}^\infty - M_{xx}^\infty \right) \right\} \\ &+ \frac{6}{h^2\sqrt{\pi a}} \int_{-a}^{+a} \left[f(t) - \left(\lambda'(t) - \frac{1}{2}\alpha \right) m(t) \right] \left(\frac{a+t}{a-t} \right)^{\frac{1}{2}} dt \\ &- \frac{6}{h^2\sqrt{\pi a}} \int_{-a}^{+a} \frac{a\lambda(t)m(t)}{(a+t)^{\frac{1}{2}}(a-t)^{\frac{3}{2}}} dt \\ &+ \frac{24}{h^2(\pi a)^{\frac{3}{2}}} \int_{-a}^{+a} m(t) \sqrt{a^2 - t^2} \int_{-a}^{+a} \frac{\lambda(s)}{\sqrt{a^2 - s^2}(t-s)} ds dt. \end{aligned} \quad (5.131)$$

Although these simplified stress-intensity factors have no physical meaning, they show remarkable similarities with K_I and K_{II} as given by (5.3)–(5.4) and (5.7)–(5.8). The remaining differences concern the double integral in the expression for k_2 and the influence of the shear stress σ_{xy}^∞ and of the torsional moment M_{xy}^∞ applied at infinity.

We shall now discuss the stress-intensity factor K_{III} and start with a comparison of the results for straight cracks (the terms of order zero). From Sections 5.2 and 5.3 it is clear that the dependence of the stress-intensity factor K_{III} on the shear stresses τ_{yz}^∞ and $p(t)$ in (5.51) is identical to the dependence of K_I on the stresses σ_{yy}^∞ and $p(t)$ in (5.3) and (5.7), and to the dependence of K_{II} on the stresses σ_{xy}^∞ and $q(t)$ in (5.4) and (5.8). This correspondence also applies to the dependence of the stress-intensity factor k_1 on the bending moments M_{yy}^∞ and $m(t)$ in (5.103), but not to the dependence of k_2 on the torsional moment M_{xy}^∞ and the generalised torque $f(t)$ in (5.104). The latter is due to the factor $(2t - a)/a$ which is typical for bending problems.

Next, we compare the results for slightly curved cracks (the terms of first order). Regarding the uniform loads applied at infinity, there is only little correspondence between the expressions for K_{III} and K_I , k_1 ; see (5.7), (5.50), and (5.112). Indeed, the first-order terms depend on τ_{xz}^∞ , σ_{xy}^∞ , and M_{xy}^∞ , respectively, but the coefficients of these stresses and moments are different. We observe even less similarity with the expressions for K_{II} and k_2 ; see (5.8) and (5.113). Regarding the stresses and moments applied to the crack surfaces, we already noticed some common features of the stress-intensity factors K_I , K_{II} and k_1 , k_2 at the beginning of this section. These features are related to the fact that two independent fracture modes exist in each of the cases of planar deformation and of plate bending. In the case of anti-plane shear, however, there exists only one fracture mode. This explains why we only find a non-zero contribution to K_{III} of first order in $\lambda(t)$ for asymmetric loading with $p^+(t) \neq p^-(t)$ as in (5.50), and not for symmetric loading as in (5.51).

The reasons for these dissimilarities are twofold. The differences are not only caused by a combination of fracture modes as discussed above, but the direction of the applied forces also influences the results. The stress-intensity factors K_I , K_{II} and k_1 , k_2 are expressed in terms of stresses and moments acting in the directions normal and tangential to the crack surfaces. These directions are related to the derivative $\lambda'(t)$ of the crack-shape function. The factor K_{III} , on the contrary, is expressed in terms of shear stresses acting in the z -direction which is constant along the crack. Thus, K_{III} depends on the derivative $\lambda'(t)$ to a lesser extent than the other stress-intensity factors. This also forms an alternative explanation for the different dependences of the stress-intensity factors on the uniform stresses and moments at infinity.

5.5 Conclusions

We have studied elastic bodies containing curvilinear cracks and subjected to in-plane stresses, out-of-plane shear stresses, and to bending and torsional moments. The stress-intensity factors K_I and K_{II} for planar deformation have been determined, and

also the factor K_{III} for thick elastic solids loaded in anti-plane shear. In addition, the stress-intensity factors k_1 and k_2 of the classical plate theory have been calculated for the bending of thin flat plates. The solutions depend on the stresses and moments applied to the crack surfaces, on the uniform loads at infinity, and on the crack-shape function $\lambda(t)$. A comparison of the results leads to the following conclusions:

1. The dependence of the stress-intensity factors k_1 and k_2 on the bending moments is similar to the dependence of the factors K_I and K_{II} on the in-plane stresses. The straight-crack solutions (the terms of order zero in $\lambda(t)$) for k_1 and K_I relate to the loads in the direction normal to the crack surfaces, and those for k_2 and K_{II} to the loads in the tangential direction. This is in accordance with their definitions. The first-order terms of k_1 and K_I typically depend on the loads in the tangential direction and on the crack-shape function, and those of k_2 and K_{II} on the loads in the normal direction; see (5.3)–(5.4), (5.7)–(5.8) and (5.112)–(5.113).
2. The differences between k_1 and k_2 on the one hand and K_I and K_{II} on the other hand, mainly concern the parameter κ related to Poisson's ratio and the multiplicative factor $(2t - a)/a$ in the integrand functions in the expressions for k_1 and k_2 . Putting $\kappa = 1$ (or $\nu = \infty$) and disregarding the multiplicative factor in (5.112)–(5.113) reveals remarkable similarities with the stress-intensity factors K_I and K_{II} , although the resulting factors \tilde{k}_1 and \tilde{k}_2 in (5.130)–(5.131) have no immediate physical meaning. In addition, the stress-intensity factor k_2 does not depend on the torsional moment M_{xy}^∞ , whereas K_{II} does depend on the shear stress σ_{xy}^∞ applied at infinity.
3. Less similarity is observed between K_{III} and the other stress-intensity factors; see (5.50). This is caused by the fact that only one fracture mode exists in the case of anti-plane shear, whereas two independent fracture modes exist in the case of planar deformation or plate bending. Moreover, the stresses in anti-plane shear are applied in the direction perpendicular to the plane of symmetry and parallel to the crack fronts; this direction is constant along the crack.
4. All stress-intensity factors K_I , K_{II} , K_{III} and k_1 , k_2 have been calculated for a crack along a circular arc and compared with the exact solutions from the literature. Good agreement has been obtained, which indicates that the derived expressions can be used for a wide variety of cracks with slight curvature.

Summarising we conclude that useful expressions for the stress-intensity factors have been derived, which enables the analysis of prolonged crack propagation along curvilinear paths under general loading conditions. The incorporation of the crack shape is necessary to produce the correct values of the stress-intensity factors and to calculate the direction of further crack propagation accurately.

Chapter 6

Uncoupled fracture approach

So far, we have investigated general properties of brittle fracture and dynamic crack propagation (Chapter 3), the consequences of bending deformation plus the effects of crack closure (Chapter 4), and the stress-intensity factors for curved cracks subject to tensile, tearing and bending actions (Chapter 5). In the present chapter we unite these results into the uncoupled dynamic fracture approach.

The method has been described briefly in Section 1.3 and will now be explained in more detail. The elastodynamic effects in a time-dependent deformation problem concern stress waves and crack propagation. There exists a certain interaction: the (dynamic) stresses determine the crack propagation, while rapid fracture initiates new stress waves. This connection is partly uncoupled in the present approach. The stresses are calculated first for the undamaged geometry without crack growth and, next, possible crack patterns are derived.

Although the main area of application is the impact safety test on television picture tubes, the uncoupled approach is also suitable for the analysis of fracture problems involving rapid crack propagation and/or dynamic loading conditions. In fact, this method can even be used to examine quasi-static crack propagation in structures under constant loads. (A deformation problem is called quasi-static when the dynamic effects can be neglected.) There is one restriction: this approach applies to thin, slightly curved, plate-like structures and is less suitable to analyse general crack propagation in thick three-dimensional solids.

6.1 Description of the method

The first step in the uncoupled analysis of fracture phenomena is the determination of the dynamic stresses in the elastic body as function of time. This can be performed analytically (if possible) or numerically, e.g. by means of a finite-element computation. For a thorough introduction into the finite-element method we refer to the textbooks by Hughes [37] and Zienkiewicz [100]. A short summary is contained in Chapter 7

as a preliminary to the hybrid fracture/damage approach. In order to perform a dynamic analysis, it is necessary that the initial equilibrium situation be calculated first. With regards to (the application to) television picture tubes, the initial state for the impact safety test is the glass bulb (screen, cone and neck) loaded by the internal vacuum. In addition to the vacuum load, the glass bulb can be subjected to extra forces induced by application of the metal rimband. Other geometries (for example test specimens) may initially be in a stress-free state or in a simple stress situation. The elastodynamic calculation continues with the addition of the impact load (or any other time-dependent external force) and the computation of the stresses for several time increments. Evidently, a quasi-static analysis can be carried out by taking the stresses constant in time and equal to the initial stress distribution.

Until this moment, the analysis is performed for the intact, unfractured geometry. The initiation of a crack is the second step in the uncoupled fracture approach. The precise location of crack initiation can be chosen freely, in combination with the initial length and direction of the crack. For television tubes, this location can for instance be at the point of impact, at one of the prescribed scratches in the case of the missile test, or even at the cone or the neck of the tube. Regarding the crack propagation, we impose some restrictions on the shape of the crack surfaces. The projection of the crack onto the middle plane of the glass screen may attain an arbitrarily curved shape. This type of cracks has been investigated in Chapter 5 and a restriction to the in-plane curvature is that linearisation of the crack shape is admitted, so that the linearised expressions for the stress-intensity factors can be used. We impose that the crack front is always a straight line and that the crack surfaces are always perpendicular to the middle plane of the screen. As a result, it is not possible to incorporate variations of the crack front over the thickness of the screen nor the amount of crack rotation. These effects may occur when the crack propagates at different speeds in the inner and outer surfaces of the screen or in different directions. In these cases, the crack front is no longer a straight line perpendicular to the middle plane of the screen, but it will rotate and attain a skew orientation with respect to the screen normal. Observations on fractured television picture tubes, however, indicate that cracks are almost perpendicular to the screen surfaces in many cases.

The third step in the uncoupled fracture approach is the determination of the crack path. After the initiation of the crack and at any intermediate stage of the fracture simulation, both the speed and the direction of further crack propagation must be calculated. Although the screen of a television tube is not entirely flat and does not have constant thickness, it can be regarded as a thin flat plate because the thickness variations and the curvature are relatively small. So, we may use the expressions for the stress-intensity factors for curvilinear cracks in plates as derived in Chapter 5. The crack path is a piece-wise linear curve with the sequential positions of the crack tip as its vertices and with the crack increments as the connecting lines. The crack-shape function $y = \lambda(x)$ for each vertex is determined by measurement of the distance to the line connecting the end points of the crack path; see Fig. 6.1 and compare with Figs. 5.1, 5.3, and 5.7. The stress distributions along the crack surfaces are derived from the elastodynamic stresses which have been calculated at step one, while

the stresses on opposite crack surfaces are taken equal. Substitution of these data into the expressions (5.3) and (5.4) produces the stress-intensity factors K_I and K_{II} , while K_{III} is derived from (5.51). The bending stress-intensity factors k_1 and k_2 of the classical plate theory are calculated from the formulae (5.112) and (5.113) and are converted into the bending stress-intensity factors K_1 and K_2 of Reissner's theory with the use of the expression (4.84).

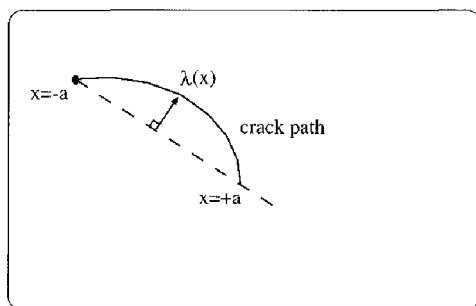


Figure 6.1: Piece-wise linear crack path and measurement of crack-shape function. The dot \bullet is the impact point and the other crack end is the propagating crack tip.

Now that all stress-intensity factors have been determined, we turn to the calculation of the crack-growth direction and speed. To this end, we use the fracture criteria discussed in Section 3.4. The two criteria have been implemented in the uncoupled approach. Although no essential differences have been observed in the obtained crack patterns, we shall consider the details of both implementations below. Regarding the circumferential stress criterion, the crack-propagation angle θ_p is determined by (3.60) and the maximum stress-intensity factor $K_{\theta\theta}(\theta_p)$ by (3.61). In these expressions, K_I and K_{II} are replaced with their "effective" values $K_I + |K_1|$ and $K_{II} + \text{sign}(K_1) \cdot K_2$ in the outer or inner side of the screen where the tensile stress is maximum, which is in agreement with (4.91)–(4.92). The crack-growth speed c is then calculated from the expression (3.74) for the dynamic energy release rate with the substitution $\mathcal{G}(\sigma, a, 0) = K_{\theta\theta}^2(\theta_p)/E$. Regarding the J -integral criterion, the crack-propagation angle θ_p is determined by (3.65) with the parameters J_1 and J_2 defined by (4.94)–(4.95) with $c = 0$. The crack-growth speed c is again calculated from (3.74) but this time with the substitution $\mathcal{G}(\sigma, a, 0) = (J_1^2 + J_2^2)^{1/2}$. For either fracture criterion, we determine the new position of the crack tip by

$$\mathbf{x}_{tip,new} = \mathbf{x}_{tip,old} + \mathbf{c} \cdot \Delta t_c, \quad (6.1)$$

where Δt_c is the time step for the crack increment and \mathbf{c} is a vector in the plane tangent to the screen with length equal to the crack speed c and with its direction determined

by the crack-propagation angle θ_p . It is emphasised that the time step Δt_c for the fracture simulation may be larger than the time step used for the computation of the elastodynamic stresses. The former time step cannot be chosen too large, because otherwise the condition for stability of the time-step algorithm will be violated.

After the determination of the new crack-tip position, the third step in the uncoupled fracture approach is repeated and the stress-intensity factors for the new, extended crack are calculated. As long as the value of $\mathcal{G}(\sigma, a, 0)$ exceeds the critical energy release rate \mathcal{G}_c , the dynamic crack propagation will continue. But when $\mathcal{G}(\sigma, a, 0)$ decreases and becomes less than \mathcal{G}_c , the crack-propagation speed c becomes zero and crack arrest occurs.

6.2 Superposition principle

The uncoupled fracture approach uses (dynamic) stress data of the unfractured geometry to predict crack patterns. This may sound contradictory, but it can be explained by the following argument for quasi-static fracture, i.e., for an instantaneous geometry containing a crack. In the first step of the analysis, we compute the elastodynamic stress distributions for an intact structure under the assumption that fracture does not occur. In the next steps, we *assume* the existence of a crack at a certain position and at a given moment of time. This crack, however, is a virtual crack in the sense that it does not exist in reality. The stresses in these positions are considered to act on the crack surfaces, opening the crack and creating a stress intensity at its tip. This leads to a paradox, since there are no stress singularities in the computed stress data. On the other hand, the surfaces of a real crack would have been stress-free. This paradox is explained with the superposition principle; see Broek [11, Sec. 3.5].

Consider the original intact elastic body loaded by external forces and with the given distribution of internal stresses, i.e., the elastodynamic solution as calculated at step one of the uncoupled fracture approach. Also consider three related configurations which are illustrated in Fig. 6.2 and which concern the fractured geometry under different loading conditions. Firstly, the body (a) contains a crack with stress-free crack surfaces and is subjected to the same external loads as the original body. Due to the presence of the crack, stress relief occurs resulting in crack opening. Secondly, the body (b) which has the same geometry as (a) is loaded by extra stresses $\sigma_{nn} = p(x)$ being applied to the crack surfaces in the direction n normal to the crack. These stresses tend to close the crack and the function $p(x)$ is chosen such that complete crack closure occurs and that the stress singularities at the crack tips vanish. Because of the disappearing stress singularities, the situation (b) coincides with the original intact geometry. The difference between (a) and (b) is obtained by subtraction. This results in configuration (c) where no externally applied forces are present; only the crack surfaces are subjected to stresses $\sigma_{nn} = -p(x)$ having opposite sign with respect to body (b). These stresses tend to open the crack and create stress singularities at the crack tips. Because of the superposition principle, the stress intensities for (a) and (c)

are identical. The stress distribution $p(x)$ is derived from the solution of problem (b) or, equivalently, from the solution for the original intact elastic body. The obtained stress distribution is then used for the calculation of the stress-intensity factors. This argument shows that the influence of the stress situation on the stress-intensity factors is correctly incorporated in the uncoupled fracture approach.

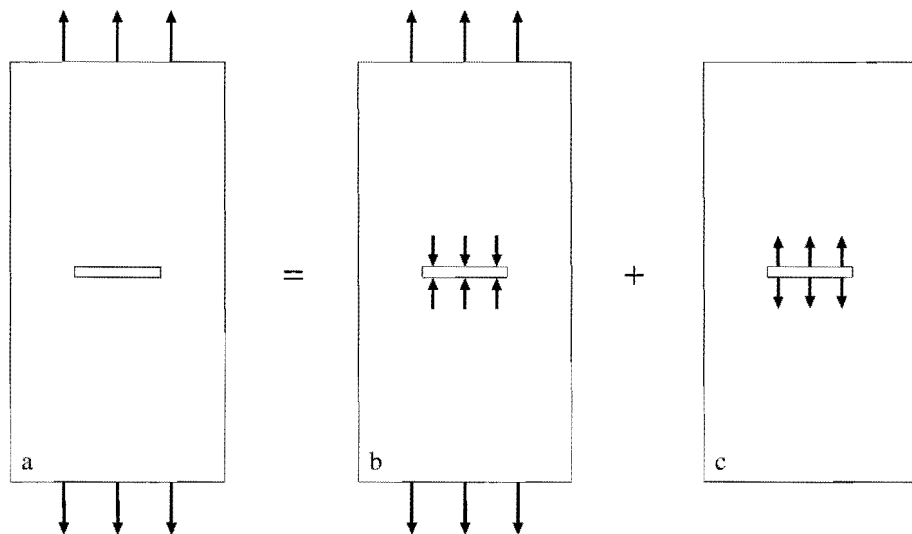


Figure 6.2: Principle of superposition: configuration (a) with external load and stress-free crack surfaces is equivalent to (b) with extra stresses closing the crack as if no crack were present plus (c) with opposite stresses applied to the crack surfaces but without external load.

This argumentation also reveals some limitations of the uncoupled fracture approach, regarding the dynamic effects. As described in Section 1.1, the stresses and the crack propagation are linked. Firstly, the fracture mechanism is based on the actual stress situation. This equally applies to dynamic and static fracture processes. Secondly, rapid crack propagation induces stress waves emanating from the moving crack tip and the continuous changes in the geometry lead to different relations between the stresses and the external loads. The latter effects, i.e. the disturbing influence of the propagating crack on the stress field, are neglected in the uncoupled fracture approach. The dynamic interaction is only incorporated in the universal functions of crack speed, $k_I(c)$ and $g_I(c)$, which relate the elastodynamic stress-intensity factor and energy release rate to their static equivalents; see Section 3.5. Because of the partial incorporation of the dynamic effects, the uncoupled approach can only produce reliable results for the initial stages of crack propagation but not over the full range of the fracture process. This is not considered as an obstructing problem, since the first and second phases of crack propagation are most important.

Finally, it is emphasised that the uncoupled fracture approach admits the analysis of only one crack at a time. It is possible to analyse multiple cracks by separate applications of the procedure described in Section 6.1. Every crack prediction starts with the initiation of a new crack, which may be chosen at a different position and with different length and/or direction. The ease-of-use of this method becomes apparent when we consider the great numerical effort involved in the dynamic finite-element computation compared to the relatively small amount of post-processing for uncoupled fracture simulations. The elaborate dynamic stress calculation for the intact geometry requires several hours of computing time, but this calculation is always performed since it is the simplest manner of gaining insight into the internal stress distributions. (To be more precise: it is the second-simplest manner after a static stress analysis for the vacuum load). The time needed to determine a crack path ranges from a few minutes to at most one hour, depending on the length of crack extension. The advantages are obvious: the elastodynamic stress data are already available and can be used again for each of the uncoupled fracture simulations, resulting in a large saving on computing time.

6.3 Application to standard tests

The uncoupled fracture approach has been embedded in the finite-element toolbox which has been developed in the MATLAB programming environment [57]. For the division of the geometries into finite elements we have utilised the mesh-generation program SEPMESH of the SEPRAN package [82]. The implementation of this toolbox has been performed in cooperation with J. Horsten.

Several tests have been carried out to investigate the accuracy and reliability of the uncoupled fracture approach. The first test concerns the possible dependences of the calculated crack patterns on the finite-element division. To this end, we study a square plate of size $l \times l$ and thickness $h = l/20$, being loaded by uniform tensile forces or uniform bending moments on two opposite sides; see Fig. 6.3. The plate is divided into $n \times n$ elements with one element over the thickness. We choose $n = 10$ and $n = 16$ and select the elements of Wilson and Taylor (see Section 7.5). These elements have eight degrees of freedom (eight corner nodes) and additional interpolation functions to ensure the correct bending stiffness. The elements have a slanted orientation such that the maximum slope of the element lines is equal to 0.10 or 0.20. This corresponds to inclination angles of 5.7° and 11.3° , respectively.

After the stress calculation a crack is initiated at the middle of one of the non-loaded sides. The initial crack length is equal to $\frac{3}{4}l_e$ with $l_e = l/n$ being the element width. The crack increments are chosen equal to $\frac{2}{3}l_e$. The fracture toughness is set equal to a small value to enforce crack growth. In Fig. 6.3 we show the crack patterns in the plate loaded by tensile forces for the various element divisions. Subsequent positions of the crack tip are marked by open circles. The prospective end point of the crack is at the middle of the other non-loaded side and is indicated by \times .

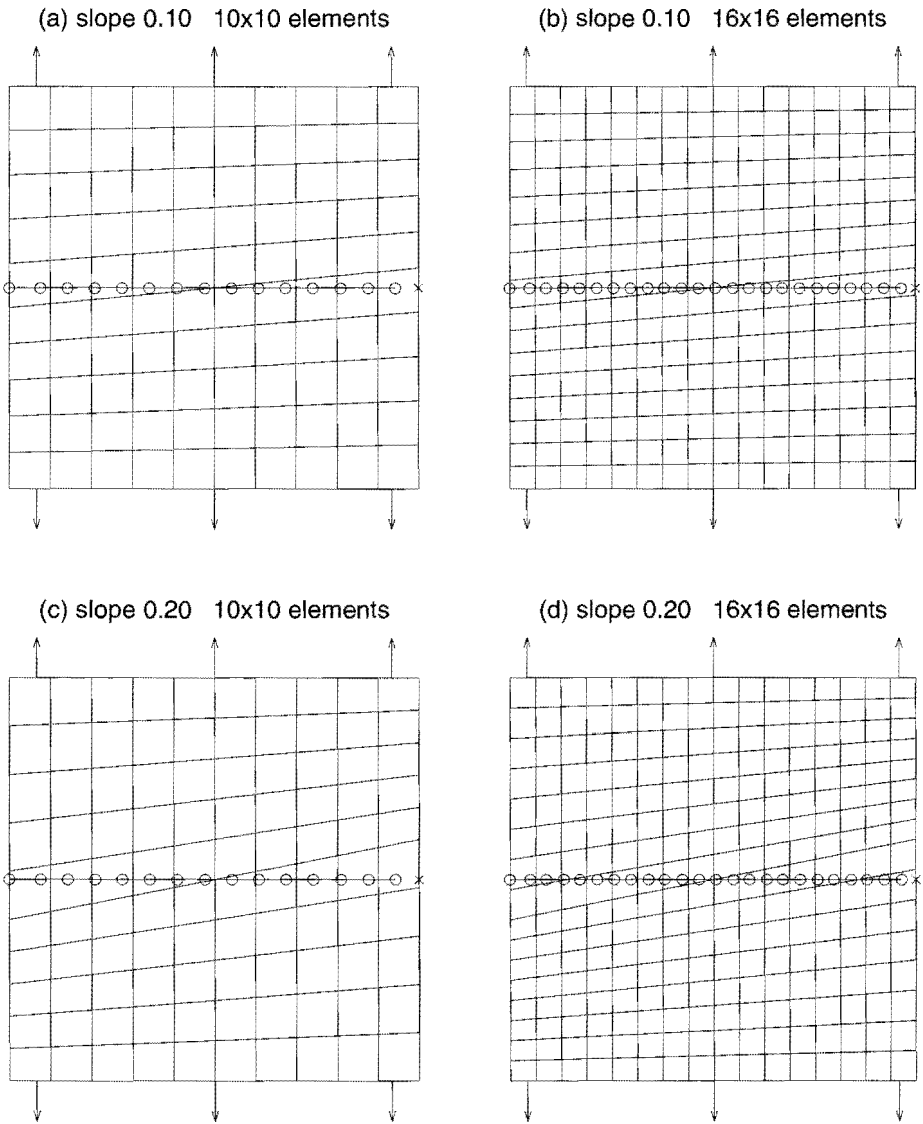


Figure 6.3: Crack patterns for a square plate loaded by uniform tensile forces, derived with the uncoupled fracture approach for various element divisions. Subsequent positions of crack tip are shown by \circ and prospective end point of crack by \times .

Because of the simple loading geometry, the fracture process can be described by the stress-intensity factor K_I for the tension problem and K_1 for the bending problem. A trivial solution is obtained with a uniform uniaxial stress state and with a straight crack path, despite the slanted element orientation. Similar results are obtained for the plate loaded by bending moments, while anti-clastic bending behaviour [90, Sec. 11]

is observed in the displacement solution due to the applied moment. Refinement of the element division and selection of other inclination angles of the mesh also produce straight crack patterns for both loading situations.

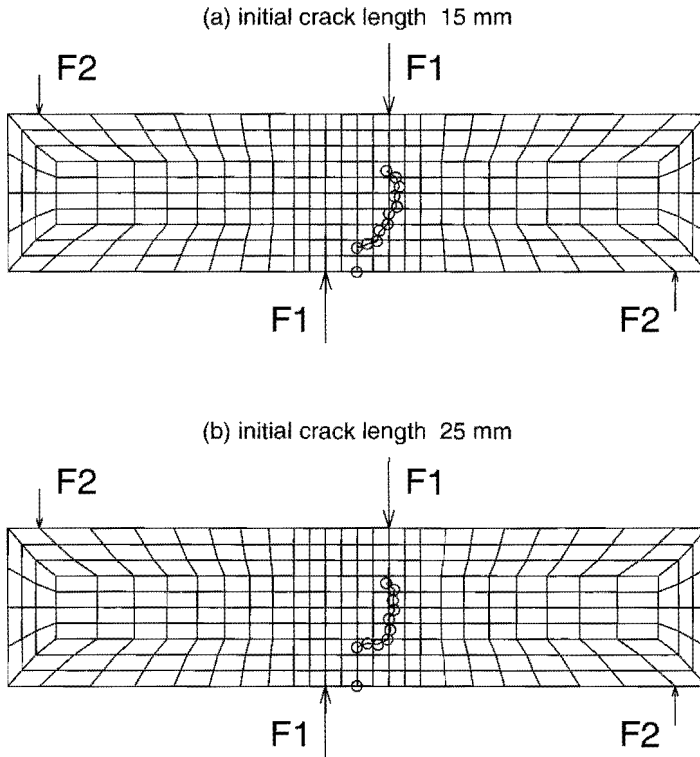


Figure 6.4: Crack patterns for a single-edge notched beam loaded under shear conditions, derived with the uncoupled fracture approach for different initial crack lengths. Subsequent positions of crack tip are shown by \circ .

Another test concerns curvilinear crack propagation under shear loads. A suitable test for the examination of shear effects was proposed by Iosipescu [39], namely a beam with a single-edge notch loaded by compressive forces applied at four different points; see Fig. 6.4. We shall adopt the dimensions of Feenstra [27, Sec. 5.1] and Schlangen [81, Sec. 3.3] and study a beam of length 440 mm, height 100 mm, and thickness 10 mm. The forces F_1 are applied at a distance of 20 mm from the plane of symmetry and the forces F_2 at a distance of 200 mm. Because of equilibrium, we have $F_1 = 10 F_2$. The beam is divided into a total of 264 elements with one element over the thickness and with refinement in the shear zone, where the elements are of size $10 \times 10 \times 10 \text{ mm}^3$. The Wilson-Taylor elements are used for a proper description of the in-plane bending behaviour.

A crack is initiated at the middle of the longest edge of the beam, in the plane of symmetry, with an initial length of (a) 15 mm or (b) 25 mm. The deformation of the beam is essentially two-dimensional and the fracture process can be described by a combination of the stress-intensity factors K_I and K_{II} . Due to the shear stresses, crack propagation will occur along a curved path with its end point on the opposite edge to the right of the point where the force F_1 is applied [81, Sec. 4.1]. The crack paths obtained with the uncoupled fracture approach as shown in Fig. 6.4 satisfy this requirement, although deviations occur near the points of crack arrest. The latter is caused by the compressive stresses near the position where the force F_1 is applied. Because of the limitations of the uncoupled approach, the crack path in this region has limited validity, but the first part is reliable.

The crack patterns of Fig. 6.4 agree with both the experimental and the numerical results of Schlangen [81, Secs. 4.1, 6.2]. The present results are better than those of Feenstra [27, Sec. 5.1], who obtained a straight crack path inclined at an angle of approximately 45° with respect to the edge. Single-edge notched beams of other dimensions have been studied by Lubliner, Oliver, Oller and Oñate [54] with the use of a plastic-damage model and by Rots [79] with smeared and discrete crack representations. It has been mentioned in [79] that the smeared rotating crack concept suffers from stress locking and only produces an agreeable crack path for the early stage of fracture, and that this path has been used as a predefined discrete crack in a subsequent fracture analysis resulting in the correct stress distributions. The crack patterns obtained in [27, 54, 79] satisfy the requirement for the end point of the crack path (to right of the point where F_1 is applied) and no particular differences with the present results or with those in [81] are observed.

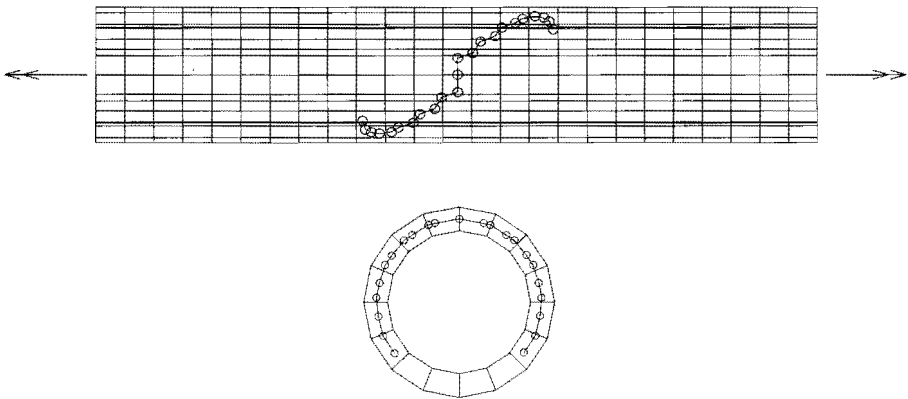


Figure 6.5: Crack patterns for a pipe loaded by torsional moments, derived with the uncoupled fracture approach. Initial crack is at middle of side view and at top of cross-sectional view. Subsequent positions of crack tip (into two directions) are shown by \circ .

A three-dimensional test problem with curvilinear crack propagation is the torsion of a hollow cylindrical pipe. The thickness of the pipe is 10 mm and the inner and outer radii are 30 and 40 mm. The pipe has a length of 400 mm and is loaded by torsional moments at both end surfaces. We choose a finite-element division with 25 elements in the axial direction, 16 elements in the circular cross section, and one element over the thickness. Again, we employ the elements of Wilson and Taylor with incompatible modes. Because of the torsional loading, a stress state with pure shear is obtained.

A crack is initiated in the middle cross section of the pipe and through the thickness. The initial crack length is $3/4$ of the element size in the circumferential direction (approx. 10.3 mm) and the crack increments are $2/3$ of the element size (approx. 9.1 mm). The early stage of fracture is dominated by mode II, but the crack deflects in such a fashion that the stress-intensity factor K_I gradually becomes more dominant while K_{II} decreases. Crack propagation is determined in two (symmetric) directions and the pipe with the calculated crack pattern is shown in Fig. 6.5. The calculation terminates when the expressions for the stress-intensity factors of Chapter 5 cannot be used anymore due to the curvature of the pipe surface. The results agree with the crack-path predictions based on the experimental work of Richard [78] and the theoretical work of Lakshminarayana and Murthy [48].

6.4 Application to television picture tubes

Consider the 36WS television picture tube with a screen of aspect ratio 16:9 (wide screen) and a diagonal of 914 mm (36 inches). One quadrant of the screen is shown in Figs. 6.6 and 6.7. We choose a Cartesian coordinate system with its origin in the center of the screen and the x - and y -directions along the major and minor axes of symmetry. The semi-length of these axes is 410 and 250 mm, respectively. The coordinates of the upper-right corner are $x = 400$ mm and $y = 225$ mm, from which we derive the aspect ratio $400/225 = 16/9$. The z -axis is along the central line of the tube running from the electron gun to the screen center over a distance of 521 mm. The material parameters for the screen and cone glasses are: Young's modulus $E = 67 \cdot 10^3$ N mm⁻², Poisson's ratio $\nu = 0.265$, and density $\rho = 2.7 \cdot 10^{-6}$ kg mm⁻³. In practice, the screen and the cone are made of different glasses. The differences in material parameters are so small, that it is expected that our choice of equal glasses will have no noticeable effect on the calculation of crack patterns.

The tube is subjected to a ball-drop impact. A steel ball with mass $m = 0.54$ kg and radius 25 mm is dropped onto the screen with a velocity $v = 5$ m s⁻¹ such that the impact energy equals $\frac{1}{2}mv^2 = 6.78$ Joule (5 ft.lb). We investigate the elastodynamic response of the television picture tube for two different impact positions, namely the so-called D-point and F-point, with coordinates $x_D = 149$ mm, $y_D = 80$ mm and $x_F = 333$ mm, $y_F = 169$ mm, respectively.

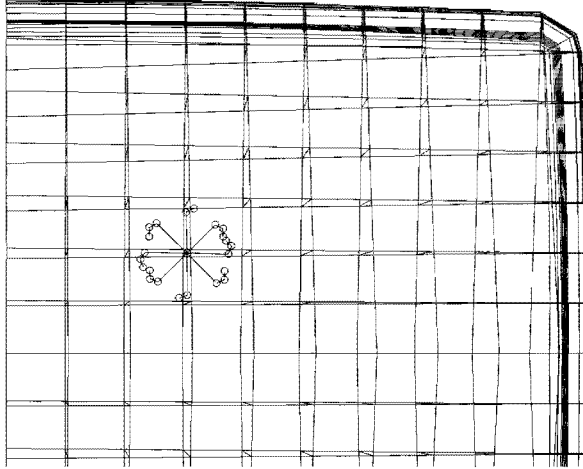
The entire tube, including cone and neck (see Fig. 1.1), is analysed with the use of the finite-element method. The screen is divided into 824 elements, the cone into 600

elements, and the neck into 44 elements, resulting in a total of 1468 volume elements and 2894 nodes. We again use the eight-node Wilson-Taylor elements (see Section 7.5) which have correct stiffness for bending and torsional deformation. In addition, 1468 four-node linear surface elements are used to apply the atmospheric pressure on the external boundary of the tube, while the internal tube boundary remains stress-free due to the vacuum. The extra forces on the outer edge of the screen introduced by the metal rimband, are modelled by 16 additional surface elements at each of the four corners of the screen. Four nodes and four extremely stiff elements are added for the modelling of the suspension of the tube at the screen corners. One node and three extra elements are used to describe the position of the steel ball, the Hertzian contact force [43, 51] during impact, and the indentation of the screen. It is emphasised that all four quadrants of the tube are analysed, although only the upper-right quadrant of the screen is shown in the figures.

The elastodynamic response of the television picture tube to the ball-drop impact is determined with an explicit time-integration based on the central-difference method; see Section 8.4 and Hughes [37, Sec. 9.1]. The investigated time interval reaches from the moment of impact until 2 ms thereafter and a time step $\Delta t = 0.141 \mu\text{s}$ is used for numerical stability. The crack patterns are calculated with a different, larger time step, namely $\Delta t_c = 2 \mu\text{s}$. This is permitted because the velocity of crack propagation is much less than the velocity of the stress waves. The crack-initiation locations are chosen in the nodal point which is nearest to the impact position (D- or F-point). The initial crack length is chosen equal to 30 mm and eight different initial crack directions are examined. The critical energy release rate is set to a small value such that crack propagation will occur as long as the stress-intensity factors K_I and K_{II} of the crack-opening modes give rise to tensile stresses at the crack tip. The results for impact at the D-point are shown in Fig. 6.6 and those for impact at the F-point in Fig. 6.7. It is obvious that application of the metal rimband has an enormous effect on the safety of the picture tubes. High compressive stresses are found in the regions around the impact positions. As a result, the stress-intensity factor K_I has a large negative value and this fact prevents any crack from extending further. On the other hand, television picture tubes without the metal rimband admit large-scale crack propagation and, therefore, cannot be regarded as safe tubes.

It is remarked that, due to the uncoupled approach, the crack patterns are only reliable for the early stage of fracture. Therefore, the examination of crack paths in the three other quadrants of the screen is not relevant. It is observed that a few cracks in Fig. 6.6(b) do not extend over larger distances. This can be explained by the stress state near the impact position: the preferred direction of crack extension is perpendicular to the direction of the largest principal stress. As a result, the cracks parallel to the direction of the largest principal stress do not propagate. Sometimes, a kink or a sharp curve is observed in an otherwise smooth crack path. This is often caused by a sudden change in the stress-intensity factors and may indicate a possible point of crack arrest. The curves in the crack paths near the edge of the screen, especially in Fig. 6.6(b), are due to the plane drawing of the three-dimensional geometry.

(a) television tube with rimband



(b) television tube without rimband

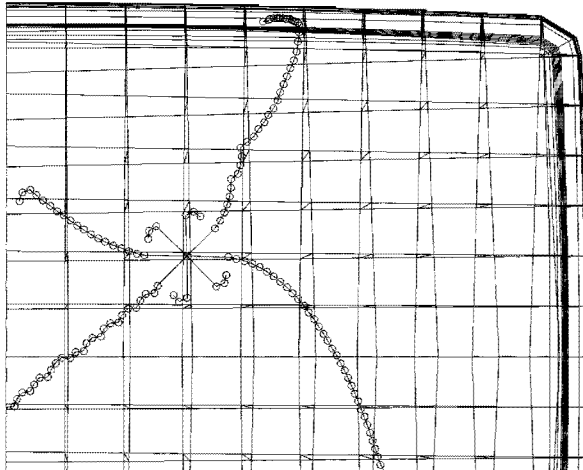
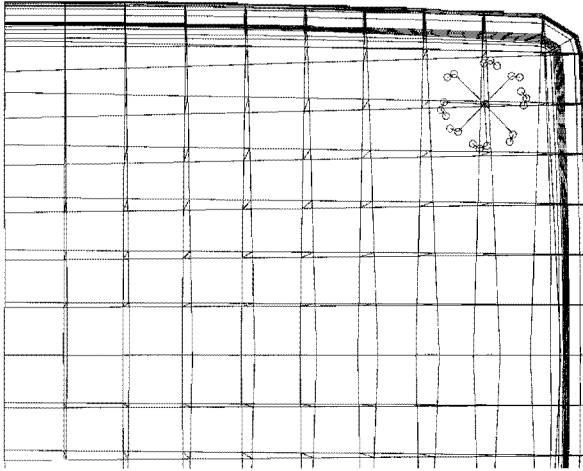


Figure 6.6: Crack patterns formed by impact on the D-point, derived with the uncoupled fracture approach, (a) with the rimband being applied and (b) without the rimband. Subsequent positions of crack tip are shown by \circ , initial crack length is 30 mm, and time step is $2 \mu\text{s}$.

(a) television tube with rimband



(b) television tube without rimband

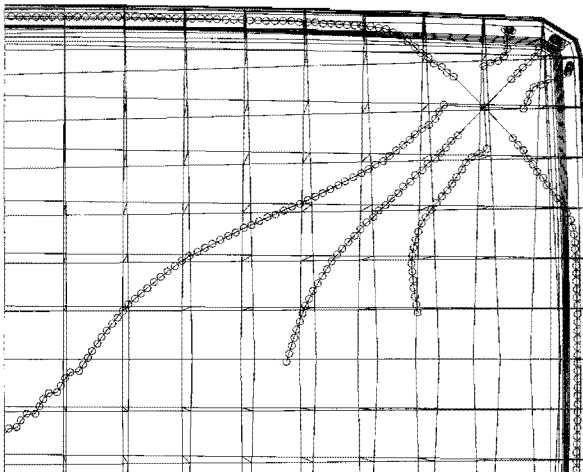


Figure 6.7: Crack patterns formed by impact on the F-point, derived with the uncoupled fracture approach, (a) with the rimband being applied and (b) without the rimband. Subsequent positions of crack tip are shown by \circ , initial crack length is 30 mm, and time step is $2 \mu\text{s}$.

6.5 Conclusions

Application of the uncoupled fracture approach to simple test problems shows that this method is not susceptible to variations in the finite-element division. This mesh independence concerns both the element size and the element orientation. In addition, application to Iosipescu's shear beam and to the torsion of a hollow pipe shows that correct crack-growth directions are derived for mixed-mode fracture. Based on these considerations, it is concluded that the uncoupled approach produces trustworthy results and that extension to more complicated problems is allowed. Because of the partial uncoupling between crack propagation and dynamic effects, the results are not fully reliable for prolonged crack propagation, especially near the point of crack arrest or final collapse. Nevertheless, good crack-path predictions are obtained for the early stage of fracture.

Concerning the impact tests for television picture tubes, good and useful results have been obtained with rather limited effort. Ball-drop tests with impact positions at the D- and F-points have been investigated for the 36WS tube with and without the metal rimband being applied to the screen edge. It is obvious from Figures 6.6 and 6.7 that application of the rimband is essential for the safety of the tube design. Television tubes with the rimband show no or little crack propagation, whereas large-scale crack propagation is observed in tubes without the rimband. Thus, we conclude that the safety of television picture tubes is significantly improved when the metal rimband is added to the tube construction.

This conclusion is confirmed by experimental knowledge. The ball-drop tests, which are performed by manufacturers of television picture tubes (or cathode-ray tubes) and by TV-set makers according to the international standards [12, 26, 64], reveal the following results for unsafe tubes. In the case of an impact at the D-point (in the central region of the screen), we mostly observe crack propagation from the impact position to the four screen corners. An impact at the F-point (near the upper-right corner of the screen) usually leads to crack propagation along the screen boundary or along the diagonal. No or little crack propagation occurs for safe tubes. These observations agree with the calculated crack patterns shown in Figs. 6.6 and 6.7. Because of the good agreement between the results of the tests and those of the simulations, we conclude that, despite its limitations, the uncoupled dynamic fracture approach is a powerful tool for the analysis of crack propagation in dynamically loaded structures.

Part III

Damage Mechanics



Chapter 7

The finite-element method

This part of the thesis discusses the hybrid fracture/damage approach which combines the benefits of fracture and damage mechanics in finite-element calculations. In order to understand the background and particular features, it is necessary to study several general aspects of finite-element techniques first. The present chapter deals with the basic concepts and indicates references for more detailed information. The books by Hughes [37], MacNeal [56], and Zienkiewicz [100] give an extensive explanation and are mentioned here with emphasis. The next chapter concentrates on the design of the hybrid fracture/damage approach and on its applications.

7.1 Concepts of the finite-element method

Consider a deformable body of linearly elastic material subjected to prescribed forces and displacements, as described by (2.1)–(2.5). For the application of finite elements a weak formulation must be derived. To this end, so-called test functions v_i are introduced, which are arbitrary, sufficiently smooth functions of the coordinates x , y , z and time t , satisfying the homogeneous boundary condition $v_i = 0$ on the part S_u of the boundary ∂V where the displacements are prescribed. The equation of motion (2.3) is multiplied by v_i and integrated over the domain V occupied by the elastic body. Application of the Gauss divergence theorem and the boundary condition (2.5) results in the problem below.

Weak formulation: determine displacements u_i , strains ε_{ij} , and stresses σ_{ij} as sufficiently smooth functions of x , y , z and t , satisfying the equations (2.1), (2.2), the boundary condition (2.4), and the equation (with summation over indices $i, j = x, y, z$)

$$\int_V (\rho \ddot{u}_i v_i + \sigma_{ij} v_{i,j}) \, dV = \int_V \bar{f}_i v_i \, dV + \int_{S_p} \bar{p}_i v_i \, dS \quad (7.1)$$

for all test functions v_i with the property $v_i = 0$ on S_u .

It is noted that the relation (2.3) and the condition (2.5) on S_p are automatically satisfied for the solution to the weak problem (7.1).

The next step towards a solution of the deformation problem is a discretisation of the elastic body and an approximation of the integrals in the weak formulation. Basically, this procedure consists of (i) dividing the domain occupied by the elastic body into small subdomains (the finite elements) and defining a set of interpolation points (the nodes), (ii) calculating the contribution of each element to the entire configuration and assembling these element contributions into large (global) matrices and vectors, and (iii) solving the matrix-vector equation by numerical techniques.

The interpolation of the displacements is based on the nodal displacements. Consider a finite element with m nodes, where node j ($1 \leq j \leq m$) with coordinate vector $\mathbf{x}_j = (x_j, y_j, z_j)$ undergoes a displacement $\mathbf{u}_j = (u_x^j, u_y^j, u_z^j)$. We introduce the interpolation or shape functions $N_j(\mathbf{x})$ associated with node j , having the property that $N_j(\mathbf{x}_i) = \delta_{ij}$. Some examples of finite elements and their shape functions are contained in the next sections. The displacements are interpolated and represented as

$$\mathbf{u}(\mathbf{x}) = \sum_{j=1}^m N_j(\mathbf{x}) \mathbf{u}_j = \left[\cdots \left| \begin{array}{ccc} N_j & 0 & 0 \\ 0 & N_j & 0 \\ 0 & 0 & N_j \end{array} \right| \cdots \right] \cdot \mathbf{u}^e = A^e(\mathbf{x}) \cdot \mathbf{u}^e, \quad (7.2)$$

where the element displacement vector is defined by $\mathbf{u}^e = [\cdots | u_x^j \ u_y^j \ u_z^j | \cdots]^T$ with the superscript T denoting the transpose. The test functions are interpolated in an analogous manner.

The strain and stress components are arranged into vectors of length 6. They are related to the nodal displacements according to the following equations:

$$\boldsymbol{\varepsilon}^e = \left[\begin{array}{c} \varepsilon_{xx} \\ \varepsilon_{yy} \\ \varepsilon_{zz} \\ 2\varepsilon_{yz} \\ 2\varepsilon_{xz} \\ 2\varepsilon_{xy} \end{array} \right] = \left[\cdots \left| \begin{array}{ccc} N_{j,x} & 0 & 0 \\ 0 & N_{j,y} & 0 \\ 0 & 0 & N_{j,z} \\ 0 & N_{j,z} & N_{j,y} \\ N_{j,z} & 0 & N_{j,x} \\ N_{j,y} & N_{j,x} & 0 \end{array} \right| \cdots \right] \cdot \mathbf{u}^e = B^e(\mathbf{x}) \cdot \mathbf{u}^e, \quad (7.3)$$

$$\boldsymbol{\sigma}^e = \left[\sigma_{xx} \ \sigma_{yy} \ \sigma_{zz} \ \middle| \ \sigma_{yz} \ \sigma_{xz} \ \sigma_{xy} \right]^T = D \cdot \boldsymbol{\varepsilon}^e = D \cdot B^e(\mathbf{x}) \cdot \mathbf{u}^e. \quad (7.4)$$

The elasticity matrix D for isotropic materials is related to the shear modulus G and Poisson's ratio ν . This matrix has size 6×6 and is equal to

$$D = \frac{2G}{1-2\nu} \left[\begin{array}{ccc|ccc} 1-\nu & \nu & \nu & 0 & 0 & 0 \\ \nu & 1-\nu & \nu & 0 & 0 & 0 \\ \nu & \nu & 1-\nu & 0 & 0 & 0 \\ \hline 0 & 0 & 0 & \frac{1}{2}(1-2\nu) & 0 & 0 \\ 0 & 0 & 0 & 0 & \frac{1}{2}(1-2\nu) & 0 \\ 0 & 0 & 0 & 0 & 0 & \frac{1}{2}(1-2\nu) \end{array} \right]. \quad (7.5)$$

After the discretisation, the displacements of all nodes in the finite-element mesh are arranged into one large vector \mathbf{U} , the global displacement vector. The integrals in

(7.1) are computed per element and the element contributions are assembled into large matrices and vectors on the global level; see Hughes [37, Chs. 2, 7]. We obtain

$$M \cdot \ddot{\mathbf{U}} + K \cdot \mathbf{U} = \mathbf{F}, \quad (7.6)$$

where M is the global mass matrix, K the global stiffness matrix, and \mathbf{F} the global right-hand side vector of the prescribed forces. The superposed dot indicates the time derivative. The global vector of the test functions is defined analogously to the global displacement vector and has been eliminated from the equation (7.6). With the symbol \mathcal{A} denoting the assembly process, the relations between the global quantities and the separate element contributions are

$$\mathbf{U} = \mathcal{A}\{\mathbf{u}^e\}, \quad (7.7)$$

$$\mathbf{F} = \mathcal{A}\{\mathbf{F}^e\}, \quad \mathbf{F}^e = \int_{V^e} (A^e)^T \mathbf{f} \, dV + \int_{S_p^e} (A^e)^T \mathbf{p} \, dS, \quad (7.8)$$

$$M = \mathcal{A}\{M^e\}, \quad M^e = \int_{V^e} \rho (A^e)^T A^e \, dV, \quad (7.9)$$

$$K = \mathcal{A}\{K^e\}, \quad K^e = \int_{V^e} (B^e)^T D B^e \, dV. \quad (7.10)$$

In these equations M^e is the element mass matrix and K^e is the element stiffness matrix. Furthermore, V^e is the volume of the element and S_p^e is the intersection of the element boundary with the part S_p of the outer boundary of the body where the tractions $\mathbf{p} = [\bar{p}_x \ \bar{p}_y \ \bar{p}_z]^T$ are prescribed. The vector $\mathbf{f} = [\bar{f}_x \ \bar{f}_y \ \bar{f}_z]^T$ represents the body forces per unit volume.

The integration is not performed analytically but by a numerical integration rule (for example a Gaussian quadrature rule) depending on the specific choice of element. The integrand is evaluated on a finite set of points (the integration points or Gauss points) and the resulting values are summed with an appropriate set of weights. The quadrature rules are designed in such a fashion that the integration is carried out exactly for a certain class of polynomials. This class includes the combinations of the shape functions in (7.9) and (7.10). Evidently, the accuracy of the results can be increased by a refinement of the element division. We may also use higher-order interpolation by creating elements with more nodes and, thus, with higher-order shape functions.

Summarising, we see that the basic ingredients in the definition of a finite element are: the nodes, the shape functions, the elasticity matrix, and the integration points. In the subsequent sections we shall discuss the standard elements and derive special elements by variations in the four basic ingredients.

7.2 Standard finite elements

The description of the finite-element method above applies to any type of element. At this point it becomes necessary to go into more detail and give specific definitions of

the elements to be used. A common three-dimensional element is the solid brick with eight nodes at the corners ($m = 8$); see Fig. 7.1(a). The local coordinates ξ , η , and ζ are in the interval $[-1, +1]$ and the physical coordinates $\mathbf{x} = (x, y, z)$ are related to the dimensionless local coordinates by

$$\mathbf{x} = \mathbf{x}(\boldsymbol{\xi}) = \sum_{j=1}^m N_j(\boldsymbol{\xi}) \mathbf{x}_j, \quad (7.11)$$

where $\boldsymbol{\xi} = (\xi, \eta, \zeta)$. Since the coordinate interpolation is completely analogous to the displacement interpolation (7.2), the element is called isoparametric. The local coordinates attain the values ± 1 at the corners such that $(\xi_1, \eta_1, \zeta_1) = (-1, -1, -1)$, $(\xi_2, \eta_2, \zeta_2) = (+1, -1, -1)$, \dots , $(\xi_8, \eta_8, \zeta_8) = (-1, -1, +1)$, etc. The shape functions for this element are linear in each of the coordinates and are given by

$$N_j(\xi, \eta, \zeta) = \frac{1}{8}(1 + \xi\xi_j)(1 + \eta\eta_j)(1 + \zeta\zeta_j), \quad (7.12)$$

for $j = 1, \dots, 8$ without automatic summation over j .

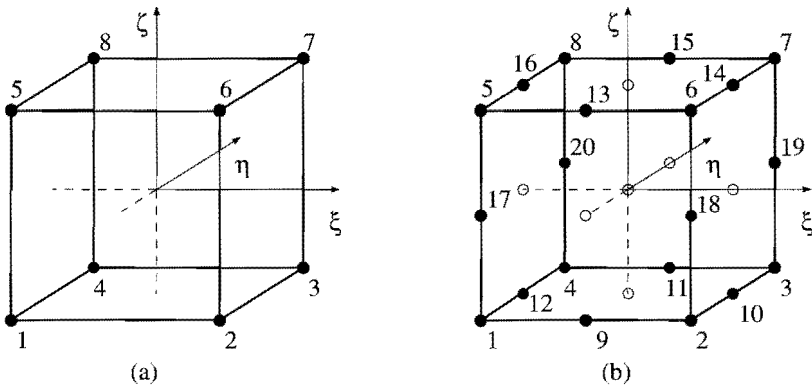


Figure 7.1: Standard brick elements in three dimensions with (a) linear and (b) quadratic shape functions.

The accuracy of approximation can be improved by the use of higher-order elements, for instance the twenty-node brick of Fig. 7.1(b), which has twelve additional nodes on each of the sides. The node-numbering sequence of Hughes [37] has been adopted. The local coordinates (ξ_j, η_j, ζ_j) of the side nodes are equal to $(0, \pm 1, \pm 1)$, $(\pm 1, 0, \pm 1)$, or $(\pm 1, \pm 1, 0)$. The interpolations of the displacements and the position are given by the relations (7.2) and (7.11) with $m = 20$. The shape functions are quadratic functions of the local coordinates and those of the corner nodes ($j = 1, \dots, 8$) are given by

$$N_j = \frac{1}{8}(1 + \xi\xi_j)(1 + \eta\eta_j)(1 + \zeta\zeta_j)(\xi\xi_j + \eta\eta_j + \zeta\zeta_j - 2), \quad (7.13)$$

while those of the side nodes are

$$N_j = \frac{1}{4}(1 - \xi^2)(1 + \eta\eta_j)(1 + \zeta\zeta_j), \quad \text{for } j = 9, 11, 13, 15, \quad (7.14)$$

$$N_j = \frac{1}{4}(1 - \eta^2)(1 + \xi\xi_j)(1 + \zeta\zeta_j), \quad \text{for } j = 10, 12, 14, 16, \quad (7.15)$$

$$N_j = \frac{1}{4}(1 - \zeta^2)(1 + \xi\xi_j)(1 + \eta\eta_j), \quad \text{for } j = 17, 18, 19, 20. \quad (7.16)$$

When the physical positions of nodes $j = 9, \dots, 20$ are in the middles of the sides, the coordinate interpolation of the quadratic element coincides with that of the linear element. This can be seen from substitution of the shape functions (7.13)–(7.16) into the equation (7.11) with the use of $\mathbf{x}_9 = \frac{1}{2}(\mathbf{x}_1 + \mathbf{x}_2)$, $\mathbf{x}_{10} = \frac{1}{2}(\mathbf{x}_2 + \mathbf{x}_3)$, etc. Other positions of the side nodes are discussed in the next section.

For increased accuracy we may add six extra nodes in the middles of the side planes and one extra node in the center of the cube. These nodes are indicated by open circles in Fig. 7.1(b) but are not numbered. A variable-node element with a total number of nodes between 8 and 27 has also been implemented. The definition of the shape functions becomes more complicated and can be found in the work of Hughes [37, Sec. 3.7]. Such finite elements are used in the hybrid approach, since they are of particular importance to form a transition between linear and quadratic elements.

The integrals (7.8)–(7.10) are calculated with the use of a numerical integration rule. This is performed by selection of a finite set of points $\boldsymbol{\xi}^g$ in which the integrand is evaluated plus a set of corresponding weights w^g , with $1 \leq g \leq n$ and n being the number of integration points. The Gaussian quadrature rule for the linear elements has $n = 2 \times 2 \times 2$ points with $\boldsymbol{\xi}^g = (\pm\sqrt{1/3}, \pm\sqrt{1/3}, \pm\sqrt{1/3})$ and weights $w^g = 1$. For the quadratic and variable-node elements we have $n = 3 \times 3 \times 3$ points, where the local coordinates ξ^g , η^g , and ζ^g are equal to 0 or $\pm\sqrt{3/5}$ with “uni-directional” weights 8/9 and 5/9, respectively. The weights w^g of the points $\boldsymbol{\xi}^g = (\xi^g, \eta^g, \zeta^g)$ are obtained by multiplication of the three uni-directional weights of each local coordinate; see [37, 56]. The integrals for the linear 8-node element can also be computed with the use of a special non-Gaussian 6-point rule and those for the quadratic 20-node brick with a non-Gaussian 14-point quadrature rule; see Irons [40]. The latter is utilised in the hybrid approach for reasons of efficiency, because the assembly time is roughly reduced by a factor 14/27.

7.3 Singular elements for fracture

For fracture-mechanics applications it is necessary that the contributions of the elements at the crack front (containing the stress singularity) are calculated correctly. This can be achieved by the design of special triangular finite elements, such that the derivatives of the shape functions contain the inverse square-root behaviour of the singular stresses; see Stern and Becker [86, 87]. Another and more appropriate

possibility is to adapt the quadratic elements in such a manner that an equal result is obtained; see Barsoum [3]. This technique is explained below.

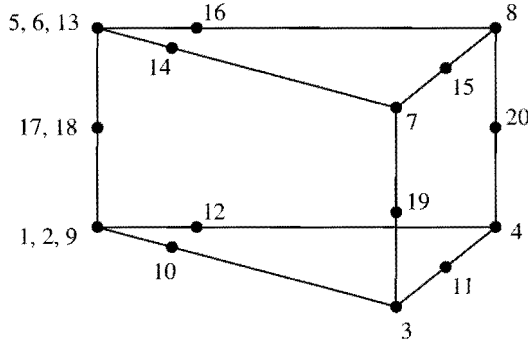


Figure 7.2: Collapsed singular element in three dimensions.

Consider a three-dimensional fracture problem which is analysed with the use of the quadratic twenty-node elements. The elements at the crack front are adapted as follows. Firstly, the corner nodes 1 and 2 and the side node 9 are chosen in the same physical position; and so are the nodes 5, 6, and 13; and the nodes 17 and 18. Secondly, the nodes 10, 12, 14, and 16 are shifted to the quarter points, while the nodes 11, 15, 19, and 20 remain mid-side nodes. Thus, one of the side planes collapses into a line (the crack front) and a triangular prismatic element is obtained; see Fig. 7.2. The physical coordinates of the nodes are given by

$$\mathbf{x}_1 = \mathbf{x}_2 = \mathbf{x}_9, \quad (7.17)$$

$$\mathbf{x}_5 = \mathbf{x}_6 = \mathbf{x}_{13}, \quad \mathbf{x}_{17} = \mathbf{x}_{18}, \quad (7.18)$$

$$\mathbf{x}_{10} = \frac{1}{4}(3\mathbf{x}_2 + \mathbf{x}_3), \quad \mathbf{x}_{11} = \frac{1}{2}(\mathbf{x}_3 + \mathbf{x}_4), \quad (7.19)$$

$$\mathbf{x}_{12} = \frac{1}{4}(3\mathbf{x}_1 + \mathbf{x}_4), \quad \mathbf{x}_{15} = \frac{1}{2}(\mathbf{x}_7 + \mathbf{x}_8), \quad (7.20)$$

$$\mathbf{x}_{14} = \frac{1}{4}(3\mathbf{x}_6 + \mathbf{x}_7), \quad \mathbf{x}_{19} = \frac{1}{2}(\mathbf{x}_3 + \mathbf{x}_7), \quad (7.21)$$

$$\mathbf{x}_{16} = \frac{1}{4}(3\mathbf{x}_5 + \mathbf{x}_8), \quad \mathbf{x}_{20} = \frac{1}{2}(\mathbf{x}_4 + \mathbf{x}_8). \quad (7.22)$$

The local coordinates (ξ_j, η_j, ζ_j) of the nodes remain unaltered, i.e., $(\pm 1, \pm 1, \pm 1)$ for the corner nodes and $(0, \pm 1, \pm 1)$, etc., for all side nodes. Substitution of (7.17)–(7.22) into (7.11) with shape functions (7.13)–(7.16) yields for the coordinate interpolation in the lower plane $\zeta = -1$ of the element:

$$\mathbf{x}(\boldsymbol{\xi}) = \left(1 - \frac{1}{4}(1 + \eta)^2\right) \mathbf{x}_1 + \frac{1}{4}(1 + \eta)^2 \left(\frac{1}{2}(1 + \xi)\mathbf{x}_3 + \frac{1}{2}(1 - \xi)\mathbf{x}_4\right). \quad (7.23)$$

We may consider $\rho = \frac{1}{4}(1 + \eta)^2$ as the dimensionless distance to the crack front. As a result, the parameter $1 + \eta$ equals $2\sqrt{\rho}$ and the shape functions (7.13)–(7.16) for the displacement interpolation depend on the square root of the (dimensionless) distance to the crack front. This precisely produces the desired inverse square-root behaviour for the near-tip stresses in fracture problems. The finite-element analysis proceeds in an identical manner as for the standard elements, with the same shape functions and the 14-point numerical integration rule.

7.4 Softening elements for damage

In damage-mechanics applications the stresses remain bounded, but a reduction of the material stiffness is imposed. The internal damage is represented as a change in the modulus of elasticity. Physically, this is interpreted as the formation of microcracks (see Figs. 1.3 and 7.3) and is accounted for in the constitutive relations between the stresses and the strains, like in (1.2). As a result, the finite elements as described in Section 7.2 can still be used; only the elasticity matrix D needs adjustment. The positions of the nodes, the shape functions, and the integration rules are not altered.

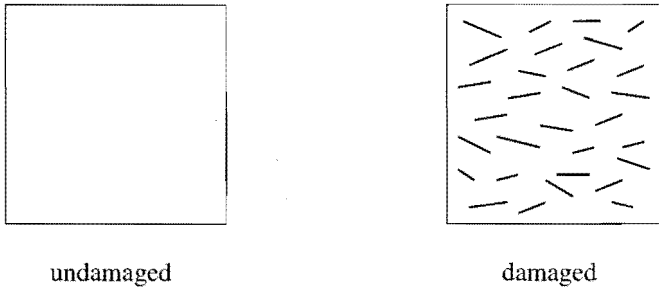


Figure 7.3: Orthotropic material damage.

There are two options. Firstly, the material damage may appear isotropically with an equal reduction of the elasticity modulus in all directions. This corresponds with a random distribution of microcracks as illustrated in Fig. 1.3. The new Young's modulus then equals $E_d = (1 - \mathcal{D})E$ with E being the original value and \mathcal{D} the damage parameter. Similarly, the shear modulus of the damaged material equals $G_d = (1 - \mathcal{D})G$, assuming the same Poisson ratio $\nu_d = \nu$. The elasticity matrix D is still given by (7.5) with E , G , and ν replaced by their reduced values E_d , G_d , and ν_d . The parameter \mathcal{D} is derived from the damage-evolution law (1.3) or any other relation or postulate for the damage increase. Strictly speaking, it is possible for Poisson's ratio to depend on the damage parameter. This is investigated in the Appendix C.2 on the basis of thermodynamics. We have chosen to let ν unchanged in the hybrid fracture/damage approach.

Secondly, anisotropic damage may occur with a preferred orientation of the micro-cracks; see Fig. 7.3. This requires a more detailed study of the damage effects, since the elasticity matrix (7.5) for isotropic material behaviour no longer applies. Namely, the stiffness in the direction perpendicular to the crack is reduced, while the stiffness parallel to the crack retains the original value of the undamaged material. The constitutive properties in this case can be described by an orthotropic material model; see Zienkiewicz [100]. General anisotropy implies that all six stress components depend on all six strain components. As a result, the D -matrix is a full symmetric matrix for which 21 elasticity constants are required. Orthotropy is a weaker form of anisotropy in the sense that the normal stresses do not depend on the shear strains and vice versa, such that the two blocks of zeros in (7.5) are retained. The orthotropic stress-strain relations are

$$\begin{bmatrix} \varepsilon_{xx} \\ \varepsilon_{yy} \\ \varepsilon_{zz} \end{bmatrix} = \begin{bmatrix} 1/E_x & -\nu_{xy}/E_y & -\nu_{xz}/E_z \\ -\nu_{yx}/E_x & 1/E_y & -\nu_{yz}/E_z \\ -\nu_{zx}/E_x & -\nu_{zy}/E_y & 1/E_z \end{bmatrix} \cdot \begin{bmatrix} \sigma_{xx} \\ \sigma_{yy} \\ \sigma_{zz} \end{bmatrix}, \quad (7.24)$$

for the normal strains and stresses, while for the shear strains and stresses we have

$$\begin{bmatrix} 2\varepsilon_{yz} \\ 2\varepsilon_{xz} \\ 2\varepsilon_{xy} \end{bmatrix} = \begin{bmatrix} 1/G_{yz} & 0 & 0 \\ 0 & 1/G_{xz} & 0 \\ 0 & 0 & 1/G_{xy} \end{bmatrix} \cdot \begin{bmatrix} \sigma_{yz} \\ \sigma_{xz} \\ \sigma_{xy} \end{bmatrix}. \quad (7.25)$$

The relation $\boldsymbol{\sigma} = D \cdot \boldsymbol{\varepsilon}$ is derived by inversion. The moduli of elasticity (E -moduli) represent the tensile stiffness in the three coordinate directions, while the G -moduli are related to shear deformation in the three coordinate planes. The parameter ν_{xy} is the contraction ratio in the x -direction when the material is subjected to tension along the y -axis, whereas ν_{yx} is defined reversely; see Fig. 7.4. The twelve elasticity parameters are not independent, because the matrix in (7.24) must be symmetric (symmetry of the stress-strain relations). The six contraction ratios are related to the E -moduli via three equations, but the shear moduli do not depend on the other constants. Thus, nine independent parameters remain. The conditions for symmetry are

$$E_x \nu_{xy} = E_y \nu_{yx}, \quad (7.26)$$

$$E_y \nu_{yz} = E_z \nu_{zy}, \quad (7.27)$$

$$E_z \nu_{zx} = E_x \nu_{xz}. \quad (7.28)$$

The presence of a crack implies a local reduction of the stiffness in only one direction. Let us assume the crack surfaces are in the xy -plane, such that material softening occurs along the z -axis and the stiffness in the two other directions remains unaltered. Using this convention, we have $E_x = E_y = E$ and $E_z = (1 - \mathcal{D})E$, where \mathcal{D} is the damage parameter and E the Young's modulus of the undamaged material. The contraction ratios are determined by the relations (7.26)–(7.28) and extra conditions for thermodynamic admissibility. From a generalisation of the results of Appendix C.3, we obtain $\nu_{xy} = \nu_{yx} = \nu_{zx} = \nu_{zy} = \nu$ and $\nu_{xz} = \nu_{yz} = (1 - \mathcal{D})\nu$ with ν being the

Poisson's ratio of the undamaged material. Since there is no preference between the x - and y -directions, the shear modulus G_{xy} is given by $G = E/2(1 + \nu)$, as for isotropic materials. The other two shear moduli G_{xz} and G_{yz} are equal and are in principle independent of the other parameters. We may for example take the arithmetic, geometric, or harmonic mean of the values G_{xy} and $E_z/2(1 + \nu_{xz})$. It is shown in Appendix C.3 by a thermodynamic analysis that either choice is acceptable.

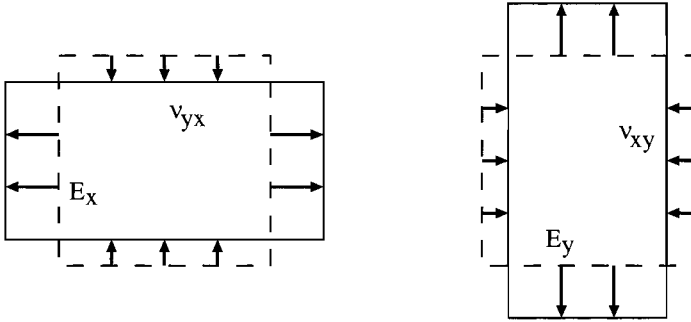


Figure 7.4: Contraction of orthotropic material.

7.5 Improved elements for bending and torsion

The standard linear elements of Section 7.2 have certain complications which do not occur for the quadratic elements. The resistance against bending and torsion appears to be too large for the linear elements. This over-stiffness is often referred to as “locking” and can be alleviated by an adaptation of the numerical integration rules or by the introduction of extra shape functions; see Hughes [37, Ch. 4] and MacNeal [56]. These options are explained below.

7.5.1 Elements with under-integration

The standard linear element exhibits an over-stiff behaviour in situations of bending or torsional deformation. The excessive rigidity can be relieved by application of a 1-point quadrature rule in the center of the element, namely $\xi^g = (0, 0, 0)$ and $w^g = 8$ with $g = n = 1$. Since the element stiffness matrix becomes rank deficient owing to this under-integration rule, extra deformation modes or so-called spurious modes may occur. In Fig. 7.5 we illustrate the two spurious modes of planar deformation. The spurious mode of type (a) is characterised by

$$u = A \xi \eta, \quad v = 0, \quad (7.29)$$

while the one of type (b) is characterised by

$$u = 0, \quad v = B \xi \eta. \quad (7.30)$$

When the under-integration rule is applied to the linear element in three dimensions, the rank deficiency of the stiffness matrix will give rise to twelve spurious modes; see Kosloff and Frazier [47]. These modes correspond to bending and torsion and are characterised by linear combinations of the following functions

$$u, v, w = \{ \xi \eta, \eta \zeta, \zeta \xi, \xi \eta \zeta \}. \quad (7.31)$$

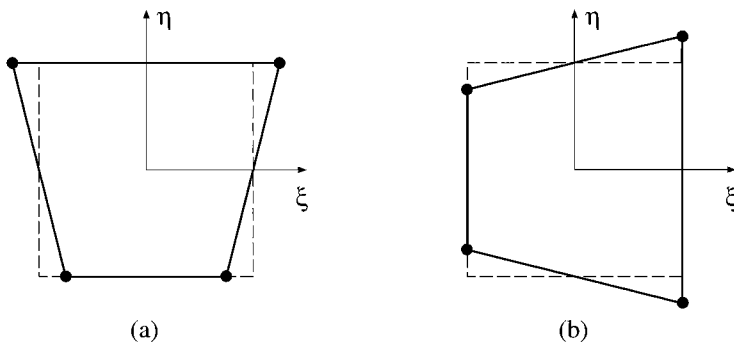


Figure 7.5: Spurious modes in planar deformation.

Because of the 1-point central integration rule, the elastic energy associated with the spurious modes (7.29)–(7.31) cannot be perceived. Therefore, these modes are sometimes referred to as zero-energy modes. In other words, the element has become too weak instead of over-stiff. This problem can be solved by adding extra stiffness terms to the under-integrated element in order to suppress undesired bending; see [37, 47, 56] and Belytschko, Ong, Liu and Kennedy [7]. This procedure works well for the four-node linear element in two dimensions and has the extra advantage of a mass matrix with small band width, such that the lumping method [37, Sec. 7.3.2] can be applied. In addition, there is the benefit that the assembly process is shortened roughly by a factor four, since one instead of four integration points is used.

It was argued in [47] that all spurious modes of the three-dimensional element could also be suppressed by adding extra stiffness. However, this appeared impossible to achieve, especially in the case of perpendicular loading of plates; see Subsection 7.5.3. All attempts to add extra stiffness against spurious torsion modes resulted in over-stiff behaviour. It remains unclear whether correct suppression of all spurious modes is possible for the three-dimensional element with complete under-integration.

An alternative approach to circumvent the occurrence of spurious modes is to apply selective under-integration; see MacNeal [56, Ch. 7]. This method consists of (i) an

evaluation of the normal strains ε_{xx} , ε_{yy} , and ε_{zz} on the usual $2 \times 2 \times 2$ Gauss points, which provides appropriate stiffness to suppress possible spurious modes, and (ii) an under-integration rule for the shear strains ε_{yz} , ε_{zx} , and ε_{xy} , which eliminates the over-stiff bending behaviour. There exist two possibilities. Either all shear strains are evaluated on one Gauss point in the center of the element or each of the shear strains is evaluated on a different set of axial Gauss points, namely two points on the x -axis for ε_{yz} , two points on the y -axis for ε_{zx} , and two points on the z -axis for ε_{xy} .

This description applies to rectangular brick elements with the element sides parallel to the global coordinate axes. Since the element stiffness matrix must be invariant to global coordinate transformations, it is necessary to express the strain components in a local Cartesian coordinate system with its axes approximately parallel to the element sides for elements with arbitrary orientation and shape. For two-dimensional elements, for example, we may take the bisectors of the angles between the element diagonals as the local coordinate directions; see MacNeal [55]. In this procedure, it is favourable that the shape of the element resembles a rectangular brick.

The element stiffness matrix is still rank deficient for both selective under-integration rules, but the degree of deficiency is less than for complete under-integration. So, a smaller number of spurious modes can be present. Suppression of these modes is not always applied, but when no disturbances are observed, the element with selective under-integration can be used safely.

7.5.2 Elements with incompatible modes

A third method to tackle the locking problems of the standard linear element is the incorporation of bending modes in the element description. Taylor, Beresford and Wilson [89] and Wilson, Taylor, Doherty and Ghaboussi [96] suggested the introduction of extra shape functions which correspond to the bending modes; see also Hughes [37, Sec. 4.7] and MacNeal [56, Ch. 8]. Since bending deformation involves linear stresses in the element, the displacements necessarily have quadratic variations. This behaviour cannot be produced by the usual shape functions (7.12) and, thus, the additional shape functions are chosen as

$$P_1(\xi) = \frac{1}{2}(1 - \xi^2), \quad (7.32)$$

$$P_2(\xi) = \frac{1}{2}(1 - \eta^2). \quad (7.33)$$

$$P_3(\xi) = \frac{1}{2}(1 - \zeta^2). \quad (7.34)$$

Because of the quadratic behaviour, the continuity of the displacements over the element boundaries cannot be guaranteed. For this reason, the bending modes are also called incompatible modes. Two of such modes are shown in Fig. 7.6. The

displacement interpolation becomes different from (7.2) and now reads

$$\mathbf{u}(\mathbf{x}) = \sum_{j=1}^8 N_j(\mathbf{x}) \mathbf{u}_j + \sum_{j=1}^3 P_j(\mathbf{x}) \mathbf{q}_j = A^e(\mathbf{x}) \cdot \mathbf{u}^e + Q^e(\mathbf{x}) \cdot \mathbf{q}^e, \quad (7.35)$$

where \mathbf{u}^e contains the nodal displacements and $\mathbf{q}^e = [\dots | q_x^j \ q_y^j \ q_z^j | \dots]^T$ the bending parameters $\mathbf{q}_j = (q_x^j, q_y^j, q_z^j)$ with $j = 1, 2, 3$. The matrix Q^e with the extra shape functions is defined analogously to the matrix A^e in (7.2), namely by

$$Q^e(\mathbf{x}) = \left[\begin{array}{ccc|ccc} \dots & P_j & 0 & 0 & \dots & \dots \\ \dots & 0 & P_j & 0 & \dots & \dots \\ \dots & 0 & 0 & P_j & \dots & \dots \end{array} \right]. \quad (7.36)$$

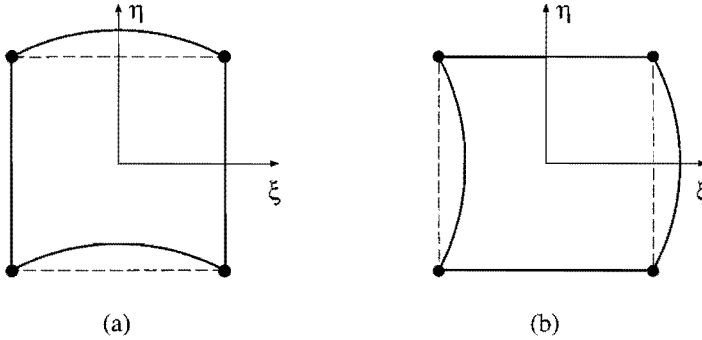


Figure 7.6: Incompatible modes corresponding to in-plane bending.

The bending parameters \mathbf{q}^e are eliminated at the element level by means of static condensation [37, 47, 56]. This procedure is explained with the calculation of the element stiffness matrix. We proceed in the usual manner and differentiate the matrices A^e and Q^e , which yields B^e of (7.3) and the new gradient matrix

$$G^e(\mathbf{x}) = \left[\begin{array}{ccc|ccc} \dots & P_{j,x} & 0 & 0 & \dots & \dots \\ \dots & 0 & P_{j,y} & 0 & \dots & \dots \\ \dots & 0 & 0 & P_{j,z} & \dots & \dots \\ \dots & 0 & P_{j,z} & P_{j,y} & \dots & \dots \\ \dots & P_{j,z} & 0 & P_{j,x} & \dots & \dots \\ \dots & P_{j,y} & P_{j,x} & 0 & \dots & \dots \end{array} \right]. \quad (7.37)$$

The element stiffness matrix is calculated in a manner similar to (7.10)² by Gaussian integration on the usual $2 \times 2 \times 2$ points. The matrix is partitioned into four parts

$$\begin{aligned} K_{uu} &= \int_{V^e} (B^e)^T D B^e dV, & K_{uq} &= \int_{V^e} (B^e)^T D G^e dV, \\ K_{qu} &= \int_{V^e} (G^e)^T D B^e dV, & K_{qq} &= \int_{V^e} (G^e)^T D G^e dV. \end{aligned} \quad (7.38)$$

It is noted that the submatrix K_{uu} coincides with the original stiffness matrix K^e , that K_{qq} is symmetric and stems entirely from the extra shape functions, and that the “mixed” submatrices satisfy $K_{uq} = K_{qu}^T$.

Next, we calculate the vector \mathbf{H}^e of the internal forces associated with the nodal displacements \mathbf{u}^e , while we assume that the internal forces associated with the bending parameters \mathbf{q}^e vanish. Therefore, we must solve the following equation for a single element

$$\begin{bmatrix} K_{uu} & K_{uq} \\ K_{qu} & K_{qq} \end{bmatrix} \cdot \begin{bmatrix} \mathbf{u}^e \\ \mathbf{q}^e \end{bmatrix} = \begin{bmatrix} \mathbf{H}^e \\ \mathbf{0} \end{bmatrix}. \quad (7.39)$$

Solving the second part for \mathbf{q}^e and substituting the result into the first part, we obtain an expression for the internal-force vector, namely

$$\mathbf{H}^e = \tilde{K}^e \cdot \mathbf{u}^e = \left(K_{uu} - K_{uq} K_{qq}^{-1} K_{qu} \right) \cdot \mathbf{u}^e. \quad (7.40)$$

The new element stiffness matrix \tilde{K}^e must be substituted for K^e in the relation (7.10)¹. Since there is no rank deficiency, no spurious modes will occur. The resulting element (in three dimensions) is an eight-node element with correct stiffness for bending and torsion and an eight-point integration rule. The assembly process, however, requires a little more time than for the standard linear element. It was shown by Kosloff and Frazier [47] that the incompatible-modes element of Wilson and Taylor [89, 96] is equivalent to the under-integrated element with additional stiffness for rectangular element geometries.

7.5.3 Comparison of improved elements

Various solutions have been suggested to improve the behaviour of the standard linear elements for bending and torsional deformation. We shall now examine the improved three-dimensional eight-node elements and apply them to the deformation of a thin flat plate subject to a perpendicular load. This is a suitable test problem, because the deformation involves bending in two directions, while the elements which are not on the axes of symmetry also undergo torsional deformation. A comparison is made with the results for quadratic 20-node elements, which serve as a benchmark because of the high accuracy of the deflection and the correct behaviour of the bending stresses over the plate thickness.

Consider a flat plate of length $2a$, width $2b$ and thickness h with $a/b = 1.40$ and $h/b = 0.10$. The plate consists of a linearly elastic material with Young’s modulus E and Poisson’s ratio $\nu = 0.30$. The Cartesian coordinates are chosen along the axes of symmetry such that $-a \leq x \leq a$, $-b \leq y \leq b$, and $-h/2 \leq z \leq h/2$. The plate is clamped (built-in) at the edges and loaded by a uniformly distributed load $hf_z(x, y) = -q$ per unit area. The load and the deflection of the plate are directed vertically downwards. Because of the symmetry, only one quarter of the plate is analysed. A division in 10×7 elements is used with one element over the thickness. Typical results for the deflection of the plate are shown in Fig. 7.7. Similar results

are obtained from investigations of plates having other dimensions. The deflection is scaled with respect to the theoretical value in the center of the plate, which is derived from Timoshenko and Woinowsky-Krieger [90, Sec. 44], viz.

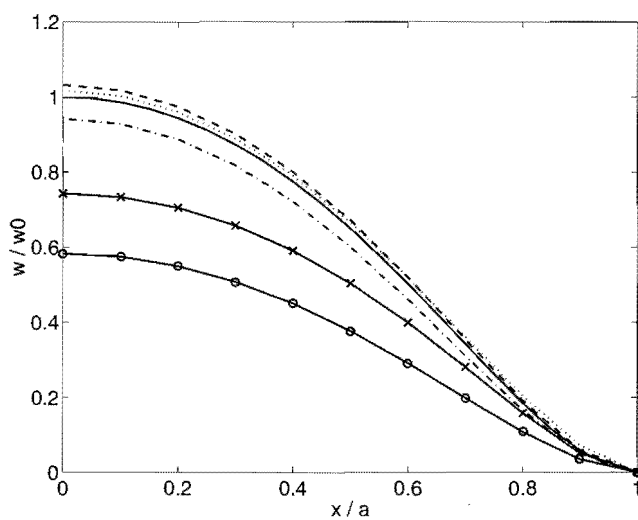
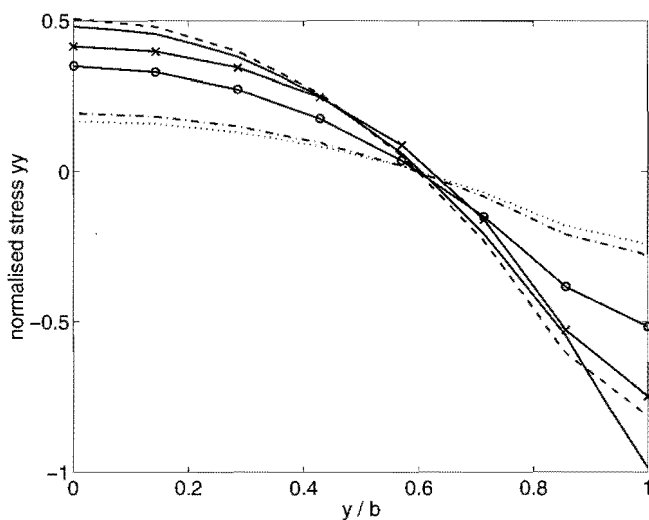
$$w_0 = w(0, 0) = -0.362 \frac{qb^4}{Eh^3} . \quad (7.41)$$

The results in Fig. 7.7 clearly show the over-stiffness of the standard linear element: the deflection is too small in comparison with the solution with the standard quadratic element. The element with complete under-integration also fails to produce the correct deflection. Since numerical investigations with this element of uni-directional bending of beams and plates did exhibit correct bending behaviour, we conclude that the locking must be caused by torsion and by bending in two directions. Therefore, the completely under-integrated element as proposed by Kosloff and Frazier [47] is not suitable for three-dimensional problems of combined bending and torsion. The elements with selective under-integration and the elements with incompatible modes produce acceptable results for the deflection. The deflection for the elements with selective central under-integration seems to be less accurate than for the elements with selective axial under-integration, but results for other plate dimensions do not confirm this assertion.

For a full appreciation of the various elements, we also compare the bending stresses which are evaluated at nodal points instead of integration points. The results of the quadratic 20-node element are again used as a benchmark. In Fig. 7.8 we show the stress σ_{yy} along the y -axis and in the lower plane of the plate, which is tensile (positive) in the center of the plate and compressive (negative) near the edges. The stresses are scaled with the theoretical maximum value, which occurs at the center of the longest edge ($y = b$) in the upper plane of the plate [90, Sec. 44]. This maximum value equals

$$\sigma_0 = \sigma_{yy}(0, b, h/2) = 1.74 \frac{qb^2}{h^2} . \quad (7.42)$$

It is observed that the incompatible-modes element yields more accurate stress results than the elements with selective under-integration. Similar results are obtained from investigations of plates having other dimensions. For these reasons, the element with incompatible bending modes as proposed by Wilson and Taylor [89, 96] is chosen for further use. This element has the advantage over quadratic elements that only eight integration points are used instead of 14 or 27, which leads to a considerable reduction in computing time for the assembly process. In addition, the mass matrix has smaller band width than for the quadratic element, which is advantageous in time-dependent problems; see Section 8.4.

Figure 7.7: Deflection of the plate along x -axis.Figure 7.8: Stress in lower plane of the plate along y -axis.

- standard quadratic elements,
- standard linear elements,
- × elements with complete under-integration,
- · - elements with selective central under-integration,
- elements with selective axial under-integration,
- - - elements with incompatible modes.

Chapter 8

Hybrid fracture/damage approach

Both fracture mechanics and continuum damage mechanics possess specific advantages and disadvantages in finite-element applications. Whereas numerical methods based on fracture mechanics require frequent adaptations of the finite-element mesh and use moving-element techniques (see Nishioka, Murakami and Takemoto [68]), methods based on damage mechanics suffer from sensitivity with respect to the element division and from damage localisation. These features have been mentioned briefly in Section 1.3 and are discussed more thoroughly in Section 8.1 below.

Because of these complications, a combination of fracture and damage mechanics within the context of the finite-element method is investigated, which leads to the so-called hybrid fracture/damage approach [36]. The various elements of Chapter 7 are joined together in such a manner that it can be expected that the disadvantages of both theories are eliminated, while their specific benefits are retained. It is noted that the hybrid fracture/damage approach, similar to the uncoupled dynamic fracture approach of Chapter 6, only applies to thin plate-like structures with slight curvature.

The work contained in the present chapter has been carried out in cooperation with J. Horsten. Our joint study of theoretical aspects (fracture, damage, dynamics) and of numerical methods (finite elements, time-step algorithms) has resulted in this new approach towards crack-growth simulation.

8.1 Discussion of continuum damage mechanics

In order to avoid continuous mesh adaptation in finite-element analyses of dynamic fracture, we study the possibilities of using continuum damage mechanics. Only one fixed finite-element division is sufficient, because failure is represented by material degradation (softening) instead of by discrete cracks. In addition to the displacements, strains, and stresses, which are used to describe the deformation, we introduce an extra parameter \mathcal{D} to represent the internal material damage; see Chaboche [14, 15, 16], Kachanov [44] and Lemaitre [50]. This parameter must satisfy a damage-evolution

equation, e.g. (1.3), which relates the damage increase to the stress state and the actual damage level. It is possible to introduce a set of damage parameters (for example \mathcal{D}_x , \mathcal{D}_y , \mathcal{D}_z), when the material damage occurs in some anisotropic fashion. For the topic of damage tensors and principal damage directions, we refer to Chaboche [14] and Murakami [61]. We restrict ourselves in this section to isotropic damage represented by one parameter \mathcal{D} .

Consider a deformable body consisting of an isotropic, softening material and subjected to uniaxial loading. The Young's modulus pertaining to the original, undamaged material is denoted by E . The constitutive relation between the stress σ and the strain ε is given by the equation (1.2) in a simple one-dimensional form, namely $\sigma = (1 - \mathcal{D})E\varepsilon$. A characteristic feature of the stress-strain relation is that the stress can decrease with increasing strain (softening behaviour). This behaviour is illustrated in Fig. 8.1(a) for ductile failure. A sudden decrease of the stress occurs for brittle failure; see Fig. 8.1(b). Generally, the damage parameter \mathcal{D} on time t will depend on the history of the strain. For a certain class of materials (including glass), the maximum strain level in time serves as a threshold for the damage increase and we may write $\mathcal{D} = \mathcal{D}(\varepsilon_{max})$ with $\varepsilon_{max} = \max\{\varepsilon(t_1) | t_1 \leq t\}$; see Chaboche [16] and Paas [72]. The relation between \mathcal{D} and ε_{max} is usually postulated on the basis of experimental results. For situations where both the strain and the damage are increasing, we may write $\mathcal{D} = \mathcal{D}(\varepsilon)$ because $\varepsilon_{max} = \varepsilon(t)$.

We distinguish several moduli of elasticity, depending on the loading situation; see Fig. 8.1(a). Firstly, when the body is loaded or unloaded and damage does not occur ($\mathcal{D} = 0$), we use the original Young's modulus E and we have the stress-strain relation $\sigma = E\varepsilon$. Secondly, when the body is being loaded and the damage increases ($\dot{\varepsilon} > 0$ and $\dot{\mathcal{D}} > 0$), we use the tangent modulus $E_t = d\sigma/d\varepsilon$. In this case, we employ the stress-strain relation in incremental form: $\dot{\sigma} = E_t \dot{\varepsilon}$, where the superposed dot indicates the time derivative. The tangent modulus is derived from (1.2) as

$$E_t = \frac{d\sigma}{d\varepsilon} = \left((1 - \mathcal{D}) - \mathcal{D}'(\varepsilon)\varepsilon \right) E, \quad (8.1)$$

where the prime ' indicates differentiation with respect to ε . Thirdly, when damage has occurred and the body is being unloaded ($\dot{\varepsilon} < 0$), we use the effective modulus $E_d = (1 - \mathcal{D})E$ of the damaged material. The stress-strain relation in this case is given by $\sigma = E_d \varepsilon$. This relation is also valid for renewed loading as long as damage increase does not occur ($\varepsilon(t) < \varepsilon_{max}$).

From Fig. 8.1(a) and the equation (8.1) it is clear, that when the damage \mathcal{D} and the damage increase $\mathcal{D}'(\varepsilon)$ are too large, the tangent modulus becomes negative. Note that $0 \leq \mathcal{D} \leq 1$, so that a large value for \mathcal{D} only cannot lead to $E_t < 0$. A negative tangent modulus has a severe implication for the one-dimensional dilatational wave speed, which is defined in analogy with (2.10) and (2.19) by

$$c_d^2 = \frac{E_t}{\rho}, \quad (8.2)$$

where ρ is the density of the material. When the tangent modulus E_t is negative, this wave speed becomes imaginary. The corresponding wave equation (2.8) in one

dimension changes from hyperbolic to elliptic and the mathematical problem becomes ill-posed. The ill-posedness leads to several peculiar phenomena, which have been described by many authors (see e.g. de Borst, Sluys, Mühlhaus and Pamin [10], Lasry and Belytschko [49], and Sluys [85]).

These phenomena are usually referred to as “localisation”. For example, the energy dissipation associated with the damage increase takes place in an infinitesimally small band (which can be compared to a discrete crack). The strain in this band attains an infinite value, while the strain in the surrounding material decreases (unloading). This localisation effect becomes more apparent in finite-element applications, where the amount of dissipated energy becomes dependent on the size of the softening elements; see Crisfield [20] and Hegen [33, Sec. 6.2]. Furthermore, a strong dependence on element size is observed in the global material response and in the peak value of the strain after localisation; see Sluys [85, Sec. 3.5].

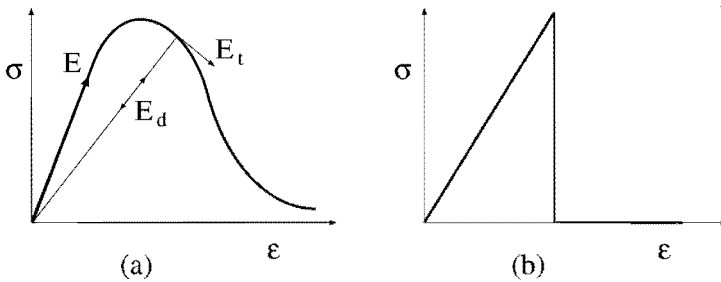


Figure 8.1: Stress-strain relations with softening material behaviour for (a) ductile failure and (b) brittle failure.

An overview of localisation problems is given in [10, 49, 85] and also in the work of Bažant and Cedolin [4, Ch. 13] on the basis of stability theory. Various solutions have been suggested by many authors. These suggestions include:

1. localisation limiters based on kinematic relations like (2.1), where the strains also depend on higher-order derivatives of the displacements [49];
2. rate-dependent constitutive behaviour, where the stresses not only depend on the strain but also on the strain rate (see [85, Ch. 4] and Needleman [65]);
3. non-local constitutive behaviour, where the stresses depend on strain values averaged over a small neighbourhood (see Pijaudier-Cabot and Bažant [73] and Vosbeek [91]); which suggestion includes gradient-dependent behaviour, where the stresses depend on the strain and the Laplacian of the strain (see [10] and [85, Ch. 5]);
4. finite elements with embedded localisation zones (see Belytschko, Fish and Engelmann [5] and Ortiz, Leroy and Needleman [71]), which zones correspond to the small bands mentioned above, where the energy dissipation takes place;

5. element-free Galerkin methods, where the displacements are interpolated on a set of nodes with the use of special weight functions instead of finite elements (see Belytschko, Lu and Gu [6, 53]). The latter two suggestions have been critically reviewed by Hegen [33].

8.2 Description of the hybrid approach

The hybrid fracture/damage approach is based on the finite-element method plus a time-stepping algorithm and utilises the various elements introduced in Chapter 7. The positive features of fracture mechanics (accuracy) and of continuum damage mechanics (flexibility) are combined in a manner described below; see also Horsten and van Vroonhoven [36]. For the sake of simplicity, we start with two-dimensional problems. The extension to three dimensions is discussed in the next section.

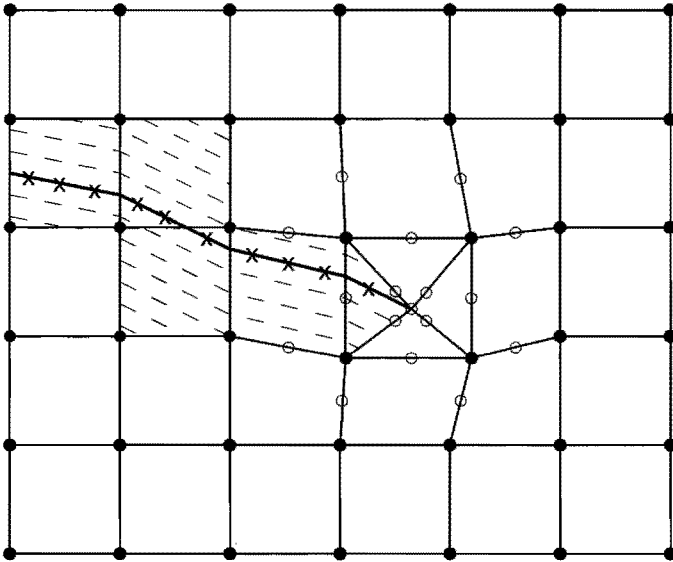


Figure 8.2: Configuration of the super-element and surrounding elements. The crack is shown as a thick solid line and anisotropic damage is displayed by dashed lines. Subsequent positions of the crack tip are marked as \times , while original nodes are indicated by \bullet and extra nodes by \circ .

As in any finite-element analysis, we start with the division of the elastic body into subdomains. We choose the improved four-node Wilson-Taylor elements of Section 7.5, because of their adjusted stiffness and the correct in-plane bending behaviour. These elements give a far better performance than the standard linear elements of Section 7.2. The singular elements for fracture-mechanics applications (see Section 7.3) are used at the crack tip by replacing the original quadrangular element with four

collapsed (triangular) elements. This is shown in Fig. 8.2. One crack-tip node, twelve mid-side nodes, and four quarter-point nodes are added, which are marked by \circ in the figure. This ensures the accurate calculation of the singular stresses in the vicinity of the crack tip. Since the displacements in the singular elements are interpolated by quadratic shape functions on the sides opposite to the crack tip, it is necessary to apply variable-node elements (see Section 7.2 and Hughes [37, Sec. 3.7]) as a transition from the singular elements to the linear four-node elements. The combination of the four crack-tip elements and the eight surrounding transitional elements is called the “super-element”. The positions of the four corner nodes of the quadrangular element which is replaced with the singular elements, are adjusted in such a manner that the four triangular elements have approximately the same size. The super-element translates with the crack tip and its structure is similar to the mesh patterns which are used in moving-element procedures based on fracture mechanics [68].

The extra nodes are also called “slave” nodes as opposed to the original “master” nodes of the elements. The slave nodes are eliminated at the super-element level by means of static condensation in a manner similar to (7.39)–(7.40). It is noted that the (four) corner nodes of the singular crack-tip elements are also eliminated and must be regarded as slave nodes too. We proceed with the calculation of the internal force vector \mathbf{H}_m associated with the displacements \mathbf{u}_m of the twelve master nodes of the super-element. Since the twenty-one slave nodes lie in the interior of the super-element, we assume that they do not convey nodal forces to the surrounding elements. Denoting the displacements of the slave nodes by \mathbf{u}_s , we obtain the following system of equations

$$\begin{bmatrix} K_{mm} & K_{ms} \\ K_{sm} & K_{ss} \end{bmatrix} \cdot \begin{bmatrix} \mathbf{u}_m \\ \mathbf{u}_s \end{bmatrix} = \begin{bmatrix} \mathbf{H}_m \\ \mathbf{0} \end{bmatrix}, \quad (8.3)$$

where the contributions of the twelve elements in the super-element to the stiffness matrix have been partitioned with respect to the master and slave nodes. We solve the second part of (8.3) for \mathbf{u}_s and substitute the result into the first part. This yields an expression for the “condensed” stiffness matrix K^{se} of the super-element:

$$\mathbf{H}_m = K^{se} \cdot \mathbf{u}_m = \left(K_{mm} - K_{ms} K_{ss}^{-1} K_{sm} \right) \cdot \mathbf{u}_m. \quad (8.4)$$

A smaller type of super-element has also been considered. This super-element has two basic configurations. When the crack tip is in the middle of an element, that element is split into four triangular crack-tip elements as in Fig. 8.2. When the crack tip is near a corner, four elements are split into eight triangles. Quarter-point nodes are added to incorporate the singular stress behaviour, but the extra mid-side nodes are not included. As a result, the triangular elements resemble the element of Fig. 7.2(a) but without node number 7, and the displacements on the sides opposite to the crack tip show linear behaviour. This smaller super-element did not provide sufficient accuracy near the crack tip and has therefore been rejected. On the other hand, super-elements of larger size were regarded as too expensive because of the increase in computational effort and in assembly time.

The position of the crack tip is marked as \times in Fig. 8.2 and is calculated at every time step by a procedure explained below. Although the crack path is determined

in a precise manner, it is not approximated by a piece-wise linear curve as described in Section 6.1 for the uncoupled dynamic fracture approach. Instead, we employ the idea of a “smeared” crack but in a different form than developed by Rots [79]. The smeared-crack concept provides extra flexibility in comparison with fracture-mechanics procedures, which require element splitting or nodal-release techniques. The softening elements for damage applications (see Section 7.4) are used for the “tail” of the crack. The damage parameter is chosen equal to $\mathcal{D} = 0.999$, resulting in a reduction of Young’s modulus by a factor 1000. When an orthotropic damage model is applied, only the elasticity modulus in the direction perpendicular to the crack path is reduced.

In the construction of the super-element it is assumed that a crack is present. At an intermediate stage of the fracture simulation, we take the crack from the previous time step, which is extended with the calculated crack increment by (6.1). At the beginning of the computation, we must initiate a crack. The precise location, length, and direction of the initial crack may be chosen arbitrarily. There is one restriction: the element containing the crack tip must be surrounded by eight elements, so that we can create a super-element as in Fig. 8.2. For television tubes, it is customary to initiate the crack at the impact position, but this is also possible at the cone, the neck, or at the extra scratches in the case of a missile test. We emphasise that only one crack can be analysed at a time. For multiple cracks the hybrid approach must be applied repeatedly.

We now turn to the selection of a crack-propagation criterion. Because of the softening zone, the influence of the crack is smeared out over a band of finite width. The global behaviour of the damaged zone resembles the response of a physical discrete crack. At the more detailed local level, however, there will occur deviations between discrete and smeared cracks. For example, the distributions of the stresses and the strains near the crack path will be less accurate in the case of a smeared crack. As a result, we cannot calculate the stress-intensity factors directly from the stresses in the material by using the integral expressions of Chapter 5.

It is more suitable to employ a criterion which focuses at the crack-tip region where fracture mechanics is applied, such as the fracture criterion based on the J -integrals; see Section 3.4. The contour for evaluation of the integrals J_k ($k = 1, 2$) is chosen inside the super-element around the crack tip as illustrated in Fig. 8.3 by a thick solid line. Five Gaussian integration points are used for each segment of the contour, which assures sufficient accuracy. The contour passes through the elements which surround the four singular elements, but the contour does not intersect with the damaged element. Namely, the J -integrals must be evaluated for contours around the crack tip from one crack flank to the other and the crack in the hybrid fracture/damage approach is represented by a damage zone. Thus, the integration is performed from one side of the damaged element through the undamaged material to the other side. Excluding the line segment through the damaged element can also be justified by an argument from damage mechanics. We have the relation $\sigma = (1 - \mathcal{D})E\varepsilon$, in which the damage \mathcal{D} increases and the stress σ remains constant due to equilibrium. As a result, there is a large augmentation of the strain ε in the damaged element and the

corresponding line segment would yield an unrealistic, large disturbing contribution to the J -integrals.

The J -integrals are used to determine the crack-growth speed and direction. The calculated values J_1 and J_2 are interpreted as components of the vector $\mathbf{J} = J_k \mathbf{e}_k$ with the unit vectors \mathbf{e}_1 and \mathbf{e}_2 being tangential and perpendicular to the crack path, respectively. The direction of crack growth is given by (3.65), so that we may say that the vector \mathbf{J} starts at the crack tip and points into the direction of crack growth. The crack-growth speed is derived from the dynamic fracture criterion (3.74) rather than from the static fracture criterion (3.64). We substitute $(J_1^2 + J_2^2)^{\frac{1}{2}}$ for $\mathcal{G}(\sigma, a, 0)$ in (3.74) and calculate the crack-growth speed c with the use of (3.71), assuming that the critical energy release rate \mathcal{G}_c is known. The crack increment is calculated according to the relation (6.1), where the time step Δt is subject to some restrictions which are discussed in the sequel.

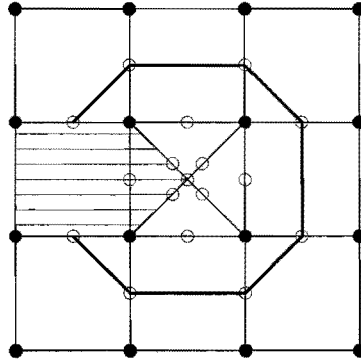


Figure 8.3: Contour inside super-element for calculation of J -integrals.

Alternatively, the direction of crack propagation can be decided on the basis of an engineering criterion: in the direction perpendicular to the largest principal stress. To this end, the stresses are calculated in all integration points of the three undamaged singular elements in the super-element. The stress components are projected onto the crack tip and averaged. The direction perpendicular to the largest principal stress in that point is taken as the crack-growth direction. The crack-growth speed c is set equal to the Rayleigh wave speed c_R . This rough estimate is acceptable, because we mostly observe large values for the energy release rate in cases of dynamic fracture. Thus, the precise crack-growth speed will not differ much from c_R (see (3.71) and (3.74)). When the largest principal stress is negative, we put $c = 0$ and crack arrest occurs. The accuracy is increased when the stresses are also evaluated in the five undamaged quadrangular elements adjacent to the three undamaged singular elements. The elements at the left-hand side of the super-element in Fig. 8.2 are thus excluded. We shall also use this refined stress criterion and compare the results with those of the J -integral criterion. Although this procedure has no profound basis in

fracture mechanics, it appears to work rather well with reasonably accurate results for the crack patterns.

8.3 Extension to three dimensions

Since here the main area of application of the hybrid fracture/damage approach is the analysis of television tubes, we focus our attention on thin plate-like structures. The division into finite elements is chosen to have only one element over the thickness of the plate, i.e. the glass screen or cone. The curvature of the surfaces and the variations in the thickness are thus incorporated, while the computing time for the assembly process is limited. Using more elements over the thickness would increase the assembly time proportionally. Moreover, because of the expected dominance of bending moments, the internal stresses will vary approximately linearly over the plate thickness such that a further mesh refinement in the thickness direction is not necessary.

A restriction of this choice is that the crack front must be taken as a straight line perpendicular to the middle plane of the plate (screen). In practice, the precise shape of the crack front may attain a general form in the cross section of the plate, due to different crack-growth speeds in the upper and lower planes of the plate. These effects are not incorporated and can only be calculated by tedious and time-consuming computations with more than one element over the thickness. Concerning the geometry, we may certainly speak of a three-dimensional analysis, but regarding the fracture behaviour we employ the simplification of a crack which is uniform over the thickness with a straight crack front, similar to the crack model described in Section 6.1.

The two-dimensional super-element has been described in the preceding section and its extension to three dimensions is straightforward. We choose the eight-node brick elements of Wilson and Taylor with improved bending behaviour (see Section 7.5) to divide the tube geometry into subdomains. The element mesh in the crack-tip region is adapted in such a manner that the upper and lower planes of the plate have similar geometries as in Fig. 8.2. Five extra mid-side nodes are added in the middle plane of the plate on the lines connecting the corner nodes in the lower and upper planes of the singular elements, including an extra node on the crack front. Thus, the crack-tip elements resemble the element of Fig. 7.2(b) and the surrounding elements have a variable number of nodes. The crack is represented by damaged elements with reduced stiffness.

The crack-propagation criteria are applied analogously in three dimensions. The J -integrals which are needed for the energy criterion, are evaluated by integration over a cylinder surrounding the crack tip. The cross sections of the cylinder in the upper and lower planes of the plate coincide with the contour depicted in Fig. 8.3. Because of the integration over the plate thickness, the influences of both tension and bending are incorporated in the crack-propagation criterion. We define the vector $\mathbf{J} = J_k \mathbf{e}_k$ (with summation over $k = 1, 2$), where the unit vectors \mathbf{e}_1 and \mathbf{e}_2 are tangential and perpendicular to the crack and $\mathbf{e}_3 = \mathbf{e}_1 \times \mathbf{e}_2$ is perpendicular to the plate. The vector \mathbf{J} is in the tangent plane of the plate and determines the direction of crack

propagation by (3.65). If the vector \mathbf{J} has a non-zero component normal to the plate due to numerical round-off errors, we use its projection onto the tangent plane. The crack-growth speed is determined in the same manner as in Section 8.2.

The alternative criterion based on the largest principal stress is also applied. The stresses are calculated in the Gaussian integration points of eight elements of the super-element, analogous to the two-dimensional stress criterion. This automatically includes the thickness effects and the bending moments. After projection to the crack front and subsequent averaging of the stresses, the direction of crack growth is determined as perpendicular to the largest resulting principal stress and in the tangent plane.

8.4 Time-step algorithm

8.4.1 Explicit method

The discretisation of the elastic body into subdomains (finite elements) has led to the matrix-vector equation (7.6) for the vector $\mathbf{U} = \mathbf{U}(t)$ of nodal displacements, which contains a second-order derivative $\ddot{\mathbf{U}}$ with respect to time t . For the numerical solution of this differential equation, we discretise the time interval in finite steps of size Δt and calculate the approximate solution on times $t_n = n \Delta t$ (for $n = 0, 1, 2, \dots$). We choose an explicit method based on central differences. The first-order and second-order derivatives $\dot{\mathbf{U}}$ and $\ddot{\mathbf{U}}$ of the global displacement vector are then approximated by

$$\dot{\mathbf{U}}(t_{n+\frac{1}{2}}) = \frac{\mathbf{U}(t_{n+1}) - \mathbf{U}(t_n)}{\Delta t}, \quad (8.5)$$

$$\ddot{\mathbf{U}}(t_n) = \frac{\dot{\mathbf{U}}(t_{n+\frac{1}{2}}) - \dot{\mathbf{U}}(t_{n-\frac{1}{2}})}{\Delta t} = \frac{\mathbf{U}(t_{n+1}) - 2\mathbf{U}(t_n) + \mathbf{U}(t_{n-1}))}{(\Delta t)^2}. \quad (8.6)$$

The truncation errors in these approximations are of the order $O((\Delta t)^2)$ for time steps $\Delta t \rightarrow 0$, so that the central-difference method is second-order accurate; see Hughes [37, Sec. 9.1]. Substitution of (8.5)–(8.6) into the equation (7.6) produces the following time-step algorithm. Firstly, the acceleration vector is calculated:

$$M \cdot \ddot{\mathbf{U}}(t_n) = \mathbf{F}(t_n) - K \cdot \mathbf{U}(t_n). \quad (8.7)$$

Secondly, the velocity and displacement vectors are updated:

$$\dot{\mathbf{U}}(t_{n+\frac{1}{2}}) = \dot{\mathbf{U}}(t_{n-\frac{1}{2}}) + \Delta t \ddot{\mathbf{U}}(t_n), \quad (8.8)$$

$$\mathbf{U}(t_{n+1}) = \mathbf{U}(t_n) + \Delta t \dot{\mathbf{U}}(t_{n+\frac{1}{2}}). \quad (8.9)$$

The initial values of the displacements and the velocities are assumed to be known: $\mathbf{U}(t_0) = \mathbf{U}_0$ and $\dot{\mathbf{U}}(t_{0-\frac{1}{2}}) = \dot{\mathbf{U}}_0$.

Since the truncation errors in (8.5)–(8.6) vanish in the limit as $\Delta t \rightarrow 0$, the time-step algorithm (8.7)–(8.9) is consistent with the differential equation (7.6). Convergence of the solution is now assured when the algorithm satisfies the stability condition, i.e., when small numerical errors are not amplified by taking one time step [37, Sec. 8.2]. The central-difference method is conditionally stable, which means that the time step must be sufficiently small. We have the following restriction (see [37, Sec. 9.1]):

$$\Delta t \leq \Delta t_{max} = \frac{2}{\omega_h}, \quad (8.10)$$

where ω_h is the maximum natural frequency of vibration of the system represented by the equation (7.6). This frequency depends on the element size h and the dilatational wave speed c_d and is proportional to c_d/h . The proportionality constant is related to the element type. From the relation (8.10) with $\omega_h \sim c_d/h$, it is clear that the time step Δt is restricted by the smallest element in the entire mesh.

We can make an estimate of the maximum allowed time step in the hybrid approach. Let us denote the maximum allowed time step for a four-node quadrangular element of size $h_q \times h_q$ by Δt_q . This time step is calculated from an eigenvalue analysis of the element mass and stiffness matrices. The critical time step in the hybrid approach is determined by the smallest side of the singular crack-tip elements, which has length $h_s = h_q/\sqrt{2}$. Hughes [37, Sec. 9.2] has derived estimates of the critical time step for several elements, e.g., $\Delta t_{max2} = h/c_d$ for the two-node linear rod element, and $\Delta t_{max3} = h/\sqrt{6} c_d$ for the three-node quadratic rod element. These estimates are extended to the two-dimensional elements in the following manner. We regard the one-dimensional estimate Δt_{max2} with $h = h_q$ as a relative measure for the quadrangular elements and Δt_{max3} with $h = h_s$ as a relative measure for the singular elements. Next, we assume that the maximum allowed time step in the hybrid approach is equal to the critical time step Δt_q of the quadrangular elements, multiplied by the ratio $\Delta t_{max3}/\Delta t_{max2}$. Thus, we obtain

$$\Delta t \leq \frac{h_s \Delta t_q}{h_q \sqrt{6}} = \frac{\Delta t_q}{2\sqrt{3}} = 0.289 \Delta t_q. \quad (8.11)$$

Since this is a rough estimate, we shall adopt $\Delta t = 0.25 \Delta t_q$ to assure the stability of the time-step algorithm. We note that this time step is of the same order as the time step for elastodynamic stress calculations (without fracture), but is much smaller than the time step Δt_c in (6.1) for the crack-path calculations in the uncoupled approach. As a result, the hybrid fracture/damage approach will require more time steps than the uncoupled approach.

The solution for the acceleration vector $\ddot{\mathbf{U}}(t_n)$ in (8.7) is immediately obtained, when the mass matrix M is a diagonal matrix. Since this is generally not the case, we apply a so-called “lumping” technique [37, Sec. 7.3.2]. The original mass matrix is replaced with the lumped matrix \tilde{M} , which is defined by placing the row sums on the diagonal:

$$\tilde{M}_{ij} = \begin{cases} \sum_k M_{ik}, & \text{if } i = j, \\ 0, & \text{otherwise.} \end{cases} \quad (8.12)$$

The errors introduced by the lumping of the mass matrix cancel the errors from the time discretisation [37, Sec. 9.1.4]. Since \tilde{M} is a diagonal matrix, the solution of the equation (8.7) does not require the inversion of a matrix. Thus, the combination of the central-difference method and the lumping technique provides an accurate and efficient time-step algorithm. The disadvantage of conditional stability is not regarded as a major drawback, because the time step should not be too large in view of the truncation errors involved in (8.5)–(8.6) and thus also in (8.8)–(8.9).

8.4.2 Implicit method

The number of time steps can be decreased by the use of an implicit method for the time-step algorithm, because such methods are mostly unconditionally stable and do not impose a restriction on the time step. We choose the implicit α -method of Hilber, Hughes and Taylor [34], which is also described by Hughes [37, Sec. 9.3]. When the displacements, the velocities, and the accelerations at time t_n are known, these quantities at time t_{n+1} are calculated from the equations

$$M \cdot \ddot{\mathbf{U}}(t_{n+1}) + (1 + \alpha) K \cdot \mathbf{U}(t_{n+1}) - \alpha K \cdot \mathbf{U}(t_n) = \mathbf{F}(t_{n+1} + \alpha \Delta t), \quad (8.13)$$

$$\mathbf{U}(t_{n+1}) = \mathbf{U}(t_n) + \Delta t \dot{\mathbf{U}}(t_n) + \frac{1}{2}(\Delta t)^2 \left[(1 - 2\beta) \ddot{\mathbf{U}}(t_n) + 2\beta \ddot{\mathbf{U}}(t_{n+1}) \right], \quad (8.14)$$

$$\dot{\mathbf{U}}(t_{n+1}) = \dot{\mathbf{U}}(t_n) + \Delta t \left[(1 - \gamma) \ddot{\mathbf{U}}(t_n) + \gamma \ddot{\mathbf{U}}(t_{n+1}) \right]. \quad (8.15)$$

The α -method is unconditionally stable and second-order accurate when $\alpha \in [-1/3, 0]$, $\beta = (1 - \alpha)^2/4$, and $\gamma = (1 - 2\alpha)/2$. It is assumed that the initial values of the displacements and the velocities, $\mathbf{U}(t_0) = \mathbf{U}_0$ and $\dot{\mathbf{U}}(t_0) = \dot{\mathbf{U}}_0$, are known. The initial acceleration $\ddot{\mathbf{U}}(t_0)$ may be determined from (8.13) with $\alpha = 0$ and $n = -1$.

The disadvantage of implicit methods is that a system of equations needs to be solved at every time step. The acceleration vector $\ddot{\mathbf{U}}(t_{n+1})$ is calculated, for example, by substitution of (8.14) into (8.13) and by solution of the matrix-vector equation with the use of direct or iterative techniques; see Golub and Van Loan [29]. This requires extra computing time and diminishes the gain of fewer time steps. Moreover, the mass matrix M and the stiffness matrix K depend on the time step because of the crack propagation and of the moving super-element. Consequently, the system of equations to be solved in the case of an implicit method is different at every time step. For these reasons, the implicit α -method can be less suitable for systems with a large number of degrees of freedom and with crack propagation.

8.5 Application to standard tests

The hybrid fracture/damage approach has been implemented in the MATLAB programming environment [57]. The generation of finite-element meshes has been done with the use of the program SEPMESH of the SEPRAN package [82]. Several tests have been performed to investigate the accuracy and reliability of this approach and to compare the results obtained with the two crack-propagation criteria based on the J -integrals and on the largest principal stress. The tests are the same as in Section 6.3.

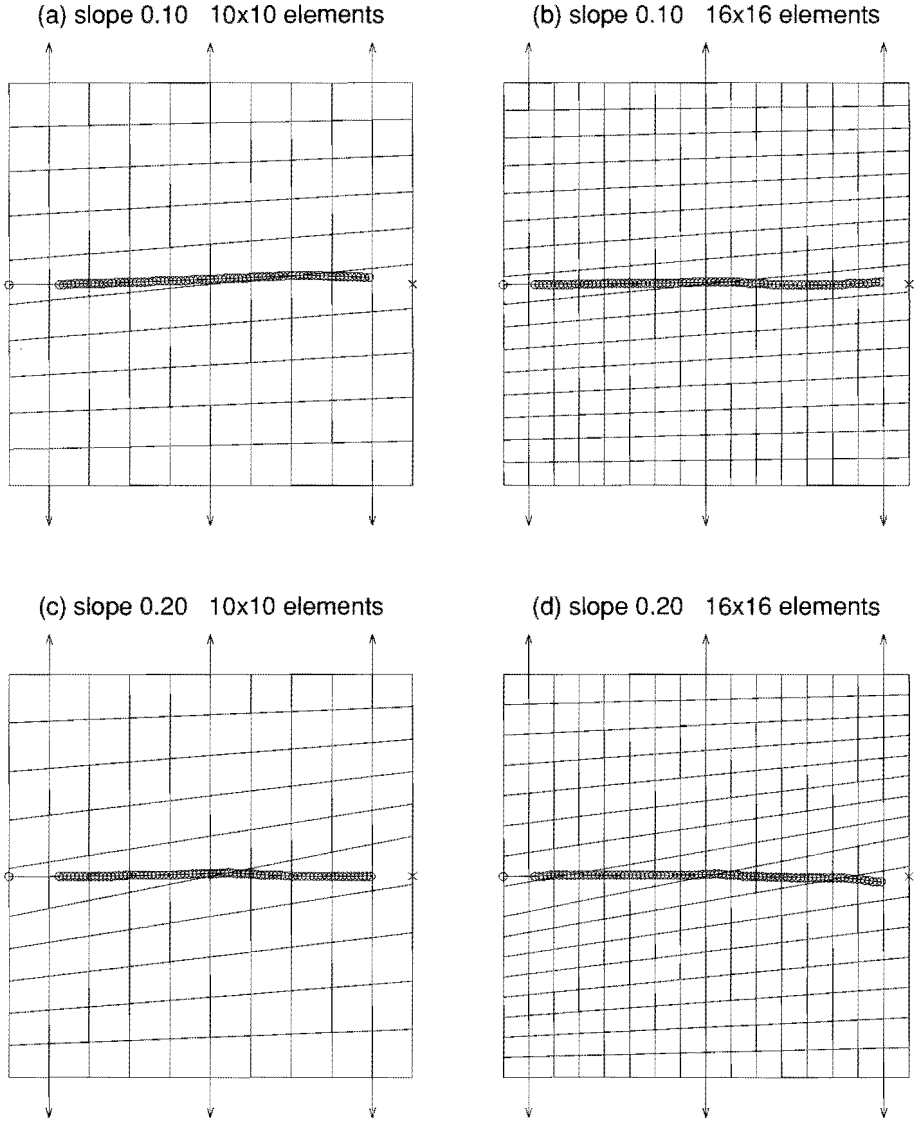


Figure 8.4: Crack patterns for a square plate loaded by uniform tensile forces, derived with the hybrid fracture/damage approach for various element divisions. Subsequent positions of crack tip are shown by \circ and prospective end point of crack by \times . Crack-propagation criterion is based on largest principal stress.

The first test concerns the possible dependences of the calculated crack patterns on the finite-element division. We study a square plate of size $l \times l$ and thickness $h = l/4$, which is loaded by uniform tensile forces or uniform bending moments on two opposite sides. The crack patterns are shown in the original element meshes for clarity.

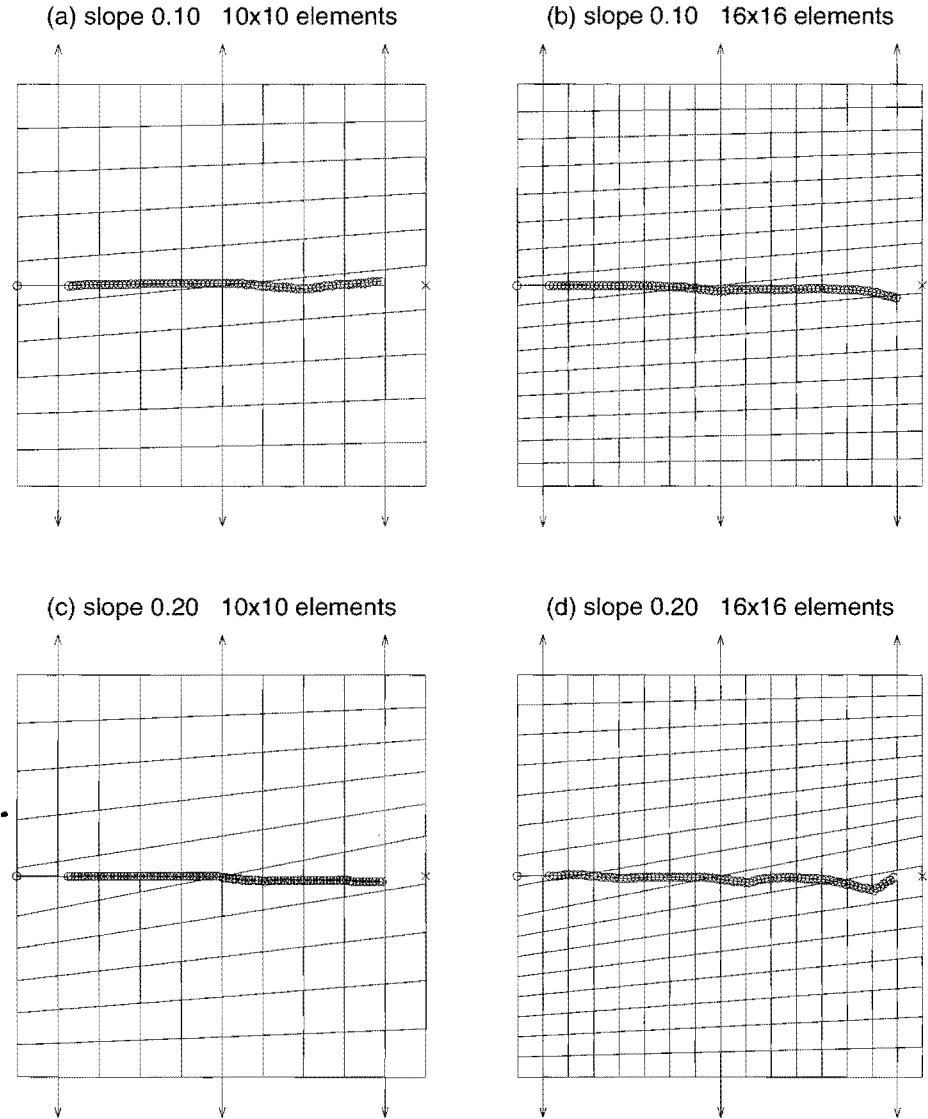


Figure 8.5: Crack patterns for a square plate loaded by uniform tensile forces, derived with the hybrid fracture/damage approach for various element divisions. Subsequent positions of crack tip are shown by \circ and prospective end point of crack by \times . Crack-propagation criterion is based on J -integrals.

The thickness of the plate is larger than in Section 6.3, because otherwise the critical time step is too small and impractical. The plate is divided into 10×10 or 16×16 elements with one element over the thickness. The Wilson-Taylor elements of Section 7.5 are used. The slanted orientation of the element lines is at most 0.10 or 0.20,

which corresponds to inclination angles of 5.7° and 11.3° , respectively. The results are shown in Figs. 8.4 and 8.5.

A crack is initiated at the middle of one of the non-loaded sides, having initial length $\frac{5}{4}l_e$ with l_e being the element width. We employ the explicit central-difference method as time-step algorithm and we assign a small value to the fracture toughness to enforce crack growth. As a result, the crack speed is approximately equal to the Rayleigh wave speed c_R and the crack increment to $c_R \Delta t \approx l_e/10$. The crack patterns in the plate loaded by tensile forces are shown in Figs. 8.4 and 8.5 for the principal-stress criterion and for the J -integral criterion, respectively. The crack patterns in the plate loaded by bending moments are similar to these results. The crack propagation should occur along straight lines, because the uniform tensile forces lead to a situation in which only the crack-opening mode (mode I) exists. Similarly, the uniform bending moments lead to a situation with only the normal-bending mode (mode 1). The computation terminates, when the crack path reaches the element on the opposite non-loaded side at the boundary of the plate and the construction of a super-element is not possible anymore.

Regarding the crack patterns in Figs. 8.4 and 8.5, we observe that the end points of the crack paths are always within one element from the prospective end points (marked by \times), which is considered as sufficiently accurate. We also observe that the results for the J -integral criterion are more sensitive to the skewed orientation of the element mesh than those for the principal-stress criterion. This can be explained by the following argument.

The contour for the computation of the J -integrals consists of seven segments (see Fig. 8.3), where five Gaussian integration points are used per segment in the circumferential direction and five in the thickness direction of the plate. This sums up to a total of 175 points where the stresses are evaluated. The criterion based on the largest principal stress uses the average of the stress tensors evaluated in all Gaussian integration points of eight elements, which yields a total of $8 \times 27 = 216$ points. This higher number of points for stress evaluation may explain the better performance of the principal-stress criterion. The accuracy of the J -integral can be improved by taking a contour at larger distance from the crack tip, but in that case the algorithm needs more computing time and becomes less efficient. Nevertheless, the results obtained with the J -integral criterion are quite acceptable. Although the crack-propagation criterion based on the (averaged) largest principal stress has no solid foundation in fracture mechanics, we conclude that this criterion produces the best results for the crack patterns.

The second test is Iosipescu's shear beam [39] with a single-edge notch, which is suitable for a study of curvilinear crack propagation under shear loads. We adopt the same specimen dimensions as in Section 6.3, viz. a length of 440 mm, a height of 100 mm, and a thickness of 10 mm. The forces F_1 are applied at a distance of 20 mm from the plane of symmetry and the forces $F_2 = F_1/10$ at a distance of 200 mm. The element division is a little more refined (274 elements), such that the crack is not initiated at the boundary between two elements but in the interior of an element. The

initial crack has a length of (a) 15 mm or (b) 25 mm and is located at the middle of the longest edge of the beam. The shear deformation leads to a situation where the crack-opening mode and the sliding mode are combined (modes I and II). We employ the implicit α -method with $\alpha = -0.3$ and use the crack-propagation criterion based on the largest principal stress.

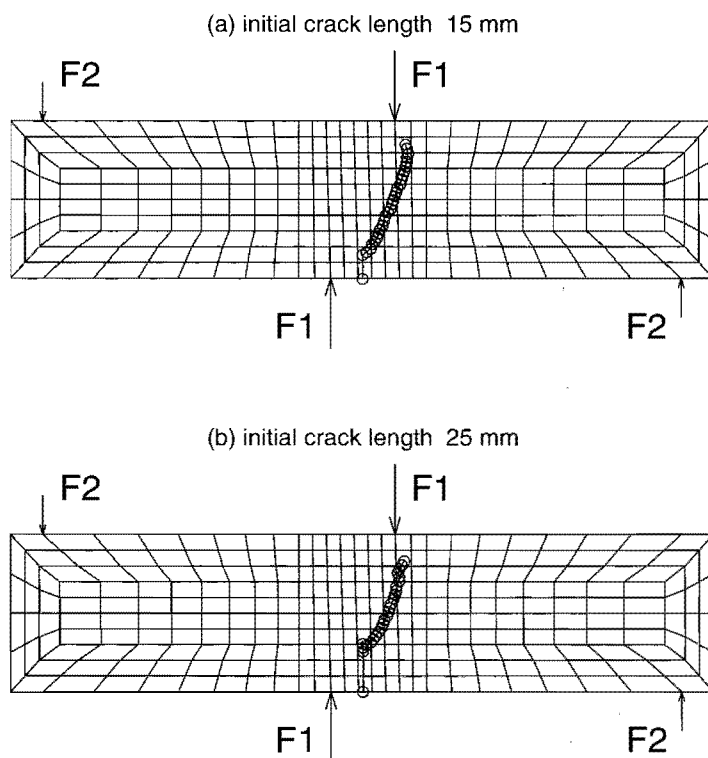


Figure 8.6: Crack patterns for a single-edge notched beam loaded under shear conditions, derived with the hybrid fracture/damage approach for different initial crack lengths. Subsequent positions of crack tip are shown by \circ .

The obtained crack paths are shown in Fig. 8.6 and satisfy the requirement that the end points are on the opposite edge of the beam to the right of the point where the force F_1 is applied. Similar results are found for various different time steps. The crack paths are not identical to the paths shown in the figure, but they lie in a small band around these paths and they always satisfy the requirement for the end point. The crack patterns agree with the results of Feenstra [27], Lubliner, Oliver, Oller and Oñate [54], Rots [79], and Schlangen [81]. We did not obtain acceptable results with the use of the crack-propagation criterion based on the J -integrals, which is due to the dominance of mode II in the early stage of fracture. This problem with the J -integral

criterion has been mentioned before in Section 3.4, where we have discussed several fracture criteria.

The third test concerns three-dimensional crack propagation in a hollow cylindrical pipe which is loaded by torsional moments at its ends. The geometry is the same as in Section 6.3, i.e., the pipe length is 400 mm and the inner and outer radii are 30 and 40 mm. The division into finite elements contains 25 elements in the axial direction, 32 in the circumferential direction, and one over the thickness. This refinement (compared to the finite-element division for the uncoupled approach) is necessary for the construction of the super-element. Otherwise, for coarser divisions, the added “slave” nodes of the super-element can lie outside the domain occupied by the pipe due to the interpolation between the “master” nodes and due to the curvature of the element and of the pipe surfaces.

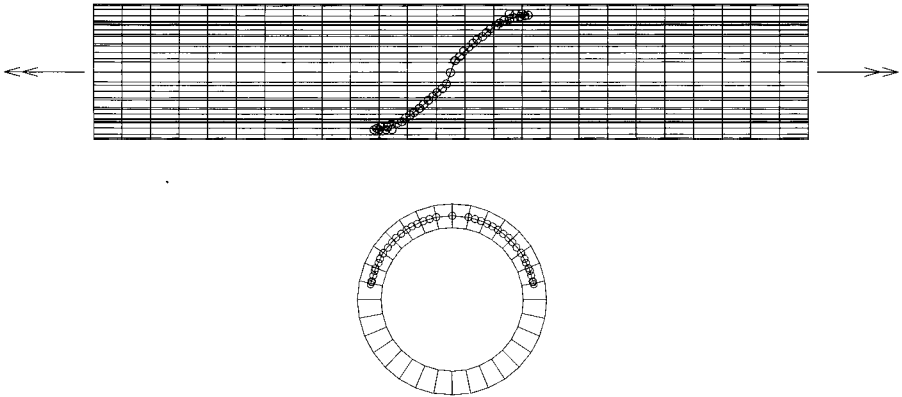


Figure 8.7: Crack patterns for a pipe loaded by torsional moments, derived with the hybrid fracture/damage approach. Initial crack is at middle of side view and at top of cross-sectional view. Subsequent positions of crack tip (into two directions) are shown by \circ .

A crack is initiated in the middle cross section of the pipe with initial length equal to $3/4$ of the element size in the circumferential direction (approx. 4.58 mm). We use the explicit time-step algorithm in combination with the crack-propagation criterion based on the largest principal stress, since the fracture process begins in mode II. Because of the restricted time step, the crack increments are approximately equal to 0.37 mm. We calculate the crack paths in two symmetric directions and terminate the calculation after 200 time steps. The results are shown in Fig. 8.7 for every tenth time step.

We observe some deviations in the crack pattern near the upper and lower boundaries in the side view of the pipe. These deviations are related to the plane drawing of the three-dimensional geometry and to the fact that the crack starts to propagate in the direction perpendicular to the axis of the pipe. At that moment, one half of the cross

section has fractured and the pipe reaches the point of final collapse. Globally, the obtained crack paths agree with those of the uncoupled approach (see Fig. 6.5) and with the predictions based on the experiments of Richard [78] and on the analyses of Lakshminarayana and Murthy [48].

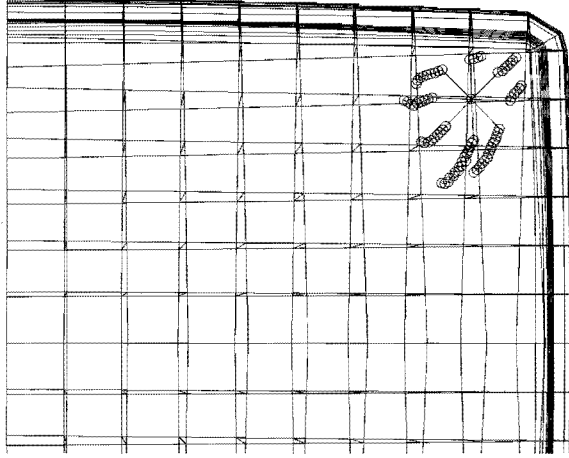
8.6 Application to television picture tubes

We have obtained trustworthy results from application of the hybrid fracture/damage approach to two-dimensional and simple three-dimensional problems. We shall now apply the hybrid approach to the ball-drop test on a 36WS television picture tube. The tube geometry, the test conditions, and the finite-element division have been discussed in detail in Section 6.4.

We study a ball impact at the F-point and use the implicit α -method with $\alpha = -0.3$ and $\Delta t = 1 \mu s$, in combination with the crack-propagation criterion based on the largest principal stress. We calculate the crack propagation in eight different directions and choose initial crack lengths of 30 mm. This requires eight separate calculations, which need several hours of computing time each. The calculations terminate when the cracks reach the edge of the screen and the construction of the super-element is not possible anymore.

The results for the crack patterns are shown in Fig. 8.8 for the tubes (a) with and (b) without the metal rimband around the screen edge. A significant influence of the metal rimband on the tube safety is observed, but the differences between figures (a) and (b) are less distinctive than in Figs. 6.6(a)-(b) and 6.7(a)-(b), which have been obtained from calculations by the uncoupled dynamic fracture approach. When the metal rimband is applied to the tube construction, only little crack propagation is calculated, followed by crack arrest. In the case that the rimband is not applied, we notice that the preferred direction of crack propagation is along the diagonal of the screen. These results agree with practical experience; see Section 6.5. Observations on the ball-drop test with impact position at the F-point reveal that crack propagation mostly occurs along the screen diagonal or the screen boundary.

(a) television tube with rimband



(b) television tube without rimband

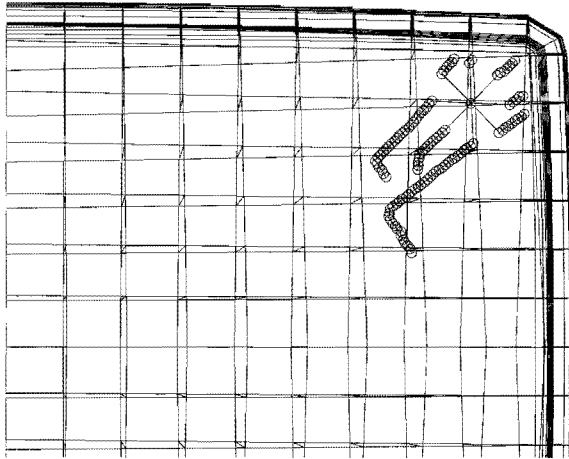


Figure 8.8: Crack patterns formed by impact on the F-point, derived with the hybrid fracture/damage approach, (a) with the rimband being applied and (b) without the rimband. Subsequent positions of crack tip are shown by \circ , initial crack length is 30 mm, and time step is 1 μ s.

8.7 Conclusions

A hybrid fracture/damage approach is proposed. Several implementations of this approach have been discussed. There are two options for the time-step algorithm: the explicit central-difference method and the implicit α -method. The crack-propagation criterion is based either on the J -integrals or on the largest principal stress at the crack tip. The former criterion has a profound basis in fracture mechanics and the latter is a practical engineering rule.

These variants of the hybrid approach have been applied to various test problems, such as a square plate loaded by tensile forces or bending moments, Iosipescu's shear beam, and a hollow cylindrical pipe subjected to torsion. The results show that all variants produce acceptable crack patterns, which are always accurate within one element from the theoretical crack paths. This concerns both single-mode and mixed-mode fracture. Since the interaction between crack propagation and stress waves is incorporated in the method, the crack paths are reliable over their full range from the point of initiation to the point of crack arrest or final collapse. Moreover, we observe that the hybrid approach is hardly susceptible to variations in the element size and in the element orientation, although the results obtained with the principal-stress criterion tend to be less sensitive to such variations than those obtained with the J -integral criterion. We also note that both the explicit and the implicit time-step algorithm produce acceptable results for the crack patterns.

Concerning the impact tests for television picture tubes, we must admit that we have obtained only moderate results with enormous computational effort. This is due to the very small time step required for an explicit time-step algorithm on the one hand and to the very large systems of equations to be solved in the case of an implicit algorithm on the other hand. We draw the same conclusion from the calculated crack patterns as for the uncoupled approach, namely that the safety of television picture tubes is clearly increased by application of the metal rimband.

Part IV

Conclusion and Perspective



Chapter 9

Conclusion

In this thesis we have investigated dynamic crack propagation in brittle materials and, in particular, the safety tests for television picture tubes (cathode-ray tubes). The aim of the present research has been formulated in Chapter 1: the development of analytical and numerical methods for the calculation of the dynamic response of a television tube to a mechanical impact and for the determination of the glass safety of a given tube design. We have proposed two new methods for the analysis of crack propagation: (i) the uncoupled dynamic fracture approach and (ii) the hybrid fracture/damage approach (see Section 1.3). General remarks on these methods and conclusions from applications to television picture tubes are presented below.

9.1 The uncoupled dynamic fracture approach

The interaction between crack propagation and stress waves in dynamic fracture processes has been partly uncoupled in this approach (see Chapter 6). The crack propagation is determined on the basis of the elastodynamic stresses calculated for the intact, unfractured geometry. The uncoupled approach does not incorporate the stress waves initiated by a moving crack tip. The analysis utilises stress-intensity factors for thin flat plates containing a crack of slightly curved shape, which are loaded by a combination of in-plane tensile forces, out-of-plane bending moments, and perpendicular shear forces. This analysis does not only necessitate a study of fracture mechanics (see Chapter 3), but also of plate bending and of curvilinear cracks.

In Chapter 4 we have studied the classical theory and Reissner's theory of plate bending for both stationary cracks and dynamically propagating cracks. The singular bending moments for the two theories have been compared, and also the deflections of the plate, the rotations of the middle plane, the perpendicular shear forces, and the energy release rates. Relations between the stress-intensity factors of the classical theory and those of Reissner's theory have been derived. We have concluded that five stress-intensity factors are sufficient for the fracture analysis of arbitrary plate-like

geometries: two factors for the in-plane tensile forces and the in-plane shear forces, two factors for the normal bending moments and the torsional moments, and one factor for the shear forces in the direction perpendicular to the plate.

Expressions for the stress-intensity factors for plates containing a curvilinear crack have been calculated in Chapter 5 with the use of complex holomorphic functions. A linearisation with respect to the shape of the crack has been performed, so that the resulting expressions are valid for slightly curved cracks. From a comparison of the linearised results with the exact stress-intensity factors for a circular-arc crack, we have concluded that the linearised expressions are sufficiently accurate even for large arc-opening angles and, thus, for a wide variety of curvilinear cracks.

Application of the uncoupled approach to several test problems has shown that reliable predictions of crack patterns are obtained. The reliability decreases with increasing crack length due to the partial uncoupling of the dynamic effects and the crack growth. Although the uncoupled dynamic fracture approach cannot determine the moment of crack arrest or final collapse with utmost precision, we conclude that this method is well capable of predicting the direction of crack propagation in the early stages of fracture. Since the elastodynamic stress data can be used repeatedly for multiple crack-path computations, an efficient and low-cost method for the calculation of crack patterns has been established.

9.2 The hybrid fracture/damage approach

The hybrid fracture/damage approach combines the advantages of fracture mechanics and damage mechanics within a dynamic finite-element method (see Chapter 8). This hybrid approach incorporates all dynamic effects, such as the interaction between stress waves and crack propagation, and creates new possibilities for the analysis of failure phenomena. The idea of a hybrid approach has arisen from a study of finite elements for fracture applications and of the concepts of continuum damage mechanics. From this study we have concluded that the single use of either fracture mechanics or continuum damage mechanics is not a proper strategy for a finite-element analysis of the impact safety tests for television picture tubes.

The hybrid approach may form a good alternative. In Chapter 7 we have examined various finite elements, which have been united in Chapter 8 in the following manner. We use the elements of Wilson and Taylor with incompatible modes to divide the configuration into subdomains. This ensures a correct description of bending and torsional deformation. In the vicinity of the crack tip fracture elements are employed for accuracy of the method; these elements incorporate the singular stress behaviour. For the rest of the crack path damage elements are employed for flexibility of the method; these elements have a reduced modulus of elasticity (softening behaviour). Thus, we have established a new method for failure analysis, which is accurate in the crack-tip region as well as flexible regarding the representation of the crack path.

Application of the hybrid fracture/damage approach to several test problems has shown that reliable predictions of crack patterns are obtained. Dependences on the finite-element division, which are known to occur in applications of standard theories of damage mechanics, have not been observed. Regarding the results for the test problems, we conclude that the hybrid approach produces correct predictions for crack propagation in two-dimensional and in simple three-dimensional geometries.

9.3 Analysis of television picture tubes

Investigations of the strength and the failure behaviour of television picture tubes start with a static finite-element calculation of the stresses in the tube due to the internal vacuum and possibly the applied metal rimband. The investigations continue with an elastodynamic finite-element calculation of the response of the intact tube to a ball-drop impact, where it is assumed that crack initiation does not occur. These calculations provide a first insight into the stress and displacement distributions. Further insight is provided by application of the two new methods for failure analysis.

We utilise the results of an elastodynamic calculation as input data in the uncoupled approach and we determine possible crack patterns with the use of a dynamic fracture criterion. Since the uncoupled approach is always applied in combination with an elastodynamic finite-element calculation, this approach constitutes a method which is easy to use and which yields useful results with relatively little computational effort. The hybrid fracture/damage approach, on the contrary, constitutes a method on its own and is employed separately from the static and elastodynamic calculations. Since the hybrid approach unfortunately requires too much computing time for large geometries, this approach cannot be applied to the impact safety tests for television picture tubes in an efficient manner.

Guided by these considerations, we conclude that the investigation of the safety of television-tube designs is preferably carried out in three steps, namely: (i) a static stress calculation, (ii) an elastodynamic stress calculation, and (iii) an uncoupled dynamic crack-path calculation. The hybrid fracture/damage approach is a useful tool for a failure analysis of specific details of the television picture tube.

We have applied the uncoupled dynamic fracture approach to the ball-drop safety test performed on a 36WS television picture tube (see Section 6.4). The tube has been subjected to the vacuum load and to a ball impact on either the D-point or the F-point. We have studied the effect of the metal rimband on the tube safety. The calculations indicate that practically no crack propagation is expected in tubes with this rimband, and that considerable crack propagation will take place in tubes without this rimband. We have also applied the hybrid fracture/damage approach to the ball-drop test on the same 36WS tube (see Section 8.6). The results concerning the crack patterns and the tube safety, however, are less clear than those obtained by the uncoupled approach, because the crack patterns obtained by the hybrid approach for tubes with or without the metal rimband are less distinctive.

The main conclusion is that the safety of television picture tubes is significantly improved by application of the metal rimband around the outer edge of the screen. This conclusion agrees with practical experience; namely, the rimband has especially been developed to diminish crack propagation in the glass screen. Moreover, there exists good correspondence between the calculated crack patterns and those observed in the television tubes when the ball-drop test is performed; the directions of crack growth are globally the same. So, we conclude that the dynamic crack propagation in television picture tubes due to a ball impact can be predicted with reasonable accuracy by simulations with the uncoupled dynamic fracture approach.

Chapter 10

Perspective

The present research has resulted in two new methods for the analysis of dynamic crack propagation in brittle materials. Although these methods have produced trustworthy results, there are still questions that have remained unanswered. These questions and other open ends of this thesis are addressed in the following two sections, together with suggestions for further research.

10.1 On fracture and damage mechanics

We start with some issues in theoretical fracture mechanics. In Chapters 3 to 5 we have investigated cracks in thin flat plates under various loading conditions. Television picture tubes, however, have a slightly curved screen of variable thickness, in particular near the screen boundary. The calculation of stress-intensity factors for curved plates and shells will enable a more accurate analysis of crack propagation near the boundary of the TV screen. A first step has been provided by Lakshminarayana and Murthy [48] and Richard [78], who derived stress-intensity factors for cracked cylindrical pipes.

In addition, we suggest the calculation of stress-intensity factors for thick flat plates with the use of Reissner's theory for plate bending in a manner similar as in Chapter 5. The problem for a thick plate containing a straight crack, which is loaded by a uniform bending moment on its outer boundary, has been analysed in Reissner's theory by Hartranft and Sih [32] and Knowles and Wang [46, 95]. The problem for a thick plate containing a curved crack, which is loaded by distributed moments on the crack surfaces, is more complicated and poses a mathematical challenge.

Regarding fracture in bending deformation, we have postulated in Section 4.7 that the relationship between the elastodynamic stress-intensity factor for a propagating crack and the corresponding equilibrium stress-intensity factor for a stationary crack is governed by the same universal function of crack speed as for fracture in planar deformation (mode I). The precise relationship between the bending stress-intensity factors can be obtained from a solution of the differential equations (4.111)–(4.113)

for a semi-infinite crack propagating at constant speed, with appropriate boundary conditions on the crack surfaces. Since the solution procedure by integral transforms as in Freund [28, Ch. 6] cannot be used, the derivation of the precise relationship poses another difficult but challenging problem in mathematics.

An issue in practical fracture mechanics concerns a fracture criterion for situations of general mixed-mode loading. We have discussed fracture criteria for situations of planar deformation in Section 3.4 and we have considered cracked plates loaded by a combination of tensile and shear forces (modes I and II) and of bending and torsional moments (modes 1 and 2) in Section 4.5. Further research is required on fracture criteria in cases where the four modes mentioned above are present simultaneously, possibly in combination with mode III or mode 3. This research should particularly concentrate on the influence of the stress-intensity factor K_2 of the twisting mode on the direction of crack propagation. Also, the possible relationship of K_2 with the stress-intensity factors K_3 and K_{III} (see Section 4.4) needs further investigation, where experimental work will play a key role.

We shall now discuss some issues in continuum damage mechanics, in relation to the hybrid fracture/damage approach. We have chosen to represent crack propagation by a sudden increase of the damage parameter \mathcal{D} from 0 to 0.999, resulting in a sudden decrease of Young's modulus E to the value $E_d = E/1000$ (see Section 8.2). The energy dissipation associated with the damage increase is related to the area beneath the curves in Fig. 8.1, in which two stress-strain relations for ductile and brittle failure behaviour are shown. Since the amount of energy dissipation in damage formulations does not always agree with the energy release rate from fracture mechanics, it is necessary to get a better understanding of the energy concepts in damage mechanics. In addition, it may be advantageous to incorporate a gradual damage increase in the hybrid approach. This will require a further study of the damage-evolution equation (such as (1.3)) for brittle failure.

It is worthwhile to investigate other possible combinations of fracture mechanics and continuum damage mechanics than in the hybrid fracture/damage approach. For example, de Borst [9] has suggested to represent a crack by a discontinuity (as usual in fracture mechanics) and to employ damage mechanics in the crack-tip region. This representation is particularly relevant to the study of structures made of concrete, where large areas of material damage may surround the crack tip. From [9] and the results of Chapter 8, it is evident that the combination of fracture and damage mechanics leads to new possibilities for failure research.

10.2 On finite-element technology

The hybrid fracture/damage approach is based on the finite-element method and has been developed in the MATLAB programming environment [57]. Therefore, we shall address some possibilities for further research into finite-element technology. The disadvantage of the hybrid approach is the large amount of computing time needed

for the calculation of crack propagation in complex three-dimensional structures. The computing time can be reduced when the program is translated into machine code with a MATLAB compiler; this compiler is not yet available but has already been announced. Another possibility is a translation of the program to a compiler-based computer language, preferably Fortran 90 (see Ellis, Philips and Lahey [21]).

One reason for the large computing time in the application of the hybrid approach to television picture tubes is the severe restriction on the time step when an explicit time-step algorithm is used. Although implicit algorithms take larger (and thus fewer) steps, they require more computational effort per time step due to the large number of degrees of freedom and are therefore less efficient than explicit algorithms. The restriction on the time step is determined by the smallest element in the finite-element division; see Section 8.4. Since the crack propagation takes place in the middle of the screen where the elements are larger, a possible strategy to increase the time step is to avoid the smaller elements at the neck of the television tube and at the edges of the screen. Another strategy is to employ an implicit/explicit time-step algorithm; see Hughes [37, Sec. 9.4]. The element mesh is then partitioned into two groups: an implicit method with a relatively large time step is used for the smaller elements and an explicit method with a smaller time step (which is still larger than the original time step in the entirely explicit algorithm) is used for the larger elements.

An important aspect of the hybrid fracture/damage approach is the construction of the super-element. Since this construction may fail for strongly curved surfaces, we recommend to investigate the use of plate elements or shell elements for the glass screen. An introduction to plate and shell elements is given by Hughes [37, Chs. 5-6]. In addition, the application of plate or shell elements may lead to an increase of the accuracy of the hybrid approach and/or to a decrease of the computing time.

The accuracy of the hybrid approach can also be improved by application of more than one element over the thickness of the glass screen. Unfortunately, this leads to a considerable increase in computing time: about a factor two for the assembly process and at least a factor four for the solution of the matrix-vector equations. It is worthwhile to investigate the alternative of having more elements over the thickness in the vicinity of the crack front only. This will improve the accuracy of the method, while the increase in computing time remains limited. Moreover, this enables a more precise calculation of the crack front over the thickness of the glass screen, whereas the hybrid approach in its present form assumes a straight crack front which is uniform over the thickness and perpendicular to the middle plane of the screen.

Finally, we recommend the further development of fracture-mechanics techniques within the finite-element method. Since procedures with moving finite elements mostly assume straight crack paths (see Nishioka, Murakami and Takemoto [68]), these procedures have yet only limited applicability. It will be a great advance when such moving-element procedures become available for the calculation of crack growth along arbitrarily curved paths. Furthermore, when a speed-up of the remeshing and assembly processes can be established, an important step forward is made towards a fully-coupled dynamic fracture analysis.

Appendices



Appendix A

On path-independent integrals

A.1 Various integration contours

The elastodynamic integrals J_k are defined by (3.52); see also [2, 28, 66, 67, 76]. For the sake of simplicity, the integration over the plate thickness is omitted in this appendix. The definition applies to a circular contour centered at the crack tip with its end points on the lower and upper crack flanks (crack surfaces) and lying inside the region of K -dominance. Let this contour be denoted by C_ε with radius $\varepsilon \rightarrow 0$, while the interior of C_ε bounded by the crack flanks is denoted by A_ε .

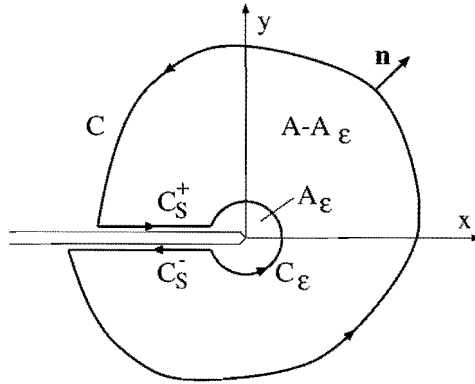


Figure A.1: Remote contour for the J -integrals.

For practical applications such as finite-element analyses, it is convenient to obtain an expression for J_k which involves an integral along a remote contour, so that the far-field solutions for the stresses and the displacements can be used. Let C be an arbitrary contour starting on the lower crack flank, surrounding the crack tip, and

ending on the upper crack flank; see Fig. A.1. The components of the outward normal to C are denoted by n_i . The curves $C_S = C_S^- \cup C_S^+$ are the two paths along the crack flanks, which connect the end points of C to those of C_ε . The domain A is the interior of C bounded by the crack flanks, such that $A - A_\varepsilon$ is the domain bounded by the closed contour $C + C_S - C_\varepsilon$. Recall that $W = \frac{1}{2}\sigma_{ij}\varepsilon_{ij}$ and $T = \frac{1}{2}\rho\dot{u}_i\dot{u}_i$ are the elastic and kinetic energy densities, respectively. Using the Gauss divergence theorem and the equations (2.14)–(2.16), we see that (3.52) transforms into

$$J_k = \lim_{\varepsilon \rightarrow 0} \left\{ \int_{C+C_S} \left((W+T)n_k - \sigma_{ij}n_j u_{i,k} \right) ds + \int_{A-A_\varepsilon} \left(\rho\ddot{u}_i u_{i,k} - \rho\dot{u}_i \dot{u}_{i,k} \right) dA \right\}. \quad (\text{A.1})$$

In the limit for $\varepsilon \rightarrow 0$, the domain A_ε shrinks to zero and the curves C_S extend to the crack tip. Since no restrictions have been imposed on the remote contour C , the expression (A.1) is independent of the choice of C . For this reason, the integrals J_k are often referred to as path-independent integrals [2, 28, 66, 67, 76]. As shown below, this terminology is not correct for J_2 in the case of dynamic fracture.

The definition (3.52) can be extended to other than circular contours shrinking onto the crack tip. It is then necessary to examine the dependence of J_k on the shape of the contour C_ε . Consider two different contours $C_{\varepsilon 1}$ and $C_{\varepsilon 2}$ around the crack tip, having the same end points on the lower and upper crack flanks, and lying inside the region of K -dominance. Subtraction of the integrals along $C_{\varepsilon 1}$ and $C_{\varepsilon 2}$ produces

$$\begin{aligned} \int_{C_{\varepsilon 1}-C_{\varepsilon 2}} \left((W+T)n_k - \sigma_{ij}n_j u_{i,k} \right) ds &= \int_{A_{\varepsilon 12}} \left(\rho\dot{u}_i \dot{u}_{i,k} - \rho\ddot{u}_i u_{i,k} \right) dA \\ &= \int_{A_{\varepsilon 12}} \rho c^2 (u_{i,\hat{x}} u_{i,k\hat{x}} - u_{i,k} u_{i,\hat{x}\hat{x}}) dA, \end{aligned} \quad (\text{A.2})$$

where $A_{\varepsilon 12}$ is the domain enclosed by $C_{\varepsilon 1}$ and $C_{\varepsilon 2}$. In the latter transition it was used that the contours are inside the region of K -dominance, so that the time derivatives may be replaced by derivatives with respect to \hat{x} multiplied by the crack-growth speed c ; see (3.15) and also (4.2)–(4.3).

It is obvious that the difference (A.2) vanishes for J_1 , corresponding to $k = 1$ or $k = \hat{x}$. This conclusion also applies to contours $C_{\varepsilon 1}$ and $C_{\varepsilon 2}$ having different end points, in which case an extra integral along the crack flanks must be incorporated in (A.2). This integral vanishes when the condition of stress-free crack flanks is imposed. Thus, J_1 is a truly path-independent integral. The relation between J_1 and the stress-intensity factors is given in (3.48) and (3.53).

For $k = 2$ or $k = \hat{y}$, however, a non-zero value is obtained in (A.2). This means that the integral J_2 does depend on the shape of the shrinking contour. Only for stationary cracks ($c = 0$) does the difference in (A.2) vanish for J_2 and both integrals J_k ($k = 1, 2$) are independent of the integration path. The relation between J_2 and the stress-intensity factors is studied in Section A.2.

A.2 Calculation for planar deformation

In the preceding section it was shown that the integral J_2 depends on the shape of the shrinking contour C_ε in the case of dynamic fracture. In the present section we summarise results for J_2 when two different integration paths are used; see Fig. A.2. The expression (3.52) with $k = 2$ has been evaluated for a circular contour with radius $\varepsilon \rightarrow 0$ by Nishioka and Atluri [67]. The result contains the product $K_I K_{II}$ according to (3.54) with the coefficient $A_{IV}^C(c)$ given by

$$A_{IV}^C(c) = \frac{(1 + \nu)(\alpha_d - \alpha_s)(1 - \alpha_s^2)}{R^2} \left(\frac{(2 + \alpha_d + \alpha_s)[4\alpha_d\alpha_s + (1 + \alpha_s^2)^2]}{2\sqrt{(1 + \alpha_d)(1 + \alpha_s)}} - 2(1 + \alpha_s^2) \right), \quad (\text{A.3})$$

where the superscript C refers to the circular contour.

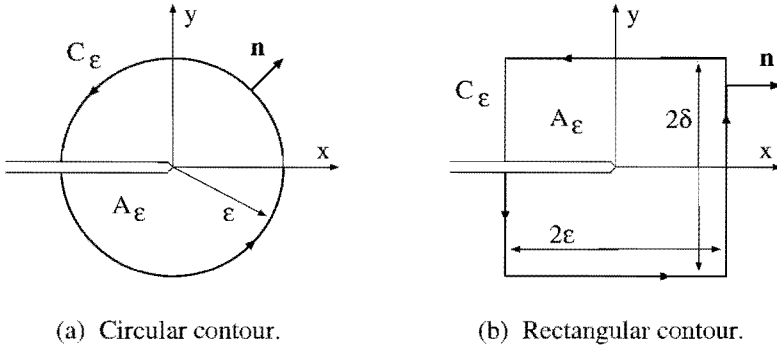


Figure A.2: Contours for the J -integrals.

In [92] a rectangular contour with height 2δ and width 2ε as in Fig. A.2(b) has been chosen for the calculation of J_2 . The limit for $\varepsilon \rightarrow 0$ has been taken first, followed by the limit for $\delta \rightarrow 0$. In this procedure there is no contribution to the integral from the parts of the contour parallel to the x -axis, while the term $(W + T)n_k$ vanishes along the parts parallel to the y -axis since $n_y = 0$ there. The result for J_2 is of the form (3.54) with the velocity-dependent coefficient equal to

$$A_{IV}^R(c) = \frac{(1 + \nu)(\alpha_d - \alpha_s)(1 - \alpha_s^2)}{R^2} \left(\frac{(\alpha_d + \alpha_s)[4\alpha_d\alpha_s + (1 + \alpha_s^2)^2]}{2\sqrt{\alpha_d\alpha_s}} - 2(1 + \alpha_s^2) \right), \quad (\text{A.4})$$

where the superscript R refers to the rectangular contour.

Obviously, the expressions (A.3) and (A.4) are different. This finding is at variance with the conclusion of Nishioka [66] who claimed on the basis of numerical calculations that the elastodynamic integrals would be independent of the shape of the contour C_ε inside the region of K -dominance. The deviation between (A.3) and (A.4), however, is not more than 1–5% for crack-growth speeds between $0.65 c_s$ and $0.80 c_s$ and even less for slower crack propagation. Consequently, the two expressions for $A_{IV}(c)$ are equivalent and may be used interchangeably for crack growth at moderate speed. When the crack-growth speed approaches the Rayleigh wave speed, the difference becomes increasingly significant. Since only crack speeds up to $0.60 c_s$ have been investigated by Nishioka, the numerical errors in the computed values in [66] are probably in the same range as the small deviations mentioned above. These observations may explain why the dependence of $A_{IV}(c)$ on the shape of the contour was not detected in [66]. Nishioka's conclusion that the integral J_2 is independent of the integration path, is therefore incorrect; see also [92].

A.3 Calculation for classical plate theory

The analysis for plate bending in the classical theory does not differ very much from the analysis for planar deformation. The integrals J_k are given by (4.77). The integral J_1 is independent of the shape of the contour C and coincides with the energy release rate \mathcal{G} . Evaluation for a shrinking circular or rectangular contour yields the expression (4.74) for $\mathcal{G} = J_1$ with velocity-dependent coefficients (4.75)–(4.76).

The integral J_2 depends on the shape of the shrinking contour C_ε inside the region of K -dominance. The expression (4.77) with $k = 2$ has been evaluated for a circular contour as in Fig. A.2(a) with radius $\varepsilon \rightarrow 0$ by Boersma [8]. The result is expressed in $k_1 k_2$ according to (4.78) with the velocity-dependent coefficient $a_4(c)$ given by

$$a_4^C(c) = \frac{(1-\nu)(3+\nu)^2(1+\alpha_d)(1-\alpha_d)^2}{4S^2} \left(\frac{(3+\alpha_d)[(1-\nu)^2\alpha_d + (\alpha_d^2 - \nu)^2]}{(1-\nu)\sqrt{2(1+\alpha_d)}} - 2(\alpha_d^2 - \nu) \right), \quad (\text{A.5})$$

where the superscript C refers to the circular contour.

Evaluation of (4.77) with $k = 2$ for a shrinking rectangular contour as in Fig. A.2(b), with the limit for $\varepsilon \rightarrow 0$ taken first, yields a similar result for J_2 with coefficient

$$a_4^R(c) = \frac{(1-\nu)(3+\nu)^2(1+\alpha_d)(1-\alpha_d)^2}{4S^2} \left(\frac{(1+\alpha_d)[(1-\nu)^2\alpha_d + (\alpha_d^2 - \nu)^2]}{(1-\nu)\sqrt{\alpha_d}} - 2(\alpha_d^2 - \nu) \right), \quad (\text{A.6})$$

where the superscript R refers to the rectangular contour.

Appendix B

On double integrals

B.1 Formula of Poincaré-Bertrand

The expressions (5.49) and (5.113), and also the expression (B.11) below, contain double integrals in which the applied loads and the crack-shape function $\lambda(t)$ occur. It will be shown that interchanging the order of integration is allowed. This is not evident, because we must take Cauchy principal values of the inner, singular integrals. Details of the analysis can be found in the work of Muskhelishvili [62, 63] and in the papers [93, 94].

We start with the transformation formula of Poincaré-Bertrand.

Theorem 1. Let L be a smooth arc or contour and let $\phi(t, s)$ be a function of t and s on L , satisfying the condition of Hölder continuity [62, Ch. 1] for both its arguments. For a fixed point t_0 on L , we have

$$\int_L \frac{dt}{t-t_0} \int_L \frac{\phi(t, s)}{s-t} ds = -\pi^2 \phi(t_0, t_0) + \int_L ds \int_L \frac{\phi(t, s)}{(t-t_0)(s-t)} dt. \quad (\text{B.1})$$

Proof. See Muskhelishvili [62, Sec. 23].

Next, we take for L the line segment $[-a, +a]$ and we make a specific choice for the function $\phi(t, s)$ by a separation of the variables t and s .

Theorem 2. Let $f(t)$ and $g(s)$ be functions of t and s on $[-a, +a]$, satisfying the condition of Hölder continuity. We have

$$\int_{-a}^{+a} f(t) \int_{-a}^{+a} \frac{g(s)}{s-t} ds dt = \int_{-a}^{+a} g(s) \int_{-a}^{+a} \frac{f(t)}{s-t} dt ds. \quad (\text{B.2})$$

Proof. Substitute $\phi(t, s) = (t-t_0) f(t) g(s)$ into (B.1).

We can now prove that interchanging the order of integration in (5.49) is allowed, by putting $f(t) = a\lambda(t)/(a+t)^{\frac{1}{2}}(a-t)^{\frac{3}{2}}$ and $g(s) = p^+(s) - p^-(s)$. Note that $\lambda(t)$ is of the order $O(t \mp a)$ for $t \rightarrow \pm a$, so that the integrals of $f(t)$ exist. See also [94].

The proof that interchanging the order of integration in (5.113) and (B.11) is allowed, is completed by putting $f(t) = \lambda(t)/\sqrt{a^2 - t^2}$ and $g(s) = m(s)\sqrt{a^2 - s^2}$. See also [93].

B.2 Solution for plate bending

The solution in Subsection 5.3.5 for slightly curved cracks in plate bending contains complicated integral expressions. We shall successively elaborate the functions $b_1(t)$ and $b_2(t)$ in (5.106)–(5.107), the functions $F_1(z)$ and $W_1(z)$ in (5.108)–(5.109) and their limiting behaviour at infinity, the constant C_1 in (5.105), and the contribution (5.110) to the stress-intensity factors.

The functions $b_1(t)$ and $b_2(t)$ with $-a \leq t \leq +a$ are expressed in terms of the boundary values $F_0^\pm(t)$ and $W_0^\pm(t)$ in (5.105). We take $m^\pm(t) = m(t)$ and $f^\pm(t) = f(t)$. With the use of (5.89)–(5.97) we derive

$$b_1(t) = 2i\tilde{C}_1 + \frac{2i\lambda(t)(m - if)'}{(1 - \nu)D} - (2i\lambda(t)b_3(t))', \tag{B.3}$$

$$b_2(t) = -(2i\lambda(t)b_4(t))', \tag{B.4}$$

where the functions $b_3(t)$ and $b_4(t)$ are defined by

$$\begin{aligned} b_3(t) &= \overline{F_0^+(t)} + \overline{F_0^-(t)} - W_0^+(t) - W_0^-(t) \\ &= \frac{\kappa M_{xx}^\infty - M_{yy}^\infty + 2i\kappa M_{xy}^\infty}{(1 - \nu)\kappa D} + \frac{(\kappa - 1)m(t) - i(\kappa + 1)f(t)}{(1 - \nu)\kappa D} \\ &+ \frac{2i(\kappa + 1)}{(1 - \nu)\kappa D \pi a^2} \int_{-a}^{+a} f(s)\sqrt{a^2 - s^2} ds, \end{aligned} \tag{B.5}$$

$$\begin{aligned} b_4(t) &= \overline{F_0^+(t)} - \overline{F_0^-(t)} + W_0^+(t) - W_0^-(t) \\ &= \frac{(\kappa - 1)M_{yy}^\infty t}{(1 - \nu)\kappa D X^+(t)} + \frac{2i(\kappa + 1)t}{(1 - \nu)\kappa D X^+(t) \pi a^2} \int_{-a}^{+a} f(s)\sqrt{a^2 - s^2} ds \\ &- \frac{1}{\pi i X^+(t)} \int_{-a}^{+a} \frac{(\kappa - 1)m(s) - i(\kappa + 1)f(s)}{(1 - \nu)\kappa D} \cdot \frac{X^+(s)}{s - t} ds. \end{aligned} \tag{B.6}$$

These expressions are substituted into (5.108)–(5.109) to produce the solutions for $F_1(z)$ and $W_1(z)$. The limiting behaviour of these functions for $z \rightarrow \infty$ is then found to be given by

$$\kappa F_1(z) + W_1(z) = -\frac{1}{2\pi i z^2} \int_{-a}^{+a} X^+(t) b_1(t) dt + O\left(\frac{1}{z^3}\right), \tag{B.7}$$

$$\kappa F_1(z) - W_1(z) = -\frac{1}{2\pi i z} \int_{-a}^{+a} b_2(t) dt - \frac{1}{2\pi i z^2} \int_{-a}^{+a} b_2(t) t dt + O\left(\frac{1}{z^3}\right). \tag{B.8}$$

It is noted that the term of order $O(1/z)$ in the latter expression vanishes. Namely, with the use of (B.4) and the properties $\lambda(t) = O(t \mp a)$ and $b_4(t) = O((t \mp a)^{-\frac{1}{2}})$ for $t \rightarrow \pm a$, we find

$$\frac{-1}{2\pi i z} \int_{-a}^{+a} b_2(t) dt = \frac{1}{\pi z} \left[\lambda(t) b_4(t) \right]_{-a}^{+a} = 0. \quad (\text{B.9})$$

The constant $\tilde{C}_1 = C_1/(1-\nu)D$ in (B.3) is determined from the condition (5.77) of Subsection 5.3.2 for single-valued displacements. We impose that the coefficient of the term of order $O(1/z^2)$ in the expansion of $W_1(z) - F_1(z)$ has zero imaginary part. From (B.7)–(B.8) we obtain the condition

$$\text{Re} \left\{ (1-\kappa) \int_{-a}^{+a} X^+(t) b_1(t) dt + (1+\kappa) \int_{-a}^{+a} b_2(t) t dt \right\} = 0. \quad (\text{B.10})$$

The solution to this equation for C_1 is derived by substitution of (B.3)–(B.6). After some algebra we find

$$\begin{aligned} C_1 &= (\mathcal{A} - \mathcal{B}) \left(M_{xx}^\infty - \frac{\kappa+2}{\kappa} M_{yy}^\infty \right) \\ &\quad - \frac{2}{\kappa \pi a^2} \int_{-a}^{+a} \sqrt{a^2 - t^2} \left((1-\kappa) \lambda'(t) m(t) + \lambda(t) m'(t) \right) dt \\ &\quad + \frac{2(\kappa+1)}{\kappa(\pi a)^2} \int_{-a}^{+a} \frac{\lambda(t)}{\sqrt{a^2 - t^2}} \int_{-a}^{+a} \frac{m(s) \sqrt{a^2 - s^2}}{s-t} ds dt, \end{aligned} \quad (\text{B.11})$$

where the parameters \mathcal{A} and \mathcal{B} depend on the crack-shape function and are defined by (5.9) and (5.116), respectively. The order of integration in the double integral may be interchanged; see Appendix B.1.

Substitution of (B.3), (B.5), and (B.11) into (5.110) produces the contribution to the stress-intensity factors, which is calculated as

$$\begin{aligned} &-\frac{3(1-\nu)D}{h^2 \sqrt{\pi a}} \int_{-a}^{+a} b_1(t) \left(\frac{a+t}{a-t} \right)^{\frac{1}{2}} dt \\ &= \frac{6\sqrt{\pi a}}{h^2} \left(-2\mathcal{A} M_{xy}^\infty + i\mathcal{B} M_{xx}^\infty + \left(\frac{\kappa+1}{\kappa} \mathcal{A} - \frac{\kappa+2}{\kappa} \mathcal{B} \right) iM_{yy}^\infty \right) \\ &\quad + \frac{6}{h^2 \sqrt{\pi a}} \int_{-a}^{+a} \left(\frac{\kappa+1}{\kappa} \lambda'(t) f(t) + \frac{1}{\kappa} \lambda(t) f'(t) \right) \left(\frac{a+t}{a-t} \right)^{\frac{1}{2}} dt \\ &\quad - \frac{12\mathcal{A}(\kappa+1)}{\kappa h^2 a \sqrt{\pi a}} \int_{-a}^{+a} f(t) \sqrt{a^2 - t^2} dt \\ &\quad - \frac{6i}{h^2 \sqrt{\pi a}} \int_{-a}^{+a} \left(\frac{1-\kappa}{\kappa} \lambda'(t) m(t) + \frac{1}{\kappa} \lambda(t) m'(t) \right) \left(\frac{2t-a}{a} \right) \left(\frac{a+t}{a-t} \right)^{\frac{1}{2}} dt \\ &\quad - \frac{12i(\kappa+1)}{\kappa h^2 (\pi a)^{\frac{3}{2}}} \int_{-a}^{+a} m(t) \sqrt{a^2 - t^2} \int_{-a}^{+a} \frac{\lambda(s)}{\sqrt{a^2 - s^2} (t-s)} ds dt. \end{aligned} \quad (\text{B.12})$$

The derivatives $f'(t)$ and $m'(t)$ are eliminated via integration by parts. We have

$$\int_{-a}^{+a} [\lambda(t) f(t)]' \left(\frac{a+t}{a-t} \right)^{\frac{1}{2}} dt = - \int_{-a}^{+a} \frac{a \lambda(t) f(t)}{(a+t)^{\frac{1}{2}} (a-t)^{\frac{3}{2}}} dt, \quad (\text{B.13})$$

$$\begin{aligned} & \int_{-a}^{+a} [\lambda(t) m(t)]' \left(\frac{2t-a}{a} \right) \left(\frac{a+t}{a-t} \right)^{\frac{1}{2}} dt \\ &= - \int_{-a}^{+a} \frac{(2t-a) \lambda(t) m(t)}{(a+t)^{\frac{1}{2}} (a-t)^{\frac{3}{2}}} dt - \frac{2}{a} \int_{-a}^{+a} \lambda(t) m(t) \left(\frac{a+t}{a-t} \right)^{\frac{1}{2}} dt. \end{aligned} \quad (\text{B.14})$$

Combining the results (B.12)–(B.14) with (5.111) finally produces the stress-intensity factors (5.112)–(5.113) for a thin flat plate containing a curvilinear crack and being loaded by bending and torsional moments.

Appendix C

On damage and thermodynamics

The damage-evolution law, which relates the rate of damage increase to the stresses and the damage in the actual situation, e.g. (1.3), is subject to several restrictions. The energy release during crack propagation or damage accumulation must satisfy the basic laws of thermodynamics, such as the Clausius-Duhem inequality. This is investigated in the first section. We continue with applications to isotropic and anisotropic (orthotropic) damage in planar deformation.

The fundamentals of thermodynamics are extensively treated in the textbooks by Eringen [25, Chs. 4, 5] and Müller [60, Sec. 5.4]. Inclusion of damage parameters in the balance laws of continuum mechanics has been studied by Chaboche [15, 16] and Lemaitre [50]. A summary is presented in the thesis of Paas [72, Ch. 2].

C.1 Clausius-Duhem inequality

Consider a continuous, elastic, deformable body with reference configuration B_0 and deformed configuration $B(t)$ at time t . The position of a material point is denoted by \mathbf{x}_0 in the reference configuration and by $\mathbf{x} = \mathbf{x}(\mathbf{x}_0, t)$ in the deformed configuration. The mass density of the material equals ρ_0 and ρ for B_0 and B , respectively. The deformation of the body is described by the deformation gradient \mathcal{F} , the Lagrange strain tensor \mathcal{E} , and the symmetric rate of deformation tensor \mathcal{L} , which are defined by [25, 60, 72]

$$\mathcal{F} = \frac{\partial \mathbf{x}}{\partial \mathbf{x}_0}, \quad (\text{C.1})$$

$$\mathcal{E} = \frac{1}{2} \left(\mathcal{F}^T \mathcal{F} - \mathcal{I} \right), \quad (\text{C.2})$$

$$\mathcal{L} = \frac{1}{2} \left(\dot{\mathcal{F}} \mathcal{F}^{-1} + \left(\dot{\mathcal{F}} \mathcal{F}^{-1} \right)^T \right), \quad (\text{C.3})$$

where \mathcal{I} is the unit tensor, \mathcal{F}^T denotes the transpose of \mathcal{F} , and the superposed dot indicates the time derivative. We have $\dot{\mathcal{E}} = \mathcal{F}^T \mathcal{L} \mathcal{F}$.

We introduce the Cauchy stress tensor $\boldsymbol{\sigma}$ and the second Piola-Kirchhoff tensor \mathcal{T} , which represent the internal stresses in the body with respect to the deformed and undeformed configurations, respectively. We also introduce the specific internal energy e , the vector \mathbf{h} of heat flow, the absolute temperature θ , the temperature gradient $\mathbf{g}_0 = \partial\theta/\partial\mathbf{x}_0$, the entropy η , and the free energy $\psi = e - \theta\eta$. These quantities must satisfy the balance laws for mass, momentum, angular momentum, and energy [25, 60, 72]. These laws read as follows:

$$J = \det \mathcal{F} = \frac{\rho_0}{\rho}, \quad (\text{C.4})$$

$$\rho \ddot{\mathbf{x}} = \operatorname{div} \boldsymbol{\sigma}^T + \rho \mathbf{b}, \quad (\text{C.5})$$

$$\boldsymbol{\sigma} = \boldsymbol{\sigma}^T, \quad (\text{C.6})$$

$$\rho \dot{e} = \boldsymbol{\sigma} : \mathcal{L} + \rho r - \operatorname{div} \mathbf{h}, \quad (\text{C.7})$$

where \mathbf{b} and r are the specific load and heat supply per unit mass, respectively, which are assumed to be known functions. The equation (C.5) is equivalent to (2.3).

The balance laws do not completely determine the deformation of the body. Extra constitutive relations are required. We impose that the principles of objectivity and of local action [25, 60] are satisfied. Generally, the constitutive quantities are characterised by the strain, the strain rate, the temperature, and the temperature gradient, and also by a set of internal damage parameters \mathcal{D} . The constitutive relations are then given by [72]

$$\boldsymbol{\sigma} = J^{-1} \mathcal{F} \cdot \mathcal{T}(\mathcal{E}, \dot{\mathcal{E}}, \theta, \mathbf{g}_0, \mathcal{D}) \cdot \mathcal{F}^T, \quad (\text{C.8})$$

$$\mathbf{h} = J^{-1} \mathcal{F} \cdot \mathbf{h}_0(\mathcal{E}, \dot{\mathcal{E}}, \theta, \mathbf{g}_0, \mathcal{D}), \quad (\text{C.9})$$

$$\psi = \psi(\mathcal{E}, \dot{\mathcal{E}}, \theta, \mathbf{g}_0, \mathcal{D}), \quad (\text{C.10})$$

$$\eta = \eta(\mathcal{E}, \dot{\mathcal{E}}, \theta, \mathbf{g}_0, \mathcal{D}), \quad (\text{C.11})$$

where \mathbf{h}_0 is the material counterpart of the heat-flow vector \mathbf{h} . In addition, we need a relation for the increase of the damage parameters \mathcal{D} : the so-called damage-evolution equation [16, 50, 72]. This equation can be expressed in the general form

$$\dot{\mathcal{D}} = \dot{\mathcal{D}}(\mathcal{E}, \dot{\mathcal{E}}, \theta, \mathbf{g}_0, \mathcal{D}), \quad \dot{\mathcal{D}} \geq 0. \quad (\text{C.12})$$

Because of (C.8), this relation includes damage-evolution equations which express the rate of damage increase in terms of the stress $\boldsymbol{\sigma}$ and the stress rate $\dot{\boldsymbol{\sigma}}$.

After the specification of the constitutive relations, the deformation behaviour of the body can be determined. The functions \mathcal{T} , \mathbf{h}_0 , ψ , and η must satisfy the second law of thermodynamics or the Clausius-Duhem inequality [25, 60, 72], which states that the local entropy production must be non-negative. In a material (or Lagrange) formulation, this law is expressed as

$$-\rho_0 (\dot{\psi} + \dot{\theta}\eta) + \mathcal{T} : \dot{\mathcal{E}} - \frac{1}{\theta} \mathbf{h}_0 \cdot \mathbf{g}_0 \geq 0. \quad (\text{C.13})$$

We now use the constitutive relation (C.10) and write the time derivative $\dot{\psi}$ in (C.13) as a derivative with respect to the basic variables (\mathcal{E} , $\dot{\mathcal{E}}$, θ , \mathbf{g}_0 and \mathcal{D}) multiplied by

time derivatives of these basic variables. This yields

$$\begin{aligned} \left(\mathcal{T} - \rho_0 \frac{\partial \psi}{\partial \mathcal{E}} \right) : \dot{\mathcal{E}} - \rho_0 \frac{\partial \psi}{\partial \mathcal{E}} : \dot{\mathcal{E}} - \left(\eta + \frac{\partial \psi}{\partial \theta} \right) \rho_0 \dot{\theta} \\ - \rho_0 \frac{\partial \psi}{\partial \mathbf{g}_0} : \dot{\mathbf{g}}_0 - \rho_0 \frac{\partial \psi}{\partial \mathcal{D}} : \dot{\mathcal{D}} - \frac{1}{\theta} \mathbf{h}_0 \cdot \mathbf{g}_0 \geq 0. \end{aligned} \quad (\text{C.14})$$

Since the variables $\dot{\mathcal{E}}$, $\dot{\theta}$, and $\dot{\mathbf{g}}_0$ can be chosen at random, the terms which are linear in these variables must vanish in order that the inequality is satisfied. As a result, we have the following conditions [25, 60, 72]

$$\frac{\partial \psi}{\partial \mathcal{E}} = 0, \quad \eta = - \frac{\partial \psi}{\partial \theta}, \quad \frac{\partial \psi}{\partial \mathbf{g}_0} = 0, \quad (\text{C.15})$$

so that $\psi = \psi(\mathcal{E}, \theta, \mathcal{D})$ and $\eta = \eta(\mathcal{E}, \theta, \mathcal{D})$. Since the damage increase $\dot{\mathcal{D}}$ cannot be chosen at random and may still depend on all other variables (see (C.12)), it is not necessary that the remaining terms vanish separately. Since we are interested in nominally elastic materials, we require that the stresses are independent of the strain rate and we adopt the usual constitutive relation for elastic materials, viz. [72]

$$\mathcal{T} = \rho_0 \frac{\partial \psi}{\partial \mathcal{E}}. \quad (\text{C.16})$$

Consequently, by virtue of (C.15), we also have $\mathcal{T} = \mathcal{T}(\mathcal{E}, \theta, \mathcal{D})$. When the constitutive relations are chosen according to the conditions (C.15)–(C.16), the Clausius-Duhem inequality reduces to [72]

$$- \frac{\partial \rho_0 \psi}{\partial \mathcal{D}} : \dot{\mathcal{D}} - \frac{1}{\theta} \mathbf{h}_0 \cdot \mathbf{g}_0 \geq 0. \quad (\text{C.17})$$

The second term of (C.17) may be omitted for isothermal situations. The remaining inequality is a condition for the relation between the elastic energy density $W = \rho_0 \psi$ and the damage parameters \mathcal{D} , where the dependence occurs through a decrease of the elasticity parameters. Therefore, we focus on the condition [15, 50, 72]

$$- \frac{\partial W}{\partial \mathcal{D}} : \dot{\mathcal{D}} \geq 0. \quad (\text{C.18})$$

Remark 1: In the case of small deformations, linearised theory can be employed, in which no distinction is made between the actual deformed configuration and the original reference configuration. Consequently, the densities ρ and ρ_0 may be equated and the differences between the Cauchy stress tensor $\boldsymbol{\sigma}$ and the second Piola-Kirchhoff tensor \mathcal{T} are negligible.

Remark 2: The damage-evolution equation (C.12) must be postulated and satisfy the inequality (C.18). We shall focus on this inequality for the elastic energy density W and the damage parameters \mathcal{D} .

C.2 Isotropic damage

Consider a two-dimensional deformable body consisting of originally undamaged, isotropic, elastic material loaded under plane-stress conditions. The original material is characterised by Young's modulus E and Poisson's ratio ν . During the deformation, damage occurs in an isotropic fashion. The stress-strain relations are given by (C.16) or, in linearised form, by (2.15). The elastic energy density is equal to

$$W = \frac{E}{2(1-\nu^2)} \left[\varepsilon_{xx}^2 + \varepsilon_{yy}^2 + 2\nu \varepsilon_{xx} \varepsilon_{yy} + 2(1-\nu) \varepsilon_{xy}^2 \right]. \quad (\text{C.19})$$

The isotropic material damage is represented by one (dimensionless) scalar parameter \mathcal{D} with values between 0 and 1. The damage is interpreted as a random distribution of microcracks (see Fig. 1.3) with \mathcal{D} reflecting the reduction in the effective area of a cross section of the damaged body [15, 50]. When damage has occurred, the original Young's modulus and Poisson's ratio are replaced with their values for the damaged material:

$$E_d = (1 - \mathcal{D}) E, \quad (\text{C.20})$$

$$\nu_d = f(\mathcal{D}) \nu, \quad (\text{C.21})$$

where the function $f = f(\mathcal{D})$ is yet unknown. This is the natural manner of defining the damage parameter [15, 50]. Other damage relations can be rewritten in the form (C.20) by redefinition and rescaling of the damage parameter. We shall propose several options for the function f below.

Substitution of (C.20)–(C.21) into (C.19) yields the energy density as a function of the damage parameter. Application of the inequality (C.18) produces

$$\begin{aligned} -\dot{\mathcal{D}} \frac{\partial W}{\partial \mathcal{D}} &= \frac{\dot{\mathcal{D}} E}{2(1-\nu^2 f^2)^2} \left[(1-\nu^2 f^2 - 2(1-\mathcal{D})\nu^2 f f') (\varepsilon_{xx}^2 + \varepsilon_{yy}^2) \right. \\ &\quad \left. + 2\nu((1-\nu^2 f^2)f - (1-\mathcal{D})(1+\nu^2 f^2)f') \varepsilon_{xx} \varepsilon_{yy} \right] \\ &\quad + \frac{\dot{\mathcal{D}} E}{(1+\nu f)^2} [1 + \nu f + (1-\mathcal{D})\nu f'] \varepsilon_{xy}^2 \geq 0, \end{aligned} \quad (\text{C.22})$$

where the prime ' indicates differentiation with respect to \mathcal{D} . Since the damage cannot decrease, we have $\dot{\mathcal{D}} \geq 0$ and the inequality (C.22) is only satisfied when the quadratic form with ε_{xx} and ε_{yy} and the coefficient of ε_{xy}^2 are non-negative definite. According to Section C.4, these conditions are met when

$$1 - \nu^2 f^2(\mathcal{D}) - 2(1-\mathcal{D})\nu^2 f(\mathcal{D}) f'(\mathcal{D}) \geq 0, \quad (\text{C.23})$$

$$1 + \nu f(\mathcal{D}) + (1-\mathcal{D})\nu f'(\mathcal{D}) \geq 0. \quad (\text{C.24})$$

We divide these expressions by $(1-\mathcal{D})^2$ and integrate from $\mathcal{D} = 0$ to the actual damage value \mathcal{D} . For $\mathcal{D} = 0$ we have the original undamaged material and, thus, we have $f(0) = 1$. The integration yields

$$1 - \frac{1+\nu}{\nu} \mathcal{D} \leq f(\mathcal{D}) \leq \left(1 + \frac{1-\nu^2}{\nu^2} \mathcal{D} \right)^{\frac{1}{2}}, \quad (\text{C.25})$$

where $0 < \nu < 0.5$ has been assumed for the original Poisson's ratio in the derivation of the lower bound. It is emphasised that *if* the function $f(\mathcal{D})$ satisfies (C.23)–(C.24), *then* the property (C.25) holds true. The reverse statement is generally not true. When (C.25) is fulfilled, i.e., the function $f(\mathcal{D})$ is between the indicated boundaries, it is still possible that this function has such an oscillating behaviour between the two limits that the conditions (C.23)–(C.24) are violated. For sufficiently smooth functions, however, this problem may not occur.

We shall now present four possible solutions for the function $f(\mathcal{D})$, which satisfy the conditions (C.23)–(C.24). Firstly, an appropriate choice is

$$f(\mathcal{D}) = 1, \quad \nu_d = \nu. \quad (\text{C.26})$$

Since Poisson's ratio does not change with an increase of damage, the shear modulus G_d and the elastic energy density W are proportional to $(1 - \mathcal{D})$, because they scale linearly with Young's modulus.

Secondly, another appropriate choice is that Poisson's ratio decreases proportionally with the damage increase, i.e.,

$$f(\mathcal{D}) = 1 - \mathcal{D}, \quad \nu_d = (1 - \mathcal{D})\nu. \quad (\text{C.27})$$

This means that when the body is loaded by uni-directional tension, the contraction in the perpendicular direction is smaller for damaged material.

A third possibility, which has globally the same property for the contraction as the previous choice, is based on the lower bound in (C.25) and is given by

$$f(\mathcal{D}) = 1 - \frac{1 + \nu}{\nu} \mathcal{D}, \quad 1 + \nu_d = (1 - \mathcal{D})(1 + \nu). \quad (\text{C.28})$$

This damage function has the special property that the shear modulus, which equals $G_d = E_d/2(1 + \nu_d)$, does not change with damage increase. It is noted that ν_d attains a negative value for $\mathcal{D} > \nu/(1 + \nu)$, but we still have $-1 \leq \nu_d \leq 0.5$.

A fourth possibility, which has the property that the contraction is larger for damaged material, is based on the upper bound in (C.25) and is given by

$$f(\mathcal{D}) = \left(1 + \frac{1 - \nu^2}{\nu^2} \mathcal{D}\right)^{\frac{1}{2}}, \quad 1 - \nu_d^2 = (1 - \mathcal{D})(1 - \nu^2). \quad (\text{C.29})$$

This damage function has the special property that the combination $E_d/(1 - \nu_d^2)$, which often occurs in expressions for plane stress, does not change with damage increase. Since we must have $\nu_d \leq 0.5$, we have the restriction $\mathcal{D} \leq (1 - 4\nu^2)/4(1 - \nu^2)$.

C.3 Orthotropic damage

Consider a two-dimensional deformable body consisting of originally undamaged, isotropic, elastic material loaded under plane-stress conditions. The original material is

characterised by Young's modulus E and Poisson's ratio ν . During the deformation, damage may occur in an anisotropic fashion with a preferred direction for the microcracks as shown in Fig. 7.3. The material behaviour is described by an orthotropic model; see Section 7.4 and Zienkiewicz [100]. The elastic energy density is derived from (7.24)–(7.25) with symmetry condition (7.26) as

$$W = \frac{1}{2(1 - \nu_{xy}\nu_{yx})} \left[E_x \varepsilon_{xx}^2 + E_y \varepsilon_{yy}^2 + (E_x \nu_{xy} + E_y \nu_{yx}) \varepsilon_{xx} \varepsilon_{yy} \right] + 2G_{xy} \varepsilon_{xy}^2. \quad (\text{C.30})$$

We characterise the orthotropic material damage by two scalar parameters \mathcal{D}_x and \mathcal{D}_y representing the reduction in the effective area of a cross section of the damaged body in two perpendicular directions. These parameters can also be interpreted as the principal values of a damage tensor with orthogonal principal directions along the x - and y -axes; see Murakami [61]. Together with E and ν of the original material, we have four parameters to describe the orthotropic material behaviour. The relations with the elasticity constants can be written as

$$E_x = (1 - \mathcal{D}_x) E, \quad (\text{C.31})$$

$$E_y = (1 - \mathcal{D}_y) E, \quad (\text{C.32})$$

$$\nu_{xy} = (1 - \mathcal{D}_y) f(\mathcal{D}_x, \mathcal{D}_y) \nu, \quad (\text{C.33})$$

$$\nu_{yx} = (1 - \mathcal{D}_x) f(\mathcal{D}_x, \mathcal{D}_y) \nu, \quad (\text{C.34})$$

$$G_{xy} = g(\mathcal{D}_x, \mathcal{D}_y) G, \quad (\text{C.35})$$

where $G = E/2(1 + \nu)$ is the shear modulus of the undamaged material. Clearly, the symmetry condition (7.26) for ν_{xy} and ν_{yx} is satisfied. The functions $f = f(\mathcal{D}_x, \mathcal{D}_y)$ and $g = g(\mathcal{D}_x, \mathcal{D}_y)$ are yet unknown and we shall propose several options for these functions below.

Substitution of (C.31)–(C.35) into (C.30) yields the energy density as a function of the damage parameters. Since $\mathcal{D}_x \geq 0$ and $\mathcal{D}_y \geq 0$ are independent variables, application of the inequality (C.18) produces two conditions:

$$-\frac{\partial W}{\partial \mathcal{D}_x} \geq 0, \quad -\frac{\partial W}{\partial \mathcal{D}_y} \geq 0. \quad (\text{C.36})$$

We shall focus on the first condition. Denoting differentiation with respect to \mathcal{D}_x by the prime ', we obtain

$$\begin{aligned} -\frac{\partial W}{\partial \mathcal{D}_x} &= \frac{E}{2(1 - \nu_{xy}\nu_{yx})^2} \left[\left(1 - 2\nu^2(1 - \mathcal{D}_x)^2(1 - \mathcal{D}_y)ff' \right) \varepsilon_{xx}^2 \right. \\ &+ \nu^2(1 - \mathcal{D}_y)^2 \left(f^2 - 2(1 - \mathcal{D}_x)ff' \right) \varepsilon_{yy}^2 \\ &+ 2\nu(1 - \mathcal{D}_y) \left(f - (1 - \mathcal{D}_x)f' - \nu^2(1 - \mathcal{D}_x)^2(1 - \mathcal{D}_y)f^2f' \right) \varepsilon_{xx} \varepsilon_{yy} \left. \right] \\ &- 2Gg' \varepsilon_{xy}^2 \geq 0. \end{aligned} \quad (\text{C.37})$$

This inequality is only satisfied, when the coefficient of ε_{xy}^2 is non-negative and the quadratic form in ε_{xx} and ε_{yy} is non-negative definite. Consequently, the function

g must be non-increasing in both its arguments and, according to Section C.4, the function f must satisfy

$$1 + \nu^2(1 - \mathcal{D}_y)^2 f^2 - 2\nu^2(1 - \mathcal{D}_x)(1 - \mathcal{D}_y)(2 - \mathcal{D}_x - \mathcal{D}_y) f f' \geq 0, \quad (\text{C.38})$$

$$- \nu^2(1 - \mathcal{D}_x)^2(1 - \mathcal{D}_y)^2 [1 - \nu^2(1 - \mathcal{D}_x)(1 - \mathcal{D}_y)f^2]^2 (f')^2 \geq 0. \quad (\text{C.39})$$

As a result of (C.39), the derivative $\partial f/\partial \mathcal{D}_x$ must vanish and, by a similar argument for the second inequality of (C.36), the derivative $\partial f/\partial \mathcal{D}_y$ too. This implies that the function f is necessarily constant. In that case, the condition (C.38) is also satisfied and the quadratic form in ε_{xx} and ε_{yy} is indeed non-negative definite.

The conditions for thermodynamic admissibility can be summarised as

$$f(\mathcal{D}_x, \mathcal{D}_y) = 1, \quad \frac{\partial g}{\partial \mathcal{D}_x} \leq 0, \quad \frac{\partial g}{\partial \mathcal{D}_y} \leq 0. \quad (\text{C.40})$$

The contraction ratios ν_{xy} and ν_{yx} in (C.33) and (C.34) are now similar to the choice (C.27) for isotropic damage behaviour. There exist several possibilities for the function g of the shear modulus. Some choices which satisfy the conditions (C.40) are

$$G_{xy} = \left(\frac{1 + \nu_{yx}}{E_x} + \frac{1 + \nu_{xy}}{E_y} \right)^{-1}, \quad (\text{C.41})$$

$$G_{xy} = \left(\frac{E_x}{2(1 + \nu_{yx})} \cdot \frac{E_y}{2(1 + \nu_{xy})} \right)^{1/2}, \quad (\text{C.42})$$

$$G_{xy} = \frac{1}{2} \left(\frac{E_x}{2(1 + \nu_{yx})} + \frac{E_y}{2(1 + \nu_{xy})} \right). \quad (\text{C.43})$$

In the case of isotropic damage, i.e., when $\mathcal{D}_x = \mathcal{D}_y = \mathcal{D}$, the two Young's moduli are equal and two contraction ratios coincide. The relations (C.41)–(C.43) reduce to the same equation

$$G_{xy} = \frac{(1 - \mathcal{D}) E}{2(1 + (1 - \mathcal{D})\nu)}. \quad (\text{C.44})$$

Thus, the shear modulus G_{xy} satisfies the additional requirement that, in the case of isotropically oriented damage, the orthotropic material must behave in an isotropic sense, namely $G_{xy} = G_d = E_d/2(1 + \nu_d)$.

C.4 Positive definite functions

Consider the quadratic form in two real variables

$$F(x, y) = ax^2 + 2bxy + cy^2. \quad (\text{C.45})$$

This function can also be cast in the matrix-vector form

$$F(\mathbf{x}) = \mathbf{x}^T A \mathbf{x} \quad \text{with} \quad \mathbf{x} = \begin{bmatrix} x \\ y \end{bmatrix}, \quad A = \begin{bmatrix} a & b \\ b & c \end{bmatrix}. \quad (\text{C.46})$$

The function is called positive definite when it attains positive values for all points $(x, y) \neq (0, 0)$; see Golub and Van Loan [29, Ch. 1]. The definition for non-negative definite (or positive semi-definite) functions is analogous. When the function attains both positive and negative values, it is called indefinite.

Since the matrix A is symmetric, it has two real eigenvalues λ_1 and λ_2 [29, Ch. 8]. The function F is positive definite if and only if both eigenvalues of A are positive. This condition can be expressed as

$$\lambda_1 + \lambda_2 = a + c > 0, \quad (\text{C.47})$$

$$\lambda_1 \lambda_2 = ac - b^2 > 0. \quad (\text{C.48})$$

Instead of (C.47), we may also impose $a > 0$ and $c > 0$. For non-negative definiteness the $>$ signs must be replaced by \geq signs.

Bibliography

1. J.D. ACHENBACH AND Z.P. BAŽANT, Elastodynamic near-tip stress and displacement fields for rapidly propagating cracks in orthotropic materials. *Transactions of ASME, Journal of Applied Mechanics* **42** (1975) 183–189.
2. S.N. ATLURI, Path-independent integrals in finite elasticity and inelasticity, with body forces, inertia, and arbitrary crack-face conditions. *Engineering Fracture Mechanics* **16** (1982) 341–364.
3. R.S. BARSOU, On the use of isoparametric finite elements in linear fracture mechanics. *International Journal for Numerical Methods in Engineering* **10** (1976) 25–37.
4. Z.P. BAŽANT AND L. CEDOLIN, *Stability of Structures. Elastic, Inelastic, Fracture, and Damage Theories*. Oxford University Press, New York (1991).
5. T. BELYTSCHKO, J. FISH AND B.E. ENGELMANN, A finite element with embedded localization zones. *Computer Methods in Applied Mechanics and Engineering* **70** (1988) 59–89.
6. T. BELYTSCHKO, Y.Y. LU AND L. GU, Element-free Galerkin methods. *International Journal for Numerical Methods in Engineering* **37** (1994) 229–256.
7. T. BELYTSCHKO, J.S.J. ONG, W.K. LIU AND J.M. KENNEDY, Hourglass control in linear and nonlinear problems. *Computer Methods in Applied Mechanics and Engineering* **43** (1984) 251–276.
8. J. BOERSMA, Private communication (1995).
9. R. DE BORST, Private communication (1995).
10. R. DE BORST, L.J. SLUYS, H.-B. MÜHLHAUS AND J. PAMIN, Fundamental issues in finite element analysis of localization of deformation. *Engineering Computations* **10** (1993) 99–121.
11. D. BROEK, *Elementary Engineering Fracture Mechanics*. Kluwer Academic Publishers, Dordrecht, The Netherlands (1986).
12. CANADIAN STANDARDS ASSOCIATION AND UNDERWRITERS LABORATORY, *Cathode-Ray Tubes*, Binational Standard CAN/CSA–C22.2 No. 228 and UL 1418, First Edition. Canadian Standards Association, Rexdale, Ontario (1992).

13. G.F. CARRIER, M. KROOK AND C.E. PEARSON, *Functions of a Complex Variable. Theory and Technique*. McGraw-Hill, New York (1966).
14. J.L. CHABOCHE, Continuum damage mechanics — a tool to describe phenomena before crack initiation. *Nuclear Engineering and Design* **64** (1981) 233–247.
15. J.L. CHABOCHE, Continuum damage mechanics: part I — general concepts. *Transactions of ASME, Journal of Applied Mechanics* **55** (1988) 59–64.
16. J.L. CHABOCHE, Continuum damage mechanics: part II — damage growth, crack initiation, and crack growth. *Transactions of ASME, Journal of Applied Mechanics* **55** (1988) 65–72.
17. C.K. CHAO AND W.J. HUANG, Antiplane problem of curvilinear cracks in bonded dissimilar materials. *International Journal of Fracture* **64** (1993) 179–190.
18. G.P. CHEREPANOV, *Mechanics of Brittle Fracture*. McGraw-Hill, New York (1979).
19. B. COTTERELL AND J.R. RICE, Slightly curved or kinked cracks. *International Journal of Fracture* **16** (1980) 155–169.
20. M.A. CRISFIELD, Local instabilities in the non-linear analysis of reinforced concrete beams and slabs. *Proceedings of the Institution of Civil Engineers, Part 2: Research and Theory* **73** (1982) 135–145, 693–694.
21. T.M.R. ELLIS, I.R. PHILIPS AND T.M. LAHEY, *Fortran 90 Programming*. Addison-Wesley Publishing Company, Wokingham, England (1994).
22. A.H. ENGLAND, A crack between dissimilar media. *Transactions of ASME, Journal of Applied Mechanics* **32** (1965) 400–402.
23. F. ERDOGAN AND G.C. SIH, On crack extension in plates under plane loading and transverse shear. *Transactions of ASME, Journal of Basic Engineering* **85** (1963) 519–527.
24. F. ERDOGAN, O. TUNCEL AND P.C. PARIS, An experimental investigation of the crack tip stress intensity factors in plates under cylindrical bending. *Transactions of ASME, Journal of Basic Engineering* **84** (1962) 542–546.
25. A.C. ERINGEN, *Mechanics of Continua*. John Wiley & Sons, New York (1967).
26. EUROPEAN STANDARD EN 60065, *Safety requirements for mains operated electronic and related apparatus for household and similar general use*. (IEC 65:1985+A1:1987+A2:1989+A3:1992, modified). European Committee for Electrotechnical Standardization CENELEC, Brussels (1993).
27. P.H. FEENSTRA, *Computational Aspects of Biaxial Stress in Plain and Reinforced Concrete*. PhD Thesis, Delft University of Technology (1993).

28. L.B. FREUND, *Dynamic Fracture Mechanics*. Cambridge University Press, Cambridge (1990).
29. G.H. GOLUB AND C.F. VAN LOAN, *Matrix Computations*. North Oxford Academic, Oxford (1983).
30. I.S. GRADSHTEYN AND I.M. RYZHIK, *Tables of Integrals, Series, and Products*. Academic Press, San Diego (1980).
31. A.A. GRIFFITH, The phenomena of rupture and flow in solids. *Philosophical Transactions of the Royal Society of London* **A221** (1920) 163–198.
32. R.J. HARTRANFT AND G.C. SIH, Effect of plate thickness on the bending stress distribution around through cracks. *Journal of Mathematics and Physics* **47** (1968) 276–291.
33. D. HEGEN, *Numerical Techniques for the Simulation of Crack Growth*. Final report of the postgraduate programme Mathematics for Industry, Eindhoven University of Technology (1994).
34. H.M. HILBER, T.J.R. HUGHES AND R.L. TAYLOR, Improved numerical dissipation for time integration algorithms in structural dynamics. *Earthquake Engineering and Structural Dynamics* **5** (1977) 283–292.
35. A.T. DE HOOP, A modification of Cagniard's method for solving seismic pulse problems. *Applied Scientific Research* **B8** (1961) 349–356.
36. J. HORSTEN AND J. VAN VROONHOVEN, A hybrid fracture-damage crack propagation model. *Localized Damage III, Computer-Aided Assessment and Control*, Proceedings of the 3rd International Conference on Localized Damage, Udine, Italy (1994) 367–374.
37. T.J.R. HUGHES, *The Finite Element Method. Linear Static and Dynamic Finite Element Analysis*. Prentice-Hall, Englewood Cliffs NJ (1987).
38. C.Y. HUI AND A.T. ZEHNDER, A theory for the fracture of thin plates subjected to bending and twisting moments, *International Journal of Fracture* **61** (1993) 211–229.
39. N. IOSIPESCU, New accurate procedure for single shear testing of metals. *Journal of Materials* **2** (1967) 537–566.
40. B.M. IRONS, Quadrature rules for brick based finite elements. *International Journal for Numerical Methods in Engineering* **3** (1971) 293–294.
41. G.R. IRWIN, Analysis of stresses and strains near the end of a crack traversing a plate. *Transactions of ASME, Journal of Applied Mechanics* **24** (1957) 361–364.
42. G.R. IRWIN, Fracture. *Encyclopedia of Physics (Handbuch der Physik)*, Vol. VI, *Elasticity and Plasticity*, S. Flügge (Ed.), Springer Verlag, Berlin (1958) 551–590.

43. K.L. JOHNSON, *Contact Mechanics*. Cambridge University Press, Cambridge (1985).
44. L.M. KACHANOV, The time to fracture under creep conditions (Translation from the Russian). *Izvestiya Akademii Nauk SSSR, Otdelenie Tekhnicheskikh Nauk* (1958), No. 8, 26–31.
45. H.A.J. KNOPS, *Numerical Simulation of Crack Growth in Pressurized Fuselages*. PhD Thesis, Delft University of Technology (1994).
46. J.K. KNOWLES AND N.M. WANG, On the bending of an elastic plate containing a crack. *Journal of Mathematics and Physics* **39** (1960) 223–236.
47. D. KOSLOFF AND G.A. FRAZIER, Treatment of hourglass patterns in low order finite element codes. *International Journal for Numerical and Analytical Methods in Geomechanics* **2** (1978) 57–72.
48. H.V. LAKSHMINARAYANA AND M.V.V. MURTHY, On stresses around an arbitrarily oriented crack in a cylindrical shell. *International Journal of Fracture* **12** (1976) 547–566.
49. D. LASRY AND T. BELYTSCHKO, Localization limiters in transient problems. *International Journal of Solids and Structures* **24** (1988) 581–597.
50. J. LEMAITRE, How to use damage mechanics. *Nuclear Engineering and Design* **80** (1984) 233–245.
51. LI YINGZHI AND D.A. HILLS, The Hertzian cone crack. *Transactions of ASME, Journal of Applied Mechanics* **58** (1991) 120–127.
52. H. LIEBOWITZ, *Fracture, An Advanced Treatise, Vols. I–VII*. Academic Press, New York and London (1968–1972).
53. Y.Y. LU, T. BELYTSCHKO AND L. GU, A new implementation of the element free Galerkin method. *Computer Methods in Applied Mechanics and Engineering* **113** (1994) 397–414.
54. J. LUBLINER, J. OLIVER, S. OLLER AND E. OÑATE, A plastic-damage model for concrete. *International Journal of Solids and Structures* **25** (1989) 299–326.
55. R.H. MACNEAL, A simple quadrilateral shell element. *Computers and Structures* **8** (1978) 175–183.
56. R.H. MACNEAL, *Finite Elements: Their Design and Performance*. Marcel Dekker, New York (1994).
57. MATLAB, *High-Performance Numeric Computation and Visualization Software. Reference Guide*. The MathWorks, Natick MA (1992).
58. V.A. MERKULOV, Flexure of plates with straight-line or circular-arc cracks. *Mechanics of Solids* **10** (1975) 146–152.

59. R.D. MINDLIN, Influence of rotatory inertia and shear on flexural motions of isotropic, elastic plates. *Transactions of ASME, Journal of Applied Mechanics* **18** (1951) 31–38.
60. I. MÜLLER, *Thermodynamics*. Pitman Publishing, Boston/London (1985).
61. S. MURAKAMI, Mechanical modelling of material damage. *Transactions of ASME, Journal of Applied Mechanics* **55** (1988) 280–286.
62. N.I. MUSKHELISHVILI, *Singular Integral Equations*. Noordhoff, Groningen, The Netherlands (1953).
63. N.I. MUSKHELISHVILI, *Some Basic Problems of the Mathematical Theory of Elasticity*. Noordhoff, Groningen, The Netherlands (1953).
64. NEDERLANDSE NORM NEN-EN 60065, *Veiligheidseisen voor elektronische en aanverwante toestellen met netvoeding voor huishoudelijk en soortgelijk algemeen gebruik*. Nederlands Normalisatie-instituut, Delft (1994). Contains [26].
65. A. NEEDLEMAN, Material rate dependence and mesh sensitivity in localization problems. *Computer Methods in Applied Mechanics and Engineering* **67** (1988) 69–85.
66. T. NISHIOKA, Invariance of the elastodynamic J integral (J'), with respect to the shape of an infinitesimal process zone. *Engineering Fracture Mechanics* **32** (1989) 309–319.
67. T. NISHIOKA AND S.N. ATLURI, Path-independent integrals, energy release rates, and general solutions of near-tip fields in mixed-mode dynamic fracture mechanics. *Engineering Fracture Mechanics* **18** (1983) 1–22.
68. T. NISHIOKA, R. MURAKAMI AND Y. TAKEMOTO, The use of the dynamic J integral (J') in finite-element simulation of Mode I and mixed-mode dynamic crack propagation. *International Journal of Pressure Vessels and Piping* **44** (1990) 329–352.
69. B. NOBLE, *Methods Based on the Wiener-Hopf Technique for the Solution of Partial Differential Equations*. Pergamon Press, London (1958).
70. E. OROWAN, Energy criteria of fracture. *Welding Journal Research Supplement* **34** (1955) 157s–160s.
71. M. ORTIZ, Y. LEROY AND A. NEEDLEMAN, A finite element method for localized failure analysis. *Computer Methods in Applied Mechanics and Engineering* **61** (1987) 189–214.
72. M. PAAS, *Continuum Damage Mechanics with an Application to Fatigue*. PhD Thesis, Eindhoven University of Technology (1990).
73. G. PIJAUDIER-CABOT AND Z.P. BAŽANT, Nonlocal damage theory. *Journal of Engineering Mechanics* **113** (1987) 1512–1533.

74. E. REISSNER, The effect of transverse shear deformation on the bending of elastic plates. *Transactions of ASME, Journal of Applied Mechanics* **12** (1945) A69–A77.
75. E. REISSNER, On bending of elastic plates. *Quarterly of Applied Mathematics* **V** (1947) 55–68.
76. J.R. RICE, A path independent integral and the approximate analysis of strain concentration by notches and cracks. *Transactions of ASME, Journal of Applied Mechanics* **35** (1968) 379–386.
77. J.R. RICE, Elastic fracture mechanics concepts for interfacial cracks. *Transactions of ASME, Journal of Applied Mechanics* **55** (1988) 98–103.
78. H.A. RICHARD, Safety estimation for construction units with cracks under complex loading. *Structural Failure, Product Reliability and Technical Insurance*, H.P. Rossmann (Ed.), Inderscience Enterprises, Geneva (1987) 423–437.
79. J.G. ROTS, Smearred and discrete representations of localized fracture. *International Journal of Fracture* **51** (1991) 45–59.
80. G.N. SAVIN, *Stress Concentration around Holes*. Pergamon Press, Oxford (1961).
81. E. SCHLANGEN, *Experimental and Numerical Analysis of Fracture Processes in Concrete*. PhD Thesis, Delft University of Technology (1993).
82. SEPRAN, *Sepra Analysis. Users Guide and Programmers Manual*. Ingenieursbureau Sepra, Leidschendam, The Netherlands (1993).
83. G.C. SIH, Stress distribution near internal crack tips for longitudinal shear problems. *Transactions of ASME, Journal of Applied Mechanics* **32** (1965) 51–58.
84. G.C. SIH, P.C. PARIS AND F. ERDOGAN, Crack-tip, stress-intensity factors for plane extension and plate bending problems, *Transactions of ASME, Journal of Applied Mechanics* **29** (1962) 306–312.
85. L.J. SLUYS, *Wave Propagation, Localisation and Dispersion in Softening Solids*. PhD Thesis, Delft University of Technology (1992).
86. M. STERN, Families of consistent conforming elements with singular derivative fields. *International Journal for Numerical Methods in Engineering* **14** (1979) 409–421.
87. M. STERN AND E.B. BECKER, A conforming crack tip element with quadratic variation in the singular fields. *International Journal for Numerical Methods in Engineering* **12** (1978) 279–288.
88. E. STERNBERG, On the integration of the equations of motion in the classical theory of elasticity. *Archive for Rational Mechanics and Analysis* **6** (1960) 34–50.

89. R.L. TAYLOR, P.J. BERESFORD AND E.L. WILSON, A non-conforming element for stress analysis. *International Journal for Numerical Methods in Engineering* **10** (1976) 1211–1219.
90. S.P. TIMOSHENKO AND S. WOINOWSKY-KRIEGER, *Theory of Plates and Shells*. McGraw-Hill Kogakusha, Tokyo (1959).
91. P.H.J. VOSBEEK, *A Micromechanical Approach to Deformation and Failure of Discrete Media*. PhD Thesis, Eindhoven University of Technology (1994).
92. J.C.W. VAN VROONHOVEN, On path-independent integrals for dynamic fracture. *Reliability and Structural Integrity of Advanced Materials*, Proceedings of 9th European Conference on Fracture ECF-9, Varna, Bulgaria (1992) 885–890.
93. J.C.W. VAN VROONHOVEN, Stress intensity factors for curvilinear cracks loaded by bending and torsional moments. *International Journal of Fracture* **68** (1994) 193–218.
94. J.C.W. VAN VROONHOVEN, Stress intensity factors for curvilinear cracks loaded under anti-plane strain (mode III) conditions. *International Journal of Fracture* **70** (1995) 1–18.
95. N.M. WANG, Effects of plate thickness on the bending of an elastic plate containing a crack. *Journal of Mathematics and Physics* **47** (1968) 371–390.
96. E.L. WILSON, R.L. TAYLOR, W.P. DOHERTY AND J. GHABOUSSI, Incompatible displacement models. *Numerical and Computer Methods in Structural Mechanics*, S.J. Fenves, N. Perrone, A.R. Robinson and W.C. Schnobrich (Eds.), Academic Press, New York (1973) 43–57.
97. M.J. YOUNG AND C.T. SUN, Influence of crack closure on the stress intensity factor in bending plates — A classical plate solution. *International Journal of Fracture* **55** (1992) 81–93.
98. M.J. YOUNG AND C.T. SUN, Cracked plates subjected to out-of-plane tearing loads. *International Journal of Fracture* **60** (1993) 1–18.
99. M.J. YOUNG AND C.T. SUN, On the strain energy release rate for a cracked plate subjected to out-of-plane bending moment. *International Journal of Fracture* **60** (1993) 227–247.
100. O.C. ZIENKIEWICZ, *The Finite Element Method*. McGraw-Hill, London (1977).

Curriculum vitae

- 21 april 1963 geboren te Eindhoven
- 1975–1981 Scholengemeenschap Augustinianum Eindhoven.
Diploma V.W.O. Gymnasium B.
- 1981–1988 Technische Universiteit Eindhoven.
Studierichting wiskunde, afstudeerrichting mechanica.
Ingenieursdiploma behaald in maart 1988 (met lof).
- Stage op het gebied van glasvezels en optische golfgeleiders bij PTT Research (dr. Neher Laboratorium) te Leidschendam.
Afstudeerproject op het gebied van stromingsleer, toegepast op extrusie- en spuitgietprocessen voor kunststoffen.
- 1988–1989 Fysisch Electronisch Laboratorium TNO in Den Haag.
Onderzoek infraroodbeeldverwerking, als militaire dienst.
- 1989–1995 Philips Natuurkundig Laboratorium te Eindhoven.
Wetenschappelijk medewerker in de groep "Mechanics" geleid door ir. B. Sastra.
Onderzoek naar breuk in chip-omhullingen (IC packaging), productie van schaduwmaskers, glasveiligheid van beeldbuizen.
Het laatste onderwerp vormt de basis van dit proefschrift.
- 1995–heden Philips Natuurkundig Laboratorium te Eindhoven.
Wetenschappelijk medewerker in de groep "Materials Mechanics and Heat Transfer" geleid door dr. J.R.R. Pankert.
Onderzoek naar het statistisch bezwijkgedrag van materialen en nieuwe veiligheidsconcepten voor beeldbuizen.

The author of this thesis was born in 1963 in Eindhoven, The Netherlands, where he received his secondary education at Gymnasium Augustinianum during the years 1975–1981. He studied mathematics at the Eindhoven University of Technology from 1981 to 1988 and specialised in mechanics and applied analysis. In March 1988, he obtained the Engineer degree in mathematics (cum laude). The subject of his thesis was free-boundary problems in viscous fluid flow, with applications to extrusion and injection moulding. After military service at the Physics and Electronics Laboratory in The Hague, he joined the Philips Research Laboratories in Eindhoven. His work on fracture mechanics and the applications to the safety of television picture tubes is the subject of this PhD thesis.

Dankwoord

Dit proefschrift is tot stand gekomen dankzij de medewerking van velen, hetzij rechtstreeks, onderzoekend, begeleidend, hetzij op de achtergrond, ondersteunend, ruimte gevend. Enkelen van hen wil ik hier met name bedanken.

De leden van de kerncommissie. De discussies met mijn eerste promotor prof. R. de Borst hebben mij een duidelijker beeld van de (on)mogelijkheden van schademechanica gegeven, hetgeen heeft bijgedragen tot het idee om de hybride breuk/schade-aanpak te ontwikkelen. Bijzondere dank ben ik verschuldigd aan prof. J. Boersma, die grote delen van het proefschrift nauwgezet heeft gecontroleerd; zijn suggesties hebben geleid tot diverse verbeteringen zowel ten aanzien van de wiskundige formuleringen als het Engels. Het enthousiasme van Fons van de Ven mag evenmin onvermeld blijven: reeds vanaf het begin van mijn studie heeft hij mijn interesse in de mechanica aangewakkerd. De opmerkingen van oud-collega's Bert de With en Frank Baaijens, vanuit andere invalshoeken, vormden een goede aanvulling.

De collega's van het Nat.Lab. Voor de aangename en gezellige sfeer, zowel tijdens het werk als daarbuiten, bedank ik alle (ex-)leden van de mechanica-groep. De discussies met Peter Rongen, Leo Tielemans, Peter van Hoogstraten, Wilbert van den Eijnde, Willem Potze en Jurgen Rusch over allerlei onderwerpen waren zeer leerzaam en/of vermakelijk. De samenwerking met Joost Horsten heeft geleid tot een unieke uitwisseling van kennis over numerieke methoden en breukmechanica. Het experimentele werk van Jos Mooren is een waardevolle ondersteuning geweest bij de uitvoering van het „impact” project.

De collega's van ITC en CFT. Voor de plezierige samenwerking gedurende het onderzoek van de glasveiligheid van beeldbuizen gaat mijn dank uit naar alle betrokkenen bij dit project: Ad van den Eeden, Jan Willem Kleine, Joop van der Wielen, Harry van der Avoort, Frank Gersmann, Fred Smits, Paul Sterken en Willem Koenders.

Familie en vrienden. Zonder hun steun was deze taak haast onuitvoerbaar geweest. In het bijzonder wil ik mijn ouders bedanken, die mij steeds hebben aangespoord tijdens mijn studie en werk, en ook mijn vrienden die veel belangstelling hebben getoond maar mij het laatste jaar eigenlijk te weinig hebben gezien. En het meest van allen: Marie-Thérèse, die mij de ruimte heeft gegeven om dit proefschrift te schrijven tijdens een drukke periode in ons leven, en die tegelijkertijd meer „muziek” in mijn leven heeft gebracht.

Stellingen

behorende bij het proefschrift

Dynamic Crack Propagation in Brittle Materials:
Analyses Based on Fracture and Damage Mechanics

van

J.C.W. van Vroonhoven

1. Door het combineren van breukmechanica en schademechanica ontstaan nieuwe mogelijkheden voor het onderzoeken van het bezwijkgedrag van materialen en constructies.

Dit proefschrift, hoofdstukken 1 en 8–10.

2. Het invoeren van een gegeneraliseerd torsiemoment in de klassieke plaattheorie is zinvol voor het berekenen van scheurgroei in dunne platen die belast worden door buigende momenten.

Dit proefschrift, hoofdstukken 2, 4 en 5.

3. Substitutie van een oneindig grote waarde voor de dwarscontractiecoëfficiënt in oplossingen voor breukproblemen volgens de klassieke plaattheorie leidt in veel gevallen tot overeenkomstige oplossingen volgens de plaattheorie van Reissner.

Dit proefschrift, hoofdstukken 4 en 5.

4. De op numerieke resultaten gebaseerde conclusie van Nishioka, dat de elastodynamische J_2 -integraal onafhankelijk zou zijn van de keuze van de integratiecontour, wordt weerlegd door analytische berekening van deze integraal voor twee verschillende contouren.

T. Nishioka, *Engineering Fracture Mechanics* **32** (1989) 309–319.

J.C.W. van Vroonhoven, *Proceedings of the 9th European Conference on Fracture ECF-9*, Varna, Bulgaria (1992) 885–890.

Dit proefschrift, appendix A.

5. Zij $a(\varphi)$ het aantal absolute punten van de polariteit φ gedefinieerd op de symmetrische partiële meetkunde $pg(s, s, \alpha)$.
 - a. Voor oneven α geldt $a(\varphi) \geq 1 + s^2/\alpha$; voorts is $a(\varphi) = 1 + s^2/\alpha$ dan en slechts dan als iedere lijn één absoluut punt bevat.
 - b. Voor even α geldt $a(\varphi) = 0$ of $a(\varphi) \geq s + 1$; voorts is $a(\varphi) = s + 1$ dan en slechts dan als iedere niet-absolute lijn 0 of 2 absolute punten bevat en ieder tweetal absolute punten door een lijn verbonden is.

P.R.J.M. Smits and J.C.W. van Vroonhoven,

Geometriae Dedicata **21** (1986) 51–54.

6. De vervaardiging van optische golfgeleiders kan worden geformuleerd als een ionenuitwisselingsprobleem tussen een gedeeltelijk afgedekt substraat en een zoutbad, onder invloed van een elektrisch veld. Dit probleem wordt door Forrest, Pagano en Viehmann op incorrecte wijze opgelost.

K. Forrest, S.J. Pagano and W. Viehmann, *IEEE/OSA Journal of Lightwave Technology* **LT-4** (1986) 140–150.

J.C.W. van Vroonhoven, Stageverslag, TU Eindhoven (1986).

7. De vrije rand in stromingsproblemen voor lineair viskeuze (Newtonse) vloeistoffen, zoals bijvoorbeeld bij extrusie- en spuitgietprocessen, kan worden berekend met behulp van de theorie van complexe functies en conforme afbeeldingen.

J.C.W. van Vroonhoven, A.J.M. Sipers and W.J.J. Kuijpers,

Journal of Engineering Mathematics **24** (1990) 151–165, 167–178.

8. In navolging van advertenties voor tabaksartikelen dienen reclameboodschappen voor technologisch hoogwaardige produkten afkomstig uit het Verre Oosten vergezeld te gaan van de waarschuwing: „Het kopen van dit produkt brengt ernstige schade toe aan de Europese c.q. de Nederlandse economie. Het kan werkloosheid en recessies veroorzaken.”
9. Gezien het overeenkomstig belang als persoonlijk vervoermiddel van het paard ten tijde van het wilde Westen en van de fiets in de huidige tijd, dient voor diefstal van deze vervoermiddelen ook een overeenkomstige strafmaat gehanteerd te worden.
10. Het grote aantal oppervlakkige, inhoudsloze televisieprogramma's staat een snelle ontwikkeling van de vlakke, platte beeldbuis niet in de weg.
11. Het proeven van bier en het brouwen van bier zijn twee verschillende zaken; toch is kennis van het één noodzakelijk voor de kunde van het ander.